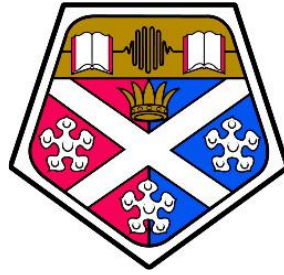


UNIVERSITY OF STRATHCLYDE  
Faculty of Engineering  
Department of Biomedical Engineering  
DOCTORATE DISSERTATION  
PhD Biomedical Engineering

**Variability In Semi-Automatic Segmentation From CT  
Images: Implications For Knee Joint Modelling**

By  
Reyhaneh Asadirad  
Supervised by Dr. Phil Riches  
Dr. Danial Kahani

A dissertation submitted in fulfilment of the requirements of the award of a  
**Doctor of Philosophy of the University of Strathclyde**  
May 2024



**UNIVERSITY OF STRATHCLYDE  
DEPARTMENT OF BIOMEDICAL ENGINEERING**

## DECLARATION

This thesis is the result of the author's original research. It has been composed by the author and has not been previously submitted for examination, which has led to the award of a degree.

The copyright of this thesis belongs to the author under the terms of the United Kingdom Copyright Acts as qualified by University of Strathclyde Regulation 3.50. Due acknowledgement must always be made of the use of any material contained in, or derived from, this thesis.

Signature of Student

Name of Student

Date

## ACKNOWLEDGMENTS

First, I would like to thank my esteemed supervisor Dr. Phil Riches for their invaluable advice, continuous support, and patience during my PhD study. His immense knowledge and plentiful experience have encouraged me throughout my academic research with his invaluable supervision. It would be impossible for me to complete my study without his support.

Additionally, I would like to express my special gratitude to Dr. Danial Kahani for his mentorship and treasured support, which influenced my research. He was always helpful with his knowledge and patient support.

I would also like to thank Dr. Monika Kerr for her technical support in my study. I would like to thank all the members of the Biomedical Engineering department who kindly encourage me to be resilient in my study.

My special appreciation goes out to my son, Amir, who was most dependent on me during his early ages and most vulnerable. During these irreversible and tough years, he was always for me. He was the only reason to face challenging years and to continue with faith.

Finally, I would like to express my gratitude to my friends and family. Without their tremendous understanding and encouragement over the past few years, I could not terminate this mission of my life.

## ABSTRACT

The knee joint is one of the most complex and weight-bearing joints in the body, making it highly susceptible to injury from various activities. Knee surgery often becomes necessary when conservative treatments fail to alleviate pain and other related disorders. In 2020, research indicated that there were nearly 60,000 total knee replacements (TKRs) for women and approximately 50,000 TKRs for men across England, Wales, Northern Ireland, and the Isle of Man. Projections suggest that by 2060, the demand for hip and knee replacements in the UK will rise by 40%.

Robotic knee surgery, a minimally invasive and computer-assisted orthopaedic surgery (CAOS), allows for precise surgical movements, leading to quicker recovery and reduced postoperative pain. However, according to NHS Patient Reported Outcome Measures (PROMs), around 4% of patients in England remain dissatisfied with their knee replacement outcomes, primarily due to implant malalignment.

Virtual 3D knee models, generated from CT and MRI scans, play a critical role in improving implant alignment before surgery. These models enable preoperative planning by allowing surgeons to virtually model the patient's knee in 3D, optimizing implant selection and simulating postoperative range of motion. However, the mechanical functionality of the knee joint remains poorly understood, and researchers are actively exploring improvements through finite element analysis (FEA).

FEA is a valuable tool for simulating the mechanical behaviour of the knee under various conditions, helping surgeons and biomedical engineers analyse stress distribution, implant stability, and soft tissue interactions. Although existing finite element (FE) knee models provide highly detailed meshes of anatomical structures like bones, cartilage, ligaments, and tendons, these models are complex, time-consuming to create, and prone to human error, making them unsuitable for analysing large image datasets.

This brings us to our primary research question: What is the impact of using simplified soft tissue models on finite element simulations of subject-specific knee joints? Can we create an FE model that incorporates elastic, homogeneous soft tissue around knee

bones instead of modelling individual ligaments and cartilage? This approach is inspired by a study by Arjmand, which replaced soft tissue in the proximal tibia with an incompressible cylindrical medium. However, that model did not adequately represent the joint's volume or surface topology.

In our study, we propose a simplified FE model where all soft tissues and bony structures are contiguous, maximizing anatomical accuracy. One of the critical steps in creating subject-specific 3D models for FEA is segmentation, which, as our systematic review revealed, suffers from significant variability. Variability in the segmentation process introduces uncertainty into the quantitative data, affecting the reliability of the resulting models.

To assess this variability, we conducted inter- and intra-observer variability tests, which are commonly performed in various fields but are notably lacking in the literature for knee joint surgeries. Our secondary aims included determining the intra- and inter-examiner variability in semi-automatic segmentation performed by one operator and 15 operators, respectively. Additionally, we sought to determine the optimal threshold values for knee joint tissues during segmentation, using thresholding techniques.

We segmented the tibia at various thresholds and compared the results to a reference tibia segmented at 205 HU. The effect of thresholding proved significant, impacting the final model by causing under- or over-segmentation. The optimal threshold values were identified as 205 HU for the tibia, 160 HU for the femur, 200 HU for the patella, and 232 HU for the fibula.

In a pilot study, intra-observer variability was assessed by having one participant segment the knee five times, with the results compared using the Cloud-to-Cloud (C2C) method. The highest similarity (93.39%) was observed between the fourth and fifth segmentations, indicating that operator experience influences the segmentation process. Following ethical approval, 15 volunteers were trained to segment the femur, tibia, and patella five times using ITK-Snap software. Graphical comparisons were performed using CloudCompare, and quantitative metrics, including Hausdorff Distance, Dice Similarity Coefficient (DSC), and Jaccard Index, were computed to

assess intra-observer variability in MATLAB. Inter-observer variability for DSC was calculated using the intraclass correlation coefficient (ICC) in IBM SPSS.

The ICC for DSC was 0.975 for the femur, 0.981 for the tibia, and 0.959 for the patella, indicating excellent reliability in the segmentation process. The femur and patella exhibited high DSC and Jaccard Index values, while the tibia had the highest Hausdorff Distance. After confirming the segmentation process's reliability, we segmented the knee twice more, including the soft tissues, making the model subject-specific.

These models were imported into Ansys for FEA, where the soft tissue was modelled as isotropic, homogeneous, and hyperplastic with a neo-Hookean material model (shear modulus: 1 MPa, Poisson's ratio: 0.45). The von Mises strain in the soft tissue following an applied force on the tibia was 1.42  $\mu\text{m}$  for the first knee and 2.43  $\mu\text{m}$  for the second, reflecting a 71% difference. The von Mises stress was 637 Pa and 728 Pa, respectively, showing a 14.2% difference. The articular cartilage experienced the highest stress and strain.

Our study successfully simplified the modelling of soft tissue in knee FE models while achieving convergence. The results demonstrated that simulation outcomes are highly sensitive to even minor variations in segmentation. Despite the tibias lower similarity (higher Hausdorff distances), the overall agreement between operators remained consistent. Our findings show good to excellent reliability for segmenting the tibia, patella, and femur in 4D CT images of the knee joint across multiple observers.

# PUBLICATIONS AND PRESENTATIONS

## Presentations

- **Reyhaneh Asadirad, Danial Kahani, Phil Riches. (Sep. 2024). Intra- and inter-observer variability of the segmentation of the knee joint.** Presented at the BioMedEng24 conference, Queen Mary University of London. (London)
- **Reyhaneh Asadirad, Danial Kahani, Phil Riches. (Sep. 2023). Evaluating the Reliability and Repeatability of ITK-Snap in Semiautomatic Segmentation of Knee Joint Structures.** Presented at the BioMedEng23 conference, Swansea University (Swansea)
- **Reyhaneh Asadirad, Danial Kahani, Phil Riches. (Sep. 2022).The effect of image threshold level on patient-specific segmentation of proximal tibia CT images.** Presented at the BioMedEng22 conference UCL (London)
- **Reyhaneh Asadirad, Danial Kahani, Phil Riches. (Sep. 2022). Intra-observer variability of CT image segmentation of the knee joint.** Presented at the BioMedEng22 conference UCL (London)

## Posters

- **Reyhaneh Asadirad, Danial Kahani, Phil Riches. (Jun. 2022). Inter- And Intra- Examiner Variability of 4DCT Image Segmentation of the Knee.** Presented at the SINAPSE (Scottish Imaging Network: A Platform for Scientific Excellence), University of Strathclyde (Glasgow)
- **Reyhaneh Asadirad, Phil Riches. (Dec. 2019). Finite Element Analysis of the Knee During Varus-Valgus Movement.** Presented at the University of Strathclyde (Glasgow)

## Table of Contents

DECLARATION .....	I
ACKNOWLEDGMENTS .....	II
ABSTRACT .....	III
PUBLICATIONS AND PRESENTATIONS .....	VI
LIST OF FIGURES .....	X
LIST OF TABLES .....	XII
List of Equations .....	XIII
LIST OF ABBREVIATIONS .....	XIII
Chapter 1 Introduction .....	2
1.1 Research background and justification.....	2
1.2. Thesis structure .....	6
1.2.1 Chapter 1 Introduction .....	6
1.2.2 Chapter 2 Theory and Literature review .....	6
1.2.3 Chapter 3 Research aims and objectives.....	8
1.2.4. Chapter 4 Effect of threshold on segmentation.....	8
1.2.5 Chapter 5 pilot experiment Intra- observer variability of segmentation of knee CT images.....	8
1.2.6 Chapter 6 Intra- Inter observer variability .....	9
1.2.7 Chapter 7 Finite element Analysis .....	9
Chapter 2 Theory and Literature review .....	10
2.1 Introduction .....	10
2.2 Knee Anatomy .....	12
2.2.1 Femur .....	12
2.2.2 Tibia .....	13
2.2.3 Patella.....	13
2.2.4 Fibula .....	13
2.2.5 Knee Ligaments .....	14
2.2.6 Muscles and Tendons.....	17
2.2.7 Meniscus .....	19
2.2.8 Bursae.....	21
2.3 Knee movement .....	21

2.3.1 Flexion-extension.....	22
2.3.2 Abduction – Adduction (Varus- Valgus) .....	23
2.3.3 Internal-External rotation and the Screw-Home Mechanism.....	23
2.4 Knee disease.....	24
2.5 Knee stability .....	24
2.6 Knee surgery success rate .....	25
2.6.1 Improving Knee Arthroplasty Results (3D Modelling and segmentation).....	26
2.7 Segmentation.....	28
2.7.1 Effect of threshold on segmentation .....	29
2.7.2 Limitation and difficulties of segmentation .....	31
2.7.3 ITK-SNAP .....	33
2.7.4 Effect of mineral density and Hounsfield unit .....	35
2.8 Segmentation assessment metrics .....	35
2.8.1 Dice similarity coefficient (DSC) .....	35
2.8.2 Jaccard Index (JI) .....	36
2.8.3 CloudCompare .....	37
2.8.4 Hausdorff Distance (HD) .....	38
2.9 Segmentation evaluation .....	39
2.9.1 ICC Intraclass Correlation Coefficient (ICC) .....	42
2.10 Finite Element Analysis .....	43
2.10.1 Finite element analysis of the knee joint.....	43
Chapter 3 Research Aims and Objectives.....	47
3.1 Primary Aim.....	47
3.2. Secondary Aim.....	48
3.3 Tertiary Aim.....	49
3.4 Quaternary Aim.....	50
Chapter 4 Effect of the threshold level on segmentation outcomes.....	52
4.1 Introduction.....	52
4.2 Image Data Collection.....	54
4.3 Methodology .....	54
4.4 Results.....	56
4.5 Discussion .....	63
4.6 Conclusion .....	65

Chapter 5 Pilot experiment of intra- observer variability of segmentation of knee CT image .....	67
5.1 Introduction .....	67
5.2 Data acquisition.....	69
5.3 Methodology .....	70
5.4 Results .....	73
5.5 Discussion .....	74
5.5 Conclusion .....	77
Chapter 6 Inter-observer variability .....	79
6.1 Introduction .....	79
6.2 Methodology .....	80
6.3 Data collection .....	81
6.3.1 Ethical Approval .....	81
6.3.2 Subject recruitment .....	81
6.3.3 Study design .....	83
6.3.4 ITK-Snap Methodology .....	84
6.4 Data Analysis .....	86
6.4.1 CloudCompare™ Analysis .....	86
6.4.2 Hausdorff Distance, Jaccard Index, Dice Similarity Coefficient.....	91
6.4.3 Inter-observer Analysis .....	91
6.5 Results .....	92
6.5.1 CloudCompare™ Analysis .....	92
6.5.2 Hausdorff Distance, Jaccard Index and Dice Similarity Coefficient .....	101
6.5.3 Inter- observer Analysis .....	106
6.6 Discussion .....	109
6.6.1 CloudCompare .....	109
6.6.2 Hausdorff Distance, Jaccards Index, Dice Similarity Coefficient .....	116
6.6.3 Inter- observer Analysis .....	118
6.7 Conclusion .....	118
Chapter 7 Effect of segmentation on FEA .....	120
7.1 Introduction .....	120
7.1 Methodology .....	122
7.1.1 ITK-Snap Analysis.....	123
7.1.2 Ansys SpaceClaim Analysis .....	126

7.1.3 Ansys Mechanical Analysis .....	127
7.2 Results .....	134
7.3 Discussion .....	137
7.4 Conclusion .....	139
References .....	140
Annexes.....	150
Appendix A .....	150
Appendix B .....	151
Appendix C .....	152
Appendix D .....	153
Appendix E .....	154
Appendix F.....	1
Appendix G.....	3
Appendix H.....	6
Appendix I.....	10

## LIST OF FIGURES

Figure 1. Finite element model by Arjmand [4] .....	4
Figure 2. Finite element modelling by McErlian [5] .....	5
Figure 3. Anterior and posterior distal femur [6].....	12
Figure 4. Anterior and posterior view of knee joint [3] .....	14
Figure 5. Transvers plane of proximal tibia; fibula is very close to tibia .....	14
Figure 6. Meniscomfemoral and meniscotibial [11] .....	16
Figure 7. sMCL and dMCL Insertion landmark [12].....	16
Figure 8. Medial, Lateral and posterior Landmarks [14].....	17
Figure 9. Hip and knee muscles [16] .....	18
Figure 10. Posterior lower leg muscles [17] .....	19
Figure 11. F for femur, T for tibia, m for meniscus, pcp for capillary plexus[14] ...	19
Figure 12. Medial and lateral menisci [18] .....	20
Figure 13. Four bursea in the knee joint[25].....	21
Figure 14. knee flexion- extension angles [15].....	22
Figure 15. knee six degree of freedom [14] .....	22
Figure 16. rolling and sliding of knee joint [14] .....	23
Figure 17. Screw-home mechanism [26] .....	24
Figure 18. knee surgery patients survey by NHS [31] .....	26
Figure 19. evolution of initial point over time [46] .....	34
Figure 20. external and internal forces makes equilibrium for the right contour [61]34	
Figure 21. Dice similarity schematic diagram [65].....	36
Figure 22. (a) input cloud point, (b) octree division of points [68] .....	38

Figure 23. Iterative closest point [67] .....	39
Figure 24. Making 3D model of knee joint from CT scan images. Left [96], middle [97], right [98].....	45
Figure 25. Effect of threshold value on tibia 3D model.....	56
Figure 26. Effect of threshold with respect to threshold value $\pm$ SD.....	57
Figure 27. Difference of tibia segmented by 130HU and other threshold values.....	58
Figure 28 Distance between reference tibia (130 HU) vs tibia with 100HU .....	58
Figure 29. Distance between reference tibia (130 HU) vs tibia with 130HU .....	59
Figure 30. Distance between reference tibia (130 HU) vs tibia with 204HU .....	59
Figure 31. Distance between reference tibia (130 HU) vs tibia with 205HU .....	60
Figure 32. Distance between reference tibia (130 HU) vs tibia with 350HU .....	60
Figure 33. Manually segmented tibia compared to semiautomatic segmented tibia. 61	
Figure 34. Internal and external differences between tibia segmented by 130HU and 205 HU.....	61
Figure 35. Comparison of three different segmented model and their mean values..	62
Figure 36. Number of points for each model .....	62
Figure 37. (a) C2C distance comparison of S1 and S2. (b) C2C distance comparison of S1 and S3.....	73
Figure 38. (a) C2C distance comparison of S1 and S4. (b) C2C distance comparison of S1 and S5.....	73
Figure 39. S1 and S2 comparisons' Histogram .....	76
Figure 40. The percentage of identical nodes for ten separate comparisons .....	77
Figure 41. Placing bubbles on interested area.....	85
Figure 42. Growing contour to which intensity is determined .....	85
Figure 43. 3D model of knee joint is made.....	86
Figure 44. (a) inner layer is removed. (b) femur with inner layer .....	87
Figure 45. Schematic dividing of the distal femur.....	88
Figure 46. Schematic dividing of the proximal tibia.....	89
Figure 47. Schematic dividing of the patella .....	90
Figure 48. C2C absolute difference of S1 with S2 and S3 .....	92
Figure 49. C2C absolute difference of S1 with S4 and S5 .....	93
Figure 50. C2C absolute difference of S2 with S3 and S4 .....	93
Figure 51. C2C absolute difference of S2 versus S5 and S3 versus S4.....	94
Figure 52. C2C absolute difference of S3 versus S5 and S4 versus S5.....	94
Figure 53. (a) C2C absolute distance of S1 vs S2 , (b) S1 vs S3 .....	95
Figure 54. (a) C2C absolute distance of S1 vs S4, (b) S1 vs S5 .....	96
Figure 55. (a) C2C absolute distance of S2 vs S3, (b) S2 vs S4 .....	96
Figure 56. (a) C2C absolute distance of S2 vs S5, (b) S3 vs S4 .....	97
Figure 57. (a) C2C absolute distance of S3 vs S5, (b) S4 vs S5 .....	97
Figure 58. (a) C2C absolute distance of S1 vs S2, (b) S1 vs S3 .....	99
Figure 59. (a) C2C absolute distance of S1 vs S4, (b) S1 vs S5 .....	99
Figure 60. (a) C2C absolute distance of S2 vs S3, (b) S2 vs S4 .....	99
Figure 61. (a) C2C absolute distance of S2 vs S5, (b) S3 vs S4.....	100
Figure 62. (a) C2C absolute distance of S3 vs S5, (b) S4 vs S5 .....	100
Figure 63. Mean DSC, JI and HD for each bone (error bar = standard error) .....	103

Figure 64. Mean DSC, JI and HD over all comparison (error bar = standard error)	104
Figure 65. Relation of each bone and comparison on DSC .....	105
Figure 66. Relation of each bone over all comparison on JI.....	105
Figure 67. Relation of each bone and overall comparison on HD .....	106
Figure 68. Average DSC ICC of femur is 0.975 .....	107
Figure 69. Average DSC ICC of tibia is 0.981 .....	108
Figure 70. Average DSC ICC of patella is 0.959.....	108
Figure 71. Example of partial volume effect between tibia, soft tissue and fibula..	110
Figure 72. A Knee joint CT image with low contrast, B knee joint CT image with high contrast .....	111
Figure 73. Contrast to noise ratio .....	112
Figure 74. Relation of Visual system to contrast and noise [128, 130] .....	113
Figure 75. Tibial distal end shows motion artefacts .....	114
Figure 76. Anterior aspect of medial condyle of femur shows maximum difference .....	114
Figure 77. Lateral proximal tibia shows maximum difference .....	115
Figure 78. Posterior proximal medial patella shows maximum difference .....	115
Figure 79. Finite element model by Arjmand [4] .....	121
Figure 80. ROI selection on ITK-Snap .....	123
Figure 81. 3D model of knee joint is made.....	124
Figure 82. The 3D model of soft tissue surrounding knee joint is made .....	125
Figure 83. Soft tissue of knee joint is shown in Meshmixer, bones are hidden .....	125
Figure 84. Meshmixer is showing 3D model of constructed bones .....	126
Figure 85. converting Stl file to CAD geometry in Ansys SpaceClaim .....	126
Figure 86. bones are converted to CAD Geometry in Ansys SpaceClaim .....	127
Figure 87. Meshing of the model in Ansys .....	133
Figure 88. Contact between tibia and soft tissue.....	133
Figure 89. Applied force on z axis of tibia .....	134
Figure 90. The green knee is first segmented knee and blue knee is second.....	134
Figure 91. C2C distance of two knee .....	135
Figure 92. Elastic strain on Soft tissue of first segmentation.....	135
Figure 93. von-Mises stress on soft tissue for first segmentation .....	136
Figure 94. Elastic strain on Soft tissue for second segmentation.....	136
Figure 95. Von-Mises Stress on Soft tissue for second segmentation .....	136
Figure 96. Right ours knee joint model.....	138

## LIST OF TABLES

Table 1. The variables and their definition used for comparison.....	72
Table 2. Five segmentation comparison results .....	74
Table 3. Participants recruitment requirements .....	82
Table 4. Assigning code for each parts of the distal femur.....	88
Table 5. Assigning code for each parts of the proximal tibia .....	89
Table 6. Assigning code for each parts of the patella .....	90
Table 7. The codes of maximum differences between segmentations of the femur ..	95

Table 8. The codes of maximum differences between segmentations of the tibia .... 98  
Table 9. The codes of maximum differences between segmentations of the patella101  
Table 10. Overall average of all comparisons of each bone ..... 102  
Table 11. Published soft tissue material properties..... 127  
Table 12. Univariate Tests ..... 6

## List of Equations

Equation 1 ..... 34  
Equation 2 ..... 35  
Equation 3 ..... 36  
Equation 5 ..... 38  
Equation 6 ..... 39

## LIST OF ABBREVIATIONS

Anterior cruciate ligament	ACL
Average Difference based on All Nodes	ADAN
Average Difference of Non Identical Nodes	ADNIN
Centre Of origin	COR
Cloud to Cloud	C2C
Computed Tomography	CT
Computer-assisted orthopaedic surgery	CAOS
Computer-assisted surgery	CAS
Cone Beam Computed Tomography	CBCT
Dice Similarity Coefficient	DSC
Digital Imaging and Communications in Medicine	DICOM
Hausdorff Distance	HD
Hounsfield unit	HU
Jaccard Index	JI
Lateral collateral ligament	LCL
Magnetic Resonance	MR

Magnetic Resonance Imaging	MRI
Medial collateral ligament	MCL
National Health Service	NHS
Number of Identical Nodes	NIN
Number of Non Identical Nodes	NNIN
Osteoarthritis Initiative	OAI
Patient Information sheet	PSI
Patient Reported Outcome Measures	PROMs
Percentage of Identical Nodes	PIN
posterior cruciate ligament	PCL
Region of Interest	ROI
Standard Triangle Language	STL
Sum of C2C Absolute Difference	SC2CAD
Three Dimension	3D
Total Knee Arthroplasty	TKA
Total knee Replacement	TKR
Total Number of Nodes	TNN
United Kingdom	UK

# Chapter 1 Introduction

## 1.1 Research background and justification

The knee joint is not only the most complex but also the main weight-bearing joint in the body, which is mainly prone to harm or injury from routine activities, including walking, jumping, climbing stairs, and participating in sports [1]. Knee surgery is a final consequence of these activities, following knee pain and other disorders that cannot be successfully managed conservatively. Despite knee surgery being a routine procedure performed worldwide, its success rate, as determined by reviewing patients' opinions after surgery, has room for improvement leading researchers to investigate strategies to enhance outcomes. The complexity of the knee joint has been the subject of countless studies and journal papers in different aspects during the past decades. Direct measurements of the knee joint cannot currently be made in vivo, and ex-vivo tests employing cadavers are both expensive and limited in their use. In order to simulate the mechanics of the knee joint, computer models such as finite element models (FEM) are an affordable option.

Robotic knee surgery is a minimally invasive computer-assisted orthopaedic surgery (CAOS) that allows for precise and controlled movements during surgery, leading to a quicker recovery and less postoperative pain. Virtual 3D knee models created from computed tomography (CT) and magnetic resonance imaging (MRI) scans are used in knee surgery to improve implant alignment. These models provide vital information for accurate implant placement, preoperative planning, and surgical decision-making.

There are a few critical steps in the making of a computational model of the knee joint, to use it for FEM or CAOS. A CT or MRI scans need to be acquired from 3D image, in which the anatomical structures need to be identified and differentiated. This process is known as segmentation. This process is fundamental in orthopaedics as it defines the shape and local topology of the bones, which is potentially critical for the model outcome. However, segmenting the knee joint for these 3D models, particularly semi-automatic methods, presents challenges due to anatomical variations and a lack of consistent methodologies. Currently, to the best of our knowledge, there has been a lack of research conducted on evaluating the segmentation of the knee joint, despite its significant functionality and importance.

Manual and semi-automatic segmentation methods involve human input, which may affect the segmentation outcome. Consequently, the first aim of this study is to evaluate the intra- and inter-observer variability of subject-specific semi-automatic segmentation of 4D CT knee joint images.

Existing finite element models are either oversimplified by ignoring most of the soft tissues that surround the knee joint or overcomplicated so that they take a lot of time to be made [2, 3]. Complex models are not suitable for large data set and fast analysis. These models usually only include a couple of the main ligaments and/or cartilage. While the knee capsule members all work together to stabilize and lubricate the knee joint to provide smooth movement. The knee capsule is known to be meniscus, bursae, ligaments, cartilage, synovial membrane, and fluid. Therefore, a second aim of this project is to develop a simplified finite element model of the knee joint that includes all the knee capsule compartments as a single soft tissue that represent more realistic representation of knee joint. The third aim was to assess the effect of segmentation variability on such a finite element model of the knee.

This idea was inspired by two studies. Arjmand et al. [4] created subject-specific FE models for 14 osteoarthritis (OA) knees and normal knees. They were looking to determine the specific proximal tibia mechanical metrics that distinguished between normal knees and OA knees. By using quantitative computed tomography (QCT) scans they evaluated the structural stiffness, von Mises stress and strain, and minimum main stress. To assess the repeatability of the FE-based mechanical measures they imaged the knees three times. CV%RMS was used to evaluate the in vivo precision of these mechanical metrics. To investigate the differences between OA and normal knees, they conducted both parametric and non-parametric statistical analyses and calculated Cohen's d effect sizes. The average CV%RMS for all FE-based mechanical measures was less than 6%. While minimum principal strain values were similar, there was an average 75% increase in minimum principal stress in OA knees compared to normal knees. There was no distinguishable change in the structural rigidity. In vivo, FE modelling could accurately measure and distinguish between mechanical metrics alterations in healthy and OA knees. This study concluded that bone stress patterns might be crucial to comprehending the pathophysiology of OA in the knee. However, the focal point of interest in this study lies in the method they used to replace soft tissue

with an incompressible cylindrical medium. This is particularly noteworthy because soft tissues are not distinguishable by CT imaging. Figure 1 illustrates the representation of soft tissue as an incompressible cylinder made by Arjmand [4], in which A is generated three-dimensional geometries of the femur, tibia, and fibula from CT images, B is meshed bones of the knee with 10-noded tetrahedral elements and C is assigned material properties for the FE model. Body mass density was mapped to the modulus of elasticity of the bones.

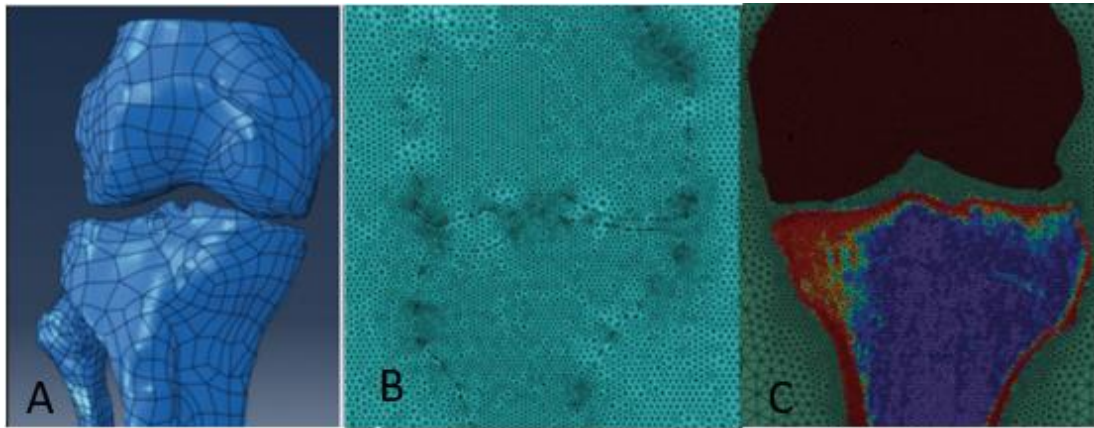


*Figure 1. Finite element model by Arjmand [4]*

In another study [5], the concept of soft tissue surrounding the knee bones is explored. This paper delves into the role of intra-osseous lesions, specifically subchondral bone cysts (SBC), in the progression of knee osteoarthritis (OA) through Finite Element Modelling (FEM) coupled with high-resolution imaging techniques (figure2). The primary objective of their study was to clear up how these lesions contribute to increased intra-osseous stress in early-stage OA patients. The surrounding soft tissue is modelled using the compressive properties of cartilage under compression at equilibrium. Soft tissue outside the bony margins is assigned the material properties of cartilage.

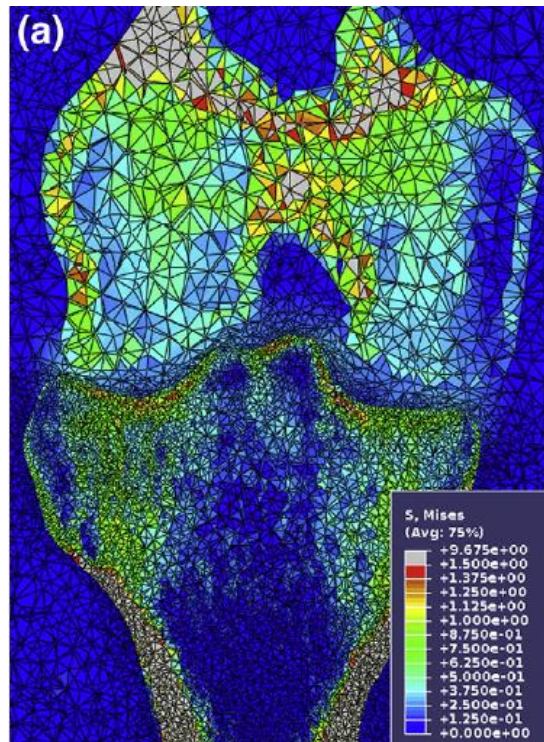


Figure 2. Finite element modelling by McErlan [5]

Therefore, to achieve the aims, five questions are considered in this study:

1. What is the optimal threshold value for segmentation of each bone in the knee joint using semi-automatic segmentation techniques, and how does it impact the accuracy of the segmentation results.
2. What is the reliability and repeatability of semi-automatic segmentation for knee joint structures in CT images when performed by a single operator?
3. What is the impact of inter-observer variability in semi-automatic segmentation of knee joint structures in CT images, performed by multiple individuals, on the accuracy and reliability of 3D knee models used in total knee arthroplasty planning and implant design?
4. Can a simplified model of the knee be easily created by replacing all knee format into two structures, one rigid body and one soft tissue?
5. Does the segmentation process, necessary to build the model, affect the outcome, i.e do small differences in the segmented models leads to any significant differences in the model output?

## **1.2. Thesis structure**

### **1.2.1 Chapter 1 Introduction**

This chapter provides a brief rationale for investigating knee joint segmentation variability. It discusses the complexity of the knee joint, its susceptibility to injury, and the challenges associated with knee surgery. It emphasizes the significance of knee surgery in managing pain and disorders resulting from routine activities. Researchers aim to enhance the success rate of knee surgeries, particularly through the use of finite element models (FEM) to simulate knee joint mechanics.

The importance of subject-specific FEM is highlighted, requiring CT or MRI scans to create 3D models for finite element analysis (FEA) and robotic knee surgeries. This section introduces the concept of robotic knee surgery as a minimally invasive and precise procedure for quicker recovery. Virtual 3D knee models derived from CT and MR scans are crucial for preoperative planning and accurate implant placement. However, challenges arise in segmenting knee joints due to anatomical variations.

This part also specifies the aims to address gaps in research by evaluating intra- and inter-observer variability in subject-specific semi-automatic segmentation of 4D CT knee joint images. It also strives to develop a simplified finite element model that includes all knee capsule compartments, providing a more realistic representation of the knee joint.

### **1.2.2 Chapter 2 Theory and Literature review**

This chapter describes the function of knee joint in mobility, and its vulnerability to wear and tear. It looks at the issue of knee instability and the necessity of exact implant placement. The utilisation of robotic surgery, 3D knee models, and different segmentation strategies are highlighted. The anatomy of the knee, including the femur, tibia, patella, fibula, ligaments, muscles, and meniscus, is also covered in this chapter. The responsibility of each component in the stability and movement of the knee joint are mentioned as well as their properties and functions.

Patient satisfaction rates for knee replacements are analysed, revealing factors contributing to dissatisfaction. The importance of accurate medical image segmentation in creating 3D virtual representations of the knee joint is highlighted. The use of 3D modelling technology during the planning stage is shown to enhance

implant alignment and soft tissue balance, resulting in improved outcomes, fewer complications, and higher patient satisfaction.

Different segmentation processes - manual, semi-automatic, and automatic - are described, highlighting their advantages and limitations. Manual segmentation is accurate but time-consuming and prone to human error, while automatic segmentation is faster but less accurate. Semi-automatic segmentation offers a balance between speed and accuracy.

The impact of the threshold level on image segmentation results is mentioned. The choice of threshold determines the inclusion or exclusion of image parts, affecting the accuracy of the segmentation. Optimal thresholding depends on the specific image and segmentation goals. Various studies, particularly in medical imaging, have highlighted the importance of threshold selection in achieving precise and reliable segmentation.

Achieving reliable data and precise surgical plans requires reducing inter- and intra-observer variability, improving repeatability, and ensuring segmentation reliability. The selection of target tissues during segmentation relies on morphological features, density, homogeneity, structure, and location. Challenges arise when identifying weak or absent parameters, leading to inaccurate or impossible outcomes.

ITK-Snap, as one of the image segmentation software, is introduced. The method of segmentation using ITK-Snap is discussed in detail in the chapter, involves the use of evolving contours to achieve accurate segmentation results. In addition, the effect of mineral density of tissue is highlighted. The absorption or attenuation of x-ray beam by the subject determines the Hounsfield Unit. The Hounsfield unit (HU) is a relative quantitative measurement of radio density used by radiologists in the interpretation of computed tomography (CT) images. The absorption/attenuation coefficient of radiation within a tissue is used during CT reconstruction to produce a grayscale image.

Segmentation is discussed as one the important steps in medical diagnosis and treatment. It will be shown that orthopaedic researchers and surgeons are concerned with the accuracy and reliability of the segmentation process. Several evaluation

studies have been conducted in different medical fields to shed light on this matter. Inconsistencies and gaps in the literature in this field are identified.

In addition, some segmentation evaluation measures and techniques, such as the Dice Similarity Coefficient (DSC), Jaccard Index (JI), Hausdorff distance (HD), and the software CloudCompare, are explained in detail to assess the segmented models of this experiment. Intra class correlation coefficient (ICC), is also described here as repeatability evaluation metric.

Finally, finite element analysis is mentioned in this chapter. It is one the most crucial applications that uses segmentation for further analysis leads to treatment and/or diagnosis.

### **1.2.3 Chapter 3 Research aims and objectives**

This chapter outlines the research aims and objectives emanating from chapter 2 related to determining the optimal threshold level on the knee joint segmentation, assessing repeatability and reliability of these segmentation and effects of segmentation variability on finite element analysis of the knee joint.

### **1.2.4. Chapter 4 Effect of threshold on segmentation**

This chapter focuses on analysing the effect of thresholding levels on the segmentation of tibia and determining the optimal threshold level for further study. Following the methodology, this chapter proceeds to explore a thorough examination of the results and subsequent discussion, each addressed separately for clarity and coherence. It discusses the visually optimal threshold value for tibia segmentation and the impact of threshold variations on tibia segmentation quality. The chapter also compares the results of manual segmentation and semi-automatic segmentation using different threshold values. The study concludes by highlighting the importance of threshold values in semiautomatic segmentation, comparing the results to previous research, and emphasizing the need for optimal threshold values for knee segmentation.

### **1.2.5 Chapter 5 pilot experiment Intra- observer variability of segmentation of knee CT images**

This chapter presents an experiment that examines the within-subject repeatability of knee joint segmentation by a single experiment observer. The study utilizes 4D CT

images acquired from a Toshiba Aquilion ONE™ 4D CT scanner. The knee joint is segmented five times in sequence using open-source ITK-Snap segmentation software. The segmentation process involves a semi-automatic approach with manual editing to ensure accuracy. The experiment focuses on segmenting the femur, tibia, and patella of the knee joint.

### **1.2.6 Chapter 6 Intra- Inter observer variability**

This study focused on intra-examiner and inter-examiner reliability, comparing segmentations within and between operators. It utilizes an anonymized 4D CT dataset to analyse the dynamic movement of the knee using the Toshiba Aquilion ONE™ 4D CT scanner. Ethic approval was followed by recruiting and training fifteen volunteers in the ITK-Snap semi-automatic segmentation software. Each participant segmented the femur, tibia, and patella five times, resulting in 225 STL mesh files. CloudCompare software was used for graphical analysis, and MATLAB was employed to obtain quantitative measures such as Hausdorff Distance, Dice Similarity Coefficient, and Jaccard Index. The findings contribute to the understanding of knee movement dynamics and highlight the potential of these methods for clinical applications.

### **1.2.7 Chapter 7 Finite element Analysis**

Conventional knee models involved production of each ligament for each person and model them individually which is time-consuming and prone to error. This chapter suggests a novel solution to these problems, by using a simplified representation that is an incompressible, isotropic, homogeneous, elastic cylinder. This replacement offers a thorough yet condensed soft tissue model that considers the ligaments, tendons, bursae, meniscus, muscles, and knee capsule. This methodology which enables computerised analysis of the knee joint is inspired by Arjmand et al.[4] and McErlain's [5] earlier work, which used comparable finite element models to evaluate mechanical metrics in healthy and osteoarthritic knees as well as the effect of intra-osseous subchondral cysts in osteoarthritis. This idea has a lot of potential for using computerised analysis in the knee joint with simpler soft tissue models. Additionally, to assess the effects of minor segmentation variations, this chapter applies finite element simulation to two consecutively segmented knee joints from Chapter 6.

## **Chapter 2 Theory and Literature review**

### **2.1 Introduction**

The knee joint, as the most complex joint in the body, plays a crucial role in enabling movement in the lower leg during numerous daily activities like walking, jogging, jumping, and climbing stairs. It is remarkably complicated and built to carry significant weight. The knee joint is prone to deterioration over time due to its frequent use, especially in older people or athletes who are active. As a result, this may ultimately end in a knee joint replacement, also known as knee arthroplasty.

Knee instability is reported in up to 72% of people with OA[1], which leads to disintegration of articular cartilage with surgeons advising total knee arthroplasties (TKA) in serious cases. In the United Kingdom, over 90,000 total knee arthroplasties (TKAs) are performed annually [2]. Although this procedure has been generally successful, 25% of patients are not fully satisfied with the outcome of the surgery [2, 3]. Implant malalignment is one of the important reasons for this dissatisfaction [4]; hence, significant efforts and advancements in technology have been made to enhance alignment in knee surgery. This includes the use of robotic surgery, Computed Assisted Surgery (CAS), Patient Specific Instrumentation (PSI), and Computed Tomography (CT) and Magnetic Resonance (MR) scans to create virtual 3D knee models. Robotic knee surgery is a type of minimally invasive procedure that utilizes a robot-assisted surgical system to perform knee joint surgery. This type of surgery allows for precise and controlled movements during the procedure, leading to a quicker recovery and less pain compared to traditional open knee surgery [158]. The popularity of robotic knee surgery varies depending on the country and region, but it has been growing in popularity in recent years because of its benefits.

Models from CT or MRI may provide a deeper understanding of the relative positions of bones in the knee, which is crucial for accurate implant placement. They also aid in preoperative planning and facilitate the surgeon's decision-making during surgery, such as determining the proper size of the implant and ensuring proper resection, alignment, and rotation. Accurate 3D models are also required for implant design [4-6], finite element analysis [7-10], and computerised surgical planning [11-13]. These

3D models are created using various software programs and image segmentation techniques [14].

Medical image segmentation refers to the process of dividing an image into different parts or regions, each representing a specific anatomical structure [159]. Image segmentation sub-divides into manual, semi-automatic and automatic processes where each one has its own advantages and disadvantages. The medical imaging research community denotes manual segmentation as the gold standard in medical imaging [15]. However, manual segmentation is very time consuming and highly influenced by the operator experience and subject to error [16]. In terms of time, semi-automatic segmentation is comparable to automatic segmentation, and in term of efficiency, it is comparable to manual segmentation.

Semiautomatic segmentation involves human input to define seed points or to refine the results of an automatic segmentation algorithm. The variability and reliability of semiautomatic segmentation depend on the skill and experience of the user, and the quality and consistency of the image data. Therefore, it is important to carefully consider the intra- and inter-observer variability and reliability when using semiautomatic segmentation.

This chapter delves into the foundational knowledge required for computer-assisted knee surgery. It provides an overview of the anatomy of the knee joint, highlighting its key components that support stability and movement, as well as cushion and lubricate the articulation. Additionally, the chapter discusses various knee diseases that can lead to arthroplasty, and covers the significance of knee stability, its related tendons, and the satisfaction rate of knee surgeries along with its causes.

Furthermore, the chapter outlines the creation of 3D model pipelines and the various types of segmentation, including their pros and cons. It highlights the impact of thresholding on 3D model segmentation, and the limitations and difficulties that affect the accuracy of the segmentation process. The chapter also introduces the ITK-snap tool and its role in the segmentation process. Additionally, the chapter covers the effect of mineral density on the creation of CT images and the use of the CloudCompare software. Finally, it provides an overview of the history of finite element analysis, which is an important aspect in the development of computer-assisted knee surgery.

## 2.2 Knee Anatomy

The largest and most complex joint in the human body is the knee joint. The femur and tibia are connected by a hinge-like joint that allows for movement such as bending and straightening of the leg. The fibula, a minor bone located in the knee that aids in stabilising the joint but is not connected to the hinge.

All parts work together to provide stability and movement of the knee joint. A layer of cartilage covers the articulating bony surfaces of the knee joint, which helps to cushion them and reduce the friction while the knee moves. In addition, the knee has a number of tendons and ligaments that support the bones allow movement and provide stability of it. Knee joint muscles plays role in strengthening as well as movement of knee joint. Menisci are present in the joint capsule to provide stability to femorotibial articulation, distribute axial load, absorb shock.

### 2.2.1 Femur

The femur at its distal end is wide with medial and lateral condyles, round prominences, that can be seen from anterior and posterior views of the knee. The medial and lateral condyles have medial and lateral protuberances called epicondyles. The medial and lateral condylar surfaces are distal to epicondyles and with smooth and round surfaces facing inferiorly, articulating with the tibia. On the inferior aspect of the distal femur, the intercondylar fossa is a trench between two condyles; also, on the anterior aspect of the distal femur, there is a groove in the centre and distal epiphysis of femur, which is named the patellar groove to articulate with patella (Figure3).

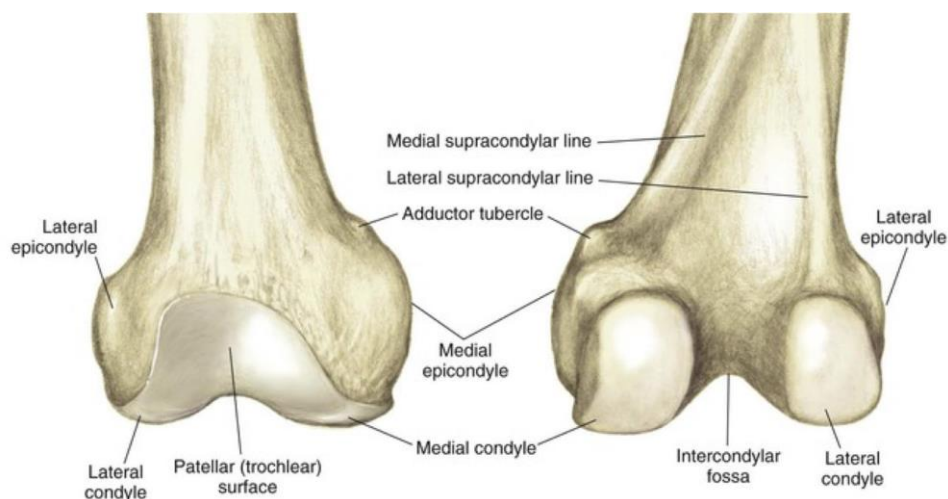


Figure 3. Anterior and posterior distal femur [6]

### **2.2.2 Tibia**

The proximal tibia joins the knee joint and has a large flat end that articulates with femur, named the tibial plateau, and beneath that are the medial and lateral condyles of the tibia. The medial condyle is bigger than lateral, they aid in weight bearing process.

### **2.2.3 Patella**

The patella is a large sesamoid bone that sits anterior to the knee and with attachment to tendons act as pulley. Its posterior aspect is covered with hyaline cartilage and articulates with the distal femur.

### **2.2.4 Fibula**

The fibula is a long bone that is a place for muscle connection and does not help weight bearing. It articulates inferiorly and posteriorly with the lateral condyle of the tibia. A ridge on the medial surface of the fibula forms the interosseous border, which connects the fibula to the tibia through the interosseous membrane [160]. This connection forms a syndesmotic joint, meaning it has very little mobility [161]. The fibula is not a weight-bearing bone like the tibia is [162]. Its primary job is to combine with the tibia to stabilise the ankle joint, hence these two bones are very close to each other. Figure 5 is the CT image used in future chapters, which is showing the close contact of tibia and fibula. There are several grooves on the distal end of the fibula for ligament attachments, which stabilise and provide leverage when the ankle moves. The lateral side of the fibular head is where the lateral (fibular) collateral ligament is attached. This ligament provides knee stability. On the other hand, the fibula itself plays a minor part in knee stability.

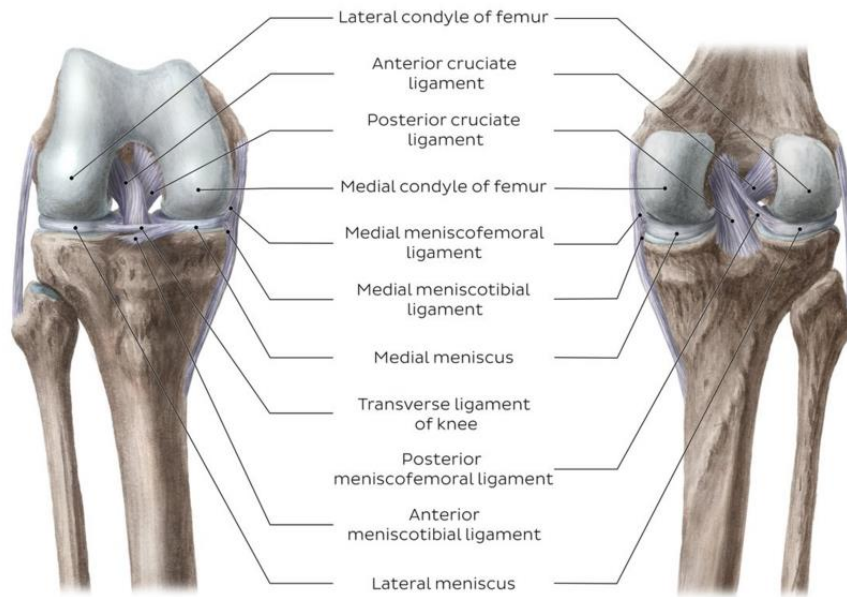


*Figure 4. Anterior and posterior view of knee joint [3]*

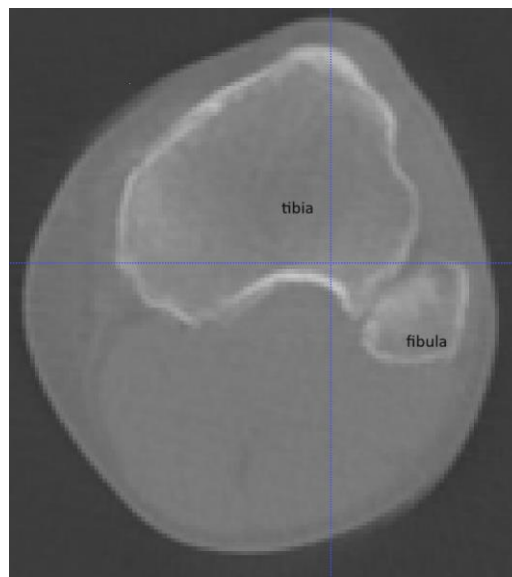


*Figure 5. Transvers plane of proximal tibia; fibula is very close to tibia*

### **2.2.5 Knee Ligaments**

The knee has eight ligaments that preserve knee stability and allow restrained movement. The anterior cruciate ligament (ACL) and posterior cruciate ligament (PCL) are located inside knee capsule. They cross each other at the centre working in opposite directions and they named from their distal attachment. The ACL is attached distally to the anterior section of the medial tibial plateau to posterior section of the

lateral epiphysis of femur and PCL is fixed to the posterior part of lateral tibial plateau to anterior part of medial femoral epiphysis. Anterior and posterior ligaments prevent femur from sliding off the tibial plateau in the anterior and posterior directions. The ACL is the main focus of the last decade studies, it plays critical role in stabilization of the knee. During normal knee motion and at 20° to 30° of knee flexion the ACL involves with minimum strain thus it is the best angle to properly assess the ACL stiffness [7].

Medial collateral ligament (MCL) and lateral collateral ligament (LCL) are extracapsular which means they are located outside of knee capsule. The MCL can be divided in to two parts, the superficial MCL (sMCL) and deep MCL (dMCL). The proximal end of the sMCL is attached to medial epicondyle of femur and distal end is fixed with medial tibia.

The primary function of superficial and deep medial collateral ligament is restraining against valgus force, and, to a lesser extent, the rotational force. The sMCL resist valgus movements through all degree of flexion, it also reduced external rotational movement at 30 degree of flexion of the knee. The dMCL prevent internal rotation of knee in 90-degree of flexion to full extension [8].

The dMCL is composed of two parts, menisconfemoral and meniscotibial. The menisconfemoral has proximal connection to femur just distal to sMCL and it blends in medial meniscus. The meniscotibial starts proximally from medial meniscus and distally to the articular cartilage of medial tibial plateau. It is thicker and shorter than menisconfemoral [9, 10].

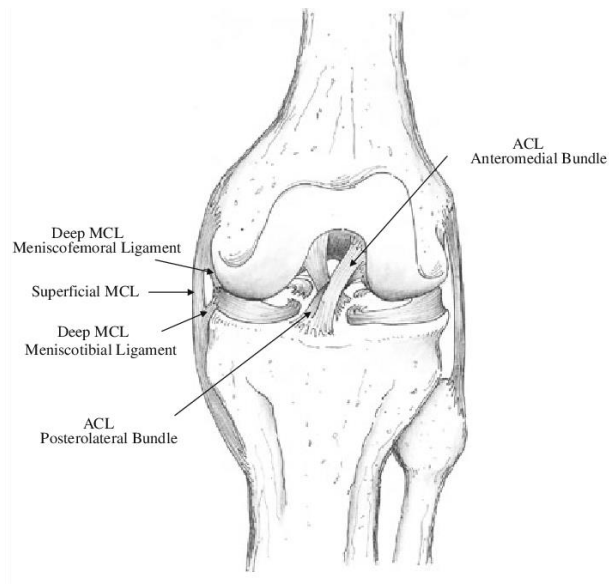


Figure 6. Menisofemural and meniscotibial [11]

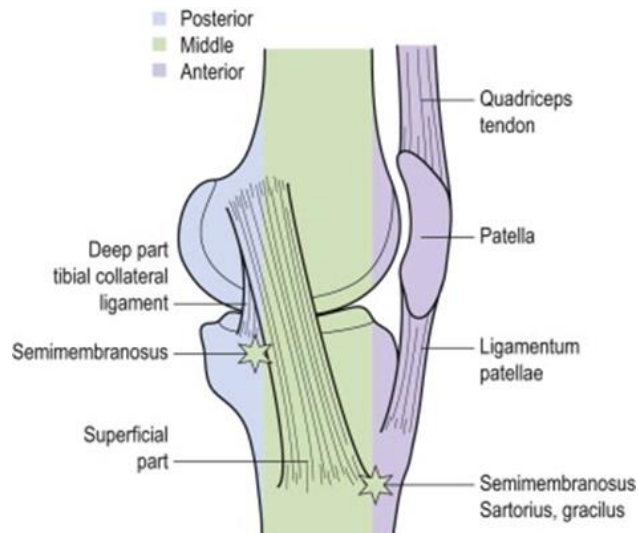


Figure 7. sMCL and dMCL Insertion landmark [12]

The LCL starts from lateral epicondyle of femur and insert to anterolateral fibular head. The primary function of LCL is restraining the varus movement during 5 to 25 degree of flexion, and the second responsibility of the LCL is to resist posterolateral rotation under 50 degrees of flexion. The LCL with help of ACL and PCL prevent Varus during full extension [13]

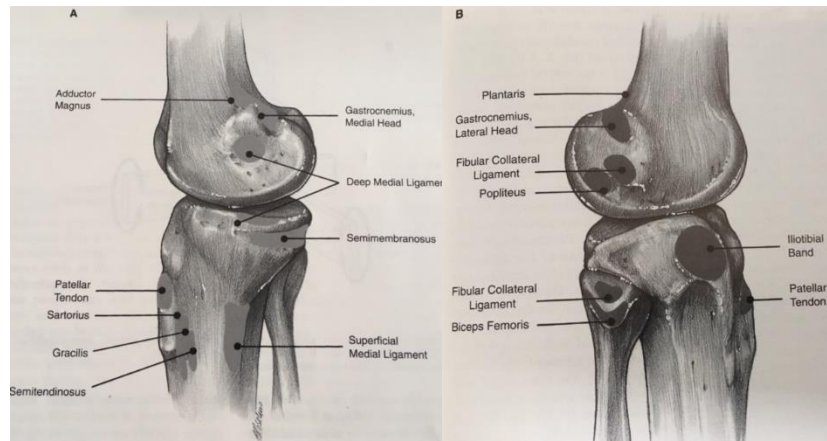


Figure 8. Medial, Lateral and posterior Landmarks [14]

The oblique popliteal ligament is placed posteriorly in the knee and protect knee from hyperextension. The transverse ligament connects two menisci and fixes them with anterior part of tibial plateau.

Also, the other two ligaments the arcuate popliteal ligament and patella ligament; which are not a point of interest in this study. Although these two minor ligaments might be relevant in the knee stability but they do not have adequate power to involve in varus-valgus movement.

### 2.2.6 Muscles and Tendons

The knee is one of the most complicated joints in the human body with fifteen muscles acting about it, eight of them with their origin proximal to the hip. The tendons of these muscles attach to the iliotibial band, proximal tibia and fibula. These muscles are the sartorius, tensor fasciae latae, rectus femoris, gluteus maximus, gracilis, biceps femoris- long head, semitendinosus, and semimembranosus (figure 9,10). Knee flexion occurs with activation of these muscles, except the rectus femoris. The rectus femoris is specifically performing the knee extension. The biceps femoris short head flexes the knee, laterally rotates lower leg when knee slightly flexed. The biceps femoris attaches proximally to the diaphysis of the femur; it crosses the knee and embeds in the fibular head and lateral condyle of the tibia [163]. Figure (9,10).

Similar to the rectus femoris, the quadriceps femoris group muscles participate in knee extension. Vastus intermedius, vastus medialis and vastus lateralis are part of quadriceps femoris muscle group that are attached to the diaphysis of the femur and insert into the patella through the quadriceps tendon; subsequently the patella is

connected to the patella tendon (also known as the patella ligament) and then to the tibial tuberosity.

In a posterior view of the knee the popliteus muscle is short muscle that paths from the lateral condyle of the femur to the medial part of the tibia. The popliteus muscle function is limited to the rotation of the femur and tibia; in this situation the fixed bone determines the direction of the rotation. (Figure 10).

The gastrocnemius and plantaris are two muscle that lie posterior to the knee, and they cross both the knee and the ankle. Their most effective function is plantarflexing the foot, but they help knee flexion as well. The gastrocnemius is two-headed muscle that attaches proximally to the lateral and medial condyles of the femur and distally to the heavy tendocalcaneus or Achilles tendon (Figure 10)

Finally, the plantaris has short belly and long distal tendon that joins the tendocalcaneus in the medial area and its proximal branch is superior to proximolateral part of gastrocnemius muscle [15].

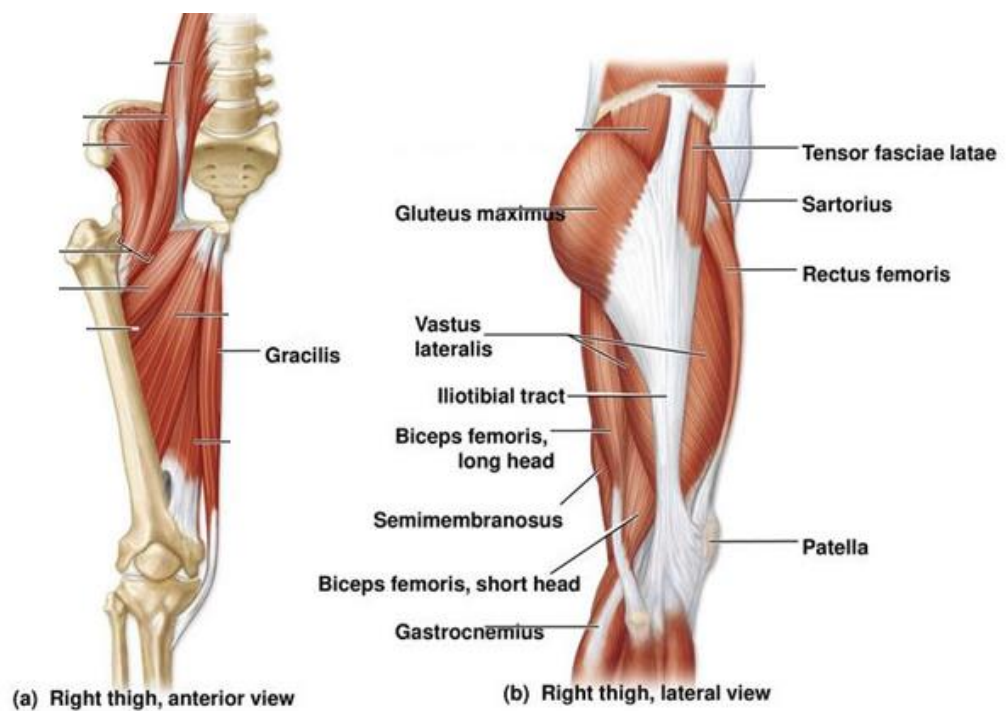


Figure 9. Hip and knee muscles [16]

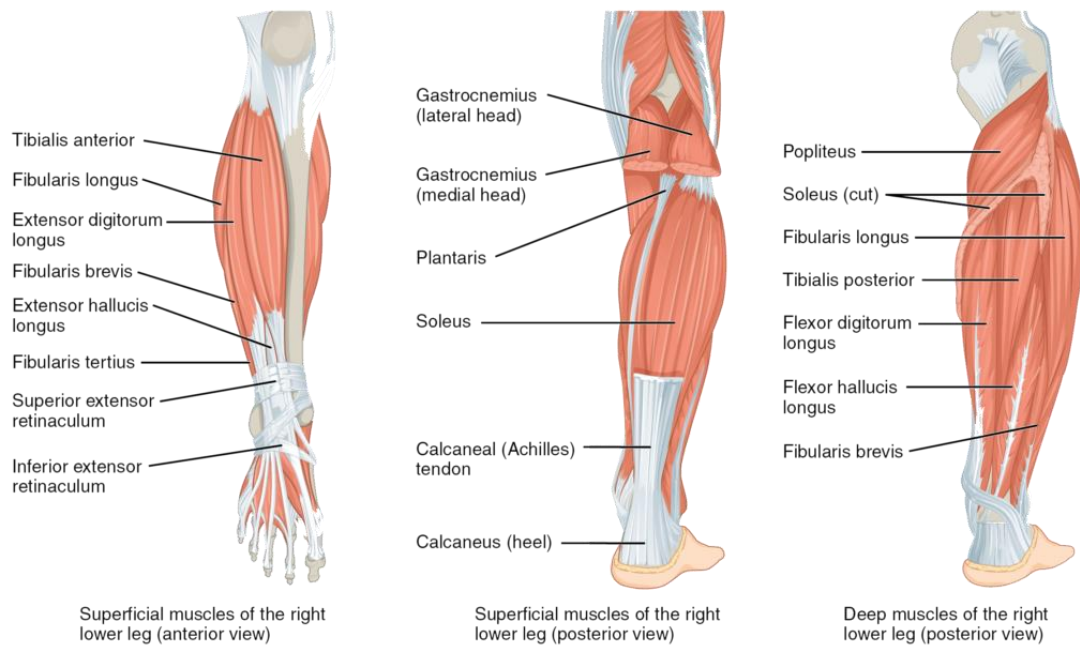


Figure 10. Posterior lower leg muscles [17]

### 2.2.7 Meniscus

Knee meniscus tissue approximately consists of 70% collagen, 10% non-collagen protein and around 10% glycosaminoglycan and glycoprotein [14]. The knee contains two menisci: the medial and lateral. The menisci are C-shaped shells that located between femoral condyle and tibial plateau. The menisci have triangular cross section as shown in Figure 11. The collagen fibres of menisci are aligned circumferentially which aid to absorb compressive forces and resist hoop stresses in the direction of circumference. The edge of menisci are connected to each other and to the tibia by the transvers ligament as shown in Figure 12 [18, 19].

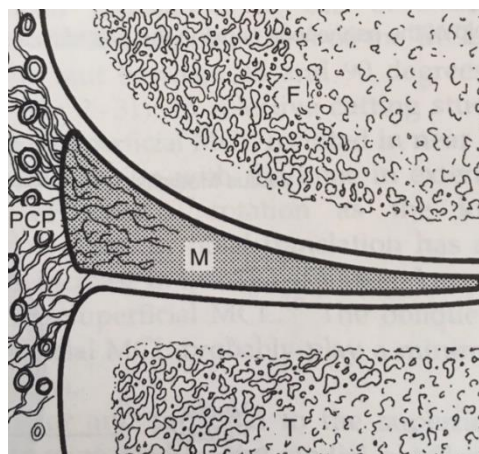


Figure 11. F for femur, T for tibia, m for meniscus, pcp for capillary plexus[14]

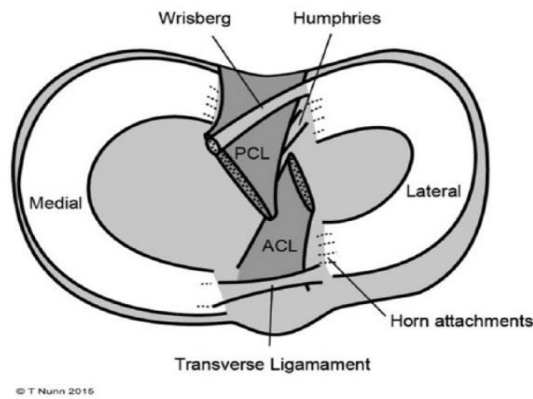


Figure 12. Medial and lateral menisci [18]

The medial meniscus is wider, thicker and more semi-circular in shape than the lateral meniscus. The medial meniscus is connected to the deep medial collateral ligament and it also has a connection to the knee capsule, rendering the medial meniscus immovable [164].

On the other hand, the lateral meniscus is more like a circle, and in contrast to medial meniscus, it shows a different shape, size, and thickness. Additionally, the lateral meniscus is not attached to lateral collateral ligament and the connection to the knee capsule is disrupted by popliteus tendon that is between it and the LCL. For these reasons, the lateral meniscus is much more movable than medial meniscus [14, 18]. The fixed medial meniscus causes less compensation of joint forces and angular movement, and thus the lateral meniscus has the higher rate of injuries [20]. Therefore, any loss in the lateral meniscus could affect the stability of the knee. During the anterior translation of the tibia on the femur, the lateral meniscus provides more stability than medial side [21, 22].

As shown in Figure 11, two menisiofemoral ligaments are hidden between the femoral condyle and tibia. The posterior horn of the lateral meniscus is connected to intercondylar field of the tibia and also attached laterally to medial femoral condyle. The anterior menisiofemoral ligament that sits anterior to posterior cruciate ligament is known as the ligament of Humphrey, and the posterior menisiofemoral ligament is termed the ligament of Wrisberg [18, 19, 23]. Only 46% of people have both of these ligaments but 100% of people have at least one of them [18].

### 2.2.8 Bursae

A bursa is a synovial fluid sac between moving structures with the purpose of decreasing the wear and tear of those structures and act as momentum arms during knee movement. The knee joint has three bursae that are close to the patella; the suprapatella, prepatella and inferapatella bursae. The suprapatella bursa lies between quadriceps tendon and the femur. The prepatella bursa is located between the patella and the skin. The infrapatella bursa is divided in to deep and superficial regions. The deep sac lies between the tibia and the posterior area of patella tendon, whilst the superficial sac separates patella ligament where meet tibial tubercle and the skin. Moreover, the bursa that is not adjacent to the patella is gastrocnemius-semimembranosus bursa. Therefore, the semimembranosus bursa is located at posteriorly to the knee joint enclose by the semimembranosus muscle and head of the gastrocnemius [24]. The schematic diagram of bursae of the knee is illustrated in Figure 13.

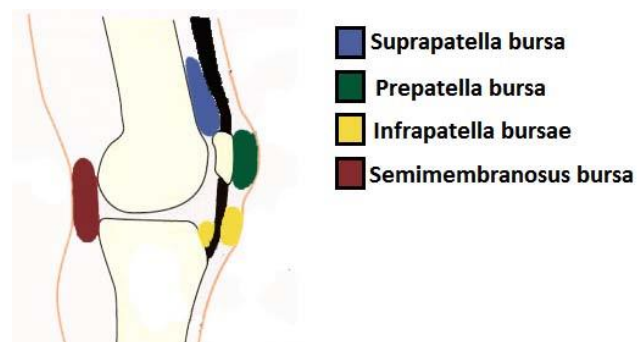


Figure 13. Four bursae in the knee joint[25]

### 2.3 Knee movement

The knee is a synovial or diarthrotic joint, with a high degree of movement. There are six different types of synovial joint in the body such as hinge, pivot, condyloid, saddle, ball and socket and gliding; the knee is hinge-like joint in which a convex surface (femur) moves on the concave surface (tibia). Maintenance of the alignment of the knee completely relies on connective tissue due to the lack of bony constraining anatomy. The knee is movable in all three planes (frontal, sagittal and transverse planes) hence it has six degrees of freedom, which are three (x, y, z direction) translations and three rotations, figure15. The highest range of knee motion is flexion-

extension about  $145^\circ$  [26]. These motions can be controlled by static internal structures as well as dynamic external structures whilst maintaining knee stability.

### 2.3.1 Flexion-extension

Flexion in the knee occurs when the angle between the leg and thigh decrease, and with an increase in the same angle, the extension happens.

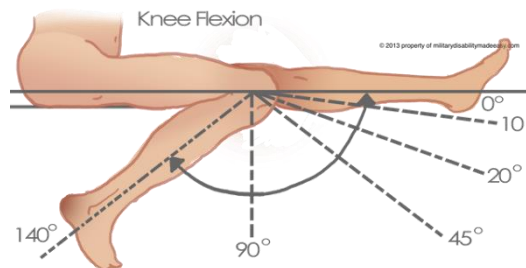


Figure 14. knee flexion- extension angles [15]

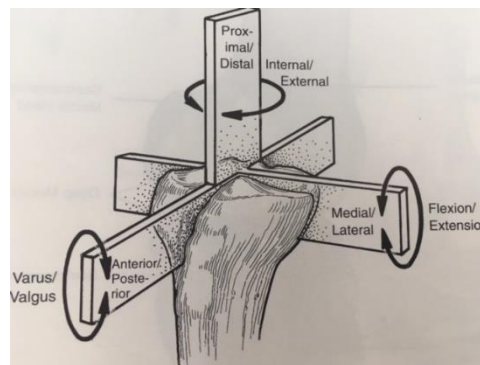


Figure 15. knee six degree of freedom [14]

Simultaneously with flexion and extension, another kind of movement is noticeable, which is sliding and rolling. Sliding of the femur on the tibia happens during knee flexion. If sliding does not occur and rotation occurs about the contact point, then the posterior metaphysis of the femur is subjected to impingement (figure16A). On the other hand, if rolling occurs and no sliding, the femur will roll off the tibia (figure16B). However, realistic knee motion involves both rolling and sliding concurrently (figure16C). The relation of sliding and rolling is not constant and are related to anatomy of joint and with the ACL as well as PCL. Therefore, some researchers believe that pure sliding happens at the last part of flexion and pure rolling appears at initial flexion [14].

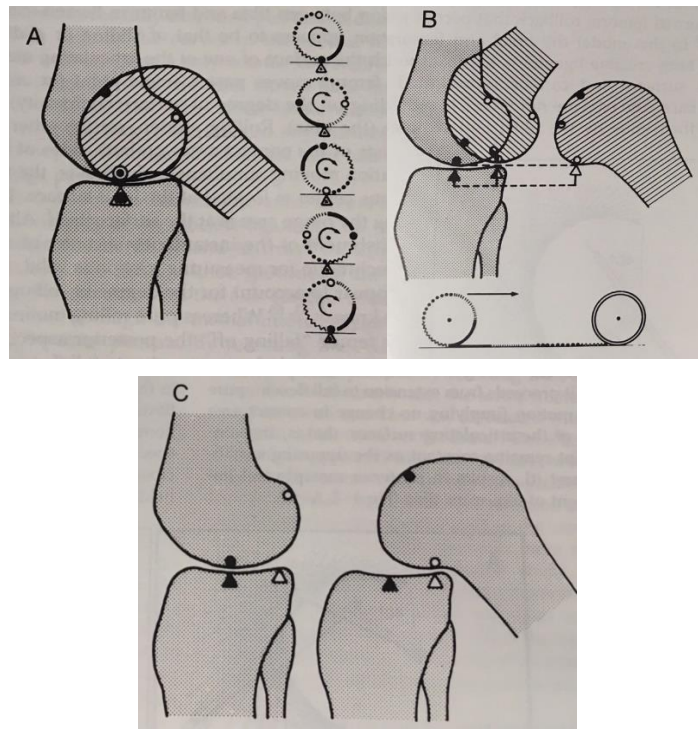


Figure 16. rolling and sliding of knee joint [14]

### 2.3.2 Abduction – Adduction (Varus- Valgus)

During normal knee gait cycle are small rotations in the frontal (or coronal) plane which are termed varus-valgus movement. The degree of this motion depends on varus or valgus shape of native knee. This movement is also related to the amount of flexion-extension in this regard at the full extension where the femur and tibia are locked, the varus-valgus is prevented, and on the other hand, when the knee is flexed at  $30^\circ$  this motion is at its highest level, although it is only few degrees [14, 26].

### 2.3.3 Internal-External rotation and the Screw-Home Mechanism

As the knee move from flexion to extension, the tibia rotates externally at the same time, this is called *screw-home mechanism*. The degree of this rotation is under study yet, however Zatsiorsky [26], believes this coincident rotation occurs mostly at finishing  $30^\circ$  of extension. Additionally, axial rotation shows independent movement from flexion-extension, when the knee is flexed between  $30^\circ$  to  $150^\circ$  [26]. It is considerable that the direction of tibial rotation is not fixed and is relevant to the prior position of tibia before extension. If the tibia during flexion is rotated externally, then

it rotates internally during knee extension, which is reversed to the definition of the screw-home mechanism.

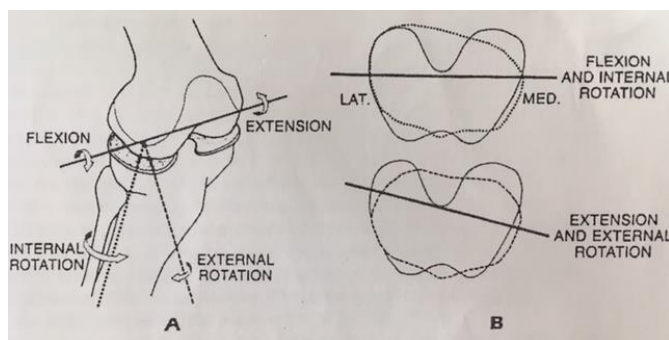


Figure 17. Screw-home mechanism [26]

## 2.4 Knee disease

Frequent knee injuries are anterior cruciate ligament (ACL) tear and rupture, meniscal tears, patellofemoral pain syndrome (PFPS) and runner's knee. However, the main knee disease that leads to knee arthroplasty is osteoarthritis. Osteoarthritis is a degenerative joint condition that results in joint pain and stiffness as the articulating cartilage is worn away [165].

## 2.5 Knee stability

Instability is not a specific knee disease, but rather a common symptom or presentation of several knee conditions. Knee instability can occur due to various factors such as ligament injuries, cartilage damage, muscle weakness, or misalignment of the bones. This can cause the knee to give way or feel unstable, leading to discomfort, pain, and difficulty in performing daily activities. In some cases, knee instability can progress and lead to further injury if left untreated.

In order to accurately and preferably interpret knee stability, it is vital to clearly define the common terms of the knee motion. In other words, the terminologies found in the literature do not show commonality. In this regard, terms such as instability, laxity, disability will be redefined according to the general agreement of the best definitions in this section.

Generally speaking, movement of the knee joint with respect to the resistance of one or more ligaments is defined as laxity. The capability of the knee joint to guide a movement or to preserve a position is defined as knee stability [21]. Thus, instability

is the inability to guide movement or maintain a specific position. Instability is a common difficulty. Knee instability has been described as a buckling or giving way in osteoarthritic knee, recorded in 72% of people [27, 28]. The stability of the knee is maintained by muscle strength, the passive ligament and joint capsule structures. Knee instability could therefore be the result of muscle weakness, joint laxity and misalignment [21].

The stabilisers of the knee can be divided into two categories: primary and secondary. Ligaments are known to be primary stabilisers coupled with muscles that considered as secondary stabilisers. However, they both act simultaneously.

As mentioned earlier, ACL, posterior cruciate ligament (PCL), medial collateral ligament (MCL), lateral collateral ligament (LCL), popliteofibular ligament, oblique popliteal, arcuate popliteal and transverse all play stabilizer roles for the knee. In this regard, the ACL stabilizes anterior and rotational displacement, whilst the PCL restricts posterior displacement. In addition, the MCL stabilizes the knee medially and becomes tense during extension and external rotation thus limiting extreme valgus stress. In a similar way, the LCL has the role of stabilizing the knee laterally, resisting excessive Varus stress and, also, during flexion it prevents external rotation [29]. Similarly, the popliteofibular ligament prevents tibial posterior translation, as well as external rotation of the tibia on the femur.

Significantly, the ACL is the most effective ligament in knee stabilization. It is responsible for 85% of the knee stability [30]; this is the reason that the ACL injured more frequently and investigated broadly in different aspects (anatomy, physiology, rehabilitation, and biomechanics) in the last decade.

## **2.6 Knee surgery success rate**

In 2019, the NHS published the Patient Reported Outcome Measures (PROMs) in England for hip and knee replacement procedure, according to this research over 90000 knee replacement procedures performed in the UK. Patients surveyed and asked to answer the following question: “How would you describe the results of your operation” 28.6% of the participants described it as excellent, 36% very good, 9% fair, and ~4% poor (Figure 18) [31]. Other recent research reported on 27372 TKR procedures of non-revised surgeries shows 17% unsatisfied with the outcome of the

procedure [32]. Nakano et al. had a systematic review of patient satisfaction of their surgery results that shows more than 50% of patient's un-satisfaction is related to intra-operative technical factors [33]. These factors can be named but not limited to, pre-imaging, imaging during surgery, chosen surgical approach, patient position, bone preparation and soft tissue handling. The imaging and the 3D model critically affect the approach chosen by the surgeon.

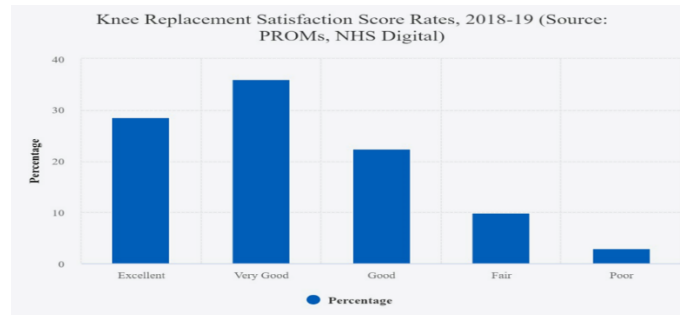


Figure 18. knee surgery patients survey by NHS [31]

The use of patient-specific, virtual models of the knee joint has become an essential component of computer-assisted orthopaedic surgery (CAOS) both before and during surgery. Over the past ten years, there has been a significant increase in the use of this novel robotic approach, especially in total knee arthroplasty (TKA), which aims to improve the alignment of arthroplasty components [4]. The critical first stage in computer-assisted orthopaedic surgery (CAS) is the medical image segmentation process. Its primary function is to segment the region of interest (ROI) accurately from the tissue around it, creating a complete 3D virtual picture of the patient's knee joint. This makes it possible to carefully arrange the placement of the implant and identify the precise amount of bone that needs to be removed. This method greatly improves process precision by customising the knee prosthesis to each patient's particular anatomy, lowering the risks of infection, deep vein thrombosis, and nerve injury [34]. Additionally, robotic knee surgery causes smaller incision during the knee procedure hence patients benefit faster recovery after operation.

### 2.6.1 Improving Knee Arthroplasty Results (3D Modelling and segmentation)

A quarter of patients who have knee arthroplasty may not be completely satisfied with the results, despite the fact that the majority of patients notice a significant improvement in pain and function after the procedure, 17% of patients expectation is

not fulfilled [32]. Some of the dissatisfaction reasons included but not limited to, patients still feel discomfort, their range of motion are limited, implant loosening and fail over time, tendons and ligaments imbalance that cause instability and pain. Misaligned implants and 3D models may have an impact on patients' comfort and relief. Incorrect implant alignment can cause pain and restricted range of motion. Better results may result from the use of 3D modelling technologies during the planning stage of surgery to help assure correct implant alignment and soft tissue balance.

3D modelling is a necessary procedure during the preoperative planning stage of surgery because it enables preoperative planning, which can help assure optimal implant alignment and soft tissue balance. Using this technology, the surgeon can model the patient's knee virtually in 3D, which can be utilised to plan the procedure, assess various implant possibilities, and simulate the patient's range of motion after the surgery.

There have been numerous studies conducted to evaluate the use of 3D modelling technology in knee arthroplasty, and they have demonstrated that its use can help to improve the accuracy of implant alignment and balance of the soft tissue, which results in better outcomes, fewer complications, and higher patient satisfaction. [35-38]

To create reliable 3D models of knee arthroplasty, or to plan CAOS procedures, segmentation is an essential step. Basically, segmentation is the process of isolating significant structures from background tissue in CT imaging data, such as the bones in the knee joint. The important structures required for successful 3D modelling are recovered through this segmentation method.

Studies have demonstrated that the accuracy of implant alignment and the balance of soft tissue can be enhanced using 3D modelling technologies. This is closely related to the segmentation step because good segmentation of the knee joint components enables more precise implant alignment and a better comprehension of the balance of soft tissue during the planning stage. Hence, it will enhance results, lower problems, and boost patient satisfaction. The next section gives more information about segmentation.

## 2.7 Segmentation

In the medical field, the segmentation term is used to separate the region of interest (ROI) from surrounding tissues. It plays an important role in computer-assisted surgery (CAS) diagnosis and treatment systems. Image segmentation process starts from a medical image modality such as magnetic resonance imaging (MRI), computed tomography (CT), X-ray, ultrasound, microscopy, dermoscopy and positron emission tomography then partition it into an interested organ or tissue by manual, semiautomatic or automatic process [39].

Image segmentation sub-divides into manual, semi-automatic and automatic processes. CT image segmentation is used excessively for medical investigation, but due to the divergence of morphology and reliance on specific operators and scanners, it involves some errors and limitations [40-42]. Although semiautomatic and automatic segmentation is well-validated in literatures, but the medical imaging research community denotes manual segmentation as the gold standard [43].

Manual segmentation is accurate because a radiologist or doctor who possesses the expertise to recognize and distinguish between various structures in the CT image data performs it. In addition, it is flexible and completely under control by observer. In challenging situations, the automatic techniques are unable to separate the structures of surrounding and the manual method is flexible and make segmentation achievable. However, It is highly time-consuming that makes the process impossible for large data set and also it is highly influenced by operator experience, and prone to human error [44].

On the other hand, automatic segmentation algorithms make process fast for huge data set and prevent bias intervention of the observer. However, it is not as accurate as manual segmentation done by a skilled radiologist or medical professional. In addition, in cases with existence of noise, contrast change and artefacts, accurate segmentation is not easily functional. Hence, automatic segmentation is one of the most complicated approaches in image segmentation and analysis [45].

Semi-automatic segmentation is faster than manual, and it is specifically advantageous when dealing with large data sets. Its predefined algorithms help to avoid bias interference of observer [46]. In consequence, this method is preferred in this study for

modelling our 4DCT image of the knee joint. However, researchers believe that slow spread of semiautomatic segmentation could be because of the inadequate literature and experience on reliability and repeatability of the process [46].

Researchers have used various software tools to assess the variability in segmentation results, either within a single operator or between multiple operators. These studies aim to compare different methods of segmentation and determine which approach provides the most accurate results. This can provide important insights into the reliability and repeatability of different segmentation techniques and help identify areas for improvement. These studies are crucial in advancing the field of medical imaging and improving the accuracy of segmentation results which some of them will be discussed in the section 8 of this chapter.

Image segmentation is affected by image quality, contrast, anatomy variation, organ overlap and threshold level. Thresholding is one of the segmentation techniques that divides pixels or regions according to their intensity levels. Pixels with intensity values above or below the threshold are divided into various segments according to the threshold, which specifies a certain threshold value. Thresholding effectively separates the image into foreground and background regions, enabling additional analysis and the extraction of information. To isolate significant regions of interest and make it easier to read and comprehend the resulting images, thresholding is a vital stage in the segmentation process. This is explained more in the following section.

### **2.7.1 Effect of threshold on segmentation**

The threshold level used for image segmentation has a significant impact on the results. It determines which parts of the image are included in the segmentation and which parts are excluded. The optimal threshold level depends on the specific image and segmentation goals. For this reason, the effect of the threshold has been studied previously, as will be discussed below.

Studies have shown that the threshold level has a significant effect on segmentation, particularly in medical imaging such as CT and CBCT scans. For example, a study investigating mandible bone segmentation from CT and CBCT scans found that the threshold value had a significant impact on the surface [51]. They emphasized that the accuracy of the segmentation depends on grey-value and threshold value that is

operator input. Segmentation is applied on the mandible by two techniques, one commercial software and experienced 3D clinician. All segmented mandible is compared to 3D model made by high resolution laser surface scanner as gold standard. As a result, they found the consistency in measurements was excellent, with an intraclass correlation coefficient (ICC) ranging from 0.923 to 1.000. The 3D models produced by the commercial software group exhibited an average deviation of  $0.330 \text{ mm} \pm 0.427$  from the gold standard, whereas the models from the Clinician's rendering showed a mean deviation of  $0.763 \text{ mm} \pm 0.392$ . Additionally, the surface models obtained through both protocols tended to have larger dimensions compared to the reference models.

Similarly, other studies have investigated the effect of image thresholding level on segmentation [50, 61-67], highlighting the importance of carefully considering the threshold level for optimal results.

Recently a study by Luca Friedli [42] investigated the effect of the thresholding value used for cranial bone segmentation from CT and CBCT using Viewbox 4 software. The generated models were superimposed to a manually selected reference model and compared by Iterative closest point (ICP). The results show that the threshold value had a significant impact on the surface. They conducted the experiment with one person to assess intra-examiner reliability, while inter-examiner reliability remains a subject of inquiry. One limitation they acknowledged was the absence of a true gold standard reference model.

Other researchers also investigated the effect of image thresholding level on segmentation for different parts of body [41, 47-53]. Since the focus of this section is on the threshold value's critical function in attaining efficient segmentation, a thorough discussion of other relevant studies has been removed for the sake of brevity, as it is not directly related to the main idea of this research.

A study [41] investigates into how different segmentation techniques affect measurements on 3D surface models made from medical scans in terms of clinical differences. The study uses a laser surface scan as the gold standard for comparison and examines the differences between a commercial company's and a doctor's segmentation (DS) method. The effect of threshold-dependent techniques on

segmentation quality is the main topic of discussion. The findings show that the segmentation process is subjective and dependent on several variables, and that the threshold selection has a significant impact on measurement accuracy. The study emphasises how crucial it is to comprehend and enhance the segmentation process to produce 3D models that are more precise and applicable to therapeutic settings.

Understanding of the inter- and intra-observer variability has been recommended to find the variability and repeatability of segmentation [42]. In this regard, researchers, and medical organizations always keen to find a precise, reliable, repeatable and accessible image segmentation algorithm to produce 3D bone models from CT or MRI scans. This has been studied few times in different fields such as cartilaginous bone tumour, upper airway, cranial one, prostate cancer, lumber spine and vertebrae [40, 42, 54-57].

Even though segmentation is widely and necessarily used in the medical industry, there are still certain limitations with it, which are discussed in the section below.

### **2.7.2 Limitation and difficulties of segmentation**

To ensure that a surgical plan is founded on reliable data and computer-assisted surgery is successfully carried out, the knee joint image must be segmented accurately. To maintain the highest level of accuracy and confidence in the surgical plan, it is crucial to reduce the inter- and intra-observer variability, repeatability, and reliability of the segmentation process, which helps the surgeons in pre-operative planning and clinical decision making for each specific patient [58].

During the segmentation process, the target organ or tissue is selected based on its morphological features, density, homogeneity, basic structure, and location. If these identifying parameters are weak or absent, the segmentation process may result in inaccurate or even impossible outcomes.

The optimization of scans during the segmentation process is influenced by four factors: spatial resolution, aliasing, contrast resolution, and artifacts.

Spatial resolution refers to the ability to detect two points in an image, leading to blurriness in cross-sectional images if there is insufficient spatial resolution. Aliasing occurs when the frequency of the sampled signal is not in line with the sampling

frequency. In other words, aliasing happens when a continuous signal like an image or an analogue audio waveform is sampled too slowly to catch its highest frequencies. Contrast resolution refers to the ability to differentiate between two densities amidst noise background. Artifacts result from CT image reconstruction that intersects with one or two high contrast faces, appearing as high pitches in the images [59].

The segmentation process will be challenging as well if the demanded structure is connected to the surrounding tissues. The perimeter surface of each tissue can be determined by establishing the threshold value, manually or by an appropriate algorithm [59].

Furthermore, the accuracy of computerized segmentation can be impacted by images with poor contrast and complex tissue geometry. The bone mineral density, which will be discussed in more detail later, also plays an important role in determining the quality of the scans. Pathological conditions, such as degeneration and arthritis, can also result in uncertainty in the segmentation boundaries [60].

Extensive use of segmentation in medical imaging leads to development of different software and algorithms. Several software packages are available in the market for medical image segmentations, Included and not limited to ITK-SNAP, 3D Slicer, MATLAB, DeepMedic, Vaa3D, Amira. Some are free and open source while others are commercial and need licenses. This study utilizes ITK-SNAP as other researchers used this software for the segmentation and it is open source software. This software will be described in detail in the following sections.

This is a popular open-source software application used for medical image segmentation. This software is used for the segmentation process of this study for the following reasons: ITK-SNAP is known for its user-friendly interface, making it accessible to researchers and clinicians who may not have extensive technical expertise in image processing. The graphical user interface (GUI) allows users to interactively segment and visualize medical images. Also, it supports a variety of medical image formats, including DICOM, NifTI, Analyze, and several others. This flexibility in file format support makes it convenient for working with different types of medical imaging data. It is a powerful and widely used open-source image analysis toolkit. The software offers 3D visualization capabilities, allowing users to view and

manipulate volumetric data in three dimensions. This is crucial for understanding the spatial relationships within medical images and verifying the accuracy of segmentations. Finally, the author of this thesis was familiar with this software.

### **2.7.3 ITK-SNAP**

ITK-SNAP, also known as the Insight segmentation and registration Toolit (ITK) is an open-source software package for medical image segmentation. The method was thoroughly explained by Yushkevich et al. [46] who discussed the utilization of active contours, commonly referred to as "snakes," for separating anatomical structures in 3D medical images. The authors proposed a user-guided active contour method that incorporates user input to improve the efficiency and reliability of the segmentation process.

The conventional active contour approach for medical image segmentation can sometimes be slow and yield inaccurate results when the object boundary is not well defined. The authors suggest an active contour method, which employs user input in the form of seed points to get around this. These seed points help direct the contour towards the object boundary and lead to fewer iterations needed for the contour to converge, resulting in improved efficiency and accuracy.

The authors of the study evaluated the proposed user-guided active contour method on 3D scans of the liver and brain. They discovered that their method significantly decreases the number of iterations needed for the contour to reach convergence, resulting in more accurate segmentation outcomes due to the initial seeds is added by the operator. However, the success of the segmentation heavily relies on the quality of the input image data. The authors also noted that the incorporation of user input makes the method more resilient to noise and capable of handling images with limited contrast. This is because the user input helps guide the contour towards the object of interest.

ITK-SNAP offers semi-automated segmentation, which involves human interaction. This segmentation process is based on classic algorithms for 3D active contour evolution. It involves the evolution of one or more contours around the object of interest, as shown in Figure 19. The initial contour is drawn, and it evolves over time to outline the entire region of interest. ITK-SNAP can process grayscale images and

perform image-processing operations to distinguish different tissue types based on their Hounsfield unit values. The evolution contour can be shown by the following equation [46]:

$$\frac{\partial C(u,v;t)}{\partial t} = F\vec{N} \quad \text{Equation 1}$$

Where  $C(u, v; t)$  is evolving contour close surface, which is dependent on time,  $t$ , and spatial variables  $u$  and  $v$ . In addition,  $\vec{N}$  is the unit normal to the contour and  $F$  means the sum of various forces, internal and external forces. Internal forces are from the geometry of the contour and try to regulate the shape of it. External forces spread information of the segmented image until the boundaries. In other words, distribution of forces outwards the foreground and inward over the background continue until the active contour get to the equilibrium at boundary of the region (Figure 20)

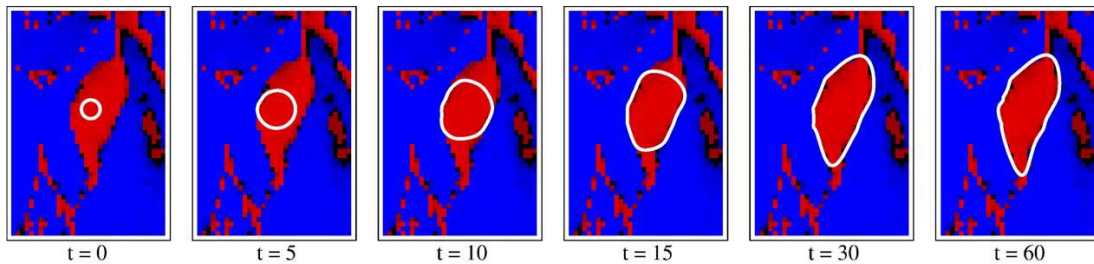


Figure 19. evolution of initial point over time [46]

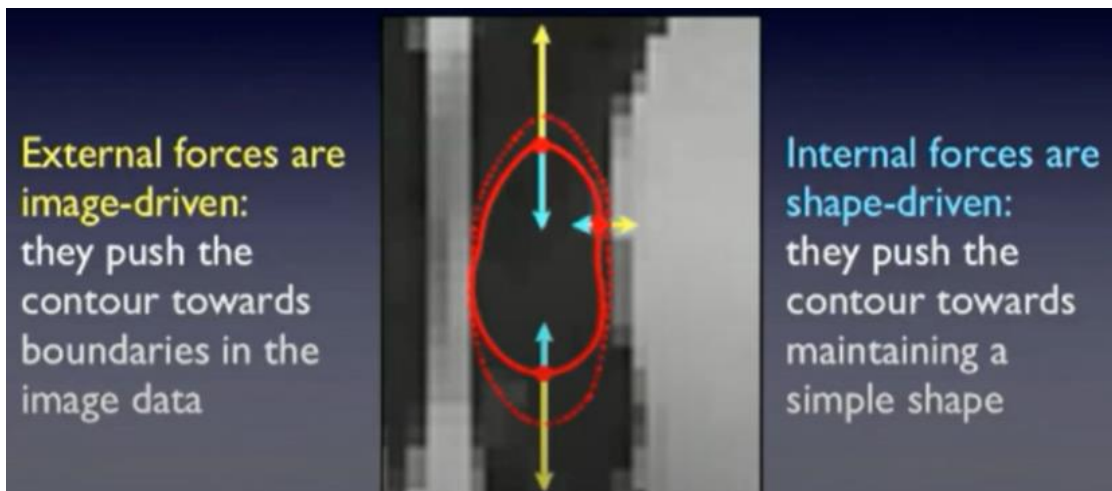


Figure 20. external and internal forces makes equilibrium for the right contour [61]

#### **2.7.4 Effect of mineral density and Hounsfield unit**

Radiologists analyse Computed Tomography (CT) images by using the Hounsfield Unit (HU), which is a relative measurement of radiodensity. The CT reconstruction process creates a grayscale image by utilizing the radiation absorption/attenuation coefficients within a tissue. The X-ray beam's absorption or attenuation is proportional to the tissue's physical density, which determines the Hounsfield Unit through a linear transformation of the initial linear attenuation coefficient. In this scale, distilled water is set to 0 HU and air is set to -1000 HU (at standard pressure and temperature). Bones can have HU values up to 1000 and metals such as steel or silver can reach over 3000 HU. The Hounsfield scale appears as grey tones on the screen, where low-density tissues have negative HU values and appear dark, while high-density tissues have positive values and appear bright due to increased X-ray beam absorption.[62]

After realising the importance effect of the Hounsfield Unit and threshold in segmentation as well as the effect that segmentation has on 3D modelling and computer-assisted surgery, it is crucial to investigate how segmentation is evaluated. Various evaluation techniques will be discussed in the following section.

### **2.8 Segmentation assessment metrics**

Two well-liked similarity measures, the Dice similarity coefficient (DSC) and the Jaccard index (JI), are employed in a wide range of applications, including image processing, data mining, and machine learning. The similarity between two sets of data is determined using both measurements. The characteristics of these two metrics, their mathematical formulations, and their applications in many domains is examined in this section as well as CloudCompare and Hausdorff Distance (HD).

#### **2.8.1 Dice similarity coefficient (DSC)**

In image processing, the Dice similarity coefficient [63] (also called the Srensen-Dice coefficient) is a similarity metric that is frequently employed. It is calculated by measuring the overlap of two comparing segmentations, divided by sum of them, multiply by two. The following formula shows dice Coefficient for data A and B:

$$\text{Dice}(A,B) = (2 |A \cap B|) / (|A| + |B|)$$

*Equation 2*

Figure 21 showing schematic diagram of DSC formula, where A is blue entity and B is red entity. Where  $|A|$  is total number of points in segmentation A and  $|B|$  is total number of point in segmentation B.  $|A \cap B|$  denotes for intersection of two data sets, which is identical points between set A and B. The Dice similarity coefficient runs from 0 to 1, with 0 represents no similarity and 1 denotes perfect similarity between the two sets. This has been used in many image evaluations [39, 58, 64].

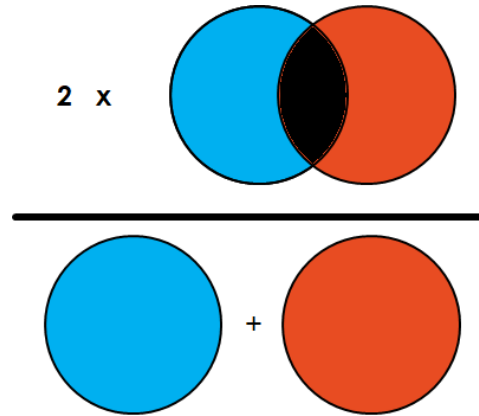


Figure 21. Dice similarity schematic diagram [65]

### 2.8.2 Jaccard Index (JI)

Jaccard index (also known as the Jaccard similarity coefficient) is also used for evaluating segmentation similarity [66]. It is the intersection of two comparing segmentation divide by union of them. Jaccard Index is used in many fields as well as medical segmentation. It defines similarity between two sets of data A and B by the following equation:

$$\text{Jaccard}(A,B) = |A \cap B| / |A \cup B|$$

Equation 3

Where  $|A \cup B|$  is union of A and B, in other words it is the combination of points in A and B, all point that are in either of them or in both. In addition,  $|A \cap B|$  is the intersection points of these two sets. Same as Dice similarity coefficient it ranges from 0 to 1, that 1 represents best overlap.

$$\text{Jaccard (A,B)} = \frac{|A \cap B|}{|A \cup B|} = \frac{|A \cap B|}{|A| + |B| - |A \cap B|}$$

*Equation 4*

Both metrics used to measure similarity in different fields, the main difference between them is that Dice coefficient is more sensitive to false negative and Jaccard index is more sensitive to false positive.

In the context of similarity metrics, a false negative in Dice coefficient would mean that elements that are similar are not being identified by the metric. The Dice coefficient is more sensitive to this, meaning that it might give a lower score if there are elements that are missed. In addition, a false positive for Jaccard index means that elements are being considered similar when they are not. The Jaccard index is more sensitive to this, meaning that it might give a lower score if there are elements that are incorrectly identified as similar [66].

The graphical comparison of the segmented 3D model is also an important step in the validation and assessment of the accuracy of the segmentation process and it is visually more visible. This can be achieved by using a software tool called CloudCompare to analyse the point clouds of the 3D model. The visualization features in CloudCompare make it easier to identify any discrepancies or inaccuracies in the segmented model. The following section provides a more detail about CloudCompare.

### **2.8.3 CloudCompare**

CloudCompare is an open-source software that specialises in comparing and analysing differences between 3D point clouds. Unlike traditional mesh-based comparison methods, CloudCompare views all entities as points. It converts meshes into point clouds with similar topology. Each triangle is made of three points called vertices. By doing so, it takes advantage of octree-based calculations to compute differences quickly, even with large numbers of points.

This software creates octrees from cloud points before calculating the difference. Octrees make the calculation of millions or billions of cloud points faster. For example it calculates the distance of 3 million points to 14000 triangles in 10 seconds [67].

An octree is a tree-structured data format that subdivides 3D points into smaller groups of nearby points, with each node having eight children. Each octree node can either be empty or hold an object. (Figure 22) This structure allows for faster searching and manipulation of large 3D datasets. [68].

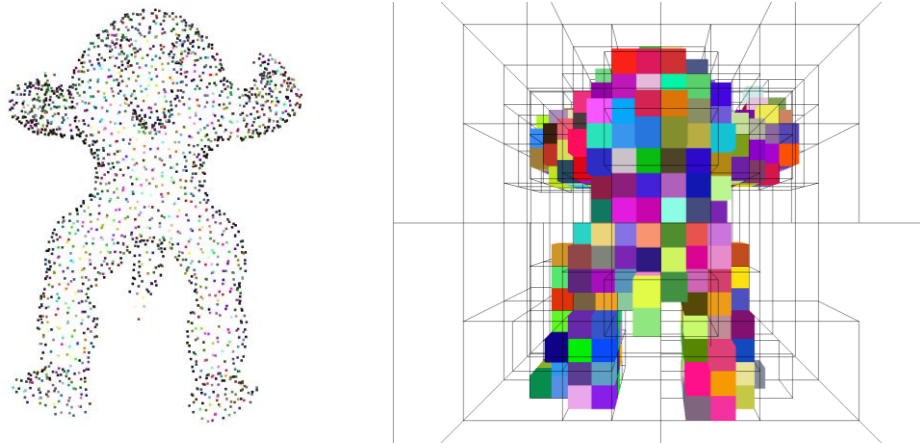


Figure 22. (a) input cloud point, (b) octree division of points [68]

CloudCompare compute the distance using iterative closest point. For each point of compared cloud, it searches for nearest neighbour point of reference cloud and manipulate the distance by Euclidean [69]. The results are effective to number of points and selecting which point cloud is reference or compared. The Euclidean distance between two points in 3d space is simply an extension of Pythagorus' theorem into 3 dimensions, and also known as the 2-norm [166].

#### 2.8.4 Hausdorff Distance (HD)

Hausdorff Distance metric used to quantify similarity or dissimilarity between two sets of data points using mathematical concept. It calculates maximum distance of the point in one set to the nearest point on the other set (Figure 23) [70].

$$h(A, B) = \max(d(a \in B), (\min d(b \in A)))$$

Equation 4

Where a is point of set A; b is point of set B. Also,  $d(a \in B)$  is the distance between point a from set A and nearest point in set B. likewise,  $d(b \in A)$  is the distance between point b in set B and nearest point is set A.

However, the maximum property function makes the Hausdorff distance an asymmetric function:  $h(A, B)$  is not necessarily equal to  $h(B, A)$ . This leads to a more general equation called forward and backward Hausdorff distance of A,B, which takes the maximum of  $h(A, B)$  or  $h(B, A)$ :

$$H(A, B) = \max(h(A, B), h(B, A))$$

Equation 5

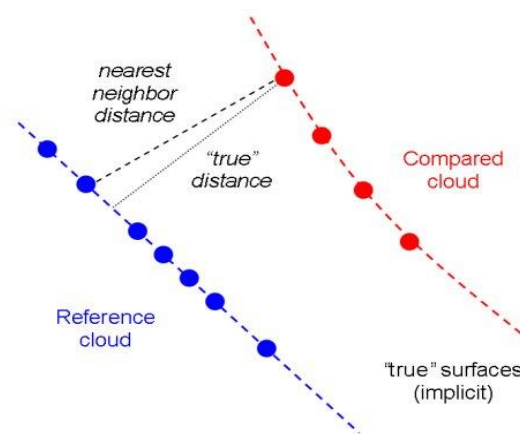


Figure 23. Iterative closest point [67]

The Hausdorff distance offers a measure of dissimilarity in practical applications that considers both the locations and configurations of the points in the sets being compared. It is a helpful tool in many geometrical and computational tasks because it captures the broad differences between the shapes or distributions of points.

## 2.9 Segmentation evaluation

Segmenting medical images is an important step in both medical diagnosis and treatment. As a result, assessing the segmentation process is a persistent concern for the researchers and surgeons [71]. Some of these evaluations are detailed below.

Semiautomatic and manual segmentation of knee cartilage is evaluated by Yu [72]. In comparison to manual segmentation, the study indicated that semi-automatic segmentation produced decreased intra-operator variability. The study also suggests that semi-automatic segmentation may be a more accurate technique for segmenting cartilage in the knee.

In addition, another study rated semi-automatic and manual segmentation but in the vascular field. Luzon [43] compared the results of manual and semi-automated segmentation techniques while building 3D reconstructions of the central mesenteric vascular models (A condition known as mesenteric vascular disease occurs when the arteries in the abdomen that provide blood to the intestines narrow as a result of the accumulation of plaque. The outcome is that the intestines receive insufficient blood flow). This study performed semi-automatic segmentation with Mimics software and manual segmentation with 3-Matic software, respectively, and compared the outcomes with CloudCompare software. The findings demonstrate that although the quantitative outcomes are satisfactory numerically, the qualitative outcomes are unclear and may lead to misunderstanding during surgery. The results of the study demonstrate the necessity for further improvement of the segmentation process to increase the precision and clarity of the outcomes.

Argüello [73] compared three different open-source segmentation software for bone structure analysis. The software under review is semi-automatic region growing of 3D Slicer, active contour segmentation of ITK-Snap and automatic segmentation of In Vesalius. They compared the outcomes of each software with CloudCompare. The effectiveness of the software was assessed using a segmentation of vertebrae. The outcomes showed that 3D Slicer's Region Growing approach had the lowest volume inaccuracy and was the fastest.

Soodmand [74] focused on a comparative analysis of four segmentation software programs and a 3D scanner to assess the accuracy of segmented femur models. Reference femur model created from an optical 3D scanner and other done by seven operators using Mimics, Amira, YaDiv and Fiji Life-Line software. This study used specific value of Hounsfield Unit for bones on CT images. They concluded that the average deviation of the segmented model done by expert operators from 3D scanner is lower than 0.79mm, which they believe is not a significant discrepancy. Additionally, this study emphasises the importance of validity of CT data reconstruction process and usage of this in various medical procedures.

Intra- and inter- observer reliability and reproducibility is clearly important, and some studies have investigated these with regard to segmentation, as detailed below.

The accuracy of manually segmenting femoral metastatic lesions in medical imaging has been assessed [75]. This study evaluated both intra-operator reliability, which measures segmentation consistency within the same operator over time, and inter-operator reliability, which measures segmentation consistency between different operators. According to the study's findings, femoral metastatic lesions can be manually segmented with moderate to good inter-operator reliability but low intra-operator reliability. The study concludes that additional investigation is required to increase the consistency of manual segmentation and provide more dependable techniques for locating and quantifying femoral metastatic lesions.

Intra- and inter-observer reliability of measurements of the calcaneus bone has been studied by Misselyn [76]. In this study, the 3D segmentation of CT image of the cancellous tarsal bone is constructed with Mimics (Materialise™, Leuven, Belgium). The study compares the results by Intraclass Correlation Coefficient (ICC). ICC of intra-observer showed upper class range, and ICC of inter-observer was good. However, the study comes to the further conclusion that strengthening measurement reliability requires thorough training and standardisation of measurement techniques. This means that to guarantee consistent and reliable results, it is crucial that the observer taking the measurement be properly trained and conversant with the measurement technique. Standardizing the measurement methodology will also enable various observers to collect measurements in a consistent way, enhancing inter-observer reliability.

A study [77] assessed the repeatability and inter- and intra- observer reliability of the measurement of total knee arthroplasty (TKA) component rotation by two-dimensional CT scans. Three independent doctors assessed 52 CT images of TKAs that were being considered for revision surgery. The findings showed that the femoral component had poor inter- observer reliability, while the tibial component and combined rotation measurements had strong inter- observer reliability. The femoral component's intra- observer reliability was good, while the tibial components and combined rotations were both very good.

A limitation within the process of semi-automatic knee joint segmentation arises from the inherent variability in knee anatomy. Developing a segmentation technique is a

significant challenge with anatomical variations observed across individuals. Accordingly, subject-specific semiautomatic segmentation method is a promising approach that can make unique anatomical characteristics of each individual's knee joint.

However, this review has highlighted that minimal research has specifically focused on the assessment of knee joint segmentation, despite the prevalence of CAOS procedures of the knee. Nevertheless, other study have been investigated which can provide insight, namely lung cancer cell segmentation [78], evaluation of segmentation of bone from micro-CT [57], assessment of bone segmentation of cone-beam CT [79], evaluating of imaging software of mandibular condyle [80] and segmentation accuracy of long bone [81]. Therefore, to the author's knowledge, this is the first time the semiautomatic segmentation of knee joint is being evaluated, including its intra- and inter- variability.

ICC has been utilized in several of the referenced studies. The subsequent section provides an explanation of it, and it will be employed in upcoming chapters for the analysis of large datasets.

### **2.9.1 ICC Intraclass Correlation Coefficient (ICC)**

In the context of reliability studies, the Intraclass Correlation Coefficient (ICC) is a statistical metric used to evaluate the consistency or reliability of measurements produced by various observers or methodologies. ICC is frequently used in engineering domain and is especially helpful when handling continuous or proportional data. It offers a means of calculating the percentage of overall measurement variability related to real differences between subjects or objects as opposed to measurement error [82]. The ICC is a value between 0 and 1, where values below 0.5 indicate poor reliability, between 0.5 and 0.75 moderate reliability, between 0.75 and 0.9 good reliability, and any value above 0.9 indicates excellent reliability [82].

ICC could be different based on the "Model" (1-way random effects, 2-way random effects, or 2-way fixed effects), and the "Definition" of relationship considered to be important (consistency or absolute agreement) [82].

## **2.10 Finite Element Analysis**

In several disciplines, including biomechanics, structural engineering, and medical research, segmentation is a crucial step before Finite Element Analysis (FEA). Segmentation is one of the important step to produce a precise representation of the objects under analysis, which separates the relevant structures of interest from the surrounding background tissue. FEA enables the analysis of complicated mechanical behaviours, such as stress distribution, deformation, and load-bearing capacities, by breaking the segmented model into smaller pieces and producing a mesh. Since the geometry and material characteristics of the objects are precisely represented in the final finite element model due to effective structure segmentation, FEA simulations can provide trustworthy predictions and insights. In this regard, this section contains more information about Finite element analysis contextualised to the knee.

When the biomedical problems are difficult, impossible, too expensive and/or time consuming to be solved analytically, computational modelling often offers a mathematical approach that can provides approximate solutions. Virtual modelling, computer simulation, and other terms are also used to refer to computational modelling. Due to considerable advancements in both software and hardware, computational approaches have become very popular. It is very useful tool to understand the physics systems. It estimates the model behaviour under embedded boundary conditions and supports. This approach divides the complex engineering problems into smaller and more manageable pieces called finite elements. Finite element method applies to skeletal system, analyse dynamic activities and motions, loading, and mechanics analysis of stress and strain at tissue levels.

In the following the use of finite element modelling is justified for the knee joint, and some literature that applied finite element on knee is mentioned:

### **2.10.1 Finite element analysis of the knee joint**

The knee joint is one of the most frequently used parts of the body, bearing 4 to 7 times a person's body weight during daily activities such as walking or running, and up to 24 times during jumping [2]. Despite this heavy usage, the knee has supporting elements, including ligaments, tendons, meniscus, bursae, muscles, and the knee capsule, that help protect it from injury or stabilize it. However, damage to these soft tissues can

cause instability and pain, as seen in 72% of osteoarthritic knees with self-reported buckling [27]. Increased joint laxity, resulting from injury or genetic conditions, is also linked to instability.

In-vivo measurement of knee joint is not practical or possible, while ex-vivo measurement is expensive and limited by the availability of cadavers. Therefore, computer models are often used to simulate knee joint mechanics, as they are reliable and cost-effective.

For decades, researchers have created mathematical models, including finite element models, to analyse the complex knee joint. Although the complexity of these models varies, they are all time-consuming due to the intricate reproduction of ligaments and cartilage, requiring significant computational power and time to run simulations. Additionally, they are not easily accessible for most pathological and mechanical studies. There is also no consensus among researchers regarding the properties of soft tissue materials in the knee.

The study of knee biomechanics through experimental means is often challenging due to the high cost and time investment, as well as the difficulty of obtaining accurate stress and strain readings, especially in the case of rare or non-reproducible native tissue. To overcome these obstacles, the FEM has become a crucial tool in biomechanics for investigating the mechanics and kinematics of various body parts and joints [83]. There are several commercially available software programs, such as ANSYS, ABACUS, LS-Dyna, and COMSOL, that use algorithms to break down complex problems into smaller, manageable pieces and solve them based on their inter-relationships [84].

In the analysis and testing of the human knee joint, FEM plays a vital role. It can demonstrate stress points within the joint, anticipate mechanical activity under different loads and conditions, simulate and analyse the behaviour of implants prior to surgery, test the implant's response post-surgery, and help identify joint problems that cause pain [85-88].

The Finite Element Method (FEM) has a long history of use in knee joint analysis, beginning with the work of Wismans et al . [89] in 1980, who established a 3D model

of the joint using FEM and concluded that the computed internal and external rotations during flexion-extension were consistent with experimental results. Similarly, Andriacchi et al. [90] in 1983 found that knee movement under loading was largely dependent on constraints to a few degrees of freedom, and Essinger et al. [91] in 1989 discovered that the movement of condylar type knee was shaped by the prosthesis's articular surface shape and figure.

Blankvoort et al. [92] in 1991 used a 3D mathematical model of the knee joint to investigate the behaviour and movement of the joint with respect to articular contact, considering both rigid and deformable contact. The material properties of ligaments and cartilage were sourced from literature. In recent years, 3D models of the knee joint have been generated from Magnetic Resonance Imaging (MRI) and Computed Tomography (CT) scans. For example, FEM models have been constructed from manually acquired CT images of cadavers by Haut et al. [93] in 1997 and by Donahue et al. [94]. Soft tissue was digitized using a laser-based 3D coordinate system. However, this system can only digitize the soft tissue of cadavers, making it impossible to use on live human knee joints. A recent review of the FEA of the knee joint has been published [95]. Figure 24 shows the steps involved in constructing a finite element model of the knee joint and mesh generation for further analysis.

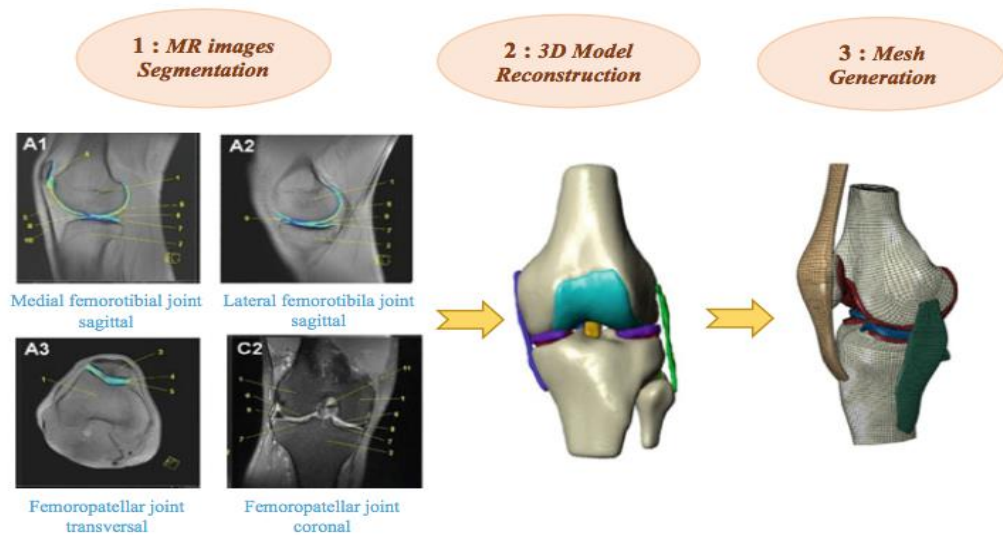


Figure 24. Making 3D model of knee joint from CT scan images. Left [96], middle [97], right [98]

Recently, researchers, Maffulli, and Rohita [99, 100] used finite element analysis to represent cartilage as a non-linear anisotropic material, which allows for the variation of material properties. This has advantages over conventional linear elastic isotropic material models, leading to improved physical model and more reliable and accurate behaviour assumptions. However, the complexity and expenses associated with this method limit the modelling of tissues in isolation, which only considers relevant assumptions and excludes the rest. This approach is suitable for certain cases but has limitations when modelling osteoarthritis in the knee joint, as it is a disease affecting the entire joint and requires investigation of the entire knee joint [101].

Mononen et al. [102] modelled the knee joint with the help of nonlinear cartilage, incorporating viscoelastic or time-dependent components. Other studies have represented cartilage as a fibril-reinforced poroviscoelastic material with different properties, for investigating chondrocyte compression during walking and cartilage deformation under compression. Dabiri [103] modelled cartilage as fibril-reinforced to examine fluid pressure and inhomogeneity of surrounding tissues. Meng [104] modelled cartilage as a fibril-reinforced biphasic material to investigate knee joint contact performance under body weight.

Studies [105-108] suggest that changes in age, gender, physical activity, and disease can alter material properties, leading to unreliable experimental quantities over time. This study aims to find material properties to represent all soft tissues around the knee joint. Many studies [108-110] used the ACL, PCL, LCL, quadriceps tendon, and patella ligament as ligament material properties. Shepherd [111] modelled cartilage material properties using human femoral condyle and tibial plateau samples. Some researchers [112] faced a lack of appropriate data and used bovine menisci samples for modelling soft tissue material properties, while LeRoux [113] used canine meniscal material properties. Other studies [114, 115] adopted material properties from a previously published review article. Kazemi [116] modelled the knee joint using MRI and adopted material properties from bovine humeral head cartilage as well as human menisci and tibial plateau.

## Chapter 3 Research Aims and Objectives

The literature review in chapter two has highlighted the importance of developing accurately 3D models of the knee joint for a variety of applications. Existing finite element models of the knee detail each anatomical structures separately, which is time consuming and computationally complex to solve the multiple contact regions. A recent study [4] suggested a way forward in which the soft tissue envelope surrounding the bony anatomy was considered a single material.

If such a method proves useful in modelling knee joint kinematics and kinetics, then the potential for this approach is very strong. However, due to the contiguous boundary between bone and soft tissue small variations in bony anatomy may give rise to localised stress concentrations in resulting analyses. It would therefore be of wise to investigate sources of variability in constructing such a model. These sources mainly are

- Inter- and intra- observer repeatability
- Thresholding level

Such an understanding gained will also be of interest to the wider biomechanics community modelling the knee and segmenting.

With this in mind, this thesis adopts the following aims:

### 3.1 Primary Aim

**Research question: What is the impact of using simplified soft tissue models, specifically an incompressible, isotropic, homogeneous, elastic cylinder representation, on finite element simulations of knee joints?**

In conventional knee joint models each ligament and lubricants must be defined separately, which takes lots of time for both the person and the model to be constructed. This study aims to use a more effective method to handle this problem by substituting the knee capsule, muscles, tendons, ligaments, bursae and meniscus with a single, incompressible, isotropic, homogeneous, elastic cylinder. This all-encompassing cylinder, which has unique material properties created to replicate the behaviour of the

soft tissues, includes all the knee capsule parameters in its representing of the soft tissues.

Consequently, the effect of repeating segmentation and existence of small change in the surface is investigated on the knee model, and stress and strain are obtained.

The primary aim is to replace the soft tissue around the knee with an isotropic, incompressible, homogeneous, elastic cylinder. This will be useful for clinical research and analysis in the following principle:

1. Simplifying complex soft tissue model and properties leads to reduce computational time and complexity
2. Reduce time consumption during ligament or other soft tissue modelling.

These sub-aims bring the following objects:

Objective 1. Inspect finite element literature.

Objective 2. Produce two 3D knee model from CT by available software and the bespoke soft tissue environment.

Objective 3. Apply restraint, support, and force in finite element software.

Objective 4. Find the effect of two different segmentation on the simulation results.

These arises three more aim to investigate.

### **3.2. Secondary Aim**

**Research Question: How thresholding affects the segmentation of 4D CT images of knee joint?**

Thresholding is a common technique used in image processing to segment an image into foreground and background regions based on the intensity values of the pixels. In medical imaging, the threshold value is used to separate the relevant structures, such as the bones and tissues of the knee joint, from the surrounding tissue or background. The choice of threshold value can have a significant impact on the outcome of the

segmentation, as different values can result in different levels of detail and accuracy in the resulting 3D model.

Reliable segmentation required a proper threshold value. Therefore, finding the optimal threshold level is an important step in the segmentation process, as it ensures that the resulting 3D model accurately reflects the structures of interest and is suitable for further analysis and interpretation. The effect of different thresholding values on the outcome 3D model of the knee joint can be evaluated by comparing the models generated using different threshold values, and assessing their accuracy, consistency, and suitability for the intended application.

The secondary aim is to find the optimum threshold level for the tibia, femur, and patella in order to get the most advantageous segmentation from the available CT image in this study. This is one of the primary steps for image segmentation and further analysis in this study.

To attain this goal, the following research goals were chosen:

Objective 1. Review literature about the threshold value and its effect on the segmentation

Objective 2. Finding the optimum threshold level for each bone

Objective 3. Compare it to the manual segmentation.

Objective 4. Implement found threshold level, perform the semiautomatic segmentation, and produce the knee joint 3D model.

### **3.3 Tertiary Aim**

**Research question: How repeatable and consistent is the segmentation process that is done by one person?**

The third mission here is to perform a Mock test for the Intra-reliability of the semiautomatic segmentation. For this purpose, the author performs the segmentation of the same femur joint CT image five times and compared them in CloudCompare. By considering the number of points in each segmentation and comparing them, the

total number of identical points between two 3D models, the percentage of identical nodes with respect to total nodes, the number of non-identical nodes, and the absolute difference between them are obtained. The measurements have been determined by the difference between the surfaces in a point-by-point manner.

The tertiary aim is to perform the repeatability and reliability of the semiautomatic segmentation process. To find out the intra- observer variability.

Objective1. Study the literature concerning bone intra- observer variability.

Objective2. Using the optimum threshold level found previously, segment the CT image of the knee joint five times and produce 3D model.

Objective3. Produce step-by-step protocol to submit to the ethical department and use them for the next experiment.

Objective4. Compare all the fifth segmentation by CloudCompare

Objective5. Assess the reliability of the semiautomatic segmentation process when performed by a single person repeatedly.

### **3.4 Quaternary Aim**

**Research question: How reliable and repeatable is the semiautomatic segmentation process is?**

ITK-Snap is a programme that is frequently used in the medical imaging sector. It offers a user-friendly interface and cutting-edge features for automated segmentation. To verify whether the semiautomatic segmentation method employing ITK-Snap is useful in clinical and research settings, it is critical to assess its repeatability and reliability. This study attempts to evaluate the repeatability and reliability of the automated segmentation process. Researchers and healthcare practitioners can decide whether ITK-Snap is appropriate for their particular applications by being aware of the tool's advantages and disadvantages.

The quaternary aim is to perform the inter-observer reliability test on semiautomatic segmentation. This is the main purpose of this study, which is subdivided into previous

aims as well. The experiment can help researchers and clinicians in the diagnosis investigation of knee joints in these principles:

1. Accurate pre-operating planning and confident surgery for surgeons
2. Personalized treatment respect to individual patient needs
3. Enhance surgical outcome
4. Minimize the invasive surgery

For these aims, the following objectives are considered:

Objective 1. Perform a thorough analysis of the literature related to inter- and intra- observer variability. This should be related to the bone as much as possible.

Objective2. Obtain the ethical approval to recruit fifteen participants to perform the segmentation.

Objective 3. Perform five times segmentation by fifteen participants and collect the raw data.

Objective 4. Write the MATLAB code to do the mathematical comparison.

Objective5. Graphically compare all the results in CloudCompare

Objective6. Import the data to SPSS IBM for statistical analysis and find Inter correlation coefficient.

## **Chapter 4 Effect of the threshold level on segmentation outcomes**

### **4.1 Introduction**

Based on pixel intensities, the threshold acts as a border, separating pixels that represent objects from those that represent backgrounds. A poorly selected threshold may result in either under- or over- segmentation. Finer details and limits may be lost in under-segmentation when objects are clustered together. However, over-segmentation causes objects to be divided into smaller, fractured sections, which introduces noise and lessens the quality of segmentation. This threshold value is called optimal threshold value that is the value that is best to segment foreground from background. Therefore, one of the most important steps in image segmentation algorithms is determining the ideal threshold. This is going to vary from CT to CT that needs to gain insight of varying threshold level.

Hence, investigators explore the impact of threshold values across numerous studies, which will be mentioned in the following. Notably, the influence of threshold levels on segmentation on mandible bone segmentation from CT and CBCT scans underscored the significant effect of the threshold value on surface outcomes [51]. The study emphasized the reliance of segmentation accuracy on both grey values and the threshold, which are operator inputs. Employing two techniques, commercial software and the expertise of a 3D clinician. The study compared segmented mandibles to a 3D model established by a high-resolution laser surface scanner as the gold standard. Results revealed excellent consistency in measurements, with an intraclass correlation coefficient (ICC) ranging from 0.923 to 1.000. Models from the commercial software group exhibited an average deviation of  $0.330 \text{ mm} \pm 0.427$  from the gold standard, while those from the clinician's rendering showed a mean deviation of  $0.763 \text{ mm} \pm 0.392$ . Furthermore, surface models from both protocols tended to have larger dimensions than the reference models.

Another recent study [42] specifically examined the influence of thresholding values on cranial bone segmentation from CT and CBCT using Viewbox 4 software. The results, assessed through superimposition and Iterative Closest Point (ICP) comparison to a manually selected reference model, highlighted the significant impact of the

threshold value on the surface. While intra-examiner reliability was assessed in the experiment, inter-examiner reliability remains a subject of inquiry, with acknowledged limitations, such as the absence of a true gold standard reference model.

Additional research has also explored the effects of image thresholding levels on segmentation for various body parts [41, 47-53]. To detect inter- and intra-observer variability, understanding and assessing variability and repeatability of segmentation have been recommended [42]. Consequently, researchers and medical organizations consistently seek precise, reliable, repeatable, and accessible image segmentation algorithms for generating 3D bone models from CT or MRI scans. This pursuit has been investigated across different fields, including cartilaginous bone tumors, upper airway, cranial bones, prostate cancer, lumbar spine, and vertebrae [40, 42, 54-57]. Similarly, other investigations delved into the impact of image thresholding levels on segmentation, emphasizing the need for meticulous consideration of threshold values for optimal outcomes [50, 61-67]. Hence, this chapter investigating the effect of the threshold value on the knee joint and finds the optimal threshold value for the available CT image.

There are three brief experiments described in this chapter. In the first experiment, the tibia was segmented by using different threshold levels. The tibia with the highest level of graphical and visual detail, detected by the author to closely resemble the actual anatomy of the tibia, was identified and referred to as the reference tibia. This reference model was manually edited with filling the cavities. Next, the tibia is segmented with variety of threshold values and compared with reference tibia.

In the second experiment, the threshold value of the reference tibia is changed to see the effect of it in the comparison. This is to ensure the reference threshold level is not biased and the human point of view is not influencing the optimum threshold value selection.

The third experiment compares a manually-segmented tibia with reference tibia and tibia which is semi-automatically segmented with other threshold value.

This chapter is necessary to determine the effect of threshold level on the tibia and to find its optimal level for use in future chapters.

## **4.2 Image Data Collection**

Image data has been collected from previous study done by Attard [117]. Briefly, ten patients were scanned using the Toshiba Aquilion ONE™ 4D CT scanner at the Clinical Research Imaging Centre (CRIC). The 3D Adaptive Integrated Dose Reduction control system (AIDR 3D) on the Aquilion ONE™ is an advanced algorithm that can lower the exposure dose by continuously adjusting the tube current during the scan to get the ideal dose at every instant based on the anatomy of the patient and the targeted region [118]. This was planned to reduce radiation dose which the patient receives during the scan.

In this previous study, the Toshiba Aquilion ONE™ 4D CT scanner was used to capture the dynamic movement of the knee. This scanner is a 320-multidetector CT (320-MDCT) scanner. It can produce continuous 4D 3D images at a distance of 16 cm along the z-axis (without the need to shift the table) because of its wide detector. This allows fast and non-invasive dynamic kinematic evaluation of the knee joint in vivo. The voxel size is reported as 0.78 x 0.78 x 0.5 mm in metadata.

To optimise the scanning methodology for the 4D CT component of the study, control volunteers knees were first scanned. Control participants for the study were recruited from the staff and student population at the University of Strathclyde. The anonymous 4D CT image data used in this study is from one of the control participants. The image is taken of both knees in the prone position during flexion.

## **4.3 Methodology**

Although multiple frames of 4D CT data were captured, a single frame of data was utilised for this study. After importing the DICOM (Digital Imaging and Communications in Medicine- is the international standard for medical images and related information) file into ITK-Snap, the first experiment involved the semi-automatic snake active contour tool to find the visually optimal threshold value. The “optimal threshold” represents the threshold value which shapes the bone with the maximum intensity, but has minimal bleed to nearby bones.

The upper threshold for consideration was fixed at 2017 HU, the maximum threshold value available for this CT image within software. The threshold value was reduced from this maximum to find the optimum threshold value. Lower threshold values

define more of the image as cortical bone, and higher threshold value include less image as cortical bone. Other parameters of importance, such as region of interest (ROI), position and coordinate of initial growing points, step size and iteration were kept constant. Holes or voids in the reference tibia were manually filled-in.

The reference tibia was then compared with other tibiae segmented with different threshold values that vary from -2048 HU to 1000 HU. The produced 3D models were exported as STereoLithography (STL) mesh files and imported to CloudCompare to compute their mean values and standard deviation of their nearest neighbour distance using iterative closest point (ICP). As all the 3D models were exported from same CT machine, software and raw DICOM, they were equal in size and already finely aligned. Rough and fine registration procedures in the CloudCompare software to best-align the surfaces were not required.

The second experiment was performed in order to find if the chosen optimal threshold affected critical anatomical landmarks in the resulting image. The first experiment was repeated with a sub-optimal reference tibia, obtained using a threshold of 130 HU. This model required the fibula to be manually erased, and any holes and voids were manually filled-in, as before.

The third experiment was designed to find the influence of manual segmentation versus semiautomatic segmentation. The tibia was segmented manually using the polygon tool in polygon mode. The manual tibia was then compared to the two assumed reference tibiae determined semiautomatically, in CloudCompare.

CloudCompare analysis involved determination of the mean difference between the point clouds as determined by the iterative closest point algorithm. At the time of this experiment, evaluation methods, such as Dice Similarity Coefficient (DSC), Hausdorff Distance (HD), Jaccard Index (JI), and Interclass Correlation Coefficient (ICC), were unknown to the author and were therefore not used. Subsequent exploration and a broader understanding of the field prompted the incorporation of these additional metrics in the later chapters.

Optimal threshold values for the femur, fibula and patella were also determined based on the above methodology, although not analysed in the same manner using CloudCompare.

#### 4.4 Results

Figure 25 illustrates tibias that are segmented with different threshold values. At a threshold of 140 HU, there is a clear bone density for the tibia, but the algorithm bleeds the tibial segmentation to the fibula. Similarly, at a threshold 200 HU, whilst there is less bone density, the fibula is still attached. At the threshold of 205 HU the bleeding to fibula is eliminated however the tibia segmentation ends up with having cavities, which needs to be edited manually. At the threshold of 300 HU the bone segmentation is very poor with many voids. The threshold of 205 HU was chosen due to the automatic elimination of the fibula from the resulting image combined with minimal manual editing. Therefore, the semi-automatic segmentation methodology determined the optimal threshold level to be 205 HU for tibia. Following gap filling, this model was set to be the reference model. Other generated models were compared with this reference model.

Figure 26 depicts the mean ( $\pm$  SD) distance between model vertices using iterative closest point algorithm (C2C). Altering the threshold causes significant effect on tibia segmentation. Above 205, the mean C2C distance increases to just over 1mm. There is a clear jump below 205 which is associated with the appearance of the fibula in the resulting images.

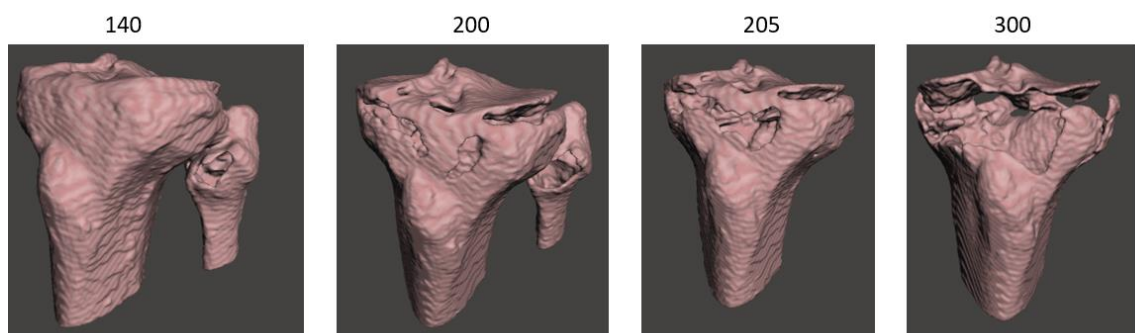


*Figure 25. Effect of threshold value on tibia 3D model*

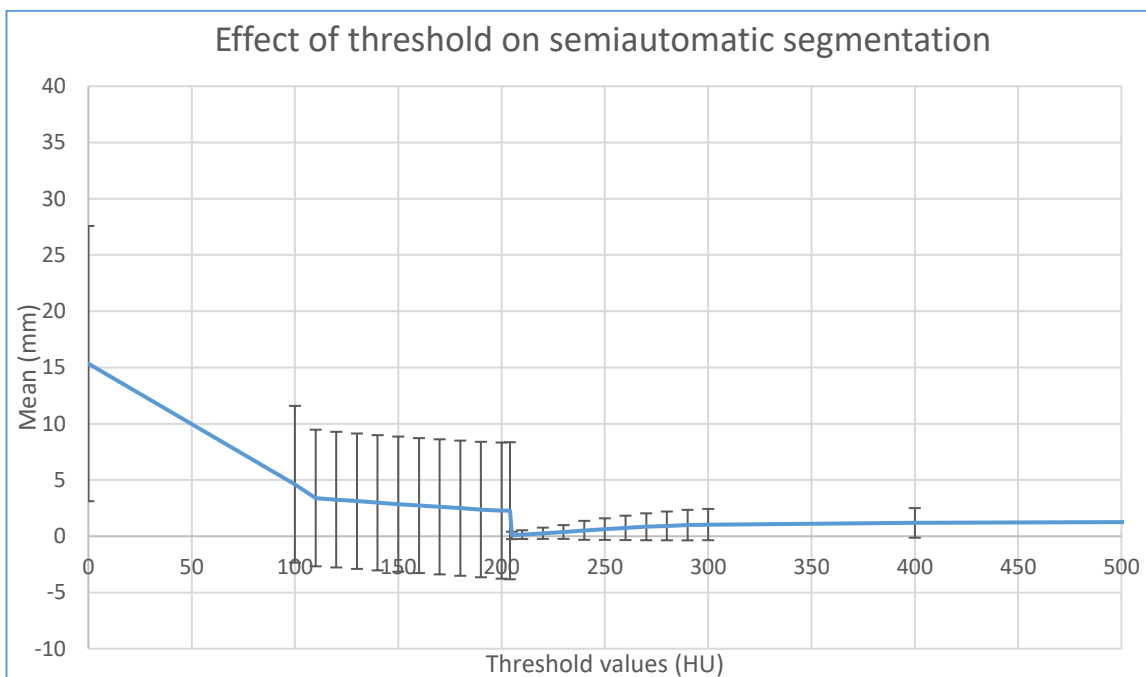


Figure 26. Effect of threshold with respect to threshold value  $\pm SD$

The second experiment is same as first experiment except the reference tibia is segmented at different threshold value. It is generated at 130 HU threshold and edited manually by filling the holes and erasing the fibula. This new reference tibia was compared with other tibia segmented with different threshold value and the results are shown in Figure 28-32. Figure 27, shows the difference in the mean values a clear drop in the error is clear from the picture.

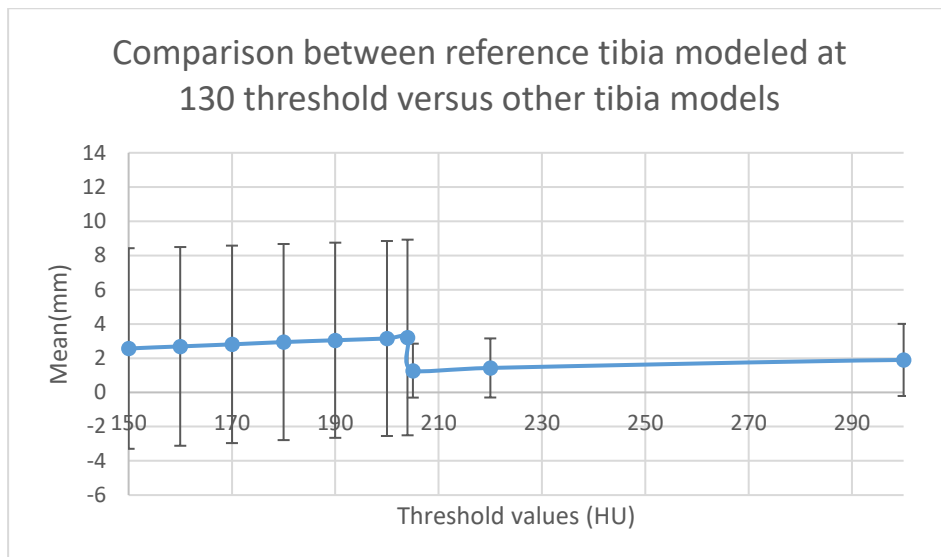


Figure 27. Difference of tibia segmented by 130HU and other threshold values

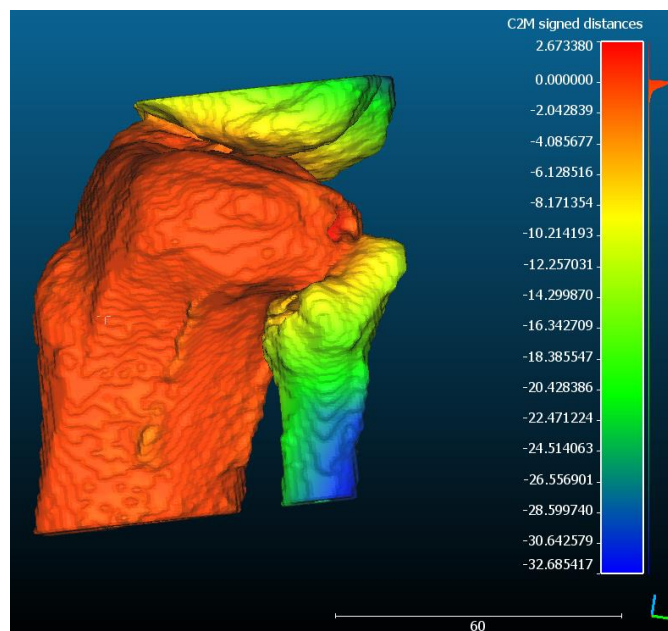


Figure 28 Distance between reference tibia (130 HU) vs tibia with 100HU

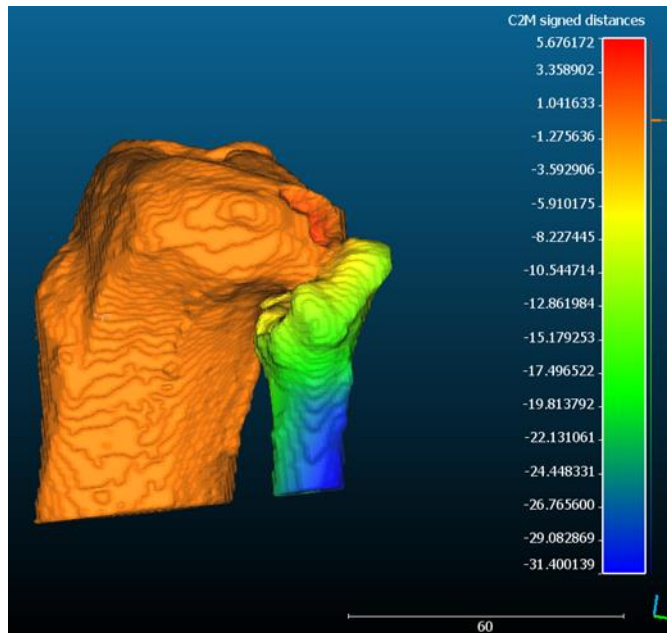


Figure 29. Distance between reference tibia (130 HU) vs tibia with 130HU

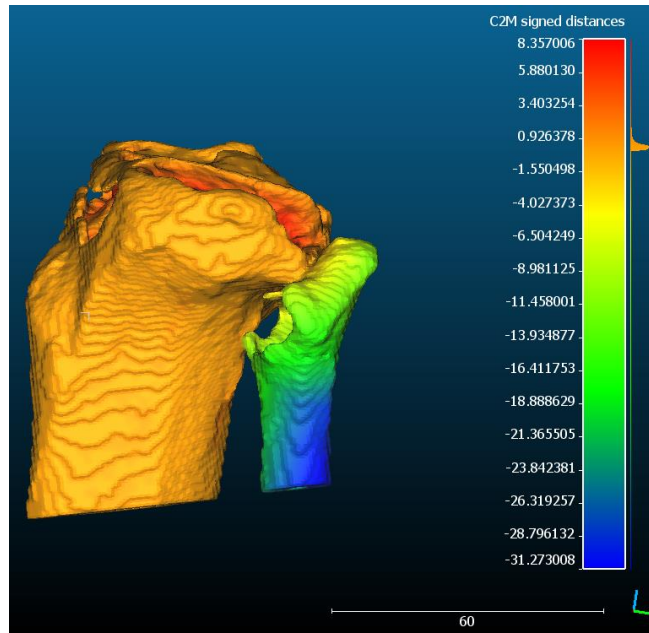


Figure 30. Distance between reference tibia (130 HU) vs tibia with 204HU

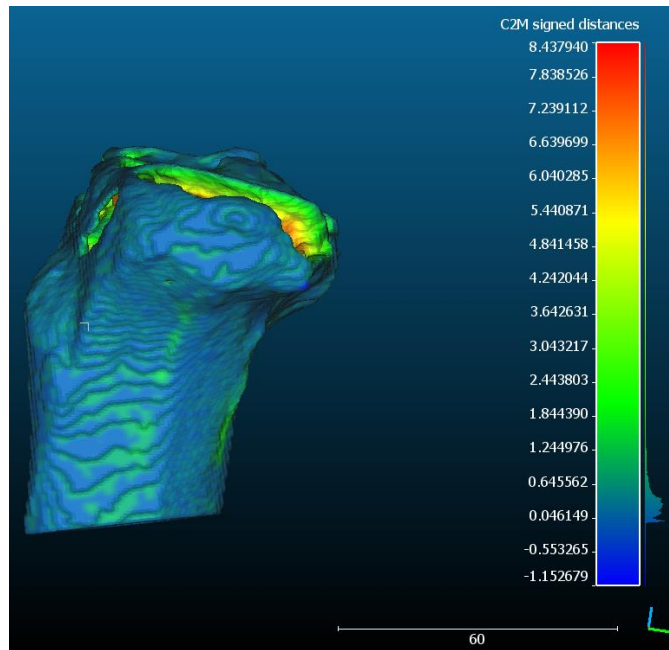


Figure 31. Distance between reference tibia (130 HU) vs tibia with 205HU

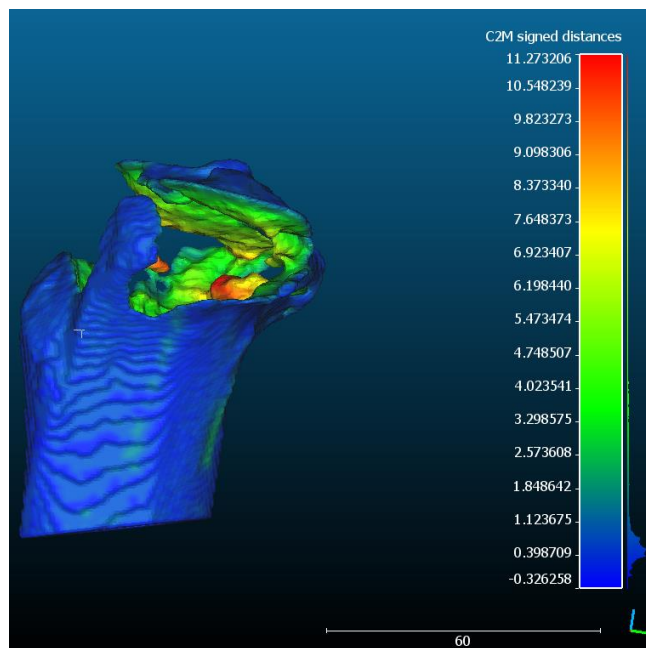


Figure 32. Distance between reference tibia (130 HU) vs tibia with 350HU

For the third experiment, the tibia was segmented manually using the polygon tool in ‘polygon mode’. Both the cortical bone and spongy bone were segmented whereas during the semiautomatic only the cortical bone was segmented which has more bone

density. Figure 33 is showing tibia segmented manually and segmented with 130 HU and 205 HU. Figure 36 represents their respective number of points. Figure 35 showing mean value of the comparison. Figure 27D illustrates comparison histogram of manually segmented tibia versus semi-automatically segmented tibia with 205 HU.

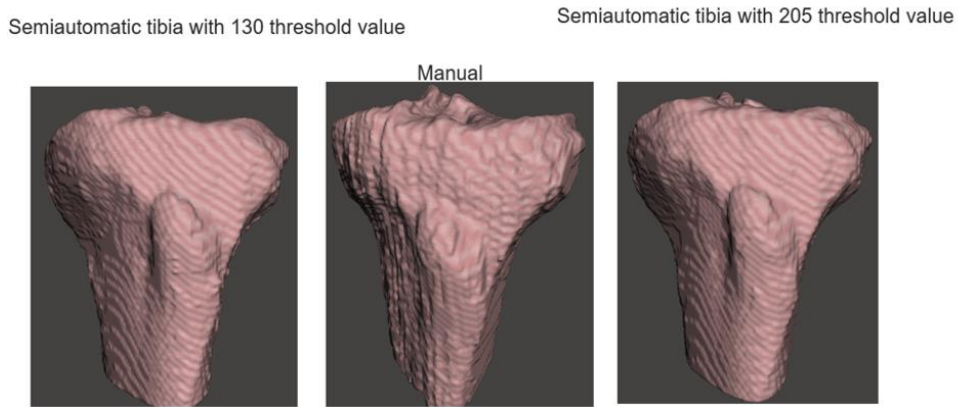


Figure 33. Manually segmented tibia compared to semiautomatic segmented tibia.

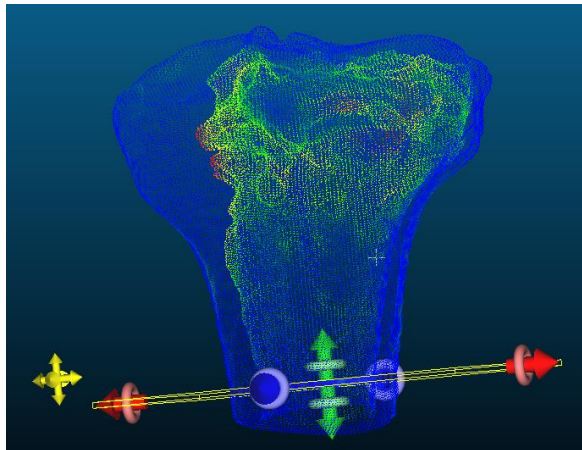


Figure 34. Internal and external differences between tibia segmented by 130HU and 205 HU

### C2C comparison between manual vs semiautomatic with 205 and 130 threshold

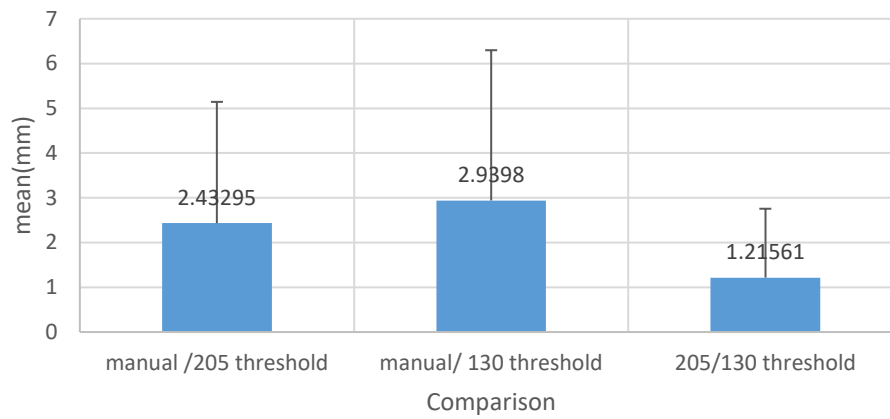


Figure 35. Comparison of three different segmented model and their mean values

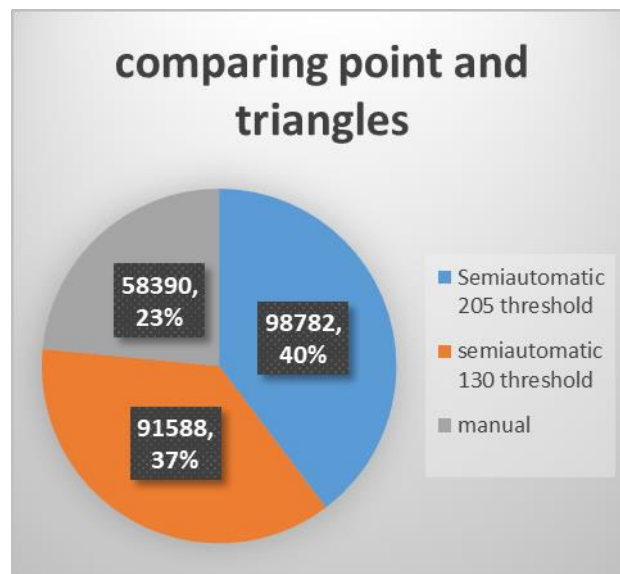


Figure 36. Number of points for each model

Optimal threshold values were determined as being 205 HU for the tibia, 160 HU for the femur, 200 HU for the patella and 232 HU for the fibula.

## 4.5 Discussion

Various imaging parameters, such as slice thickness, reconstruction algorithms, and contrast enhancement techniques, directly influence the accuracy of image segmentation techniques [41]. These parameters affect the contrast and sharpness of anatomical structures in medical images, necessitating careful consideration and adjustment of threshold values for precise segmentation. Furthermore, variations in imaging protocols across different scanners and imaging centres can introduce complexities, underscoring the need for robust segmentation methods adaptable to diverse imaging conditions [119].

The selection of an appropriate threshold value is critical for accurate image segmentation, as demonstrated by the experiments in this study. Even minor variations in the threshold value can significantly affect the final segmented model, leading to under-segmentation or over-segmentation of the desired anatomical structures [42]. The study identified the optimal threshold values for accurately segmenting various bones within the knee joint from CT images: 205 HU for the tibia, 160 HU for the femur, 200 HU for the patella, and 232 HU for the fibula.

The differences in ideal threshold values across bones can be attributed to several factors. Firstly, varying bone densities affect their appearance on CT scans, requiring different threshold values for precise segmentation. Secondly, each bone's internal structure and shape influence its CT appearance, necessitating distinct threshold values. Additionally, factors such as CT scanner type, imaging protocols, acquisition characteristics, image noise, and artifacts can influence the segmentation process, justifying threshold value adjustments [120].

This study also highlights the potential influence of operator bias in manual segmentation. The comparison between manual and semi-automatic segmentation revealed that semi-automatic segmentation using optimal threshold values could produce more accurate models with less human error than manually segmented models. This finding aligns with previous research and underscores the advantages of semi-automatic segmentation techniques in reducing subjective biases [121, 122].

Furthermore, the experiments revealed that the choice of reference model threshold value does not significantly affect the identification of the critical threshold point for

optimal segmentation. This observation suggests that the optimal threshold value is an inherent property of the image data and is not influenced by the initial reference model used for comparison. Figures 26 and 27 show that changing the threshold value of the reference model does not affect the critical point where sudden change happened. This research compared the manual segmentation, using polygon tools, versus semiautomatic segmentation with two different threshold values Figure 33, that can be interpreted as semi-automatic segmentation could be as reliable as manual segmentation or even more realistic and prevent human bias error.

The quantitative data supports the significant effect of threshold values on the final segmentation model (Figure 26, Figure 27). The curves show sharp breaks and become highly nonlinear at the optimal threshold values, indicating the critical points for segmentation accuracy. Additionally, the manually segmented models were smaller, with fewer points and triangles, compared to the semi-automatic models, potentially due to the "Koch snowflake" theory, where manual segmentation may have a smaller perimeter with less fine detail [123]. Figure 25-27 shows 205 HU is optimal threshold for tibia in this case. At this point, the curve breaks sharply and the curve become extremely nonlinear. Figure 35, 36, quantitatively supports the idea that the manually segmented model of tibia is smaller than semiautomatic tibia and has less number of points and triangle. It also represents that the tibia model with optimal threshold value shows most bone density than smaller threshold value (130 HU).

The results align with previous studies [72], emphasizing that the accuracy of segmented 3D models highly depends on grayscale values and threshold values, which are often chosen manually by operators. Image quality, grayscale levels, noise, artifacts, and inhomogeneity can further complicate the segmentation process, highlighting the importance of robust segmentation methods and carefully selected threshold values.

In clinical practice, accurately segmented 3D models play a crucial role in guiding surgical interventions and optimizing patient outcomes. Deviations from optimal threshold values can lead to inaccuracies in surgical planning and execution, potentially compromising patient safety and surgical efficacy [168]. Therefore, ensuring the precision of segmentation methods through the selection of threshold

values is paramount for achieving reliable clinical outcomes and enhancing patient care.

While manual segmentation approaches offer high precision, they are often time-consuming and labour-intensive. In contrast, semi-automatic segmentation techniques strike a balance between accuracy and efficiency, leveraging computational algorithms to streamline the segmentation process while minimizing human intervention. By optimizing computational efficiency, researchers can accelerate the generation of segmented models.

The generalizability of optimal threshold values across different patient populations, anatomical regions, and imaging modalities is an important area of investigation. While specific threshold values of this study may be identified for a particular cohort or imaging protocol, their applicability to broader clinical contexts requires validation across diverse datasets. Future research efforts should focus on identifying factors influencing the generalizability of threshold values and developing robust segmentation methods that can adapt to independent imaging conditions.

Educationally, segmented 3D models offer immense value for medical training, anatomical visualization, and patient education. Interactive anatomical models enable students, clinicians, and patients to explore complex anatomical structures and pathological conditions in a virtual environment, fostering deeper understanding and facilitating informed decision-making. By using segmentation techniques to create new educational resources, researchers can enhance the learning experiences of healthcare professionals and empower patients to actively participate in their healthcare journey.

Moreover, efforts should be made to reduce potential biases in dataset selection and ensure equitable representation of patient demographics to uphold the ethical integrity of segmentation research.

#### **4.6 Conclusion**

This chapter provides insights into the effects of threshold selection on image segmentation accuracy, particularly for segmenting knee joint bones from CT images.

Threshold value selection is a critical step in image segmentation, as it directly affects the quality and accuracy of the segmented models. Optimal threshold values were identified for segmenting different bones of the knee joint, namely tibia (205 HU), femur (160 HU), patella (200 HU), and fibula (232 HU).

Semi-automatic segmentation using the optimal threshold values can produce more accurate and detailed models compared to manual segmentation, reducing the potential for human bias and error.

These findings contribute to the development of more reliable and accurate image segmentation techniques for medical imaging applications, particularly in the field of orthopaedics and joint analysis.

## **Chapter 5 Pilot experiment of intra- observer variability of segmentation of knee CT image**

### **5.1 Introduction**

For applications in knee surgery and biomechanics, accurately segmenting the structures of the knee joint from CT scans is an essential first step in creating subject-specific finite element models. However, there are challenges, as this procedure involves identifying and differentiating between soft tissues and bony structures, which is not always easy.

"Intra-observer variability" describes the degree of variation or inconsistency in segmentation results when the same observer repeats the segmentation task on the same set of images in the context of medical imaging, especially with CT scans. In other word, it evaluates the consistency and repeatability of the segmentation procedure as perceived by a single observer [44]. Evaluating the variability of segmentation within a single operator and across different operators is of interest to scientists. Some points of consideration include the following.

The impact of inter- observer manual segmentation variability on the reproducibility of 2D and 3D CT and MRI patients with cartilaginous bone tumors were investigated by another study [54] in which three radiologists independently performed manual contour-focused segmentation on unenhanced CT, T1-weighted, and T2-weighted MRI, drawing both 2D and 3D regions of interest (ROIs). The study extracted 783 and 1132 features from original and filtered 2D and 3D images, respectively. Intra-class correlation coefficient (ICC) was used to assess feature stability. The results shows that 2D and 3D features of cartilaginous bone tumors extracted from unenhanced CT and MRI are reproducible. However, some degree of inter observer segmentation variability emphasizes the need for reliability analysis in future studies utilizing these segmentation techniques.

Also a study [75] evaluated inter- and intra- operator reliability of manual segmentation of CT scans of femoral metastatic lesions. For this study two operators independently segmented 54 metastatic femurs (19 osteolytic, 17 osteoblastic, and 18 mixed). Dice coefficients (DCs) were calculated to assess reliability, with a DC > 0.7

indicating good reliability. The results revealed generally poor inter- and intra-operator reliability for lesion segmentation. Inter-operator DCs were 0.54 ( $\pm 0.28$ ) and 0.50 ( $\pm 0.32$ ) for the first and second segmentations, respectively. Intra-operator DCs were 0.56 ( $\pm 0.28$ ) for operator one and 0.71 ( $\pm 0.23$ ) for operator two. Larger lesions showed significantly higher DCs compared to smaller lesions. Femurs with larger mean segmentation volumes demonstrated good inter- and intra-operator DCs ( $> 0.7$ ) in 83% and 93% of cases, respectively. Additionally, no significant difference was observed between the mean DCs of osteolytic, osteoblastic, and mixed lesions. The study concludes that manual segmentation of femoral bone metastases is challenging, emphasizing the need for a segmentation protocol to reduce variability and the potential use of computer-assisted segmentation tools in the future.

Intra- and inter- observer reliability of measurements on 3D images of the calcaneus bone was studied by Misselyn [76]. Four observers with different medical backgrounds assessed the 3D segmentations of preoperative, postoperative, and uninjured calcanei from 54 patients. The MeVisLab™ software calculated the 3D orientation angle of the subject. The intra- and inter-observer reliability was assessed using the intra-class correlation coefficient (ICC). Intra-observer ICC for the 3D orientation angle ranged from 0.699 to 0.890. Inter-observer ICC for preoperative measurements was 0.828, for postoperative measurements was 0.692, and for uninjured measurements was 0.776. The results indicate good to excellent reliability for the 3D orientation angle on 3D images of the calcaneus bone.

Another study [77] evaluated inter- and intra- observer reliability and repeatability of 2D CT scans of TKA component rotation. They considered fifty-two CT scans of TKAs, which were independently measured by three physicians. Inter-observer reliability was assessed using intra-class correlation coefficients (ICCs), and repeatability was calculated. The ICC for the femoral component was 0.386 (poor), while it was 0.670 (good) for the tibial component. The combined rotation measurement had an inter-observer ICC of 0.617 (good). Intra-observer ICC for the femoral component was 0.606 (good), and for the tibial component, it was 0.809 (very good).

Although precise segmentation is essential in creating realistic finite element models of the knee joint, there is a significant research gap regarding the assessment of variability and repeatability of the knee joint in this subject. This gap is particularly significant considering the nature of the knee joint and the necessity for precise segmentation to capture its complex anatomical structures. Hence, this study endeavours to address this gap by investigating the variability and repeatability of knee joint segmentation. As a preliminary step towards optimizing protocols for a larger experiment encompassing both intra- and inter-observer variability, this chapter serves as a pilot study focusing solely on intra-observer variability.

Rational:

This work seeks to close this gap by assessing the intra-observer variability of subject-specific semi-automatic segmentation of 4D CT knee joint images. This section offers insights into the consistency and reliability of the segmentation process by performing a thorough examination of segmentation outcomes acquired repeatedly by the same observer. This research is vital for advancing the development of realistic finite element models, ensuring that the simulated knee joint mechanics accurately represent the complexities of the in vivo physiological conditions. The findings from this investigation hold the potential to enhance the overall accuracy and effectiveness of knee surgery planning and biomechanical simulations and crucial for further study.

## **5.2 Data acquisition**

The data acquisition for this chapter followed a similar protocol to that described in Chapter 4. Collected by a colleague for another study [117], ten patients were randomly selected for in-depth assessment using the Toshiba Aquilion ONE™ 4D CT scanner at the Clinical Research Imaging Centre (CRIC). Employing the 3D Adaptive Integrated Dose Reduction control system (AIDR 3D) on the Aquilion ONE™, radiation exposure was minimized by continuously adjusting the tube current based on the patient's anatomy and the targeted region [118].

The Toshiba Aquilion ONE™ 4D CT scanner, a 320-multidetector CT (320-MDCT) scanner, captured dynamic knee movement. Continuous 4D 3D images were acquired every 16 cm along the z-axis without the need to shift the table. The voxel size,

reported as 0.78 x 0.78 x 0.5 mm in metadata, facilitated fast and non-invasive dynamic kinematic evaluation of the knee joint in vivo.

To optimize the scanning methodology for the 4D CT component, control volunteers were initially scanned. Participants were recruited from the staff and student population at the University of Strathclyde. The 4D CT images used in this chapter are from control participants, with images taken of both knees in the prone position during flexion.

### **5.3 Methodology**

In this study, a single observer conducted an evaluation to assess the consistency and variability in segmenting the knee joint from a CT scan. The knee joint was segmented five times in sequence using 4D CT images, which were imported as DICOM files into the open-source ITK-Snap segmentation software. To determine the optimal threshold values for each bone segmentation, the results from the previous chapter's analysis were utilized. An operator with experience in segmentation and anatomy knowledge performed the segmentation process. The operator repeated the segmentation process five times while maintaining consistent experimental parameters. The only variable parameter was the manual editing performed by the operator to fill in any holes or remove irregularities.

The experiment utilized 4D CT images of both knees from a 45-year-old male taken in the prone position during flexion. The DICOM files were imported into ITK-Snap software to segment the knee bones, namely the femur, tibia, and patella, at zero degrees flexion. The segmentation procedure was carried out semi-automatically. For the right knee, a region of interest (ROI) was selected by the observer, and its location and size were recorded to ensure consistency across repetitions. The ROI had the following coordinate position (x,y,z): (76,188,8) and size (x,y,z): (158,143,307). Four labels were defined to identify the tibia, femur, patella, and fibula. The fibula label was used to obtain a better view and shape of the tibia but was excluded from the final 3D model to simplify the knee model. The pre-segmentation mode employed thresholding, with the upper threshold fixed in 2017, the maximum available threshold value for the CT image within the software. The lower threshold values were

determined through previous experiments, with the optimal values for tibia, femur, and patella thresholding set at 205 HU, 160 HU, and 200 HU, respectively.

After selecting the bubbles to initiate the segmentation contour, the operator applied semiautomatic, active contour thresholding to distinguish the knee bones from surrounding tissues. The contour expanded until the intensity of the surrounding environment changed, resulting in a three-dimensional representation of the knee bone. The outcome was a 3D model that included the tibia, femur, and patella. However, the tibia and femur exhibited cavities that needed to be filled by the operator. The resulting 3D model was then edited to fill in these holes or remove any irregular shapes in relation to the CT image, and an STL file was saved. This entire procedure was repeated five times, resulting in Segmentation1 (S1), Segmentation2 (S2), Segmentation3 (S3), Segmentation4 (S4), and Segmentation5 (S5).

Next, the segmented patella, femur, and tibia were imported individually as STL files into CloudCompare and merged to create a single knee joint model. CloudCompare automatically removed duplicated vertices and faces from each component. The resulting models from the first segmentation (S1) were compared to the second (S2), third (S3), fourth (S4), and fifth (S5) segmentations using the Iterative closest point (ICP) for cloud-to-cloud distance (C2C) metric. The comparisons were performed in pairs, such as S1 vs. S2, S1 vs. S3, and so on. The results were analysed by calculating the mean distance, creating graphical representations, and generating histograms. This process was repeated for subsequent pairs of segmentations (S2 vs. S3, S2 vs. S4, and so on) until all ten comparisons were completed. CloudCompare generated a histogram as output for the comparison, illustrating the distribution of absolute distances between numbers and indicating the frequency of each distance value. These values modified in excel and recalculated as the following variables. Table1 gives details about these variables.

Table 1. The variables and their definition used for comparison.

Number of Identical Nodes (NIN)	This refers to the count of nodes that are identical between two compared model
Total Number of Nodes (TNN)	This represents the overall number of nodes in the model
Percentage of Identical Nodes (PIN)	PIN is the ratio of the number of identical nodes (NIN) to the total number of nodes (TNN), expressed as a percentage
Number of Non-Identical Nodes (NNIN)	NNIN indicates the count of nodes that are not identical in the two model
Sum of C2C Absolute Differences (SC2CAD)	SC2CAD refers to the total sum of absolute differences in measurements, specifically node-to-node differences, within the models. These differences are measured in millimeters (mm)
Average Difference of Non-Identical Nodes (ADNIN)	ADNIN represents the average difference, in millimeters (mm), between non-identical nodes in the system. It provides insights into the level difference among two models
Average Difference Based on All Nodes (ADAN)	ADAN is the average difference, in millimeters (mm), calculated across all nodes in the system. This value takes into account both identical and non-identical nodes, providing a comprehensive measure of the overall differences within the system.

## 5.4 Results

Five segmented knees, segmented by one participant, are compared using Cloud-to-Cloud (C2C) method. Segmentations are named as S1 for first segmentation, S2 for second segmentation and so on. Figure 37, 38 shows example of points cloud comparison in the following format: S1/S2 (S1 compared to S2), S1/S3, S1/S4, S1/S5, S2/S3, S2/S4, S2/S5, S3/S4, S3/S5, S4/S5, which make ten comparisons for one person. All ten comparison is added to Appendix F.

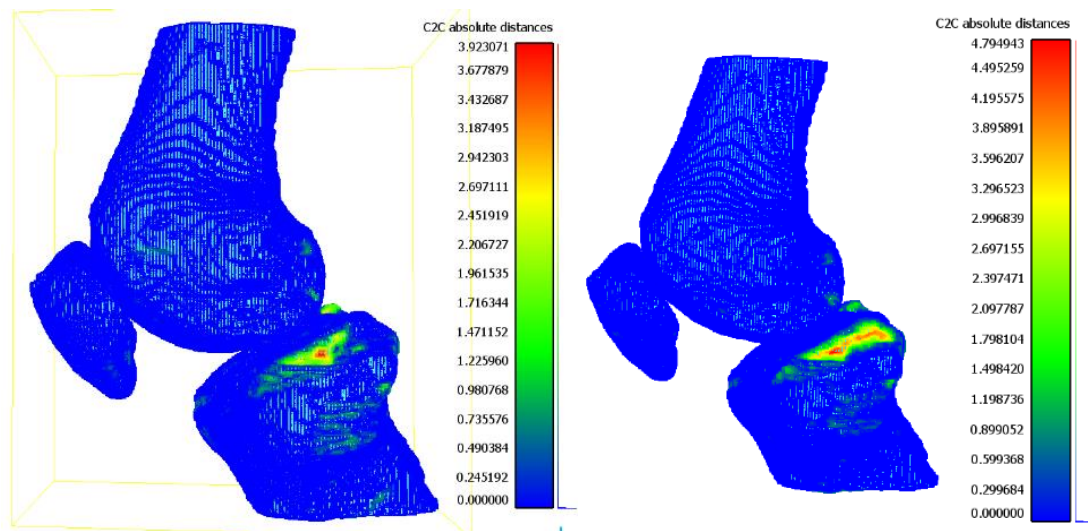


Figure 37. (a) C2C distance comparison of S1 and S2. (b) C2C distance comparison of S1 and S3

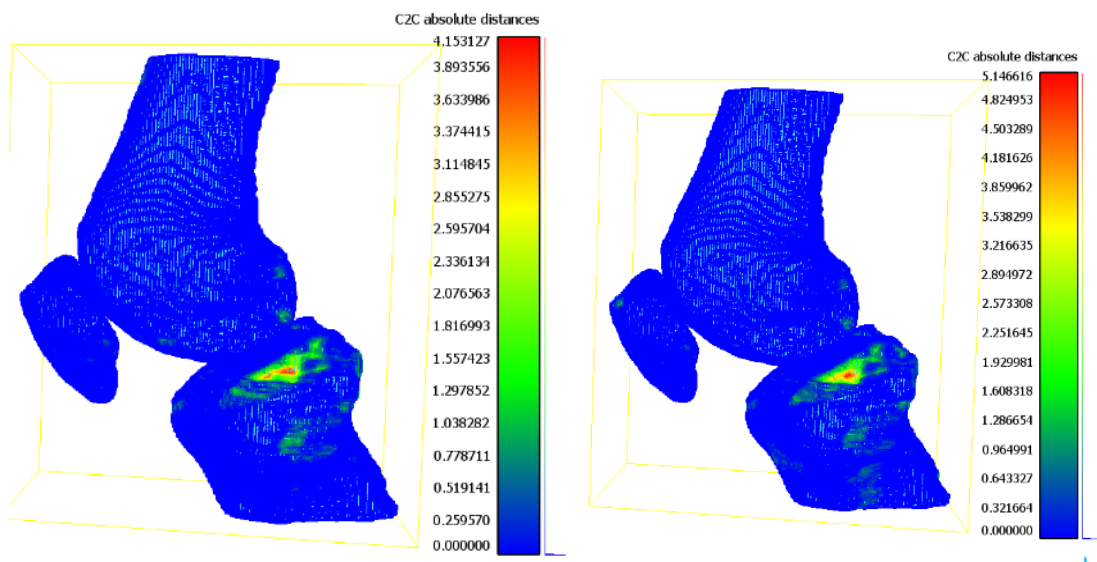


Figure 38. (a) C2C distance comparison of S1 and S4. (b) C2C distance comparison of S1 and S5

Significantly, the lateral proximal region of the tibia consistently exhibited the greatest disparity among all segmentation comparisons. The comparison output data is compiled on table (2). Table2 shows ten paired wise comparisons between five segmentations generated by one participant. The percentage identical nodes between fourth and fifth segmentation is 93.39%, which is the highest similarity, then third and fourth with 92.71% similarity. Then it decreased to 89.21%, for second and fifth times.

Table 2. Five segmentation comparison results

	NIN	TNN	PIN	NNIN	SC2CAD	ADNIN	ADAN
S1/S2	108490	118157	91.82%	9667	3608.398	0.373	0.031
S1/S3	108303	118157	91.66%	9854	4636.154	0.470	0.039
S1/S4	107410	118157	90.90%	10747	4126.886	0.384	0.035
S1/S5	106628	118157	90.24%	11529	4363.697	0.378	0.037
S2/S3	106953	118073	90.58%	11120	4304.483	0.387	0.036
S2/S4	106072	118073	89.84%	12001	3978.638	0.332	0.034
S2/S5	105338	118073	89.21%	12735	4125.371	0.324	0.035
S3/S4	109545	118162	92.71%	8617	3538.664	0.411	0.030
S3/S5	109081	118162	92.31%	9081	3322.485	0.366	0.028
S4/S5	110124	117919	93.39%	7795	2419.658	0.310	0.021

## 5.5 Discussion

This experiment shows that graphically, there is not a significant difference between five segmentations performed by one person. Reassuringly, segmentations are over 90% identical, with average errors on the order of the dimension of one voxel. However, whether 90% similarity is sufficient is another question that warrants further consideration. As mentioned earlier, the voxel size is  $0.78 \times 0.78 \times 0.5$ mm, the diagonal of the voxel is 1.21mm, therefore the critical distance is set as 1.21mm, this means any differences  $>1.21$ mm is definitely more than one voxel.

The voxel size of  $0.78 \times 0.78 \times 0.5$  mm played a crucial role in enabling fast and non-invasive dynamic kinematic evaluation of the knee joint in vivo. This voxel size, achieved using the Toshiba Aquilion ONETM 4D CT scanner, strikes a balance between spatial resolution and acquisition speed.

A smaller voxel size would provide higher spatial resolution, allowing for more detailed visualization of the knee joint structures. However, it would also require longer scan times, which could introduce motion artifacts and increase radiation

exposure for the participants. On the other hand, a larger voxel size would enable faster scans but at the cost of reduced image quality and potential loss of fine anatomical details.

The chosen voxel size of 0.78 x 0.78 x 0.5 mm represents an optimal compromise between these factors. It provides sufficient spatial resolution to capture the complex geometry of the knee joint, including the femur, tibia, and patella, while allowing for rapid image acquisition. The fast scan times minimize the risk of motion artifacts, which is particularly important when imaging dynamic knee movements.

Moreover, the non-invasive nature of the 4D CT scanning protocol, combined with the optimized voxel size, ensures participant comfort and safety. The participants can undergo the scans without the need for invasive procedures or contrast agents, reducing the overall risk and increasing the feasibility of conducting dynamic kinematic studies on a larger scale.

The lateral proximal region of the tibia, which consistently displayed the highest level of difference across all segmentation comparisons, indicating a recurring pattern of variability in that specific anatomical area. However, the aggregation and average distance measures show different. This indicates that, for some reason, this specific part of the tibia is more prone to inconsistency in the segmentation process, possibly due to its anatomical complexity or challenges in distinguishing it clearly.

However, when all the segmentations are aggregated and measured using average distance metrics, the overall results suggest a smaller difference. This means that while individual comparisons show notable variability in this region, when you take an average or combine all the data, the variability seems less significant. This could imply that the variability is localized but doesn't heavily impact the overall segmentation accuracy across the entire tibia.

The Table 2 could be explained as if there is constancy of operator decision making for the first two segmentations during segmentation process and editing of the 3D model, regardless of how accurate the results were graphically. After the third segmentation, the operator may have developed more experience and confidence to

change his/her mind during the process, so the difference of second and fourth and fifth process is much higher.

The ADAN values, which represent the average difference in millimeters across all nodes, are consistently low, with the highest value being 0.039 mm for the S1/S3 comparison.

These findings demonstrate the robustness of the semi-automatic segmentation methodology and the operator's ability to generate consistent results across multiple segmentations. The high percentage of identical nodes and sub-voxel average differences suggest that this approach can be reliably employed to create accurate, subject-specific 3D models of the knee joint for various applications, such as finite element analysis and surgical planning.

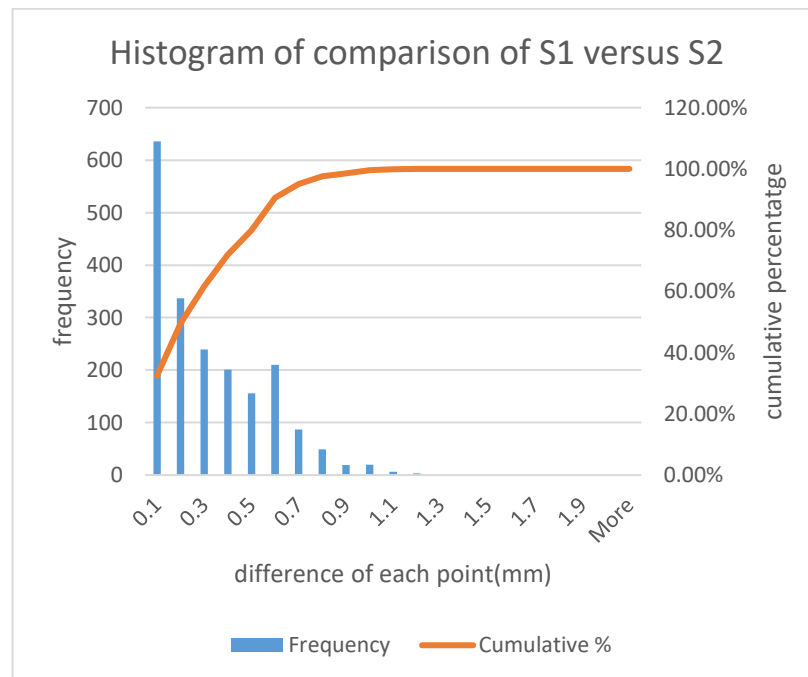


Figure 39. S1 and S2 comparisons' Histogram

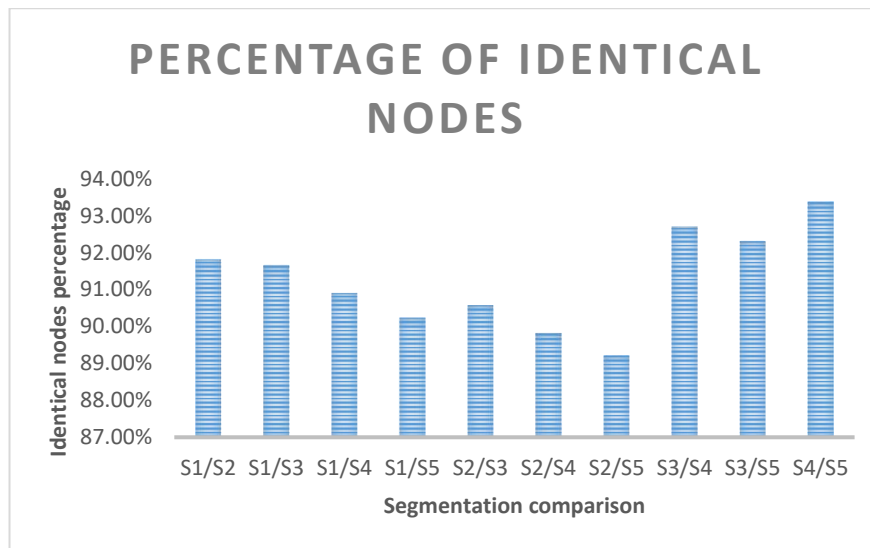


Figure 40. The percentage of identical nodes for ten separate comparisons

Figure 39 shows the histogram of non-identical points between first and second segmentation; it represents that around 600 points have around 0.1 millimetre of difference and approximately 300 points have 0.2 millimetre and so on.

The consistency in segmentation results also highlights the potential for other studies and comparisons of knee joint morphology across different populations or disease states. However, to further validate these findings and establish the generalizability of the segmentation methodology, future studies should investigate inter-observer variability and include a larger cohort of participants with diverse characteristics.

## 5.5 Conclusion

The intra-observer variability assessment of semi-automatic segmentation of 4D CT knee joint images provides valuable insights into the consistency and reliability of the segmentation process. The high percentage of identical nodes (over 90%) and the sub-voxel average differences between segmentations demonstrate the robustness of the methodology and the operator's ability to generate consistent results. These findings have important implications for future research and applications in knee joint segmentation and modelling. The low intra-observer variability suggests that the semi-automatic segmentation approach can be reliably employed to create accurate, subject-specific 3D models of the knee joint by one operator. These models can serve as the foundation for various applications, such as finite element analysis, surgical planning, and the development of personalized treatment strategies for knee disorders. Furthermore, the consistency in segmentation results highlights the potential for

longitudinal studies and the comparison of knee joint morphology across different populations or disease states. However, to further validate these findings and establish the generalizability of the segmentation methodology, future studies should investigate inter-observer variability and include a larger cohort of participants with diverse characteristics.

## Chapter 6 Inter-observer variability

### 6.1 Introduction

The subject of musculoskeletal research has undergone a revolution by the medical imaging, especially the use of 4D CT, which offers dynamic insights into joint anatomy. Knee bone segmentation is one of the crucial uses of 4D CT that has attracted attention due to its potential to improve orthopaedic treatment planning and diagnostic accuracy. However, repeatability within the same observer (intra-observer) and consistency and agreement between multiple observers (inter-observer) are major factors in segmentation accuracy. To ensure the validity of the collected data and the ensuing clinical interpretations, the investigation of intra- and inter-observer variability in 4DCT knee bone segmentation is essential.

Variability can affect the general reliability of the segmentation process and inject uncertainty into quantitative data. Therefore, it is essential to comprehend and reduce these variabilities to fully utilise 4D CT for knee bone segmentation. Some researchers have addressed the challenge of intra- and inter-observer variability in bone segmentation which are mentioned in the following.

A paper by Dominique Misselyn [76] et al. investigates the reliability of measurements on 3D images of the calcaneus bone, particularly focusing on the 3D orientation angle of the calcaneal posterior subtalar (PTC) joint facet. The researchers conducted 3D segmentations of preoperative, postoperative, and uninjured calcaneus bones in 54 patients. Four observers with different medical backgrounds delineated the 3D segmentations of their calcaneus bone by Mimics™ using their DICOM CT images of the injured side and MeVisLab™ software calculated the 3D orientation angle of the PTC. They found that the intra-observer ICC values for the 3D orientation angle of the PTC ranged from 0.699 to 0.890. Also, inter-observer ICC for preoperative measurements was 0.828, for postoperative measurements was 0.692, and for uninjured measurements was 0.776.

Also, Patrik F. Raudaschl [124] discusses the significance of automated organ and structural delineation in medical imaging, along with the difficulty of choosing the best segmentation techniques for a range of uses. The brainstem, mandible, chiasm, bilateral optic nerves, bilateral parotid glands, and bilateral submandibular glands were

among these structures. The mandible was the only bony segmented structure, as it exhibits high contrast compared to surrounding tissues and relatively low shape variation compared to most soft-tissue organs it has higher Dice coefficient and less error. However, a significant challenge in mandibular segmentation lies in accurately excluding the teeth, which have similar grey values to the bone. Furthermore, the presence of dental implants in some datasets introduces image noise, particularly affecting the mandibular region. They evaluated the segmentation by Dice similarity coefficient, 95% Hausdorff distance (HD). They achieved Dice scores  $> 0.8$  and an average 95% HD  $< 5$  mm for mandible.

On the other study the reproducibility of nasal bone was not promising. The paper [125] explores the reproducibility of assessing fetal nasal bones through ultrasound in the first trimester. The study aims to investigate the variability in identifying fetal nasal bones and its implications for the detection of trisomy 21 (Down syndrome). The research involved 1040 ultrasound examinations at 11–14 weeks of gestation, focusing on nasal bone identification. Three experienced operators assessed 657 video-loops, classifying cases into categories of present, uncertain, or absent nasal bones. Intra-observer variability was evaluated by having each operator review a subset of 100 video-loops. The inter-operator variability, assessed using the Kappa index, showed fair reproducibility, with values ranging from 0.26 to 0.37. Intra-operator variability yielded Kappa values between 0.35 and 0.48. The study concludes that the assessment of fetal nasal bones is only fairly reproducible.

According to insufficiency of research on the variability of bone segmentation and the absence of studies examining the variability of the knee joint, this chapter explore into investigating both intra- and inter-observer variability within the knee joint segmentation process.

## **6.2 Methodology**

This study focuses on assessing the intra-examiner and inter-examiner reliability of knee segmentations using an anonymized 4D CT dataset. Fifteen volunteers were recruited and trained in ITK-Snap software to segment the femur, tibia, and patella. The graphical analysis was performed using CloudCompare software, while quantitative measures such as Hausdorff Distance, Dice Similarity Coefficient, and

Jaccard Index were employed to assess intra-observer variability using MATLAB. Inter-observer variability (ICC) for the Dice Similarity Coefficient (DSC) of the femur, tibia, and patella was calculated using IBM SPSS. The results demonstrate the reliability of the segmentation process. The findings contribute to the potential clinical applications of these methods.

### **6.3 Data collection**

The data acquisition process for Chapter 6 mirrored the methodologies outlined in Chapters 4 and 5. Initially collected by a colleague for another study [117], ten people volunteered for detailed assessment using the Toshiba Aquilion ONE™ 4D CT scanner at the Clinical Research Imaging Centre (CRIC). Eight had knee joint replacements of unknown description and 2 control participants had non-pathological knees. Radiation exposure was minimized using the 3D Adaptive Integrated Dose Reduction control system (AIDR 3D) on the Aquilion ONE™, adjusting the tube current based on the patient's anatomy and targeted region [118].

The Toshiba Aquilion ONE™ 4D CT scanner, a 320-multidetector CT (320-MDCT) scanner, facilitated the capture of dynamic knee movement. Continuous 4D 3D images were obtained at 16 cm along the z-axis without the need to shift the table. The voxel size, as reported in metadata, was 0.78 x 0.78 x 0.5 mm, enabling rapid and non-invasive dynamic kinematic evaluation of the knee joint in vivo.

The 4D CT images used in this chapter are from a single control participant, with images taken of both knees in the prone position during flexion.

#### **6.3.1 Ethical Approval**

All procedures detailed below were approved in line with University procedures by the Departmental Ethics Committee in May 2022 (approval letter is attached in appendix A).

#### **6.3.2 Subject recruitment**

Fifteen volunteers from the Department of Biomedical Engineering were recruited to perform semi-automatic segmentation of the collected data. All the recruited volunteers were active and healthy adults recruited from staff and students at the University of Strathclyde. This proposal sought to determine the variability of CT segmentation within a defined volunteer group of people with an appropriate

background in biomedical engineering. Thus, our cohort consisted of those typically recruited to such positions and they were generally aware of the procedures involved. Since the aim is to describe the variability within this group, and participants are not split into different groups, a sample size calculation is not possible. Nevertheless, 15 participants felt sufficient to descriptively characterise the variability of the group with regards to CT segmentation. All volunteers were invited for the experiment by a recruitment email (the email is attached in appendix B) through biomedical department of Strathclyde university email.

The participant information sheet (PIS is attached in appendix C) given to participants who accepted to take part in the experiment and explained to them verbally as well. They were clarified any concern they had by signing the consent form (consent form is attached in appendix D)

The inclusion/exclusion criteria and any further screening procedures were as follow and are all self-reported.

*Table 3. Participants recruitment requirements*

Inclusion Criteria	Exclusion Criteria
Ability to use a standard, mouse-operated Windows PC, without additional accessibility features	Age below 18 or over 60
To be in training for a biomedical engineering degree, or equivalent technical competence (having at least 6 months of experience working in biomedical related field), understanding of knee anatomy and the intended outcome of the process of segmentation	Colour blind
Self-reported “good” eyesight with or without glasses or contact lenses	Unable to sit for two hours
To be able to sit comfortably in front of a computer for about 2 hours	Any type of Tremor
	Non adequate field of vision

	Visuospatial neglect
	Attention deficit disorder
	Any neurological condition affecting movement or mood
	Any symptoms associated with Covid-19 including a new continuous cough, a high temperature or loss or change to your sense of smell or taste.

### 6.3.3 Study design

This study uses an anonymised 4D CT data set previously collected [117] in dynamic movement of knee by the Toshiba Aquilion ONE™ 4D CT scanner from a single person without history of knee pathology. These are same data used for chapter 5.

The volunteers attended training sessions, so the ITK-snap semi-automatic segmentation software package was explained to them (verbally and/or written) and they were supplied with a short tutorial document as well as exemplar datasets to do practice segmenting the bones of the knee. Volunteers stopped training when they felt themselves confident and competent in the use of the software and their ability to segment the bones of the knee.

On the experimental day, the volunteers were asked to perform the same methodology as the tutorial on a previously unseen dataset (DICOM image). The methodology is detailed in section 6.3.4. The participants were asked to segment the provided image five times to assess within-subject variation. All fifteen operators segmented the same femur, tibia and patella five times and the output 3D models were saved as STL mesh files providing 75 files per bone and 225 files in total to be analysed.

The segmentation results were analysed by CloudCompare™ software [67] to examine the intra-examiner reliability. The STL files were also read into Matlab™ to examine the inter-examiner reliability by determining the Hausdorff Distance (HD), Dice similarity Coefficient (DSC) and Jaccard index (JI) [126].

#### **6.3.4 ITK-Snap Methodology**

The 4D CT image from a patient in the DICOM format was imported in an open-source segmentation tool called ITK-Snap. The scan reference number was J2045969 and the knee is in approximately 45° flexion. The ROI (region of interest) and threshold filter was determined and fixed to keep the experimental conditions fixed for all participants. The position of the ROI in the X, Y, and Z axes was recorded as 274, 157, and 1, respectively, and its size in X, Y, and Z axis were 148, 235, 310 respectively. As mentioned in chapter 4, changing the threshold levels on segmentation can greatly vary the resulting image and therefore it must be controlled in this study. By decreasing the threshold level, the generated contour may bleed into the surrounding soft tissue and by increasing the threshold level, more bone tissue is removed, which results in increasing the cavity volume. A compromise must be met to create an “optimal” image for segmentation. The upper threshold was fixed at 3523 HU (the maximum allowable) with the lower threshold fixed at 160 HU for the femur, 205 HU for the tibia and 200 HU for the patella. The same threshold levels were used for all 225 segmentation trials in order to maintain consistency throughout the experiment.

In order to initialize the segmentation from the surrounding tissues (Figure 41), each operator introduced “bubbles” into the areas of interest. This crucial step provides the software with information regarding the intensity (HU) by which the contour can expand and form the boundary. This step is the only operator-influenced step prior to manual editing.

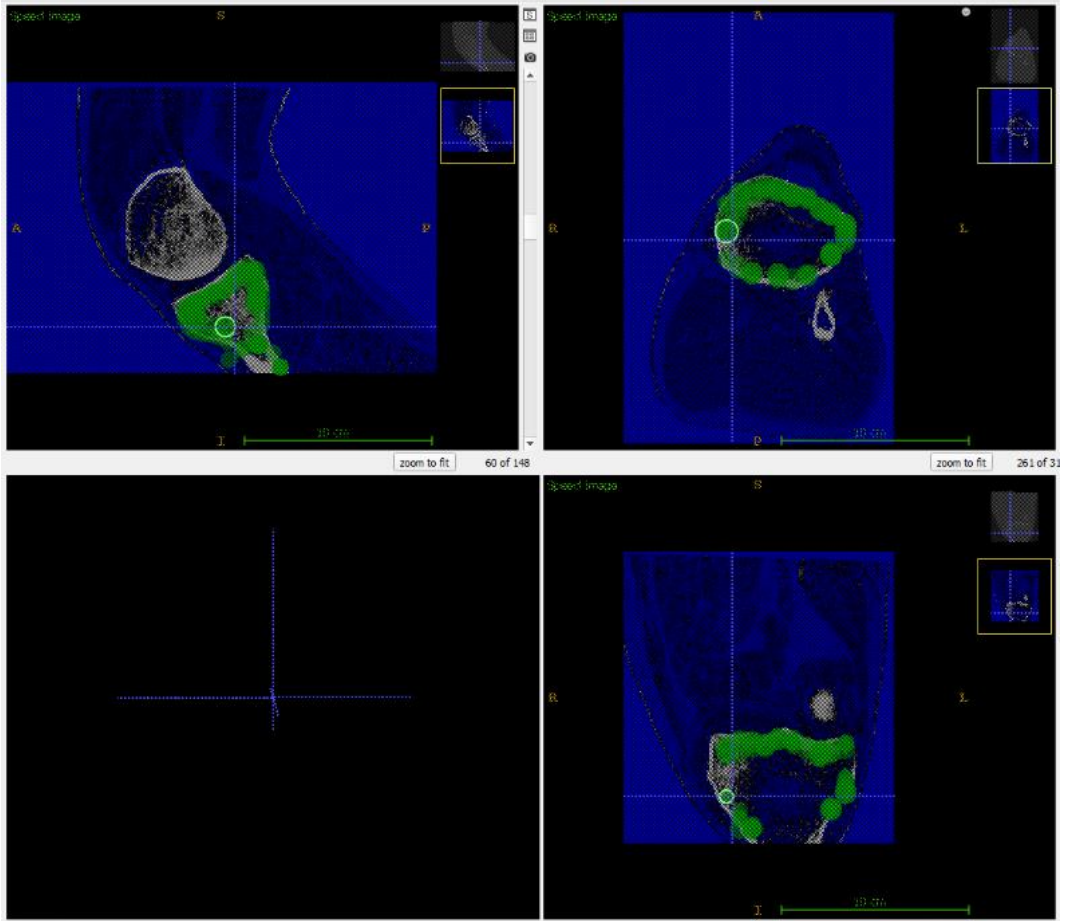


Figure 41. Placing bubbles on interested area

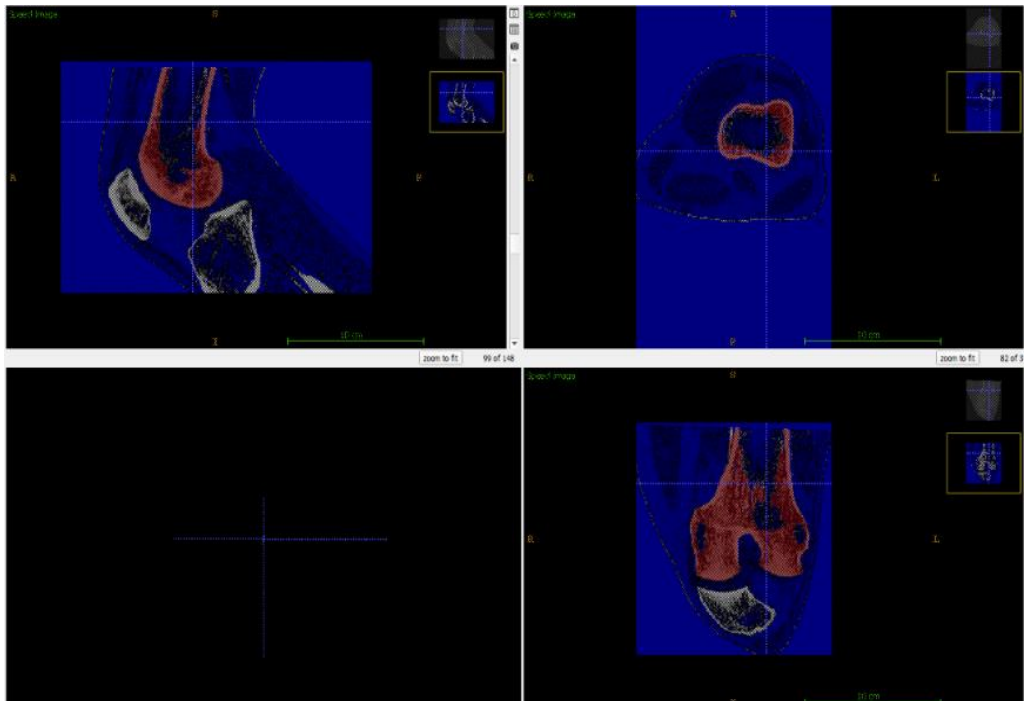
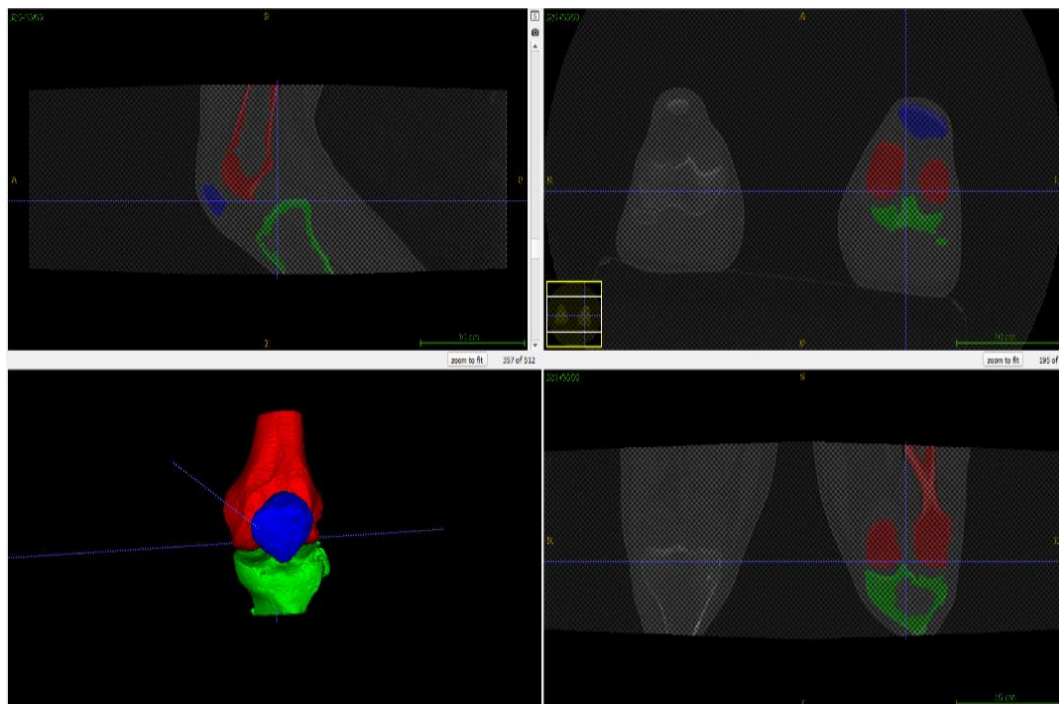


Figure 42. Growing contour to which intensity is determined

In the next step, the operator executed and controlled the evolution of the segmented region until manually stopped (Figure 42). The software would stop the segmentation evolution after 9999 iterations, but the operators often stopped this before this number of iterations was reached. An exemplar 3D model of the knee joint shown in fourth window (Figure 43), and the generated model may include cavities within the cortical bone. Therefore, the operator was required to manually edit the model by using the paintbrush tool and to fill in the cavities as per the guidelines provided in the training session. They were asked to remove the fibula from tibia as it was too close to tibia and the contour bleeding to fibula was inevitable. It is important to note that the fibula stabilises the ankle joint and does not directly affect the knee joint [127]. The segmented and edited femur, tibia and patella were saved as STL mesh files.



*Figure 43. 3D model of knee joint is made*

## **6.4 Data Analysis**

### **6.4.1 CloudCompare™ Analysis**

CloudCompare™ was used to perform two functions: importantly the interior surface of the bones removed and additionally, the software provided a useful graphical depiction of the differences between the point clouds created by the STL files.

STL files only provide information regarding the surfaces of objects. The bones in this study will have both an external surface, defining the exterior of the bony surface, and an internal surface defining the interior medullary cavity. As this study focus on the outer surface only, the inner surface was manually removed for all bones in CloudCompare (Figure 44). The process of removing the inner surface is a long and time-consuming procedure that was done by the author. The step-by-step screenshot of the process of removing the inner layer of one tibia is available in Appendix E.

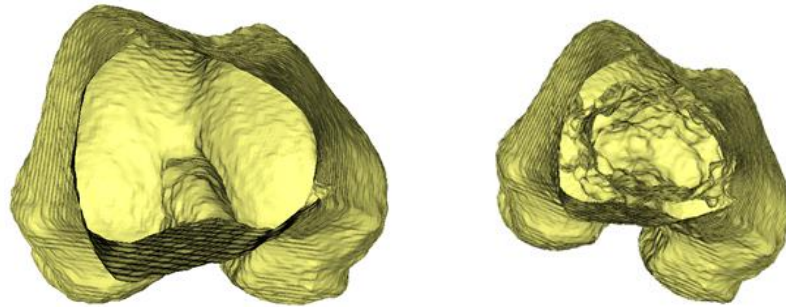


*Figure 44. (a) inner layer is removed. (b) femur with inner layer*

To assess intra-observer variability, for each operator, all 10 combinations of the five segmentations from each individual were compared. To achieve this, the first segmentation (S1) was imported into CloudCompare™, followed by the import of the second segmentation (S2). Subsequently, the vertices of S1 were compared to those of S2 using C2C absolute distance. C2C is the CloudCompare™ terminology for iterative closest point analysis (REF section in section 2.8.3). An example of a resulting scalar field of differences between S1 and S2 is shown in Figure (39). The differences were visualized using colour coding, where red indicates the maximum difference, followed by yellow and green, while blue indicates no difference between the two models. This process was repeated for each possible segmentation pairing (i.e. S1/S2, S1/S3, S1/S4, S1/S5, S2/S3, S2/S4, S2/S5, S3/S4, S3/S5, and S4/S5).

The resulting visual representations of the point cloud comparisons were then analysed with regards to the location of the maximum C2C distance. The anatomy of each bone was divided into regions and location of the maximum difference in between the two

segmentations was coded accordingly. This enabled the regions of the knee joint most likely to be poorly segmented to be identified.

#### 6.4.1.1 Femur

The location of the maximum distance between each comparison of the femur was determined and each area is given a code.

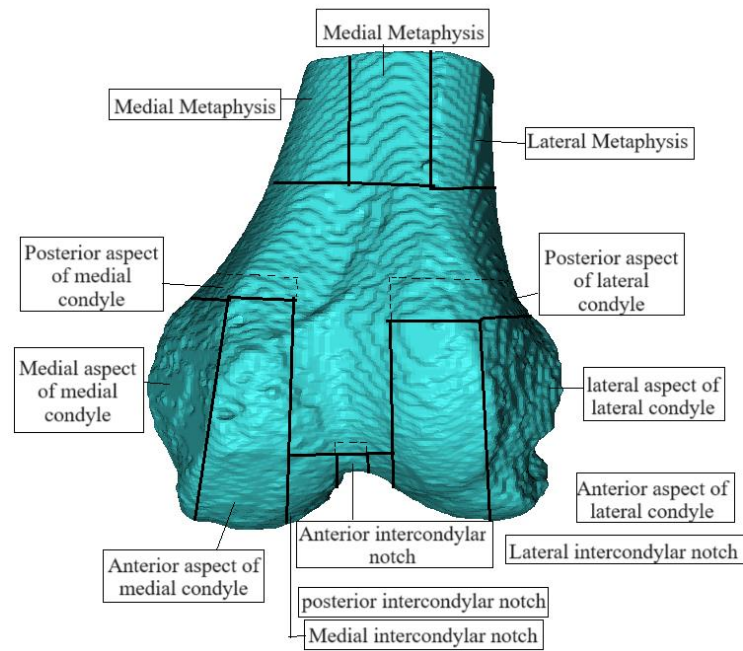


Figure 45. Schematic dividing of the distal femur

Table 4. Assigning code for each parts of the distal femur

Codes for femur Anatomical Positions	
Codes	Anatomical positions
Code1	Anterior aspect of medial condyle
Code2	Medial aspect of medial condyle
Code3	posterior aspect of medial condyle
Code4	Anterior Intercondylar notch

Code5	Middle Intercondylar notch
Code6	posterior Intercondylar notch
Code7	Lateral Intercondylar notch
Code8	Medial Metaphysis
Code9	Lateral Metaphysis
Code10	Posterior aspect of lateral condyle
Code11	lateral aspect of lateral condyle
Code12	Anterior aspect of lateral condyle

#### 6.4.1.2 Tibia

Tibia is divided schematically into nine section to help understand the frequency of location with largest distance between operators.

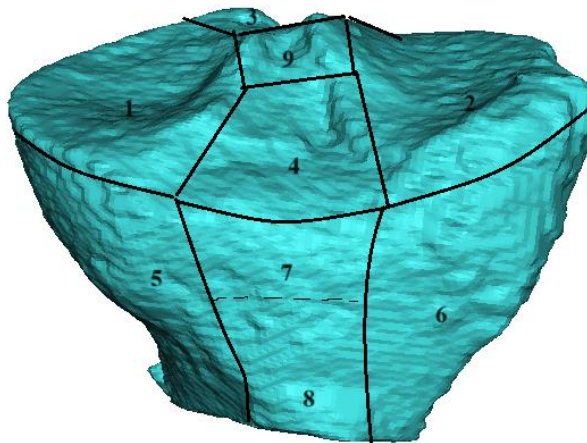


Figure 46. Schematic dividing of the proximal tibia

Table 5. Assigning code for each parts of the proximal tibia

Codes for tibia Anatomical positions	
Code 1	Medial proximal tibia
Code 2	Lateral proximal tibia
Code 3	Posterior proximal tibia
Code 4	Anterior proximal tibia
Code 5	Medial distal tibia
Code 6	Lateral distal tibia
Code 7	Posterior distal tibia

Code 8	Anterior distal tibia
Code 9	Intercondylar eminence

### 6.4.1.3 Patella

The location of the maximum distance between each comparison of the patella was determined and each area is given a code.

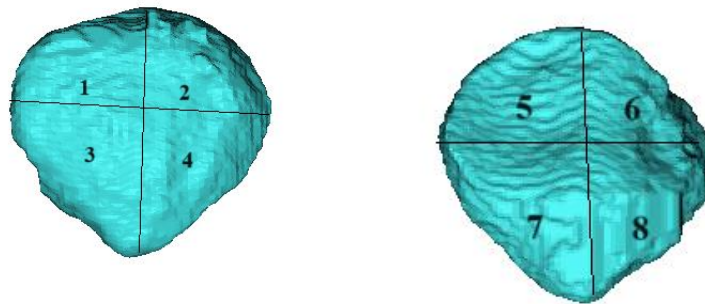


Figure 47. Schematic dividing of the patella

Table 6. Assigning code for each parts of the patella

Codes for Patella Anatomical positions	
Codes	Anatomical positions
Code1	Anterior proximal medial
Code2	Anterior proximal lateral
Code3	Anterior distal medial
Code4	Anterior distal lateral
Code5	Posterior proximal lateral
Code6	Posterior proximal medial
Code7	Posterior distal lateral
Code8	Posterior distal medial

### **6.4.2 Hausdorff Distance, Jaccard Index, Dice Similarity Coefficient**

The edited femur, tibia, and patella were subjected to a mathematical comparison using MATLAB. All 255 STL files were analyzed, resulting in 2776 comparisons for the femur, 2776 for the tibia, and 2776 for the patella, including both intra and inter comparisons.

Briefly, point clouds were created from the STL files and were aligned using the matlab function *pcregrid*. Subsequently, the Hausdorff distance between the two aligned point clouds was determined, and the maximum, mean, median and standard deviation of the Euclidean distances were also determined. Using a threshold value of 1.2mm, corresponding to the approximate size of a voxel in the image, the number of points with their closest Euclidean neighbour less than this threshold were determined. These were considered identical points for the purpose of calculating the Dice Similarity Coefficient and the Jaccard Index including determination of the false positive and false negatives (see sections 2.8.1 and 2.8.2). Finally, volume similarity was also determined.

The Matlab code used to generate these measures may be found in Appendix G

#### *6.4.2.1 Statistical analysis*

For each bone (femur, tibia, patella), there were 10 possible point cloud comparisons between different segmentations, and this was repeated for 15 observers. The Dice Similarity coefficient (DSC), Jaccard Index (JI) and the Hausdorff distance (HD) were analysed with repeated-measures ANOVA with 'bone' and comparison (e.g. S1 vs S2) as main effects, including their interaction. The Greenhouse-Geisser p-value was taken as this provides a conservative p-value. Subsequent post-hoc pairwise comparisons were made, with Bonferroni-adjustment. Significance was taken when  $p \leq 0.05$ .

### **6.4.3 Inter-observer Analysis**

Further inter-observer analysis was performed using the interclass correlation coefficient (ICC). The DSC measures for each person, for each comparison were assessed to find out the consistency between the observers using the two-way random effect model is chosen, as suggested by Koo [82].

## 6.5 Results

### 6.5.1 CloudCompare™ Analysis

This section details the Location of maximum C2C distances

#### 6.5.1.1 Femur

An exemplar visual representation of an intra-examiner comparison of femur, segmented by a single individual using CloudCompare™, is presented below. Bones have been rotated to locate and identify the largest difference between two segmentations, which is marked as red colour.

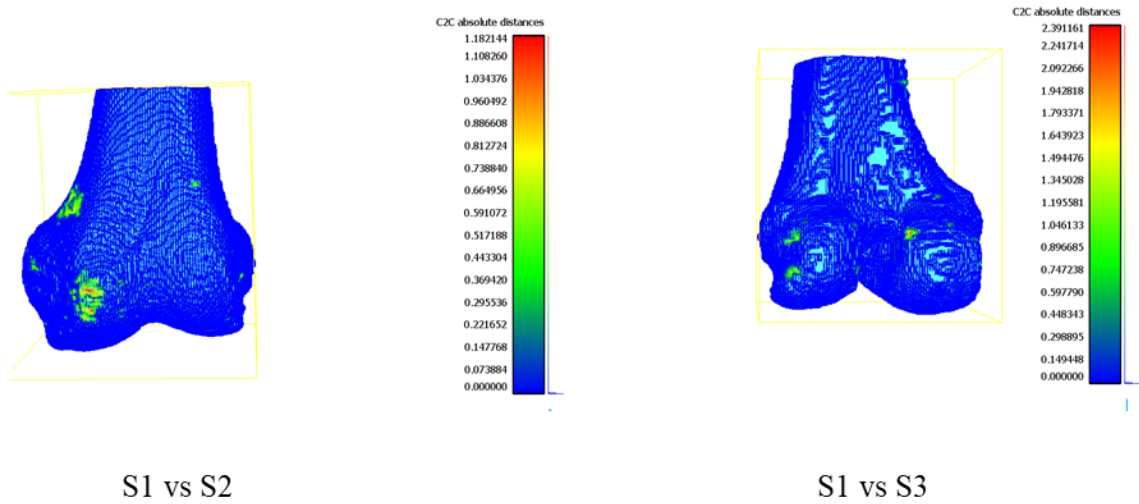
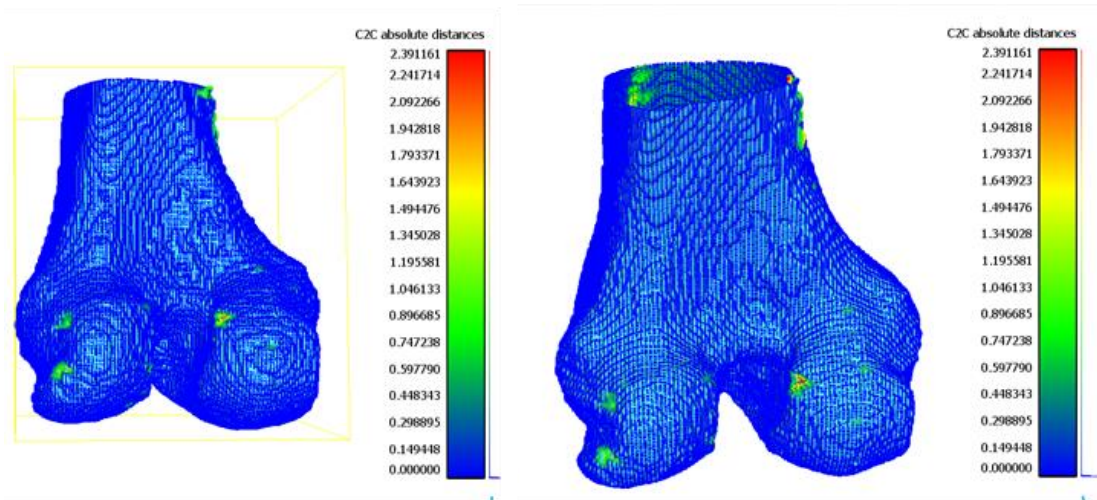


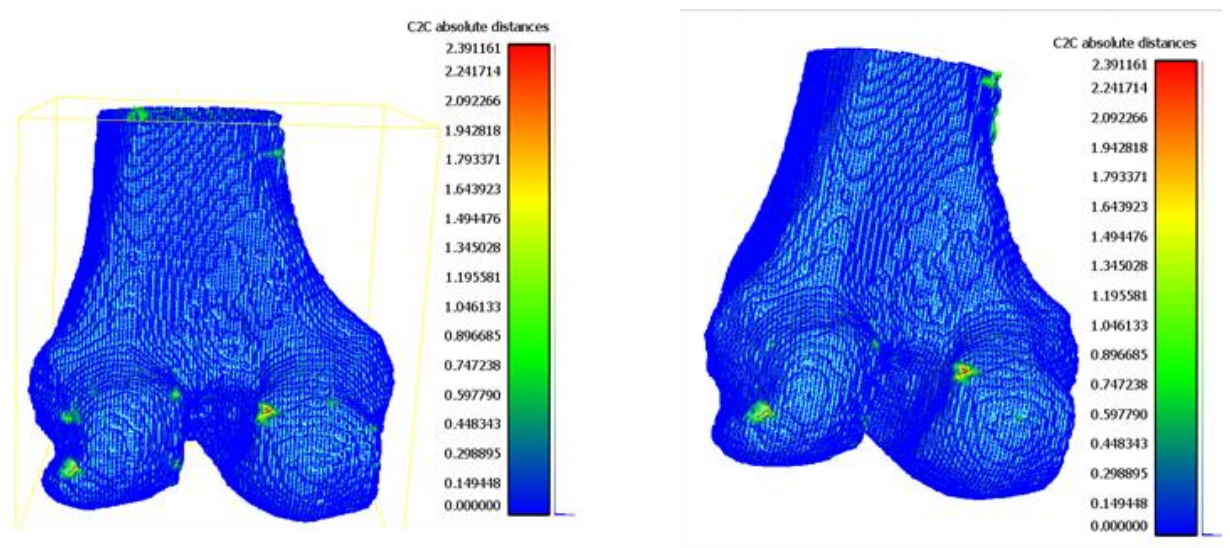
Figure 48. C2C absolute difference of S1 with S2 and S3



S1 vs S4

S1 vs S5

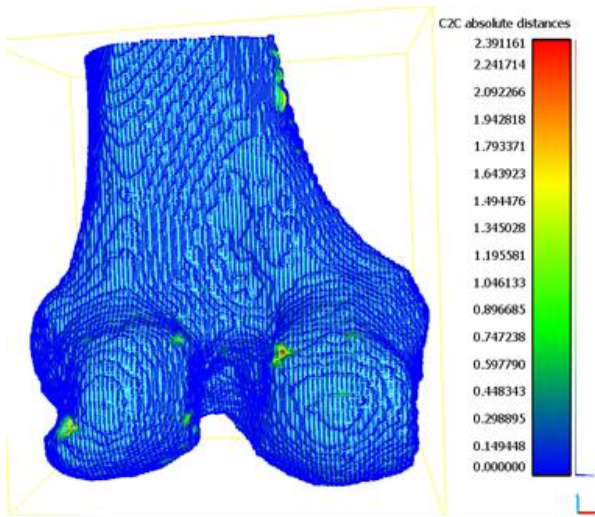
Figure 49. C2C absolute difference of S1 with S4 and S5



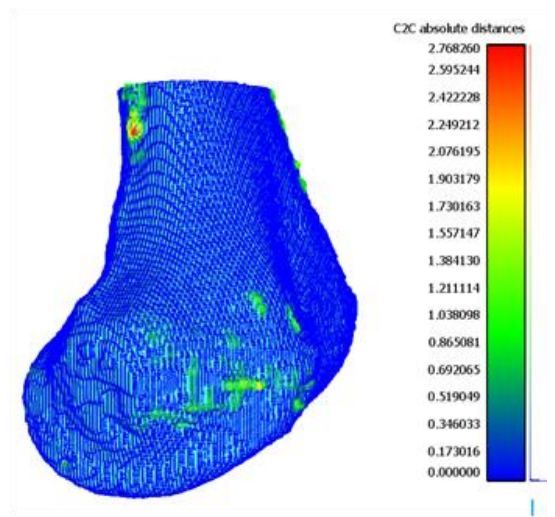
S2 vs S3

S2 vs S4

Figure 50. C2C absolute difference of S2 with S3 and S4

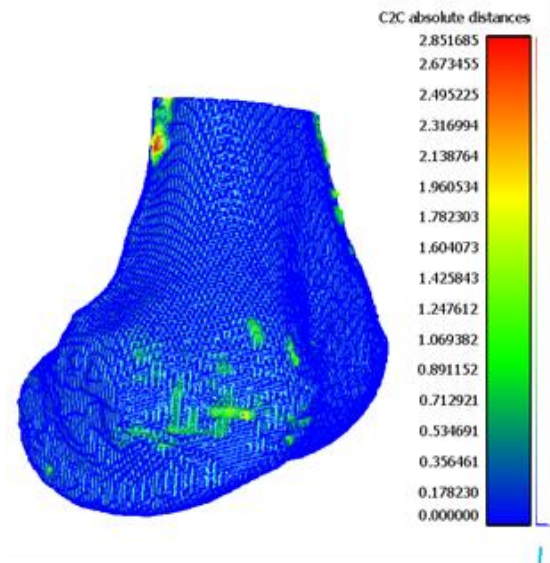


S2 vs S5

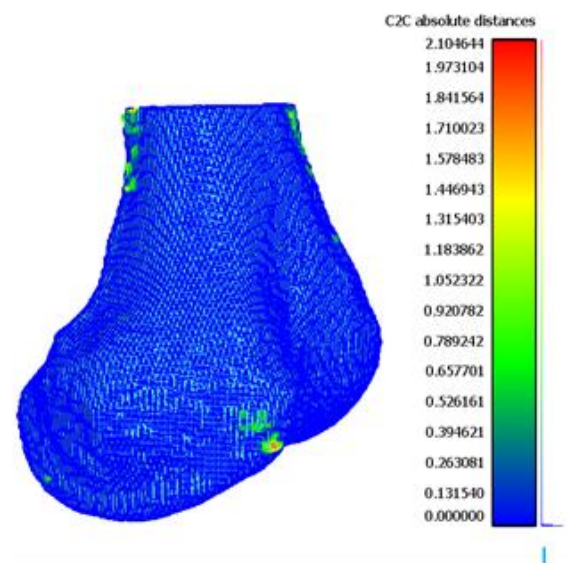


S3 vs S4

Figure 51. C2C absolute difference of S2 versus S5 and S3 versus S4



S3 vs S5



S4 vs S5

Figure 52. C2C absolute difference of S3 versus S5 and S4 versus S5

With reference to table 4, the positions of the maximum differences between segmentations of the femur are provided in the table below:

Table 7. The codes of maximum differences between segmentations of the femur

		Segmentation Comparison									
		S1S2	S1S3	S1S4	S1S5	S2S3	S2S4	S2S5	S3S4	S3S5	S4S5
Participant	P1	1	3	3	3	3	3	3	8	8	1
	P2	1	11	6	6	11	6	6	6	6	8
	P3	2	2	2	2	2	11	11	2	2	9
	P4	11	11	11	11	2	2	2	2	2	1
	P5	1	8	1	8	8	8	8	9	9	9
	P6	9	1	8	8	1	8	8	8	8	1
	P7	8	10	8	8	8	8	8	8	8	8
	P8	11	11	11	11	8	3	3	1	8	8
	P9	1	9	8	8	1	1	1	8	1	9
	P10	9	1	8	8	8	9	8	8	8	9
	P11	8	8	1	8	8	8	1	8	8	8
	P12	1	1	1	1	1	1	1	8	8	8
	P13	1	1	3	1	1	1	1	1	1	1
	P14	1	1	1	1	10	10	10	8	1	1
	P15	8	9	9	8	8	8	8	9	9	1

Forty one out of 150 (27%) of the biggest differences occur in the anterior aspect of the medial condyle and 52/150 (35%) occur in the medial metaphysis. Other regions which also show occasional maximum differences are the medial aspect of the medial condyle (8%), the lateral metaphysis (9%) and the lateral aspect of the lateral condyle (8%).

### 6.5.1.2 Tibia

The following illustration is the intra-examiner comparison of the tibia performed by the first operator.

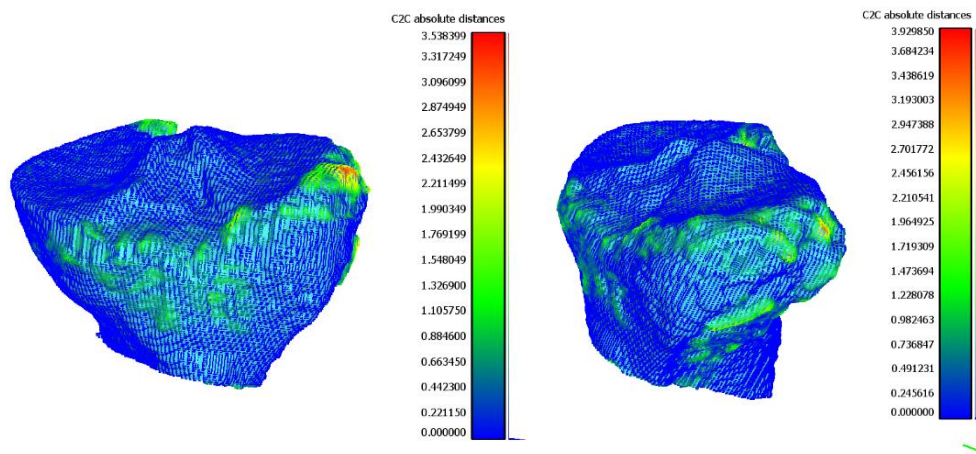


Figure 53. (a) C2C absolute distance of S1 vs S2 , (b) S1 vs S3

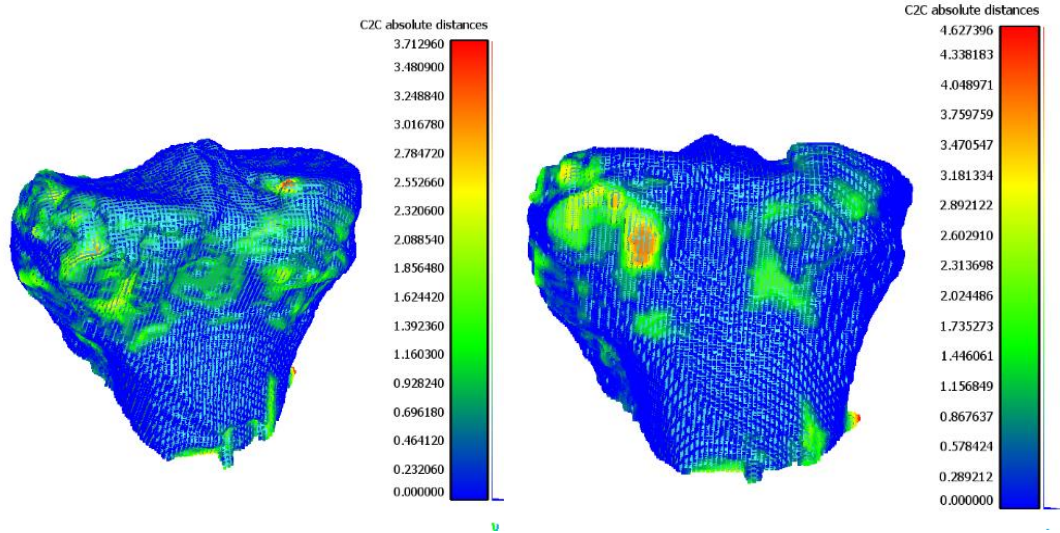


Figure 54. (a) C2C absolute distance of S1 vs S4, (b) S1 vs S5

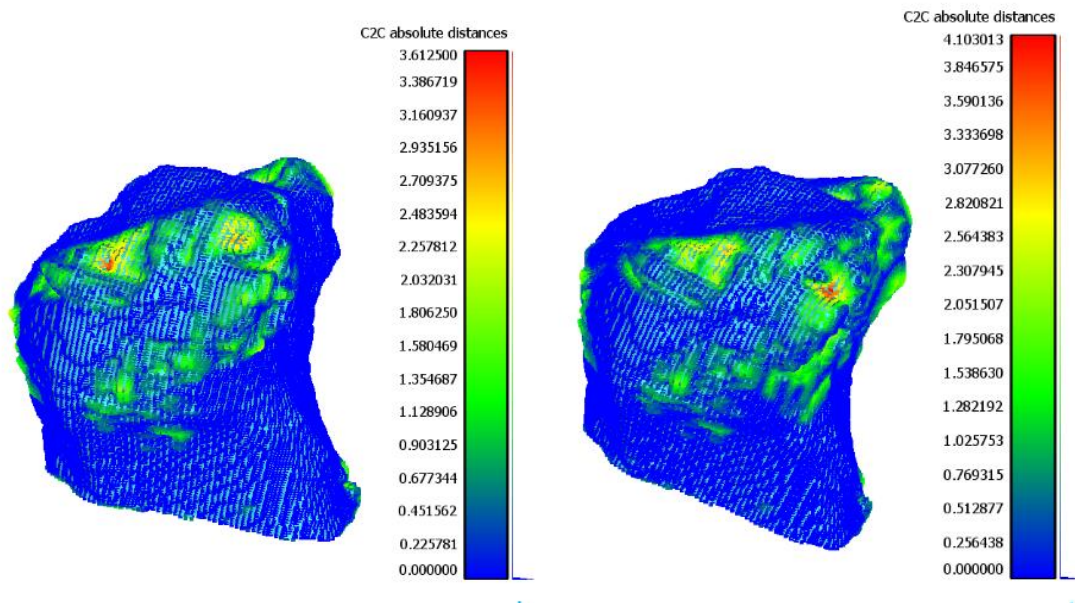


Figure 55. (a) C2C absolute distance of S2 vs S3, (b) S2 vs S4

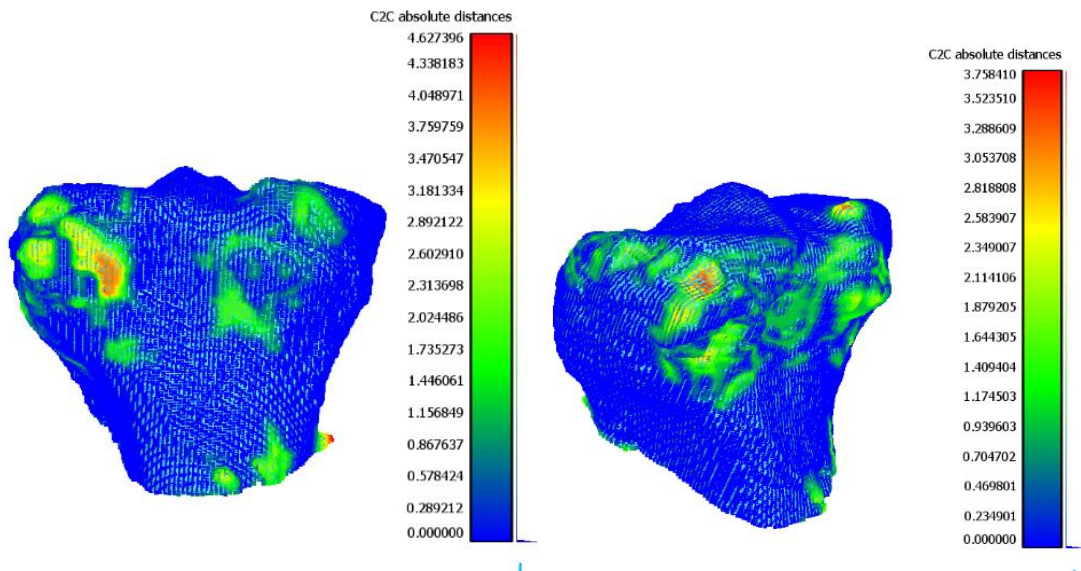


Figure 56. (a) C2C absolute distance of S2 vs S5, (b) S3 vs S4

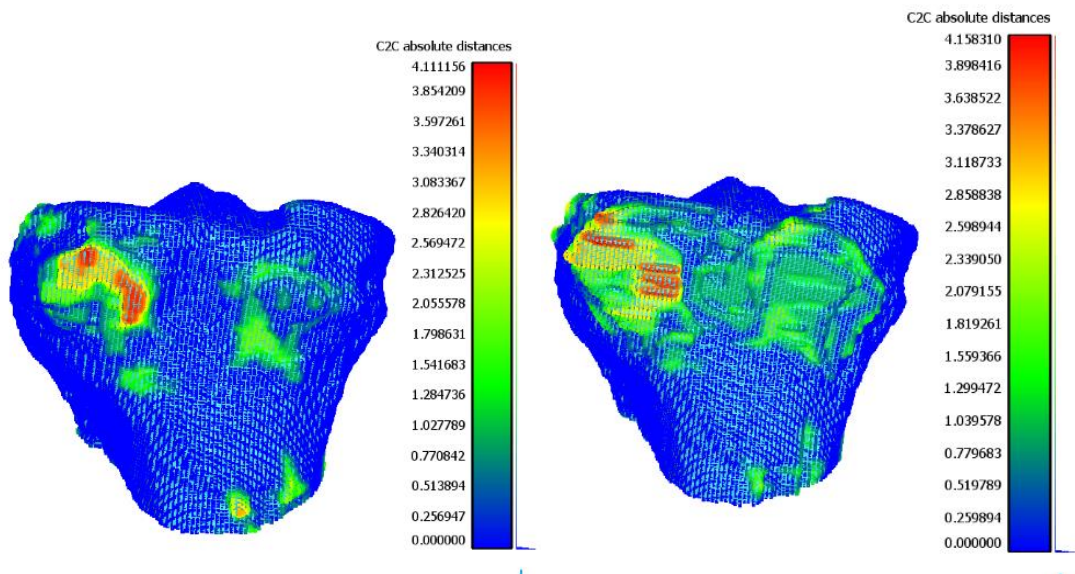


Figure 57. (a) C2C absolute distance of S3 vs S5, (b) S4 vs S5

Table 8. The codes of maximum differences between segmentations of the tibia

		Graphical tibia comparison									
		S1S2	S1S3	S1S4	S1S5	S2S3	S2S4	S2S5	S3S4	S3S5	S4S5
Participant	P1	2	2	3	2	2	2	2	2	2	2
	P2	2	2	2	2	2	3	3	2	2	2
	P3	7	7	7	2	2	2	2	2	2	2
	P4	7	7	7	7	3	2	2	2	2	2
	P5	2	5	5	5	9	9	3	2	2	2
	P6	2	2	2	2	2	2	2	7	7	2
	P7	7	7	6	7	7	7	2	7	7	2
	P8	7	7	7	7	3	7	2	3	3	2
	P9	2	7	7	7	7	7	7	7	2	2
	P10	7	7	2	7	2	2	7	2	2	7
	P11	2	2	7	2	2	7	2	7	2	2
	P12	7	2	7	7	7	2	2	7	7	2
	P13	2	2	2	2	7	2	2	2	2	2
	P14	3	3	3	3	2	2	2	2	2	2
	P15	2	2	2	2	3	3	2	2	7	2

More than half (86 out of 150, 57%) of the comparison shows maximum difference in lateral proximal tibia. Posterior distal tibia is next with 44/150 (29%) of the biggest differences. Maximum difference is repeated 14 times in 150 total comparison which is 9%. Medial distal tibia (2%), lateral distal tibia (1%) and intercondylar eminence (1%) are other regions with occasional maximum differences.

#### 6.5.1.3 Patella

Also, the following presentation displays the results of the intra-examiner comparison of the patella conducted by the first individual.

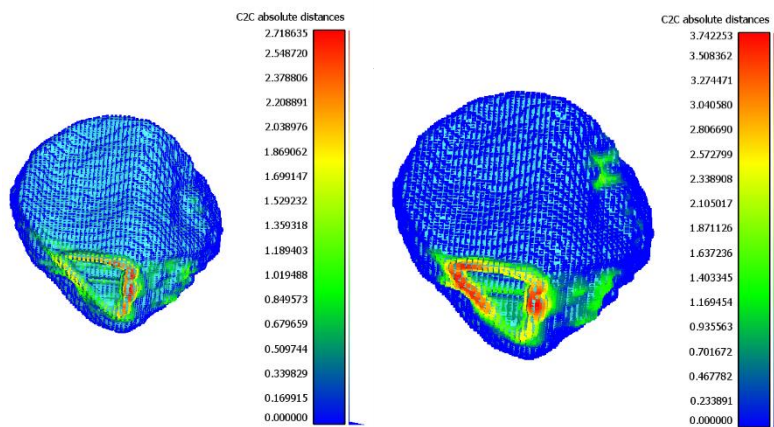


Figure 58. (a) C2C absolute distance of S1 vs S2, (b) S1 vs S3

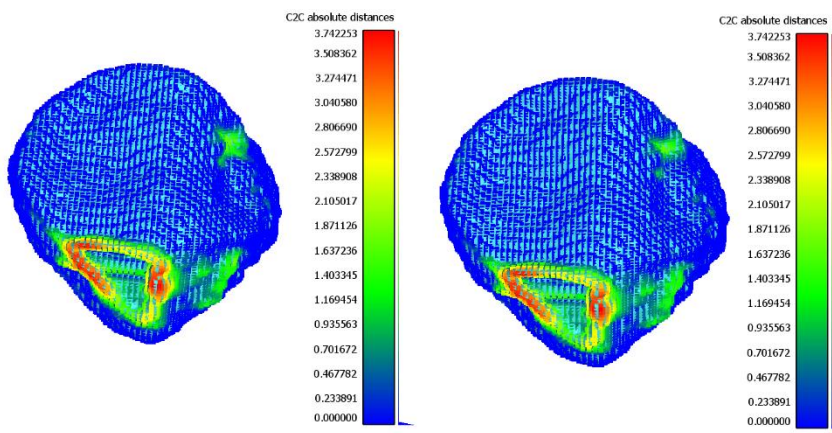


Figure 59. (a) C2C absolute distance of S1 vs S4, (b) S1 vs S5

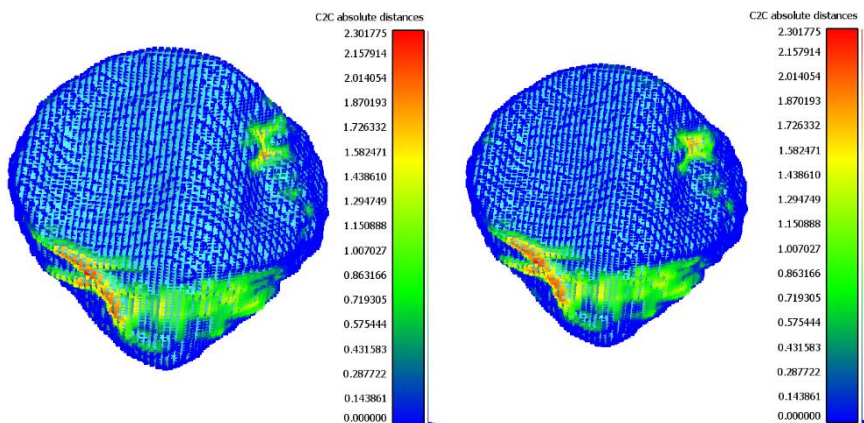


Figure 60. (a) C2C absolute distance of S2 vs S3, (b) S2 vs S4

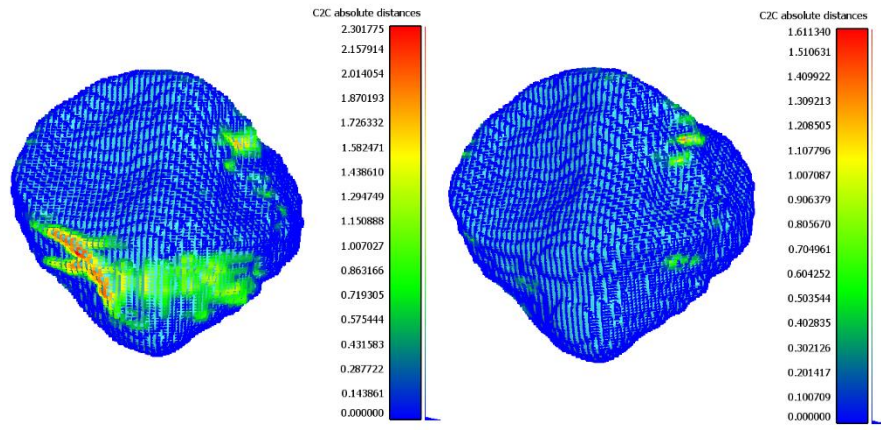


Figure 61. (a) C2C absolute distance of S2 vs S5, (b) S3 vs S4

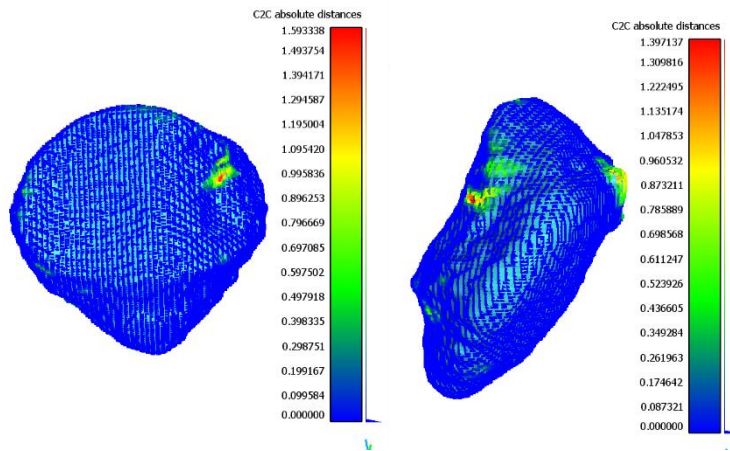


Figure 62. (a) C2C absolute distance of S3 vs S5, (b) S4 vs S5

Table 9. The codes of maximum differences between segmentations of the patella

		Graphical patella comparison									
		S1S2	S1S3	S1S4	S1S5	S2S3	S2S4	S2S5	S3S4	S3S5	S4S5
Participant	P1	7	7	7	7	7	7	7	6	6	6
	P2	8	8	8	8	1	7	2	2	2	2
	P3	8	8	8	8	7	7	7	8	8	8
	P4	8	8	8	8	8	8	8	7	8	7
	P5	6	6	6	2	2	2	2	2	6	6
	P6	8	8	8	8	8	8	8	6	6	6
	P7	7	2	6	6	2	6	6	6	2	2
	P8	2	2	6	2	6	2	6	2	6	6
	P9	6	6	6	6	6	6	6	2	2	2
	P10	6	2	2	6	2	6	6	6	6	2
	P11	6	6	6	6	2	2	2	2	2	2
	P12	6	6	6	6	6	6	2	2	2	6
	P13	6	8	2	2	6	2	2	2	2	6
	P14	8	6	8	8	6	8	8	6	6	2
	P15	8	2	8	8	8	7	6	8	8	6

54/150 (36%) comparison shows the maximum difference is at posterior proximal medial part of patella, 42 cases (28%) of maximum difference is at Anterior proximal lateral, 25% is at posterior distal medial, 10% at posterior distal lateral and 1% at Anterior proximal medial.

### 6.5.2 Hausdorff Distance, Jaccard Index and Dice Similarity Coefficient

Table 10 describes the overall average ( $\pm$ SD) values for all 2776 comparisons for the femur, tibia and patella.

Table 10. Overall average of all comparisons of each bone

	Femur	Tibia	Patella
DSC	0.925 ± 0.076	0.793 ± 0.103	0.894 ± 0.042
JI	0.868 ± 0.114	0.668 ± 0.131	0.811 ± 0.068
HD (mm)	2.788 ± 0.693	5.289 ± 2.299	2.142 ± 0.787
Maximum Eucl. Distance (mm)	2.989 ± 0.789	4.845 ± 1.916	2.198 ± 0.804
Mean Eucl.	0.036 ± 0.05	0.143 ± 0.101	0.050 ± 0.044
Median Eucl.	0 ± 0	0.001 ± 0.003	0 ± 0
Vol Similarity (%)	0.002 ± 0.035	0.002 ± 0.023	-3.1*10 <sup>(-4)</sup> ± 0.013

The DSC, JI and HD varied significantly between bones (Figure 63,  $p < 0.001$ ). Regarding the DSC, the femur had a higher coefficient than the tibia ( $p < 0.001$ ), but it was not different to the patella ( $p = 0.146$ ). The tibia also had a lower DSC than the patella ( $p = 0.002$ ). Jaccard indexes demonstrated the same differences (femur vs tibia,  $p < 0.001$ ; femur vs patella,  $p = 0.057$ ; tibia vs patella,  $p = 0.001$ ). Finally, in an opposite pattern, the mean Hausdorff distance were significantly higher for the tibia than for the femur and patella (femur vs tibia,  $p < 0.001$ ; femur vs patella,  $p = 0.008$ ; tibia vs patella,  $p < 0.001$ ).

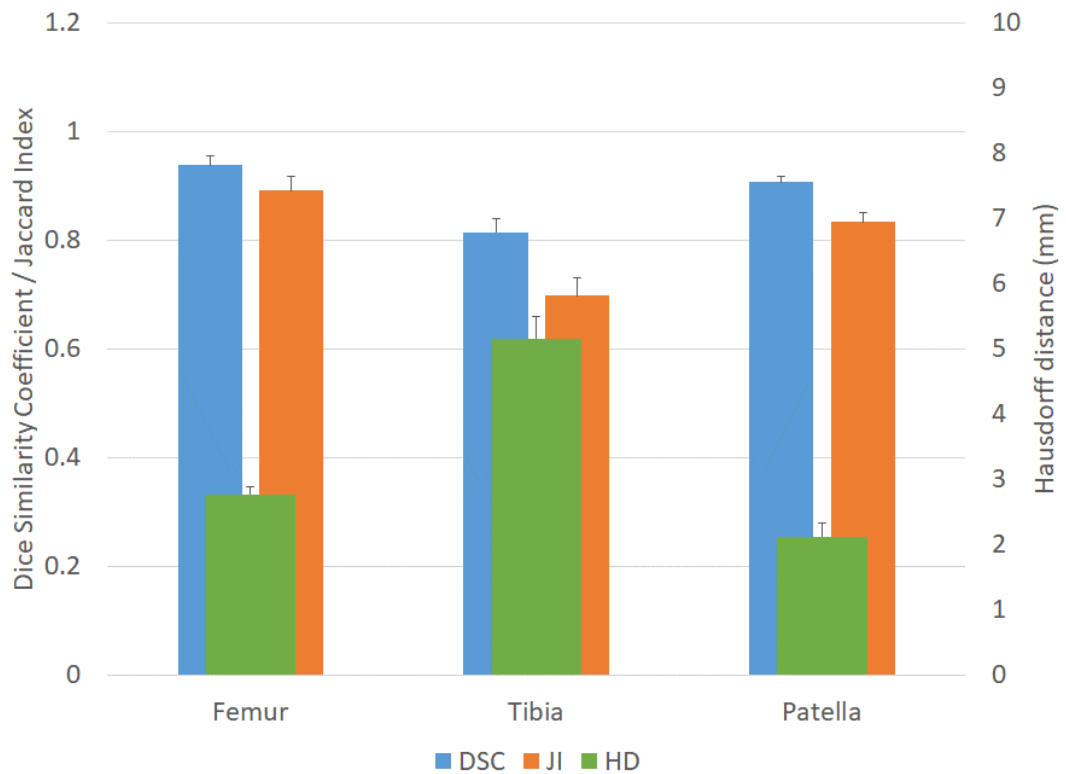


Figure 63. Mean DSC, JI and HD for each bone (error bar = standard error)

The comparison sequence had no significant effect on the DSC, JI and HD variables (Figure 64), as the p values are 0.087, 0.077 and 0.055 respectively. However, these p values are very close to the 5% level, therefore they are suggesting a trend that there possibly could be an effect, but statistical convention dictate there is no effects of bone and comparison on the measurement matrixes. With regards to Figure 64 it could be said that there may be a trend for increasing DSC and JI measures, and a decreasing HD measure, but it is clearly not conclusive, visually or statistically.

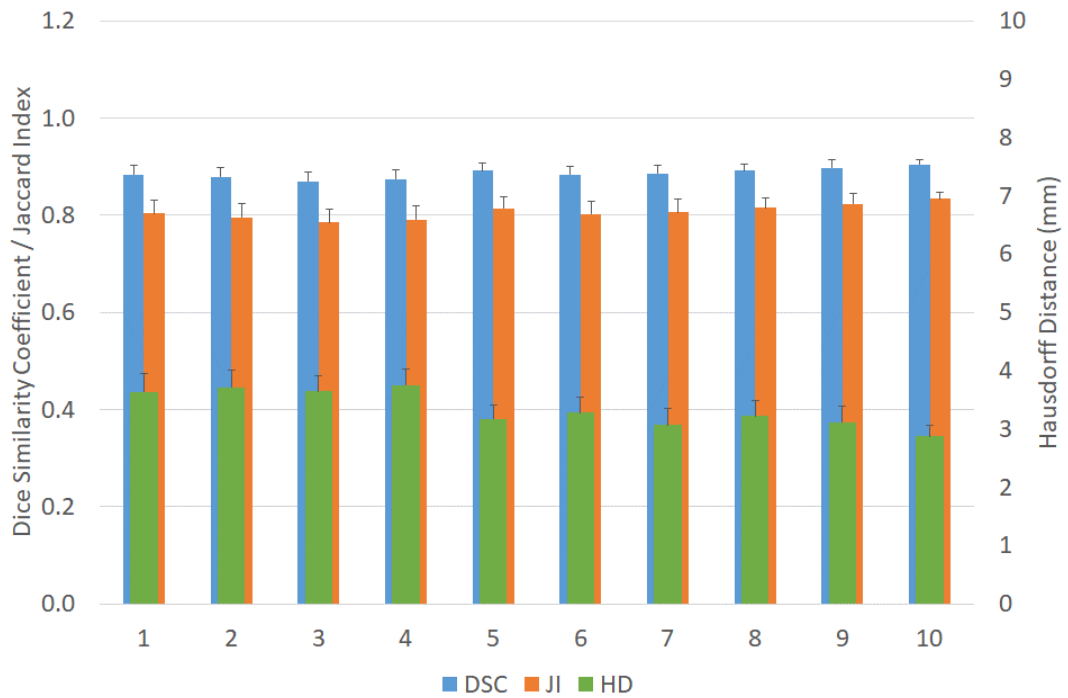


Figure 64. Mean DSC, JI and HD over all comparison (error bar = standard error)

No interaction of bone and comparison sequence was found, as the Greenhouse-Geisser p values were 0.462, 0.454 and 0.283 for DSC, JI, and HD respectively.

The full statistical output may be seen in Appendix H.

The above analysis combines all three bones; however, one should ascertain as to whether any particular bone of the knee joint is more susceptible to segmentation errors. The mean DSC of the three bones, against comparison sequence, is illustrated in figures 65. In accordance with Figure 63, femur has the highest similarity overall the experiment, followed by the patella and then tibia. The lack of an interaction effect is evidenced by the similarity in variation with comparison sequence for each of the bones.

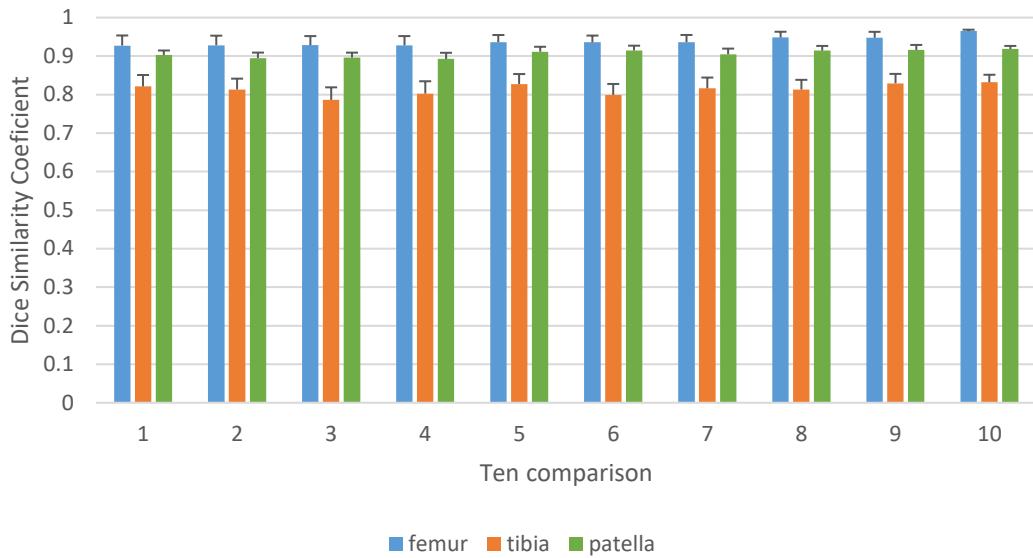


Figure 65. Relation of each bone and comparison on DSC

Figure 66 is also representing the average JI of all bones over all the segmentation, which showing same behaviour as DSC, tibia has less mean JI than Femur and patella.

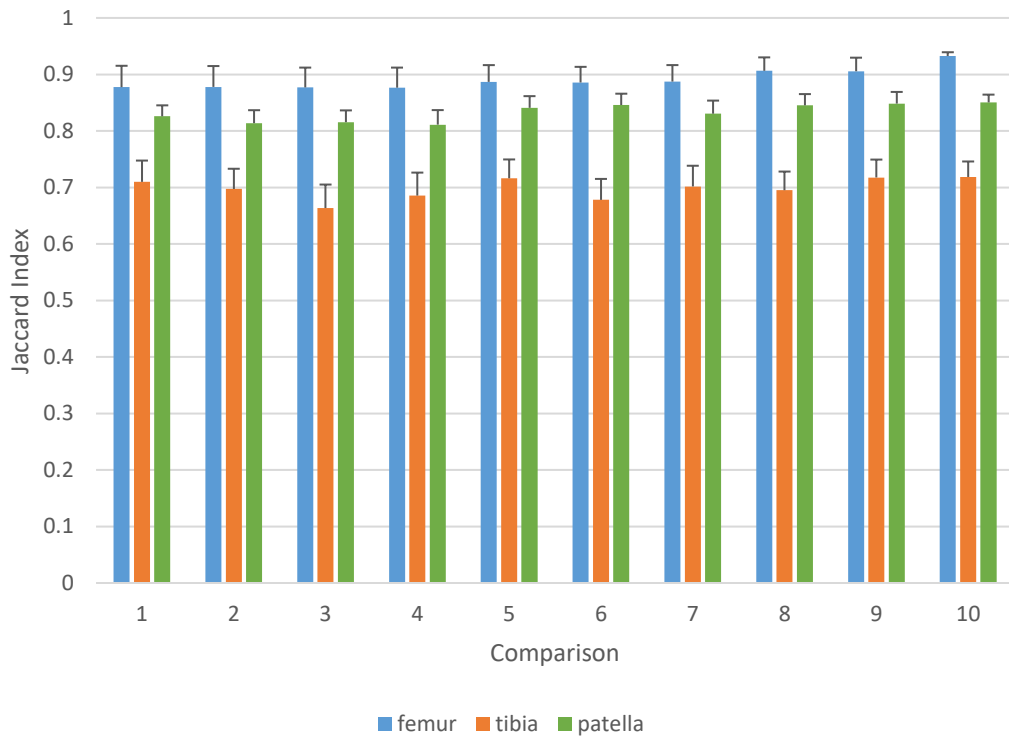


Figure 66. Relation of each bone over all comparison on JI

Figure 67 depicts the average HD of each bone against the comparison sequence. Clearly the tibia has a higher HD than the femur and patella, as described above in the main effect of bone on HD. The interaction p-value is 0.283, and whilst non-significant, the figure suggests that whilst the femoral HD value remains constant, the HD for the tibia and patella may drop after comparison 4, indicative of a possible learning effect.

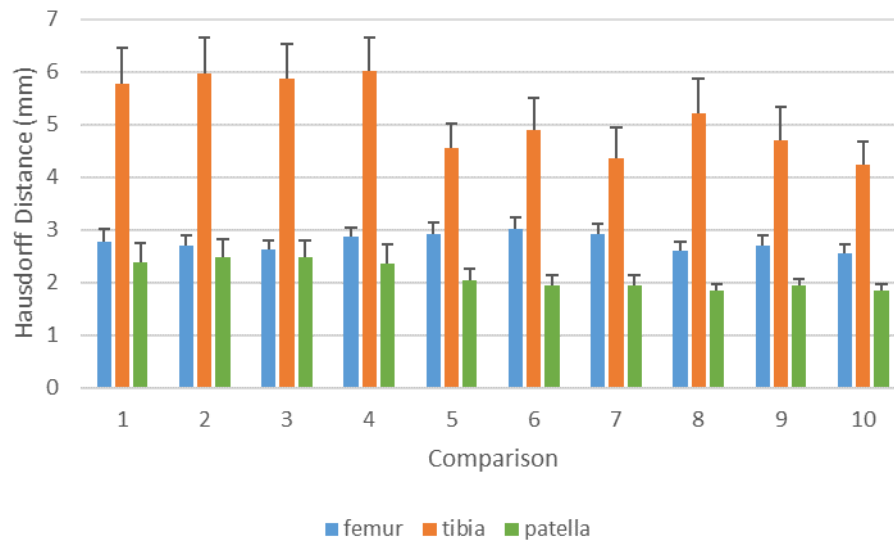


Figure 67. Relation of each bone and overall comparison on HD

### 6.5.3 Inter- observer Analysis

#### 6.5.3.1 Femur

The average inter-class correlation coefficient (ICC) of femur using DSC is shown in Figure 68. The data that is used for this calculation is available at Appendix I. ICC of DSC of femur is 0.975.

P_ID	P1	P2	P3	P4	P5	P6	P7	P8	P9	P10	P11	P12	P13	P14
DSCFS1S2	0.96	0.96	0.75	0.62	0.96	0.95	0.96	0.96	0.97	0.96	0.97	0.97	0.97	0.97
DSCFS1S3	0.91	0.96	0.75	0.64	0.95	0.98	0.97	0.96	0.97	0.96	0.98	0.97	0.96	0.97
DSCFS1S4	0.94	0.94	0.77	0.65	0.94	0.96	0.97	0.96	0.97	0.96	0.99	0.97	0.97	0.96
DSCFS1S5	0.93	0.95	0.76	0.65	0.94	0.96	0.97	0.96	0.97	0.96	0.98	0.97	0.97	0.97

DSCFS2S3	0.90	0.96	0.74	0.79	0.97	0.96	0.97	0.96	0.97	0.97	0.98	0.96	0.97	0.97
DSCFS2S4	0.93	0.94	0.75	0.79	0.94	0.94	0.97	0.96	0.97	0.98	0.98	0.97	0.97	0.97
DSCFS2S5	0.93	0.95	0.75	0.78	0.95	0.95	0.98	0.96	0.97	0.97	0.99	0.97	0.97	0.97
DSCFS3S4	0.92	0.96	0.75	0.91	0.96	0.96	0.98	0.97	0.97	0.97	0.99	0.97	0.96	0.97
DSCFS3S5	0.92	0.97	0.75	0.91	0.97	0.97	0.98	0.97	0.97	0.97	0.98	0.97	0.97	0.96
DSCFS4S5	0.97	0.97	0.94	0.93	0.97	0.96	0.98	0.97	0.97	0.98	0.98	0.97	0.97	0.97

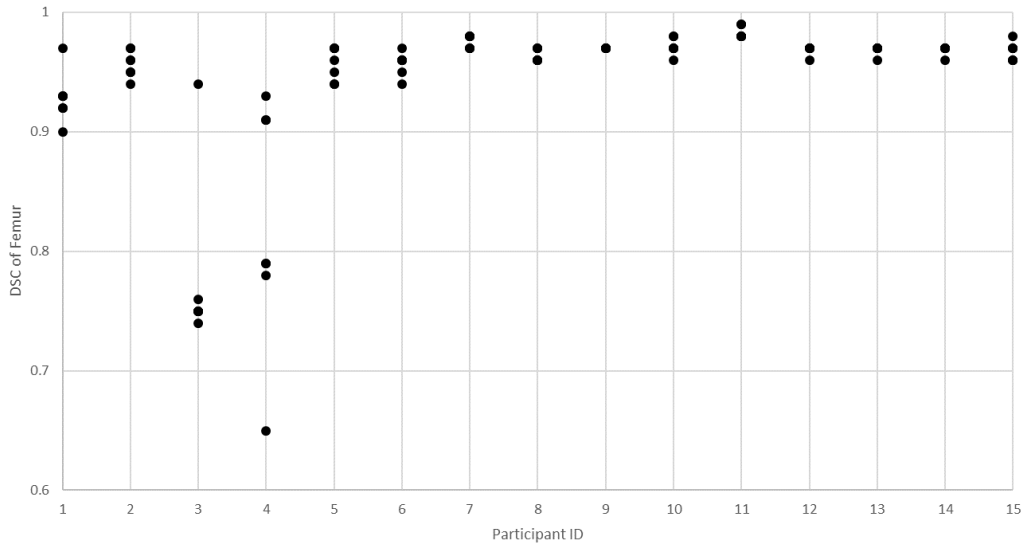


Figure 68. Average DSC ICC of femur is 0.975

### 6.5.3.2 Tibia

Figure 69 plotted the aggregation of Dice Similarity Coefficient of segmentation of tibia for fifteen people. Which shows the ICC is 0.981.



## **6.6 Discussion**

### **6.6.1 CloudCompare**

The CloudCompare analysis not only provides valuable insights into segmentation variability but also offers a visual understanding of specific anatomical regions prone to challenges. These insights are crucial for improving segmentation protocols, especially in mitigating issues such as partial volume effects, image quality, and noises. By identifying problematic areas susceptible to variability, segmentation protocols can be refined to enhance accuracy and consistency in delineating tissue boundaries. Following section provides more detail about these and illustrates them in our case study.

#### *6.6.1.1 Partial volume effects*

Partial volume effects occur when a single voxel (3D pixel) in a medical image contains a mixture of two or more different tissue types, such as bone and soft tissue. This happens at the boundaries or interfaces between different tissues, where the voxel encompasses a partial volume of each tissue type. As a result, the voxel value represents an average of the intensities or densities of the different tissues, leading to blurring or inaccurate representation of the tissue boundaries.

In the context of segmentation, partial volume effects can cause inaccuracies in the delineation of boundaries between different structures or tissues. This is because the segmentation algorithm may struggle to correctly classify voxels that contain a mixture of intensities, leading to errors in the final segmented region.

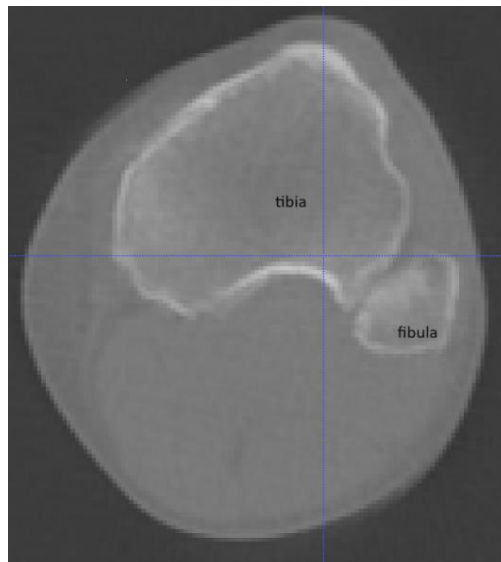


*Figure 71. Example of partial volume effect between tibia, soft tissue and fibula*

The boundary between the tibia and the surrounding muscles or other soft tissues, seems to contain a partial volume of bone (from the tibia) and a partial volume of soft tissue (Figure 71). Similarly, at the interface between the tibia and the fibula, voxels may encompass both bone structures, leading to ambiguous intensities and potential misclassification during segmentation (Figure 71). This factor may contribute to the increased segmentation variability observed in the tibia compared to the femur and patella.

The presence of voxels containing a mixture of intensities from different tissues at these boundaries could have led to inconsistencies in how the segmentation algorithm classified these voxels. As a result, different operators may have obtained slightly different segmentation results, particularly in regions where partial volume effects were more pronounced, such as the lateral proximal tibia or the distal end of the tibia (where motion artifacts were also present).

#### *6.6.1.2 Image quality: contrast and noise*

Contrast in CT medical imaging refers to difference between x-ray attenuated by body and x-ray transmitted through body. Therefore, the CT image shows lighter areas for bones as more x-ray stopped by bones and fewer x-rays hit the detector. In the same manner, it shows darker areas as more x-ray transmitted and hit the detectors. Very low image contrast results in low contrast sensitivity and low visibility as shown in

Figure 72A; and high contrast also reduced visibility in the very light and dark areas (Figure 72B).

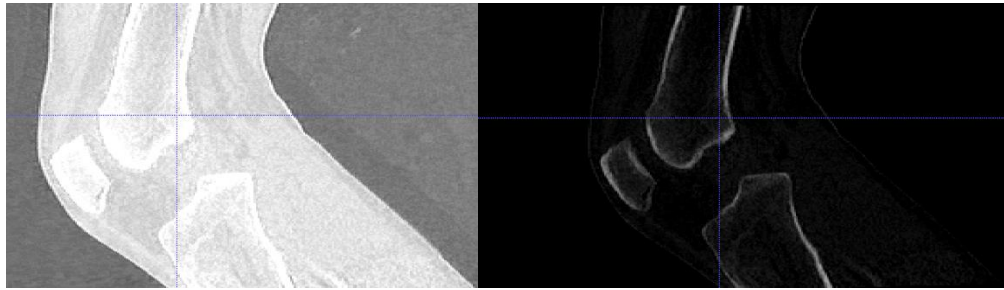


*Figure 72. A Knee joint CT image with low contrast, B knee joint CT image with high contrast*

Additionally, CT images may contain noise, which can be caused by low radiation dose, hardware imperfections and patient motion during scanning. Noise can make it difficult to distinguish between relevant structures and background, leading to segmentation errors.

Now, there is probability for the CT image that may contain both low contrast and noise at same time. Figure 73 shows the ratio of contrast over noise chart. Contrast is signal level of a given region above the background. In the following image the first row and column show signal with 20HU above the background with 40HU so the contrast is 20 HU (numbers are arbitrary), so if there is more contrast and less noise, the image is more visible. If the noise increase over contrast, the noise to ratio reduces and become harder to visualise it (Figure 73).

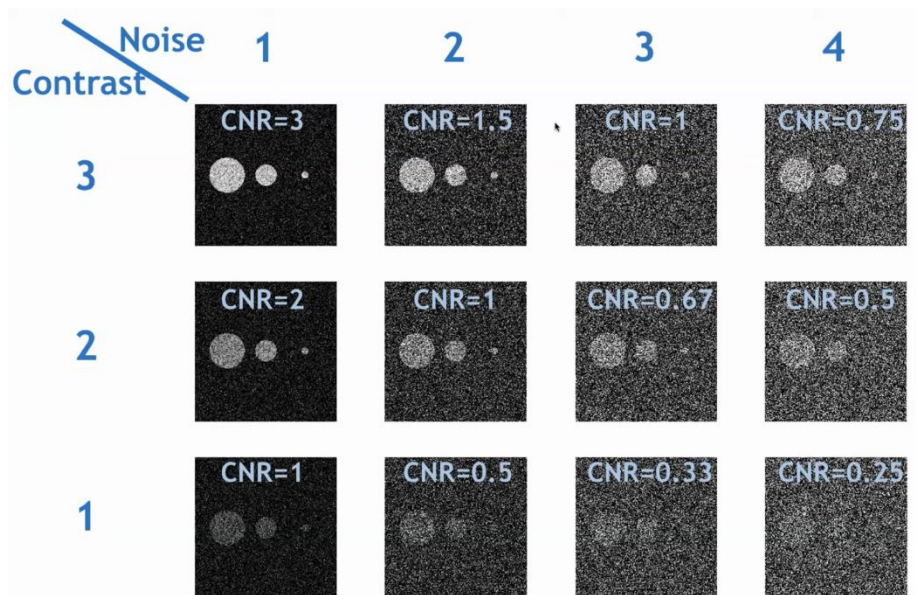


Figure 73. Contrast to noise ratio

### 6.6.1.3 Rose model effect

On the other hand Albert Rose [128] published a study as Rose model, that mentioned human visual system is related to contrast, by, square root of area multiply by number of photons. Where V is human visual system, C is contrast, A is area, and N is number of photons, which is related to Noise. The noise is inversely proportional to the square root of the number of photons used to make the image. In other words, if the number of photons used is quadrupled, the noise in the resultant image should be halved [129].

$$V \sim C \sqrt{(A \cdot N)}$$

This equation means that smaller objects need higher contrast to be seen by human eye, Figure 74. In this regard, the hypotheses suggests that the tibia has more irregular boundaries and smaller anatomical features compared to the femur and patella. According to the Rose model, these smaller features and intricate boundaries may have lower contrast and be more susceptible to the effects of noise, making them less visible or detectable during the segmentation process.

The irregular boundaries of the tibia may result in regions with lower contrast, as the transition between bone and soft tissue may be more gradual or blurred.

Additionally, In the context of the semi-automatic segmentation process used in this study with the ITK-Snap software, the Rose model highlights the potential challenges faced in segmenting regions with low contrast or high noise levels.

The software's segmentation algorithm may struggle to accurately delineate boundaries or detect smaller features in regions with low contrast-to-noise ratios, as predicted by the Rose model. This could partially explain the higher variability observed in segmenting the tibia, which has more irregular boundaries and smaller anatomical features compared to the femur and patella.

However, the software allowed for user input and manual editing, which could compensate for these challenges to some extent. By manually adjusting the segmentation results or providing additional guidance operators could potentially overcome the limitations imposed by low contrast or noise and improve the segmentation accuracy of challenging regions. Or may could cause more human error.

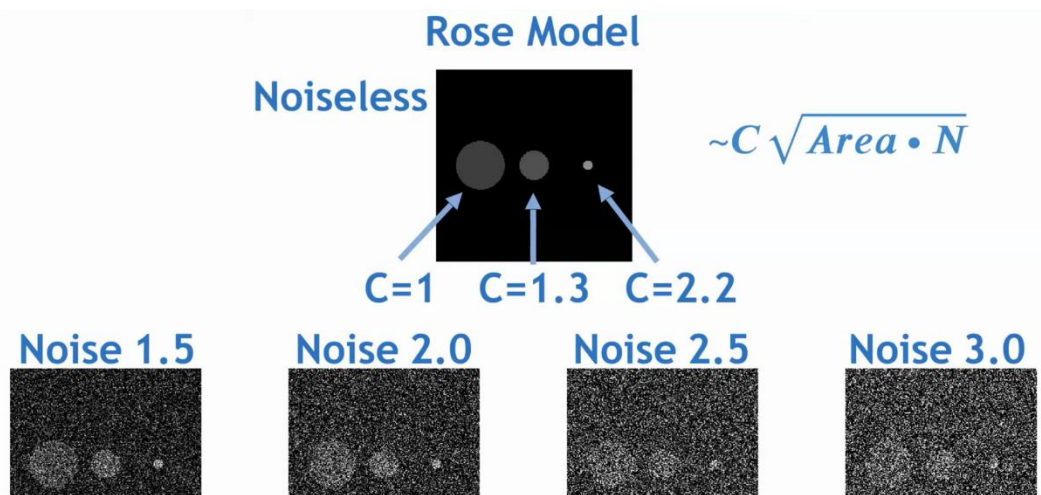


Figure 74. Relation of Visual system to contrast and noise [128, 130]

On the other point of view, considering the semi-automatic segmentation feature, the level of user interaction and input during the segmentation process may affect the identification of irregular boundaries. Investigating the impact of user involvement on the software's ability to detect smaller areas could guide improvements in user interfaces and segmentation algorithms.

#### 6.6.1.4 Motion Artefacts

This phenomenon occurs when x-ray photons, initially directed towards a specific detector, are deviated due to sudden patient movements, resulting in inaccurate information.

In this study, despite the acquisition of three CT images per second, motion artefacts from patient movements during image acquisition are visible near the distal end of the tibia, which leads to inaccurate data throughout the segmentation process. (Figure 75). Patient movement causes blurring, streaking, or shading, during a CT scan.



*Figure 75. Tibial distal end shows motion artefacts*

Figure 76 illustrates the anterior aspect of the medial condyle of femur with maximum difference. Lack of enough contrast, low bone density, and pathological situation could cause this.



*Figure 76. Anterior aspect of medial condyle of femur shows maximum difference*

In the tibia, the lateral proximal region showed the most variability (Figure 77). The hypothesis comes from the idea that the surface texture of the tibia might affect the performance of segmentation software. Irregularities in the surface, such as bumps or grooves, could lead to misinterpretations by the segmentation algorithm.

Additionally, the density of the tibia's bone structure may also affect the visibility of certain areas. Higher bone density could potentially obscure smaller regions, making them less distinguishable.



*Figure 77. Lateral proximal tibia shows maximum difference*

Figure 78 shows the patella with the posterior proximal medial region had the greatest differences.



*Figure 78. Posterior proximal medial patella shows maximum difference*

### **6.6.2 Hausdorff Distance, Jaccards Index, Dice Similarity Coefficient**

The quantitative similarity metrics showed significant differences between the bones, with the tibia having lower similarity (higher Hausdorff distances) compared to the femur and patella. This aligns with the CloudCompare analysis showing high variability in the tibia.

While the tibia still shows good agreement (DSC = 0.793), it has a lower DSC compared to femur and patella. This might be attributed to the motion artefact, because of movement during four-dimensional CT scan and the quality of the scan.

Across all metrics, the femur showed the best segmentation consistency. The patella showed good consistency by DSC.

Both femur and patella show high agreement in segmentation among different observers, as indicated by the high DSC values and ICC. This suggests that the segmentation process for these bones is more reliable and reproducible than tibia.

This result is consistent with Raudaschl [124] study, in which they highlight the lack of consensus on the best automated segmentation method due to the diversity of structures and a wide variety of segmentation algorithms. They evaluated the segmentation methods on head and neck CT. Six teams participated in the segmentation process, segmenting nine structures in head and neck CT images, including the brainstem, mandible, chiasm, bilateral optic nerves, and bilateral salivary glands. Mandible was the only bony structure that they segmented, which had the highest DSC as 0.814 that was average between three operator groups, and average maximum HD is 25.42mm. Comparing to the achieved average DSC over all bones in our study, which is 0.87, are very consistent with their results, suggesting good performance.

However, their results show a big inconsistency with our study in maximum HD. Our maximum HD is related to tibia which is 5.289mm but their HD among three teams is 56.128mm, 15.391mm and 4.749mm. They mentioned this could be due to upper part of mandible which was thin, and because they had different segmentation techniques for auto-segmentation. They emphasize that more general-purpose segmentation technique is needed and all the teams should have used same technique.

Other study is done by Ataei [76] assessed the inter- and intra-operator reliability of manual segmentation of femoral metastatic lesions. Two operators conducted segmentation twice for each femur, and Dice coefficients (DCs) were calculated to assess reliability. A Dice coefficient greater than 0.7 was considered indicative of good reliability. While their study demonstrated good reliability, it appeared to be less consistent than our study. This discrepancy may be attributed to the irregular and unpredictable shapes of bone metastatic than healthy bones. They mentioned simpler surfaces are easier to segment and they saw improved reliability for larger volumes.

#### *6.6.2.1 Learning trend*

On the other point of view, figures 65, 66, 67 shows a trend. The trend (although not statistically significant) for increasing DSC and JI and decreasing HD may be suggestive of a learning curve for the participants and the segmentations proceeded. Comparing the 4<sup>th</sup> segmentation with the 5<sup>th</sup> segmentation, across all bones, seemed to have the highest similarity scores and the lowest Hausdorff distance. However, any such learning effect is fairly minimal and may not be clinically meaningful when translated to future modelling scenarios.

#### *6.6.2.2 Presence of Fibula*

The presence of the fibula in close proximity to the tibia emerges as a potential influencing factor, contributing to the tibia's higher HD and lower similarity compared to the femur and patella. Distinguishing between the borders of these two bones also presented challenges for the operator (Figure 77). The close spatial relationship between the tibia and fibula appears to have led to the bleeding of the initial seed of segmentation into the neighbouring tibia. This phenomenon may have occurred due to the challenges in precisely delineating the boundaries between the two closely situated bones. Consequently, manual intervention by the operator was necessitated to rectify this bleed, introducing an element of subjectivity into the segmentation process. Additionally, Distinguishing between the borders of the tibia and fibula emerged as a notable challenge for the operator. The anatomical proximity and potential similarities in radiodensity between these bones may have made it difficult to establish clear and distinct boundaries during the segmentation process.

### **6.6.3 Inter- observer Analysis**

The ICC analysis demonstrates excellent inter-rater reliability for the femur, tibia and patella segmentations. ICC values were 0.975, 0.981 and 0.959 for the three bones respectively. According to Koo [82] et al. this means there is a good to excellent reliability for the segmentation of tibia patella and femur on 3D images of the knee joint between the different observers (Koo and Li 2016).

The high ICC values for DSC in all three bones demonstrate that ITK-Snap provides a reliable platform for segmentation. Considering the level of experience among operators and the agreement among them, suggests that the tool is consistent across observers with different experience, enhancing its utility in clinical or research settings.

In comparison with Misselyn [76] paper which they got 0.828 ICC on preoperative measurements and their inter-observer ICC for postoperative measurements was calculated as 0.692. The high agreement is in line with the results of femur, patella and tibia of this study, however the 0.69 is moderate reliability of the measurement, which could be because, presence of the implants in post operation cases. Their preoperative has high agreement that is line with our study, but their postoperative study are not inline. They suggest another probability for this, which is the lack of perfect symmetry of the calcaneus bone in the human body and also by the variation of the measurements.

### **6.7 Conclusion**

The results demonstrate the reliability of the segmentation process. The findings contribute to the potential clinical applications of these methods. Additionally, statistical analysis using SPSS software reveals a significant effect of bone on the measurement variables. The study also observes an improvement in segmentation similarity over time, particularly for the femur.

In conclusion, the comprehensive analysis of knee joint segmentation using quantitative metrics of Intra- observer variability, CloudCompare visualization, and inter-observer reliability assessments has provided valuable insights into the challenges of the process. While challenges such as image quality, motion artefacts, proximity of the fibula, and irregularities in bone structure impact segmentation

outcomes, the study emphasizes the importance of refining protocols, optimizing algorithms, and providing targeted operator training. The consistent inter-observer reliability signifies the potential clinical utility of the segmentation tool, reinforcing its reliability in diverse applications. The findings contribute to the ongoing efforts to enhance the accuracy and reproducibility of musculoskeletal imaging.

## **Chapter 7 Effect of segmentation on FEA**

### **7.1 Introduction**

Differences in segmentation of the bones may manifest in differences in subsequent computations models, as these are based on segmented data. These models are used in hospitals for surgical planning, and also in academic research. Many research questions utilise finite element models of bone to determine stress and strain in response to external loads and moments [131-133]. It is therefore of interest to determine the effect of small changes in the topology of the segmented models on the numerical outputs. This chapter details an example in which this is achieved.

In FE models of orthopaedic interest, if a part of the bony anatomy is not in contact with another structure, e.g. cartilage or ligament, then a small variation in that surface is unlikely to have an effect on the meaningful output of the model, with the exception of very localised stress and strain. However, if the bony surface is in contact with another structure in the model (e.g. ligament insertion points, articular cartilage), then uncertainty in the true location of the bony surface may spread uncertainty into these other structures, which may or may not, be of academic or clinical importance. Therefore, to maximise the potential for identifying the importance of the bony surface, a model that has as much contact area surrounding the bone as possible, is a sensible approach.

In conventional knee models, the process of individually defining each ligament for every person and model is not only time-consuming but also susceptible to human error. They are also complicated to create; often segmenting multiple tissue types, and are currently not suitable for analysing large image data sets. To overcome these challenges, this chapter uses an approach that replaces the ligaments, tendons, bursae, meniscus, muscles, and the knee capsule with a simplified representation as an incompressible, isotropic, homogenous, elastic volume. This methodology is particularly suited to work with CT data because the soft tissues are not easily distinguishable in CT images.

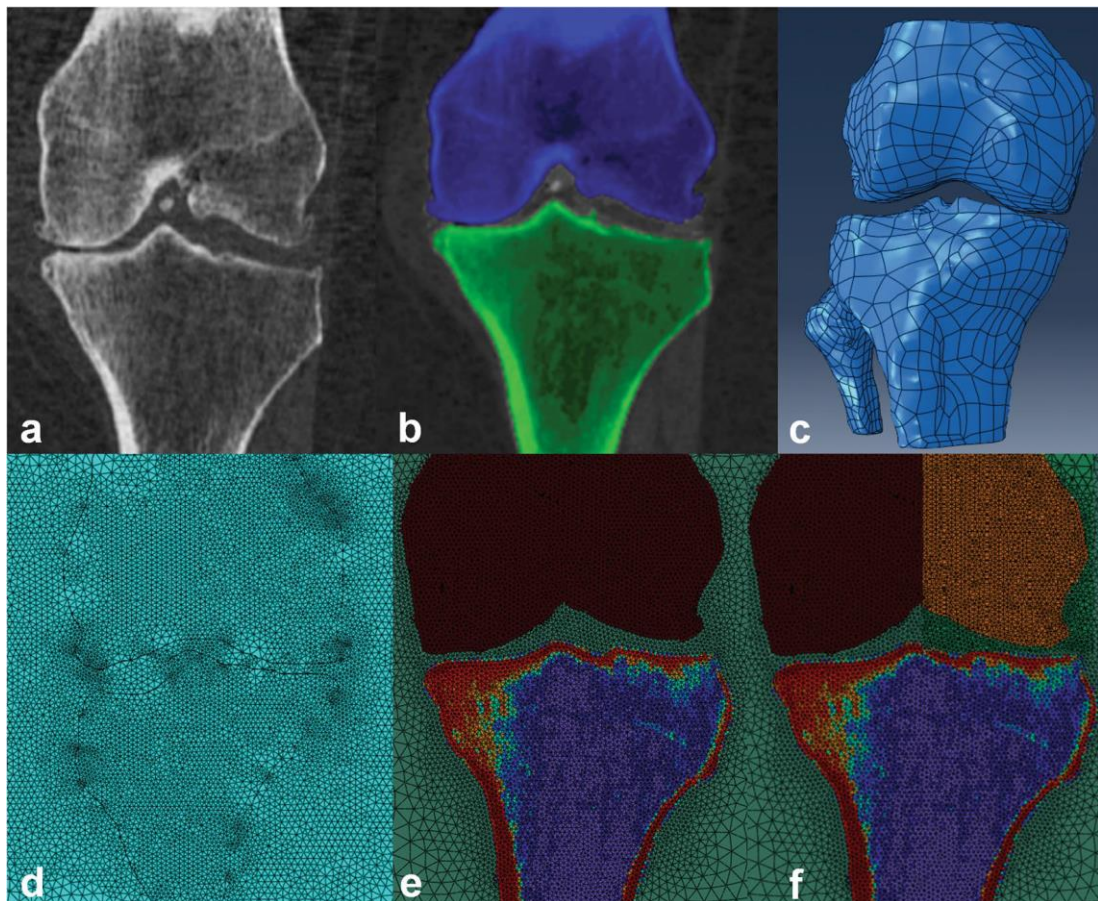


Figure 79. Finite element model by Arjmand [4]

This concept has been inspired by Arjmand et al. [4], who made a FE model to describe the mechanics of the proximal tibia in normal and OA knees. Their work built on McErlain et al. [5] who used the same methodology to investigate the effect of intra-osseous subchondral cysts in Osteoarthritis (OA) knee.

Arjmand et al. [4] developed individualised FE models for 14 knees affected by osteoarthritis (OA) and normal knees. Their objective was to identify specific mechanical characteristics in the proximal tibia that distinguish between normal and OA knees. Utilizing quantitative computed tomography (QCT) scans, they analysed structural stiffness, von Mises stress, strain, and minimum principal stress. The study concluded that FE modelling in this manner effectively measures and distinguishes biomechanical differences between healthy and OA knees. Importantly, the study focused on the method of replacing soft tissue with an incompressible cylindrical medium, which is not representative of the volume of the joint and surface topology,

which may have implications for the material properties chosen for the tissue. Figure 79 illustrates the representation of soft tissue as an incompressible cylinder.

Prior to this, McErlain et al. [5] investigated intra-osseous lesions such as subchondral bone cysts (SBC), in knee osteoarthritis (OA) progression. The soft tissue surrounding the joint was modelled using the compressive properties of cartilage under compression at equilibrium, with properties of cartilage assigned to all soft tissue outside the bony margins.

The above two research studies [4, 5] created soft tissue models, but they did not make them patient-specific based on individual images. This chapter extends their approach as the soft tissue surrounding the knee is derived exclusively from subject-specific segmentation of a real patient CT image, differentiating it from the previous models that bounded the bony anatomy in a cylinder of soft tissue. This approach maximises the contact area between bone and soft tissue, making it ideal to assess the effect of segmentation.

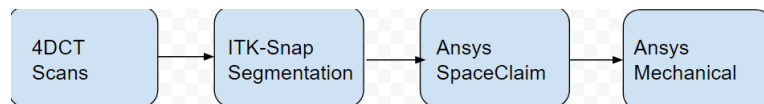
Therefore, the primary aim of this chapter is to use a simplified soft tissue model, specifically an incompressible, isotropic, homogeneous, elastic volume in an FE simulation of knee joint loading to assess small differences in bone topology due to variability in segmentation. To do this, the study replicates and enhances a method for constructing knee joint models by replacing the traditional approach of defining individual ligaments, muscles, tendons, ligaments, bursae, and meniscus with a comprehensive, all-encompassing external knee joint surface.

The outcomes of this research will contribute to a better understanding of the feasibility and advantages of utilising simplified soft tissue models in finite element simulations of knee joints, with potential implications for clinical research and analysis. Moreover, and uniquely, it will highlight the role that segmentation plays in the numerical outcome of models based on CT and MRI images.

## **7.1 Methodology**

In this section two subject-specific finite element models were constructed in Ansys Workbench (*Ansys 2022 R2*).

As before, the four dimensional (3D + time) Computed Tomography scan of the knee joint from a healthy man is taken, with the person lying in prone position and successive images were taken during knee flexion providing a 4DCT dataset [117]. The DICOM image was imported to ITK-Snap for segmentation and creating 3D representation of the images. The following process flowchart outlines the steps, 4DCT scans are initially segmented using ITK Snap software. Subsequently, Ansys Spaceclaim converts the surface only data into solid representations. Finally, Ansys Mechanical performs the analysis on the resultant model.



### 7.1.1 ITK-Snap Analysis

One image (N3018368) was selected as it had less moving artefact and had a relatively extended knee joint. The right knee was selected for analysis (Figure 80Figure 80).



Figure 80. ROI selection on ITK-Snap

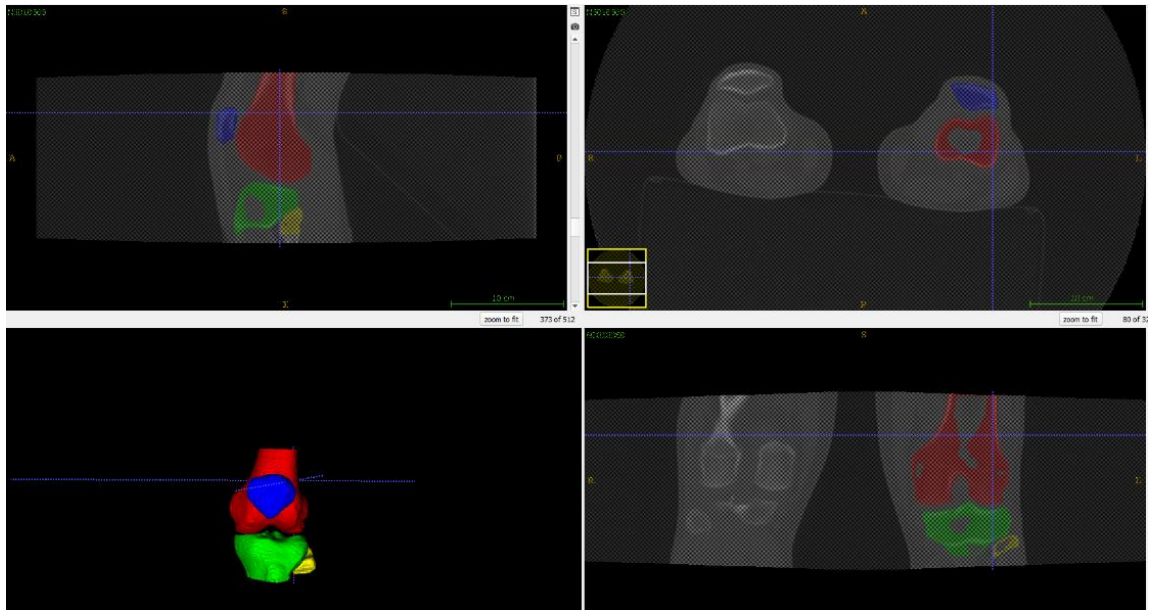


*Figure 81. 3D model of knee joint is made*

Labels were defined for the femur, tibia, fibula, patella and soft tissue. The previously-described thresholding method was used to make the binary image. The optimal threshold value was found, as mentioned in chapter 4, for each bone. The optimal threshold values for the tibia, femur, patella, fibula and soft tissue were 205HU, 160HU, 200HU, 232HU, -400HU respectively. The upper threshold level was kept as the maximum available and lower threshold level was the optimal threshold. The operator initialised the contour by giving bubbles in the regions. The contour expands its progression and stops at the point where there is a variation in Hounsfield Units (HU).

As the tibia and fibula are very close to each other, the contour bleeds. To overcome this problem during segmentation, first the tibia is segmented normally, then a mask is placed on the tibia when performing segmentation of the fibula. The action of the mask is to prevent bleeding from the fibula to the tibia. Every orthogonal viewpoint of the image is checked and inspected for any holes.

By updating the fourth window, the 3D model is constructed for the cortical part of bones whilst the spongy parts of bones are not included. This spongy part and any hole on the cortical area are filled manually by using the paintbrush tool (Figure 81)

After all the bones are segmented, the bones are masked and the soft tissue is segmented to ensure no bleeding into the bone regions (Figure 82)

Figure 83 and Figure 84 depict the bony anatomy of the knee joint and the soft tissue in Meshmixer™.

The constructed 3D model was saved as a stl file; however, stl files only represent the surfaces of the objects. Therefore, before any analysis could be done, they needed to be converted to solid geometry files. Hence, they were imported to Ansys SpaceClaim 2022 R2, to be converted to CAD geometry to be able to use in Ansys mechanical.

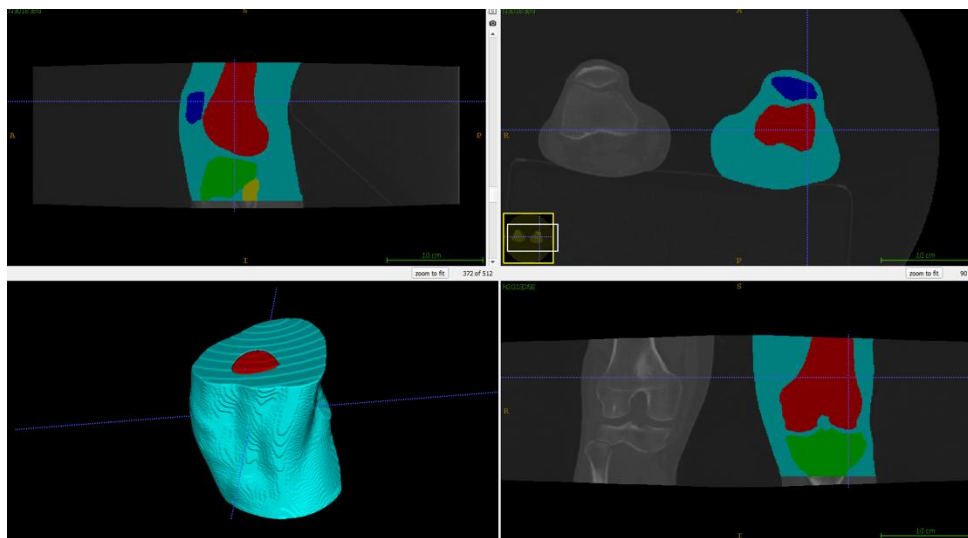


Figure 82. The 3D model of soft tissue surrounding knee joint is made

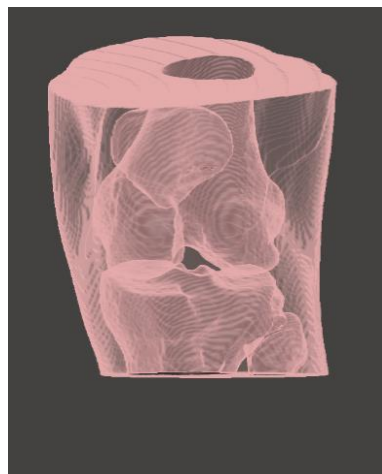


Figure 83. Soft tissue of knee joint is shown in Meshmixer, bones are hidden

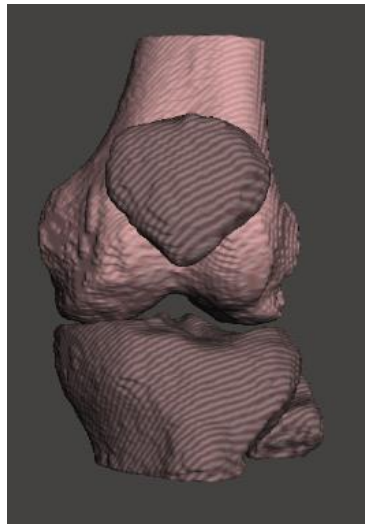


Figure 84. Meshmixer is showing 3D model of constructed bones

### 7.1.2 Ansys SpaceClaim Analysis

The stl file was imported and checked for any problematic facets. Then with the Auto Skin tool it was converted to geometry. The repair tool was used to look for any gaps, missing faces, stitches, split edges, sharp edges and duplicated edges and tried to make sure it is poreless (Figure 85Figure 85). All bones are created successfully as geometry (Figure 86Figure 86).

The final CAD geometry was saved as a SpaceClaim file (.scdoc) and imported to Ansys worckbench™.

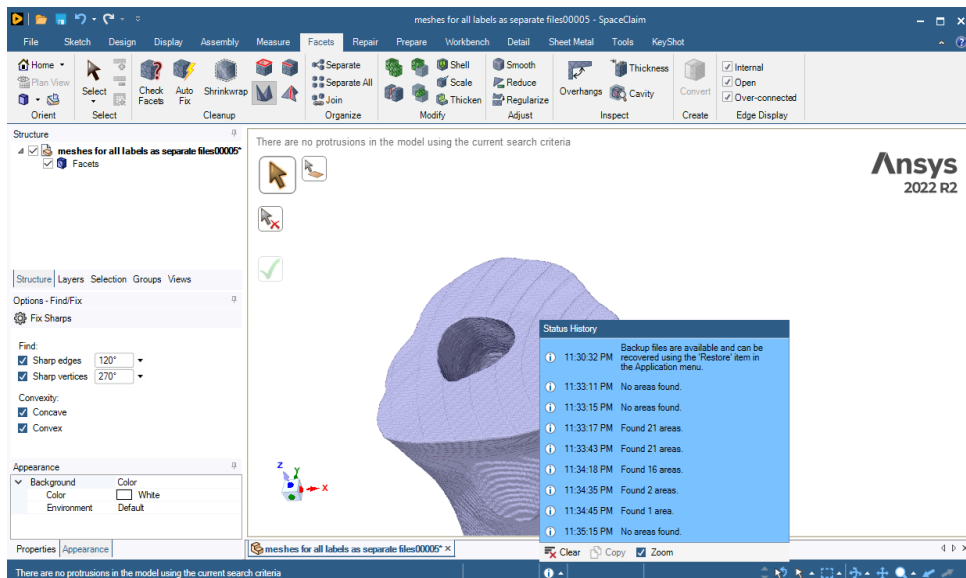


Figure 85.converting Stl file to CAD geometry in Ansys SpaceClaim

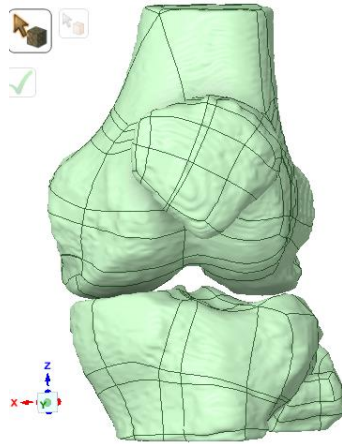


Figure 86. bones are converted to CAD Geomtry inAnsysSpaceClaim

### 7.1.3 Ansys Mechanical Analysis

In the Ansys 2022 R2 Workbench, the units are set as millimetre and a static structural system was chosen and the knee joint was imported. The literature was studied to find appropriate and relevant soft tissue material properties, which are listed in (Table 11). The literature describe different material properties for soft tissue and, obviously, there is no consensus for a specific material characteristic for soft tissue around knee joint. Based on these data, this study used a hyperelastic neo-Hookean material with a shear modulus of 1 MPa and a Poisson's ratio of 0.45 for soft tissue in the Engineering data section, to make it constitutively simple but able to withstand large deformation gives the best chance for model solution.

Table 11. Published soft tissue material properties

Author	Tissue type	Elastic Modulus (MPa)	Poisson's ratio
Noyes [134]	Young human ligament	111	
	Old human ligament	65.3	
Butler [135]	ACL	278-310	
	PCL	280-447	
	ACL	375-25	

Butler [136]	Anteromedial fiber human ligament	238	
	Anterolateral fibers human ligament	285.9	
	posterior fibers human ligament	154.9	
Race [137]	Anterolateral fibers of human PCL	248	
	posteromedial fibers of human PCL	145	
Quapp [138]	Longitudinal ligament	38.6	
	Transverse ligament	1.7	
Chandrashekar [139]	ACL total	113	
	Male	128	
	Female	99	
Wang [140]	Cartilage	10	0.05– 0.45
	Menisci	20–140	0.2
Pena [85]	Cartilage	5	0.46
	Menisci	59	0.49
	ACL	1.95	
	PCL	3.25	
	MCL	1.44	
	LCL	1.44	
Pen˜a [114]	Cartilage	5	0.46
	Menisci	59	0.49

	ACL	5.83	
	PCL	6.06	
	MCL	6.43	
	LCL	6.06	
Guo [141]	Cartilage	5	0.45
	Menisci	59	0.46
Mootanah [115]	Cartilage	25	0.45
	Menisci	20–120	0.2-0.3
	ACL	154	
	PCL	40	
	MCL	43	
	LCL	56	
Kazemi [116]	Cartilage	0.26– 1600	0.36
	Menisci	0.5–28	0.36
	ACL	10–14,000	
	PCL	10–14,000	
	MCL	10–14,000	
	LCL	10–14,000	
Kazemi [142]	Cartilage	0.41–367.14	
	Menisci	0.0–12.84	
	ACL	46.47–1118.60	
	PCL	46.47–1118.60	
	MCL	46.47–1118.60	
	LCL	46.47–1118.60	
Donlagic [143]	Cartilage	67.6	0.3
	Menisci	130	0.3
	ACL	200–260	

	PCL	200–260	
	MCL	114–134	
	LCL	114–134	
Li [144]	Cartilage	3.5–10	0.45
Li [96]	Cartilage	5	0.45
Blankevoort [97]	Cartilage	5	0.45
Blankevoort [92]	Cartilage	5	0.45
Bendjaballah [98]	Cartilage	12	0.45
	Menisci	8–15	0.45
Bendjaballah [2]	Cartilage	12	0.45
	Menisci	8–15	0.45
Bendjaballah [145]	Cartilage	12	0.45
	Menisci	8–15	0.45
Jilani [146]	Cartilage	12	0.45
	Menisci	8–15	0.45
Moglo [147]	Cartilage	12	0.45
	Menisci	8–15	0.45
Shirazi [148]	Cartilage	12	0.45
	Menisci	8–15	0.45
Yang [149]	Cartilage	15	0.45
	Menisci	20–140	0.2–0.3
Beillas [150]	Cartilage	20	0.45
	Menisci	250	0.45
	ACL	150	
	PCL	150	
	MCL	60	
	LCL	60	

Asgari [151]	Cartilage	5	0.46
	Menisci	250	0.3
	ligament	345	0.22
lance franzer [152]	Cartilage	50	0.45
	Menisci	20,120	0.3,0.45
	ligament	300	0.3
Kang [153]	Cartilage	15	0.47
	Menisci	20,120	0.20,0.3
Silvia [154]	Cartilage	13	0.475
	Menisci	53	0.49
	ACL	169	0.45
	PCL	177	0.45
	MCL	362	0.45
	LCL	228	0.45

The tibia, femur, patella, and fibula were set to have rigid stiffness behaviour as this would maximise the effect on the soft tissue of the bony topology variation. This was considered a valid assumption as bones have much higher stiffness compare to soft tissues [155]. As rigid bodies do not deform, this assumption also simplified the numerical problem during finite element simulation and reduced the computational time and storage requirements.

Bodies can pass through each other by default in Ansys, so it was essential to add a contact definition between the tissues to prevent penetration [156]. However, the tibia and femur should not be in contact directly, as there are intervening soft tissues. Nevertheless, a “no separation” contact between tibia and femur was selected which allows the two bone to slide without resistance, but they cannot separate [131, 157]. This extra contact is defined in case of movement or applied force the tibia and femur contact each other.

“Bonded” contact was selected between the tibia and fibula, tibia and soft tissue, femur and soft tissue, patella and soft tissue, fibula and soft tissue, so that the respective objects can neither separate nor slide at the contact interface. The contact body was the soft tissue and the target body was the bones, with asymmetric behaviour, (rigid bodies can only have asymmetric behaviour) (Figure 88Figure 88).

A nominal force of 1N is applied vertically to the tibia to compress the joint space. (Figure 89Figure 89). This force was chosen to keep the analysis simple, but any differences due to topology should be visible numerically as a percentage difference. Further, a low force gives the maximum opportunity for the convergence of a solution, which may be problematic given the large number of contact interfaces, and reduces the strain in each element, which is also computationally advantageous. A fixed boundary condition was imposed on the femur, fixing it in 6 degrees of freedom. The tibia, fibula, patella and soft tissue had no boundary conditions imposed and were unconstrained.

The finite element analysis was applied to two differently-segmented knee joints, as described in chapter six. All the boundary conditions, force and variable items remain same, with the only difference be as the difference in the two segmentations.

The geometries were automatically meshed in Ansys using a combination of elements with tetrahedral ‘tet4’ elements. The model contained 43956 nodes and 206503 elements in total (Figure 87Figure 87). In order to construct a coherent, contiguous and solvable mesh, some smoothing of the mesh was automatically conducted, using default settings, during the meshing operation. It is likely that mesh smoothing would be conducted in every FE analysis and so, whilst this step seems to affect the differences between the meshes, precisely what this analysis is trying to investigate, it is an integral part of FE analysis and unavoidable. This analysis is therefore seeking to identify differences in the outputs despite this mesh smoothing. We expect the mesh smoothing to lessen the differences between the two models, although the final nodal structures of the meshes have not been analysed.

In case of large localised deformation, large deflection analysis was enabled. A mesh convergence analysis was not conducted as we were computing similar mesh densities

but with slightly different geometries. The analysis took approximately 30 minutes to compute, and the mesh.

Total deformation and von Mises stress and strain were the considered outputs of the model, chosen to give a single indicative value for the mechanics at any given point.

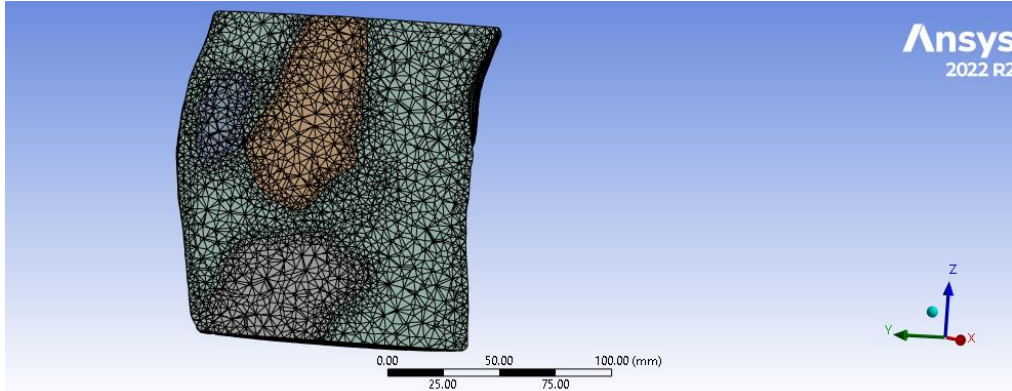


Figure 87. Meshing of the model in Ansys

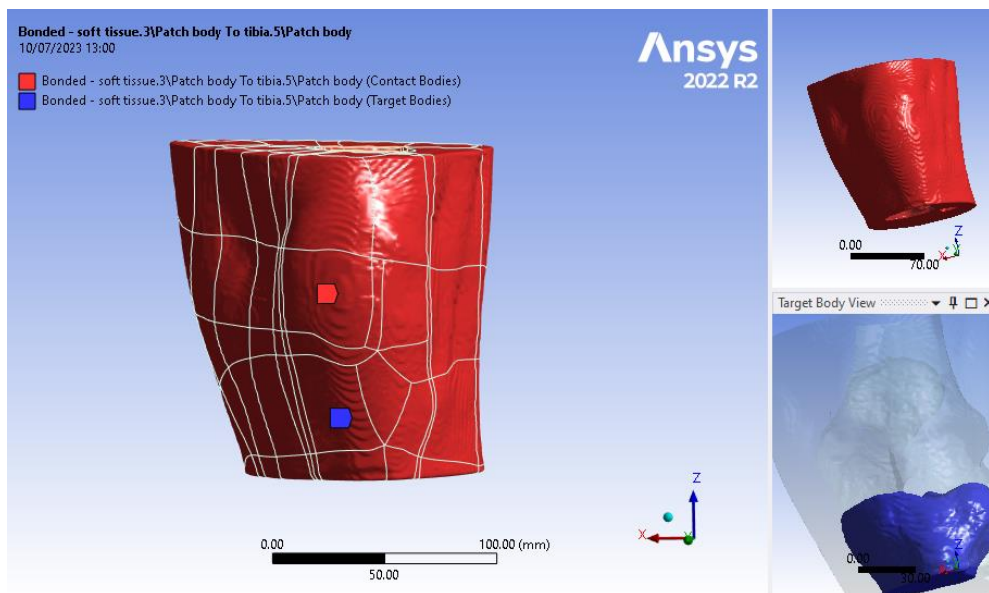


Figure 88. Contact between tibia and soft tissue.

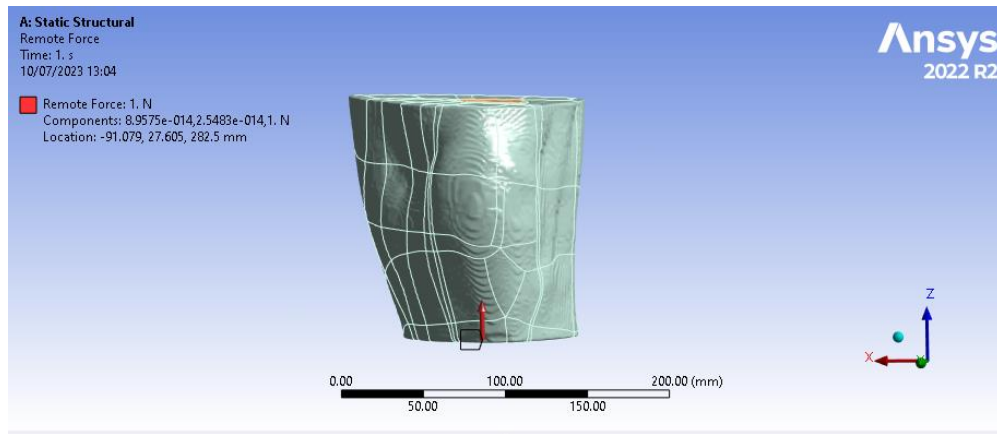


Figure 89. Applied force on z axis of tibia

## 7.2 Results

Before analysing the Ansys results, this section describes the small difference between the two knee joints prior to importing into Ansys. Figure 90 illustrates the difference between the two segmented knees, with the maximum Euclidian difference calculated in CloudCompare as 5.57 mm (Figure 91). These figures show that the femurs are similarly segmented, but the extremities of the tibial plateau and fibula head are the regions that show the greatest differences.

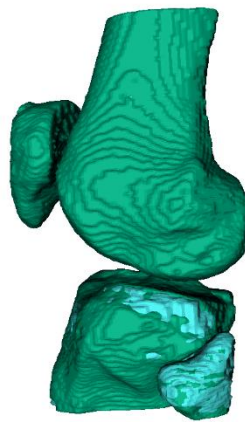


Figure 90. The green knee is first segmented knee and blue knee is second

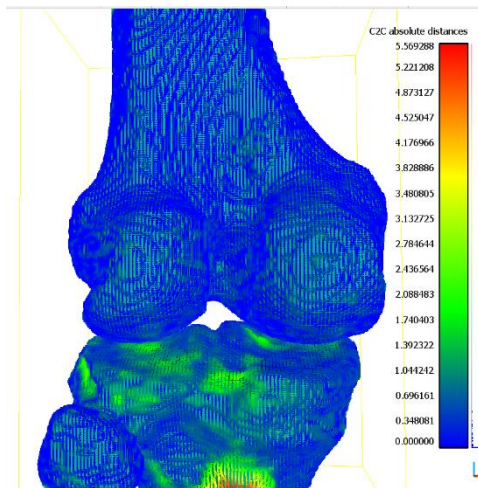


Figure 91. C2C distance of two knee

Figure 92 shows the von Mises strain of the soft tissue following the applied force on the tibia. One knee had a maximum of  $1.42\mu\epsilon$  (Figure 92), whilst the other a value of  $2.43\mu\epsilon$  (Figure 94), a difference of 71%.

With regards to von Mises stress, the maximum stress for the one knee was 637 Pa and the other 728 Pa, corresponding to a 14.2 % difference. The maximum stress and strain on both knees is in the soft tissue between femur and tibia (Figure 92-Figure 95), where the articular cartilage is.

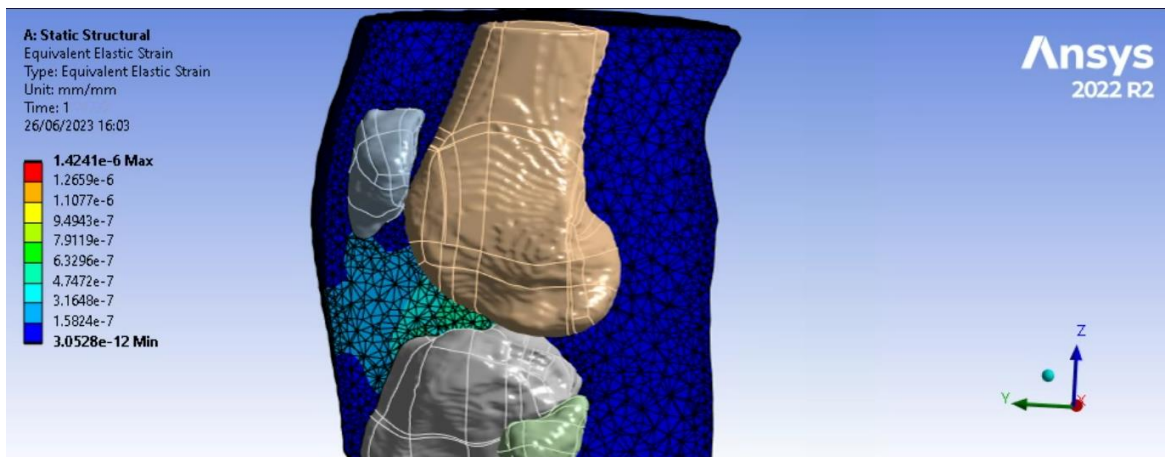


Figure 92. Elastic strain on Soft tissue of first segmentation

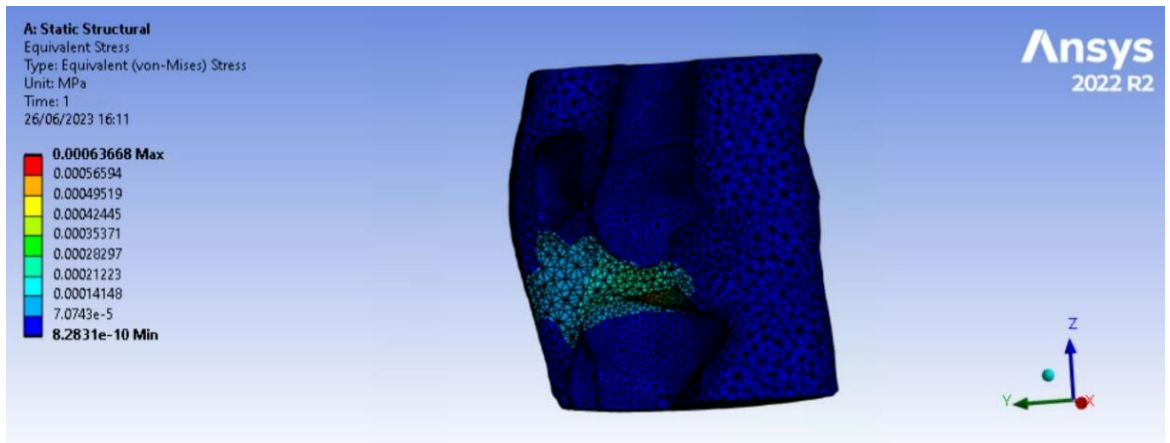


Figure 93.von-Mises stress on soft tissue for first segmentation

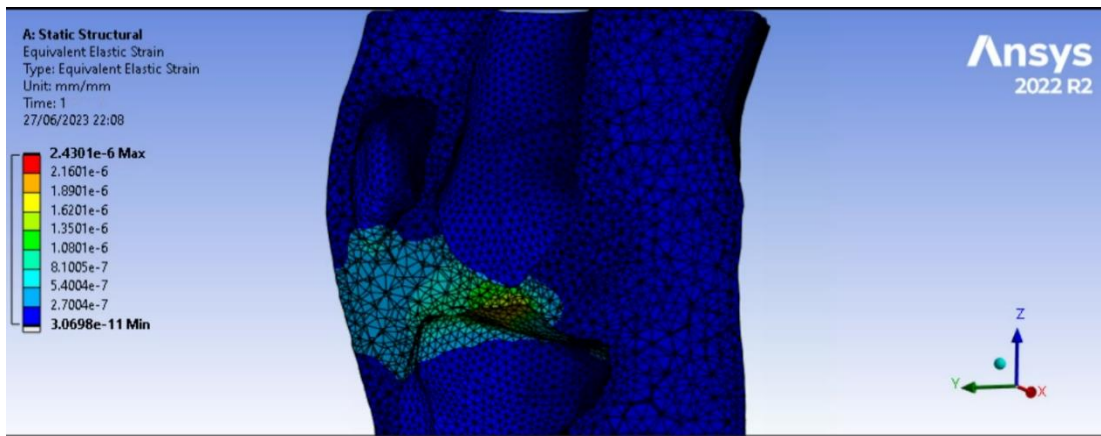


Figure 94. Elastic strain on Soft tissue for second segmentaion

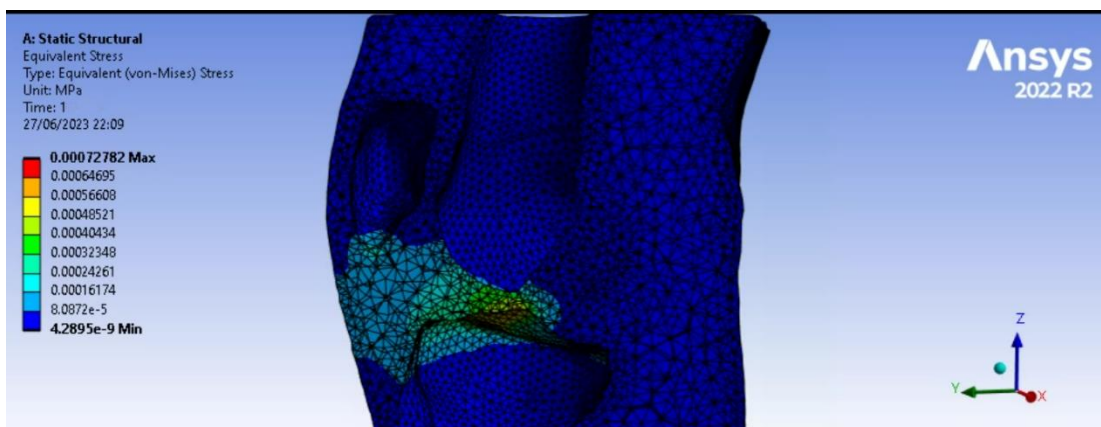


Figure 95. Von-Mises Stress on Soft tissue for second segmentation

### 7.3 Discussion

The goal of the current study is achieved which was to introduce a unique method that makes use of simplified soft tissue representations along with finite element analysis to overcome the problems with traditional knee joint modelling. The outcomes of this innovative approach offer insightful information about how the knee joint structures behave in various segmentation circumstances.

The examination of the impact of small differences in knee joint segmentation on simulation results produced interesting findings. The observed variations in the distribution of strain and stress between two subsequent segmentations by the same operator highlight how sensitive simulation results are to segmentation variations. The experiment showed that even little variations in the delineation of structures can result in significant variations in the expected mechanical response. The reliability and repeatability of simulation-based research must be carefully considered about the maximum strain variation that can be up to twice as great between the two segmentations.

5.6mm of variation in the 3D model made by operator caused elastic strain applied on the soft tissue to increase by 71%. This sensitivity of the system, emphasizing the critical impact of operator-induced variations on the biomechanical outcomes.

These results are in line with Arjmand [4] paper in utilizing a cylinder of tissue with an isotropic homogeneous material to model soft tissue of the knee joint. They incorporate subject-specific bone density-modulus mappings for proximal tibia from 1MPa to 25 GPa. Also, they modelled the femur bones with isotropic linear material properties  $E = 500\text{GPa}$  and a Poisson's ratio of 0.3; while we used rigid body material for all bones which is impeded in the Ansys software, this may be because of the difference of Abaqus software they used.

Although, we both chose the homogeneous, incompressible, and isotropic material for soft tissue but they chose young's modulus of 10Mpa for it, and ours is 1MPa.

We subjectively modelled it from a patient CT image and it is actual knee model of the patient. So it is more complex model than their, especially with presence of patella which they removed it from image. (Figure 96)

They used bonded contact between bone (the femur, tibia and fibula) and the soft tissue cylinder same as ours. We both highlight the sensitivity of FE model outcomes to small variations in factors like segmentation.

They fixed the proximal femur in all directions except the longitudinal axis of femur, which a uniform displacement of 1mm applied, while we fully fixed femur and applied 1N force on distal tibia.

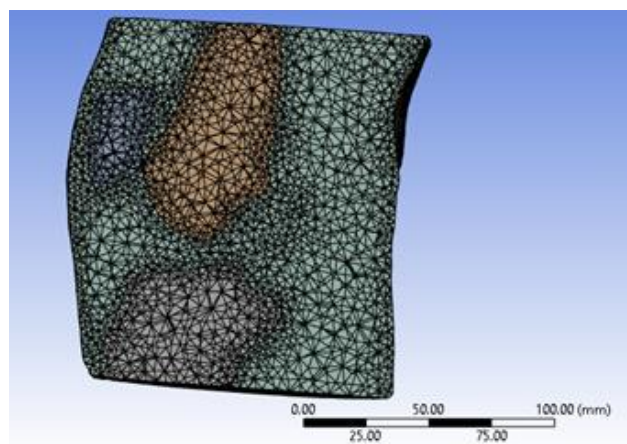


*Figure 96. Right ours knee joint model*

### **Clinical Implications**

The findings of this study have significant implications for clinical and research applications. The observed sensitivity to segmentation highlights the necessity for accurate and standardized segmentation techniques given the difficulties in precisely identifying soft tissue features and delineating anatomical structures in imaging data. Clinically, this work emphasises the significance of precise picture segmentation in patient-specific simulations, especially when therapy planning or intervention evaluation are involved. The variations identified in the study highlight the necessity of extensive validation and sensitivity analysis in patient-specific simulations to take into account any potential uncertainties in the segmentation process.

### **Further investigation**

The use of simplified soft tissue models in this study opens up an amazing new area for investigation. Future research could examine the relationship between the accuracy of predictions made using more complicated and anatomically accurate models versus the computational efficiency gained by utilizing simplified models. Additionally, attempts to improve segmentation procedures' automation and standards might reduce the effects of operator-dependent variability.

### **Limitations**

It is vital to recognize that this study has several limitations. Despite being logical, the material properties chosen for soft tissues might not accurately represent the wide range of mechanical behaviours experienced in reality. Additionally, the limited generalization of the results is due to the small sample size of two knees. Additional research with bigger sample numbers might offer a more thorough understanding of the effects of segmentation variability.

The other limitation was the default mesh smoothing. To ensure the creation of a unified and solvable mesh, automated mesh smoothing was implemented during the meshing process, utilizing default settings. Mesh smoothing is a standard practice in finite element (FE) analysis, aimed at enhancing mesh coherence and stability. While this process may influence the variations between meshes, which is the focal point of this analysis, it remains an inevitable aspect of FE analysis.

This study aims to discern discrepancies in outcomes despite the application of mesh smoothing. It is anticipated that mesh smoothing will reduce differences between the two models, although a detailed examination of the final nodal structures of the meshes has not been conducted.

### **7.4 Conclusion**

In summary, this study presents a unique method for modelling knee joints that combines simplified soft tissue models with finite element analysis. The study of segmentation variability's impact highlights how sensitive simulation results are to even minor segmentation variations. These results highlight the necessity of careful validation in patient-specific simulations and conventional segmentation techniques.

## References

1. Davis, K. *How to prevent and treat knee injuries*. 2017 [cited 2023; Available from: <https://www.medicalnewstoday.com/articles/299204>.
2. Bendjaballah M, S.-A.A., Zukor D, *Finite element analysis of human knee joint in varus-valgus*. *Clinical Biomechanics*, 1997. **12**(3): p. 139-148.
3. Jun Sun, S.Y., Yan Jiang, Duo Wai-chi Wong, Ming Zhang, Jizhou Zeng, Kuan Zhang, *Finite element analysis of the valgus knee joint of an obese child*. *BioMed Eng OnLine*, 2016. **15**(3): p. 310-321.
4. Arjmand, H., et al., *Mechanical Metrics of the Proximal Tibia are Precise and Differentiate Osteoarthritic and Normal Knees: A Finite Element Study*. *Sci Rep*, 2018. **8**(1): p. 11478.
5. McErlain, D.D., et al., *Subchondral cysts create increased intra-osseous stress in early knee OA: A finite element analysis using simulated lesions*. *Bone*, 2011. **48**(3): p. 639-46.
6. Ahn, L. *Pediatric Knee Trauma Radiographic Evaluation*. 2021 [cited 2024; Available from: <https://www.orthobullets.com/pediatrics/322103/pediatric-knee-trauma-radiographic-evaluation>.
7. A E Ellison, E.E.B., *Embryology, anatomy, and function of the anterior cruciate ligament* *Orthop Clin North Am*, 1985. **1**(16): p. 3-14.
8. Pallavi Juneja , J.B.H., *Anatomy, Bony Pelvis and Lower Limb, Knee Medial Collateral Ligament*. StatPearls [Internet]. Treasure Island (FL): StatPearls Publishing, 2022.
9. Sprouse RA, M.A., Harris GD, *Braces and Splints for Common Musculoskeletal Conditions*. *Am Fam Physician*, 2018. **15**(10): p. 570-576.
10. Tadlock BA, P.L., Covassin T, Caswell SV, Lincoln AE, Kerr ZY, *Epidemiology of knee internal derangement injuries in United States high school girls' lacrosse, 2008/09-2016/17 academic years*. *Res Sports Med*, 2018(14): p. 1-12.
11. Anoka, N.N., J. *Consideration of growth factors and bio-scaffolds for treatment of combined grade II MCL and ACL* 2011; Available from: [https://www.researchgate.net/figure/Deep-and-superficial-MCL-and-ACL-double-bundle-anatomy\\_fig1\\_51560386](https://www.researchgate.net/figure/Deep-and-superficial-MCL-and-ACL-double-bundle-anatomy_fig1_51560386).
12. Waldman, S.D. *Medial Collateral Ligament Syndrome*. 2019; Available from: <https://www.sciencedirect.com/topics/medicine-and-dentistry/medial-collateral-ligament>.
13. Hinkle, C.Z., *Fundamental of anatomy and movement : a workbook and guide*. 1997: St. Louis 288.
14. Scott, W.N., *The Knee*. Vol. 2. 1994: St. Louise : Mosby-Year Book. 1481.
15. SINGH, A.P. *Knee Range of Motion and Movements*. 2013 [cited 2019; Available from: <https://boneandspine.com/knee-range-of-motion/>.
16. Parks, M. *Muscles Legs and Hips*. 2018; Available from: <https://slideplayer.com/slide/13080093>.
17. Duggan, C. *Muscle chart*. 2015; Available from: <http://www.massagelongbeachca.com/muscle-chart/>.
18. Bryceland JK, P.A., Nunn T, *Knee Menisci*. *Cartilage*, 2017. **8**(2): p. 99-104.

19. MESSNER, K.G., J, *The menisci of the knee joint. Anatomical and functional characteristics, and a rationale for clinical treatment.* Anatomy, 1998: p. 161-178.
20. Hirschmann, M.M.I., W, *Complex function of the knee joint: The current understanding of the knee.* Knee Surg. Sports Traumatol. Arthrosc, 2015. **23**: p. 2780-2788.
21. M. van der Esch, M.S., J. Harlaar, N. Wolterbeek, D. L. Knol, J. Dekker, *Knee varus-valgus motion during gait- a measure of joint stability in patients with osteoarthritis?* Elsevier, Osteoarthritis and Cartilage, 2008(16): p. 522-525.
22. Haviv, B.B., S.; Kosashvili, Y.; Thein, R, *Which patients are less likely to improve during the first year after arthroscopic partial meniscectomy? A multivariate analysis of 201 patients with prospective follow-up.* Knee Surg. Sports Traumatol. Arthrosc, 2016. **24**: p. 1427-1431.
23. A. Bintoudi, K.N., and I. Tsitouridis, *Anterior and Posterior Menisiofemoral Ligaments: MRI Evaluation.* Anatomy Research International, 2012. **2012**.
24. PS, C., *Bursae around the knee joints.* Indian J Radiol Imaging, 2012. **22**: p. 27-30.
25. Jones, O. *The knee joint* 2018; Available from: <https://teachmeanatomy.info/lower-limb/joints/the-knee-joint>.
26. Zatsiorsky, V.M., *Kinematics of human motion.* 1998: Champaign, IL : Human Kinetics. 419.
27. Wallace, D.T., P.E. Riches, and F. Picard, *The assessment of instability in the osteoarthritic knee.* EFORT Open Rev, 2019. **4**(3): p. 70-76.
28. Nguyen U-SDT, F.D., Niu J, et al, *The impact of knee instability with and without buckling on balance confidence, fear of falling and physical function: The Multicentre Osteoarthritis Study.* Osteoarthr Cartil, , 2014. **22**(4): p. 527-534.
29. Gollehon, D.L.T., P.; Warren, R, *The role of the posterolateral and cruciate ligaments in the stability of the human knee. A biomechanical study.* J. Bone Jt. Surg, 1987. **69**: p. 233-242.
30. Ellison, A.B., E, *Embryology, anatomy, and function of the anterior cruciate ligament.* Orthop. Clin. N. Am, 1985. **16**: p. 3-14.
31. PROMs Analytical Team, N.D. *Finalised Patient Reported Outcome Measures (PROMs) in England for Hip & Knee Replacements, April 2018 – March 2019.* 13 Feb 2020 21 February 2022 5:39 pm; Available from: <https://digital.nhs.uk/data-and-information/publications/statistical/patient-reported-outcome-measures-proms/finalised-hip--knee-replacements-april-2018--march-2019/author-copyright-licensing>.
32. Robertsson O, D.M., Pehrsson T, Knutson K, Lidgren L, *Patient satisfaction after knee arthroplasty A report on 27,372 knees operated on between 1981 and 1995 in Sweden.* Acta Orthop Scand, 2000. **3**(71): p. 262–267.
33. Naoki Nakano, e.a., *Why are patients dissatisfied following a total knee replacement? A systematic review.* International Orthopaedics, 8 July 2020. **44**: p. 1971–2007.
34. TheKneeDoc. *Robotic knee replacement surgery: How does it work, and what are the benefits?* 2021 [cited 2022 29/09/2022]; Available from:

<https://www.thekneedoc.co.uk/robotic-knee-replacement-surgery-how-does-it-work-and-what-are-the-benefits/>.

35. Bae, D.K. and S.J. Song, *Computer assisted navigation in knee arthroplasty*. Clin Orthop Surg, 2011. **3**(4): p. 259-67.
36. Haritnian, E.G. and A.L. Pimpalnerkar, *Computer Assisted Total Knee Arthroplasty: Does it Make a Difference?* Maedica (Bucur), 2013. **8**(2): p. 176-81.
37. Kobayashi, A., et al., *Comparison of analog 2D and digital 3D preoperative templating for predicting implant size in total knee arthroplasty*. Comput Aided Surg, 2012. **17**(2): p. 96-101.
38. Kumar, P., et al., *Application of 3D Printing in Hip and Knee Arthroplasty: A Narrative Review*. Indian J Orthop, 2021. **55**(Suppl 1): p. 14-26.
39. Guo, Y. and A.S. Ashour, *Neutrosophic sets in dermoscopic medical image segmentation*, in *Neutrosophic Set in Medical Image Analysis*. 2019. p. 229-243.
40. Cook, D.J., et al., *Variability of manual lumbar spine segmentation*. Int J Spine Surg, 2012. **6**: p. 167-73.
41. Engelbrecht, W.P., et al., *The influence of the segmentation process on 3D measurements from cone beam computed tomography-derived surface models*. Clin Oral Investig, 2013. **17**(8): p. 1919-27.
42. Luca Friedli, D.K., Georgios Kanavakis, Demetrios Halazonetis, Nikolaos Gkantidis, *The effect of threshold level on bone segmentation of cranial base structures from CT and CBCT images*. Scientific Reports, 2020. **10**(7361).
43. Luzon, J.A., et al., *Semi-automated vs. manual 3D reconstruction of central mesenteric vascular models: the surgeon's verdict*. Surg Endosc, 2020. **34**(11): p. 4890-4900.
44. Rathnayaka, K., et al., *Effects of CT image segmentation methods on the accuracy of long bone 3D reconstructions*. Med Eng Phys, 2011. **33**(2): p. 226-33.
45. Bankman, I.N., *Handbook of Medical Image Processing and Analysis [internet Resource]*. 2009, Amsterdam : Elsevier.
46. Yushkevich, P.A., et al., *User-guided 3D active contour segmentation of anatomical structures: significantly improved efficiency and reliability*. Neuroimage, 2006. **31**(3): p. 1116-28.
47. Liang, X., et al., *A comparative evaluation of Cone Beam Computed Tomography (CBCT) and Multi-Slice CT (MSCT). Part II: On 3D model accuracy*. Eur J Radiol, 2010. **75**(2): p. 270-4.
48. Wang, L., et al., *Automated bone segmentation from dental CBCT images using patch-based sparse representation and convex optimization*. Med Phys, 2014. **41**(4): p. 043503.
49. Loubele, M., et al., *Image quality vs radiation dose of four cone beam computed tomography scanners*. Dentomaxillofac Radiol, 2008. **37**(6): p. 309-18.
50. Hassan, B., et al., *Influence of scanning and reconstruction parameters on quality of three-dimensional surface models of the dental arches from cone beam computed tomography*. Clin Oral Investig, 2010. **14**(3): p. 303-10.

51. Fourie, Z., et al., *Segmentation process significantly influences the accuracy of 3D surface models derived from cone beam computed tomography*. Eur J Radiol, 2012. **81**(4): p. e524-30.
52. Vandenberghe, B., S. Luchsinger, J. Hostens, E. Dhoore, and R. Jacobs. , *The Influence of Exposure Parameters on Jawbone Model Accuracy Using Cone Beam CT and Multislice CT*. Dento-maxillo-facial Radiology 2012. **41**(6): p. 466-74.
53. Ya-bo Yan, W.q.T.-x.q., Ee-Chon Teo, Wei Lei, *The effect of threshold value on the architectural parameters and stiffness of human cancellous bone in micro CT analysis*. Journal of Mechanics in Medicine and Biology, 2012. **12**(05).
54. Gitto, S., et al., *Effects of Interobserver Variability on 2D and 3D CT- and MRI-Based Texture Feature Reproducibility of Cartilaginous Bone Tumors*. J Digit Imaging, 2021. **34**(4): p. 820-832.
55. Zimmerman, J.N., S.R. Vora, and B.T. Pliska, *Reliability of upper airway assessment using CBCT*. Eur J Orthod, 2019. **41**(1): p. 101-108.
56. Chen, M.Y., et al., *Variability in accuracy of prostate cancer segmentation among radiologists, urologists, and scientists*. Cancer Med, 2020. **9**(19): p. 7172-7182.
57. I. H. Parkinson, A.B.a.N.L.F., *Variation in segmentation of bone from micro-CT imaging: implications for quantitative morphometric analysis*. Australasian Physical & Engineering Sciences in Medicine, 2008. **31**(2): p. 160-4.
58. Li, J., et al., *Medical image segmentation in oral-maxillofacial surgery*, in *Computer-Aided Oral and Maxillofacial Surgery*. 2021. p. 1-27.
59. Luccichenti, G., et al., *3D reconstruction techniques made easy: know-how and pictures*. Eur Radiol, 2005. **15**(10): p. 2146-56.
60. Soininvaara, T., et al., *Measurement of bone density around total knee arthroplasty using fan-beam dual energy X-ray absorptiometry*. Calcif Tissue Int, 2000. **67**(3): p. 267-72.
61. Pouch, A. *ITK-SNAP User Training, Session 5: Automatic Segmentation*. 2013; Available from: [https://www.youtube.com/watch?v=4Qzm3kIZJIU&t=338s&ab\\_channel=ITK-SNAP](https://www.youtube.com/watch?v=4Qzm3kIZJIU&t=338s&ab_channel=ITK-SNAP).
62. Broder, J. and R. Preston, *Imaging the Head and Brain*, in *Diagnostic Imaging for the Emergency Physician*. 2011. p. 1-45.
63. Dice, L.R., *Measures of the Amount of Ecologic Association Between Species*. Wiley on behalf of the Ecological Society of America, 1945. **26**(3): p. 297-302.
64. Kitamura, A.D.Y.D.L.C.I.P.F., *Deep Learning in Neuroradiology: A Systematic Review of Current Algorithms and Approaches for the New Wave of Imaging Technology*. Radiology: Artificial Intelligence, 2020. **2**(2).
65. VARUN, Y. *Understanding DICE COEFFICIENT*. 2020; Available from: <https://www.kaggle.com/code/yerramvarun/understanding-dice-coefficient>.
66. Jeroen Bertels, T.E.B., Maxim Berman, Dirk Vandermeulen, Frederik Maes, Raf Bisschops, Matthew B. Blaschko, *Optimizing the Dice Score and Jaccard Index for Medical Image Segmentation Theory and Practice*, in *MICCAI*

- 2019, LNCS 11765 22nd International Conference, D.S.e. al, Editor. 2019, Springer Nature Switzerland AG 2019: Shenzhen, China. p. 92–100.
67. Girardeau-Montaut, D., *CloudCompare v2.12 alpha*. 2020.
  68. Lao, Y. *Ocree*. Open3D: A Modern Library for 3D Data Processing 2019; Available from: <http://www.open3d.org/docs/latest/tutorial/geometry/octree.html>.
  69. Jain, M.-P.D.a.A.K., *A Modified Hausdorff Distance for object Matching*. Proc. International Conference on Pattern Recognition, 1994: p. 566-568.
  70. Rote, G., *computing the minimum Hausdorff distance between two point sets on a line under translation*. Information processing letters, 1991. **38**: p. 123-127.
  71. Simon K. Warfield, K.H.Z., and William M. Wells., *Simultaneous Truth and Performance Level Estimation (STAPLE): An Algorithm for the Validation of Image Segmentation*. IEEE TRANSACTIONS ON MEDICAL IMAGING, 2004. **23**(7): p. 903-921.
  72. Yu, H.J., et al., *Comparative study of intra-operator variability in manual and semi-automatic segmentation of knee cartilage*. Osteoarthritis and Cartilage, 2016. **24**: p. S296-S297.
  73. Argüello, D., H.G. Sánchez Acevedo, and O.A. González-Estrada, *Comparison of segmentation tools for structural analysis of bone tissues by finite elements*. Journal of Physics: Conference Series, 2019. **1386**(1).
  74. Soodmand, E., et al., *Interlaboratory comparison of femur surface reconstruction from CT data compared to reference optical 3D scan*. Biomed Eng Online, 2018. **17**(1): p. 29.
  75. Ataei, A., et al., *Evaluation of inter- and intra-operator reliability of manual segmentation of femoral metastatic lesions*. Int J Comput Assist Radiol Surg, 2021. **16**(10): p. 1841-1849.
  76. Misselyn, D., et al., *Intra- and inter-observer reliability of measurements on 3D images of the calcaneus bone*. Comput Methods Biomech Biomed Engin, 2021. **24**(5): p. 579-583.
  77. Königsberg, B., et al., *Inter- and intraobserver reliability of two-dimensional CT scan for total knee arthroplasty component malrotation*. Clin Orthop Relat Res, 2014. **472**(1): p. 212-7.
  78. Zhuang, M., et al., *Variability and Repeatability of Quantitative Uptake Metrics in (18)F-FDG PET/CT of Non-Small Cell Lung Cancer: Impact of Segmentation Method, Uptake Interval, and Reconstruction Protocol*. J Nucl Med, 2019. **60**(5): p. 600-607.
  79. Loubele, M., et al., *Assessment of bone segmentation quality of cone-beam CT versus multislice spiral CT: a pilot study*. Oral Surg Oral Med Oral Pathol Oral Radiol Endod, 2006. **102**(2): p. 225-34.
  80. Lo Giudice, A., et al., *Evaluation of Imaging Software Accuracy for 3-Dimensional Analysis of the Mandibular Condyle. A Comparative Study Using a Surface-to-Surface Matching Technique*. Int J Environ Res Public Health, 2020. **17**(13).
  81. Van den Broeck, J., et al., *Segmentation accuracy of long bones*. Med Eng Phys, 2014. **36**(7): p. 949-53.

82. Koo, T.K. and M.Y. Li, *A Guideline of Selecting and Reporting Intraclass Correlation Coefficients for Reliability Research*. J Chiropr Med, 2016. **15**(2): p. 155-63.
83. N. A. Ahmad, S.P., K. Amudha, M. K. A. Ahmed Khan, I, *Elamvazuthi, Biomechanics of Hip, Knee and Ankle joint loading during ascent and descent walking*. Procedia Computer Science, 2014. **42**: p. 336-344.
84. Kumar Sahu, N.K., Ajay, *A Review of Use FEM Techniques in Modeling of Human Knee Joint*. JBBBE, 2016. **28**: p. 14-25.
85. Pena, E.B., Calvo, M.A., Martinez, M., Doblare, *A three-dimensional finite element analysis of the combined behaviour of ligaments and menisci in the healthy human knee joint*. Journal of Biomechanics, 2006. **30**: p. 1686-1701.
86. X. Zhang, R.Z.G., *Experimental measurement and modelling analysis on mechanical properties of inuostapedial joint*. Biomech. Model. Mechanobio, 2011. **110**: p. 713-726.
87. P. K. Tomaszewski, N.V., S.K. Bulstra, G.J. Verkerke, *A comparative finiteelement analysis of bone failure and load transfer of osseointegrated prostheses fixations*. Ann. Biomed. Eng, 2010. **38**: p. 2418-2427.
88. S. Farrokhi, J.H.K., C.M, Powers, *Individuals with patellofemoral pain exhibit greater patella femoral joint stress: a finite element analysis study*. Osteoarthr.Cartilage, 2011. **19**: p. 287-294.
89. Wismans, J.A.C., *A three-dimensional mathematical model of the knee-joint*. Journal of Biomechanics, 1980. **13**(8).
90. Andriacchi, T.P., *Model studies of the stiffness characteristics of the human knee joint*. Journal of Biomechanics, 1983. **16**(1): p. 23-29.
91. Essinger, J.R., *A mathematical model for the evaluation of the behaviour during flexion of condylar-type knee prostheses*. Journal of Biomechanics, 1989. **22**(11-12): p. 1229-1241.
92. Blankevoort, L., & Huiskes, R, *Ligament-bone interaction in a three-dimensional model of the knee*. Journal of Biomechanical Engineering, 1991. **113**(3): p. 263-269.
93. Haut, T.L., Hull, M. L., & Howell, S. M, *A high accuracy three-dimensional coordinate digitizing system for reconstructing the geometry of diarthrodial joints*. ASME-PUBLICATIONS-BED, 1997. **36**: p. 17-18.
94. Donahue, T.L.H., *A finite element model of the human knee joint for the study of tibio-femoral contact*. Journal of Biomechanical Engineering, 2002. **124**(3): p. 273-280.
95. Schütz, U.H.W., *The Transeurope footrace project: Longitudinal data acquisition in a cluster randomized mobile MRI observational cohort study on 44 endurance runners at a 64-stage 4,486 km transcontinental ultramarathon*. BMC Medicine,, 2012. **10**(1): p. 78.
96. Li G, G.J., Kanamori A, Woo S, *A validated three-dimensional computational model of a human knee joint*. Journal of Biomechanical Engineering, 1999. **121**(6): p. 657-662.
97. Blankevoort L, K.J., Huiskes R, Grootenboer H, *Articular contact in a three-dimensional model of the knee*. Journal of Biomechanics, 1991. **24**(11): p. 1019-1031.

98. Bendjaballah MZ, S.-A.A., Zukor D, *Biomechanics of the human knee joint in compression: reconstruction, mesh generation and finite element analysis*. Knee, 1995. **2**(2): p. 69-79.
99. Maffulli, N., *Laxity versus Instability*. Orthopedics, 1998. **21**(8): p. 837-842.
100. Rohita R. Patel, D.E.H., Charles A. Bush-Joseph, Bernard R. Bach, Jr, and Thomas P. Andriacchi., *Comparison of Clinical and Dynamic Knee Function in Patients with Anterior Cruciate Ligament Deficiency*. The American Journal of Sports Medicine 2003. **31**(1): p. 68-74.
101. Küpper, J.C., Loitz-Ramage, B, Corr, D.T, Hart, D.A, and Ronsky, J.L, *Measuring Knee Joint Laxity: A Review of Applicable Models and the Need for New Approaches to Minimize Variability*. Clinical Biomechanics, 2006. **22**(1): p. 1-13.
102. Mononen M, J.P., To"yra"s J, Jurvelin J, Kiviranta I, Korhonen R, *Alterations in structure and properties of collagen network of osteoarthritic and repaired cartilage modify knee joint stresses*. Biomechanics and Modeling in Mechanobiology 2011. **10**(3): p. 357-369.
103. Dabiri Y, L.L., *Influences of the depth-dependent material inhomogeneity of articular cartilage on the fluid pressurization in the human knee*. Medical Engineering & Physics 2013. **35**(11): p. 1591-1598.
104. Meng Q, J.Z., Wilcox R, Fisher J, *Computational investigation of the time dependent contact behaviour of the human tibiofemoral joint under body weight*. Journal of Engineering in Medicine 2014. **228**(11): p. 1193-1207.
105. Chandrashekar N, M.H., Slaughterbeck J, Hashemi J. 2006. Sex-based differences in the tensile properties of the human anterior cruciate ligament. Journal of Biomechanics 39(16):2943–2950 *Sex-based differences in the tensile properties of the human anterior cruciate ligament*. Journal of Biomechanics 2006. **36**(16): p. 2943-2950.
106. Kleemann R, K.D., Cedraro A, Tuischer J, Duda G, *Altered cartilage mechanics and histology in knee osteoarthritis: relation to clinical assessment (ICRS Grade)*. Osteoarthritis and Cartilage, 2005. **13**(11): p. 958-963.
107. O, L., *Mechanical properties of dried defatted spongy bone*. Acta Orthopaedica Scandinavica 1976. **47**(1): p. 11-19.
108. Woo SL, H.J., Adams DJ, Lyon RM, Takai S. , *Tensile properties of the human femur-anterior cruciate ligament-tibia complex. The effects of specimen age and orientation*. American Journal of Sports Medicine 1991. **19**(3): p. 217-225.
109. Staubli HU, S.L., Brunner P, Rincon L, Nolte LP, *Mechanical tensile properties of the quadriceps tendon and patellar ligament in young adults*. American Journal of Sports Medicine 1999. **27**(1): p. 27-34.
110. Race A, A.A., *The mechanical properties of the two bundles of the human posterior cruciate ligament*. Journal of Biomechanics, 1994. **27**(1): p. 13-24.
111. Shepherd DE, S.B., *The 'instantaneous' compressive modulus of human articular cartilage in joints of the lower limb*. Rheumatology, 1999. **38**(2): p. 124-132.
112. Skaggs D, W.W., Mow V, *Radial tie fibers influence the tensile properties of the bovine medial meniscus*. Journal of Orthopaedic Research, 1994. **12**(2): p. 176-185.

113. LeRoux MA, S.L., *Experimental and biphasic FEM determinations of the material properties and hydraulic permeability of the meniscus in tension*. Journal of Biomechanical Engineering, 2002. **124**(3): p. 315-321.
114. Peña E, C.B., Martinez M, Palanca D, Doblare' M, *Finite element analysis of the effect of meniscal tears and meniscectomies on human knee biomechanics*. Clinical Biomechanics, 2005. **20**(5): p. 498-507.
115. Mootanah R, I.C., Reisse F, Carpanen D, Walker RW, Koff MF, Lenhoff MW, Rozbruch SR, Fragomen AT, Dewan Z, Kirane YM, Cheah K, Dowell JK, Hillstrom HJ, *Development and validation of a computational model of the knee joint for the evaluation of surgical treatments for osteoarthritis*. Computer Methods in Biomechanics and Biomedical Engineering, 2014. **17**(13): p. 1502-1517.
116. Kazemi M, L.L., Savard P, Buschmann M, *Creep behavior of the intact and meniscectomy knee joints*. Journal of the Mechanical Behavior of Biomedical Materials, 2011. **4**(7): p. 1351-1358.
117. Attard, A., *4D CT BASED ANALYSIS OF KNEE KINEMATICS*, in *Biomedical Engineerign*. 2020, University of Strathclyde. p. 485.
118. Toshiba, *Dynamic Volume Imaging - Special Issue*. Toshiba Medical Systems Journal, 2008.
119. Wang, Y., et al., *Different CT slice thickness and contrast-enhancement phase in radiomics models on the differential performance of lung adenocarcinoma*. Thorac Cancer, 2022. **13**(12): p. 1806-1813.
120. Choi, B.S., J.M. Kim, and H.S. Han, *Decision-making factors and their thresholds for total knee arthroplasty in lateral tibiofemoral osteoarthritis patients: a retrospective cohort study*. Knee Surg Relat Res, 2022. **34**(1): p. 41.
121. Goh, T.Y., et al., *Performance analysis of image thresholding: Otsu technique*. Measurement, 2018. **114**: p. 298-307.
122. Varghese, B.A., et al., *Investigating the role of imaging factors in the variability of CT-based texture analysis metrics*. J Appl Clin Med Phys, 2024. **25**(4): p. e14192.
123. Cheryl A. Griffith, M.L.L., *Computer Graphics and the Eigenfunctions for the Koch Snowflake Drum*, in *Progress in Inverse Spectral Geometry*. 1997.
124. Raudaschl, P.F. and P. Zaffino, *Evaluation of segmentation methods on head and neck CT: Auto-segmentation challenge 2015*. Med Phys, 2017. **44**(5): p. 2020-2036.
125. Senat, M.V., et al., *Intra- and interoperator variability in fetal nasal bone assessment at 11-14 weeks of gestation*. Ultrasound Obstet Gynecol, 2003. **22**(2): p. 138-41.
126. R2021a, M., *The MathWorks , Inc.*, Natick, Editor. 2021: Massachusetts, United States.
127. Gupton M, M.A., Kang M. . *Bony Pelvis and Lower Limb: Fibula*. 2023; Available from: Available from: <https://www.ncbi.nlm.nih.gov/books/NBK470591/>.
128. Rose, A., *The Sensitivity Performance of the Human Eye on an Absolute Scale*. J. Opt. Soc, 1948. **38**: p. 196-208.
129. Lisi, M. *CT Radiographic Techniques*. 2024; Available from: <https://www.upstate.edu/radiology/education/rsna/ct/technique.php#:~:text=F>

[or%20a%20quantum%20noise%20limited,resultant%20image%20should%20be%20halved.](#)

130. Nett, B., *X-ray Contrast and Size / Object Detection in Medical Imaging for Techs.* 2022, How Radiology Works. p. 7.39.
131. Halloran, J.P., A.J. Petrella, and P.J. Rullkoetter, *Explicit finite element modeling of total knee replacement mechanics.* J Biomech, 2005. **38**(2): p. 323-31.
132. Anna Gustafsson a, J.S.b., Lorenzo Grassi a, Per Aspenberg b, Hanna Isakssona,\*, *Strains caused by daily loading might be responsible for delayed healing Bone* 2016. **88**: p. 125-130.
133. Peters, *Tissue material properties and computational modelling of the human tibiofemoral joint: a critical review.* PeerJ 2018. **6**(1).
134. Noyes, F. and E. Grood, *The strength of the anterior cruciate ligament in humans and Rhesus monkeys.* 1976. **58**(8): p. 1074-1082.
135. David L. Blw\_Er, M.D.K., Donald C. Stouffer, *Comparison of material properties in fasilcle-bone units from human patellar tendon and knee ligaments.* biomechanics and Modeling in Mechanobiology, 1986. **19**(6): p. 425-432.
136. DAVID L. BUTLER, Y.G., MATTHEW D. KAY, JOHN F. CUMMINGS, and M.S.L. SETH M. FEDER, *Location-dependent variations in the material properties of the anterior cruciate ligament.* biomechanics 1992. **25**(5): p. 511-518.
137. AMIS, A.R.a.A.A., *THE MECHANICAL PROPERTIES OF THE TWO BUNDLES OF THE HUMAN POSTERIOR CRUCIATE LIGAMENT J* biomechanics, 1994. **27**(1): p. 13-24.
138. Quapp K, W.J., *Material characterization of human medial collateral ligament.* Journal of Biomechanical Engineering 1998. **120**(6): p. 757-763
139. Chandrashekar N, M.H., Slauterbeck J, Hashemi J. , *Sex-based differences in the tensile properties of the human anterior cruciate ligament.* Journal of Biomechanics, 2006. **39**(16): p. 2943-2950.
140. Wang, Y., Fan, Y., & Zhang, M, *Comparison of stress on knee cartilage during kneeling and standing using finite element models.* Medical Engineering & Physics, 2014. **36**(4): p. 439-447.
141. Guo Y, Z.X., ChenW. , *Three-dimensional finite element simulation of total knee joint in gait cycle.* Acta Mechanica Solida Sinica 2009. **22**(4): p. 347-351
142. Kazemi M, L.L., *Aviscoelastic poromechanical model of the knee joint in large compression.* Medical Engineering & Physics 2014(8): p. 998-1006.
143. Donlagic D, C.B., Heric D, Cibula E, Zazula D, Potocnik B, *A patient-specific knee joint computer model using MRI data and 'in vivo' compressive load from the optical force measuring system.* Journal of Computing and Information Technology 2008. **16**(3): p. 209-222.
144. Li G, L.O., Rubash H, *Variability of a three-dimensional finite element model constructed using magnetic resonance images of a knee for joint contact stress analysis.* Journal of Biomechanical Engineering, 2001. **123**(4).

145. Bendjaballah M, S.-A.A., Zukor D, *Biomechanical response of the passive human knee joint under anterior–posterior forces*. *Clinical Biomechanics* 13(8):625–633, 1998. **13**(8): p. 625-633.
146. Jilani A, S.-A.A., Bendjaballah M, *Biomechanics of human tibio-femoral joint in axial rotation*. *Knee*, 1997. **4**(4): p. 203-213.
147. Moglo K, S.-A.A., *On the coupling between anterior and posterior cruciate ligaments, and knee joint response under anterior femoral drawer in flexion: a finite element study*. *Clinical Biomechanics*, 2003. **18**(8): p. 751-759.
148. Shirazi R, S.-A.A., Hurtig M, *Role of cartilage collagen fibrils networks in knee joint biomechanics under compression*. *Journal of Biomechanics* 2008. **41**(16): p. 3340-3348.
149. Yang NH, N.-H.H., Canavan PK, Vaziri A, *Effect of frontal plane tibiofemoral angle on the stress and strain at the knee cartilage during the stance phase of gait*. *Journal of Orthopaedic Research* 2010. **28**(12): p. 1539-1547.
150. Beillas P, P.G., Tashman S, Yang K, *A new method to investigate in vivo knee behavior using a finite element model of the lower limb*. *Journal of Biomechanics*, 2004. **37**(7): p. 1019-1030.
151. Asgari M., K.S.S., *Crash Injury Analysis of Knee Joint Considering Pedestrian Safety*. *J Biomed Phys Eng*, 2019. **9**(5): p. 569–578.
152. Frazer, L.L., Santschi, Elizabeth M, and Fischer, Kenneth J, *Impact of a Void in the Equine Medial Femoral Condyle on Bone Stresses and Peak Contact Pressures in a Finite Element Model*. *Veterinary Surgery*, 2018. **48**(2): p. 237-246.
153. Kang, K.-T., Son, Juhyun, Kwon, Sae Kwang, Kwon, Oh-Ryong, Park, Joon-Hee, and Koh, Yong-Gon, *Finite Element Analysis for the Biomechanical Effect of Tibial Insert Materials in Total Knee Arthroplasty*. *Composite Structures*, 2018. **201**: p. 141-150.
154. Silvia Pianigiani, D.C., M. D’Aiuto, W.Pascale, B. Innocenti, *Sensitivity analysis of the material properties of different soft-tissues: implications for a subject specific knee arthroplasty*. *Muscles Ligaments Tendons J*, 2018. **7**(4): p. 546-557.
155. Lee, H.-H., *Finite Element Simulations with ANSYS Workbench 17*. 2017, USA SDC Publications, Stephen Schroff.
156. newman, p. *MPC contact regions / boundary conditions conflict*. *General Mechanical* 2018; Available from: <https://forum.ansys.com/forums/topic/mpc-contact-regions-boundary-conditions-conflict/>.
157. Harris, M.D., et al., *A Combined Experimental and Computational Approach to Subject-Specific Analysis of Knee Joint Laxity*. *J Biomech Eng*, 2016. **138**(8).

# Annexes

## Appendix A

Thank you for the above revised ethics application.

The Departmental Ethics Committee is satisfied with all changes in the revised application and gave their approval for this project with immediate effect.

Good luck with your project and remember you must inform us in writing of any changes to the project and any unforeseen circumstances which arise during the project.

Regards

*Linda Gilmour (Secretary to)*  
Departmental Ethics Committee

Regards

*Linda Gilmour*

Secretary to Professor Stuart Reid  
/Administrative Assistant  
University of Strathclyde  
Department of Biomedical Engineering  
Wolfson Building  
106 Rottenrow East  
Glasgow G4 0NW

## Appendix B

This is Reyhaneh Asadirad, 4<sup>th</sup> year Biomedical Engineering PhD student. We would like to study the influence of the operator on performing the semi-automatic segmentation. The title of this study is "Inter- and intra-examiner variability of 4DCT image segmentation of the knee" and the chief investigator of this study is Dr. Phil Riches.

CT images of the knee are used for planning some types of knee surgeries, e.g. knee joint replacements. In order to do so, the bony parts of the knee need to be identified, and this is known as segmentation. Segmentation can be done manually, semi-automatically, or fully automatically. It is mainly done semi-automatically in which some part of the segmentation process is performed by an operator and some by the computer. The purpose of this research is to investigate the influence of the operator on performing the semi-automatic segmentation. We are asking the question: does their outcome vary if they perform the same segmentation multiple times? We also want to determine whether different operators generate different segmentations of the same CT image.

Participating in this study is completely voluntarily and participants have the right to withdraw from the experiment at any time. Participating, not participating or withdrawing from this research will no way influence your standing or relationship within the University. However, by participating to this project, you can gain some image processing segmentation experience.

The research team are inviting participants over 18 years of age to attend to 4 sessions of training. Each training session will last up to 1h. During the training session, a tutorial sheet will provide written guidance on the segmentation process. Once trained, volunteers will attend the experimental session for approximately two hours. Participants will be allowed to reference the tutorial to remember the steps involved. The volunteers will be asked to segment the same CT scan image file five times in order to determine the variability within a person. The exclusion and inclusion criteria outlined below:

As a Biomedical Engineering student, you have the ideal technical and anatomical understanding for this project. We are only recruiting Biomedical Engineers, as this process would be typically done by a biomedical engineer as part of their job.

We have some necessary inclusion and exclusion criteria, which are:

### Inclusion Criteria

- Ability to use a standard, mouse-operated Windows PC, without additional accessibility features
- Two negative lateral flow tests in the week prior to training and the experimental sessions
- To be in training for a biomedical engineering degree, or equivalent technical competence, understanding of knee anatomy and the intended outcome of the process of segmentation
- Self-reported "good" eyesight with or without glasses or contact lenses
- To be able to sit comfortably in front of a computer for about 2 hours



### Participant Information Sheet

**Name of department:** Biomedical Engineering

**Title of the study:** Inter- and intra-examiner variability of 4DCT image segmentation of the knee

#### Introduction

Hello. This project is led by Reyhaneh Asadirad, a PhD student in the Department of Biomedical Engineering, and supervised by Dr Phil Riches and Dr. Danial Kahani, also in the Department of Biomedical Engineering. We hope you can consider volunteering for this important study.

#### What is the purpose of this research?

CT images of the knee are used for planning some types of knee surgeries, e.g. knee joint replacements. In order to do so, the bony parts of the knee need to be identified, and this is known as segmentation. Segmentation can be done manually, semi-automatically, or fully automatically. It is mainly done semi-automatically in which some part of the segmentation process is performed by an operator and some by the computer. We would like to study the influence of the operator on performing the semi-automatic segmentation. We are asking the question: does their outcome vary if they perform the same segmentation multiple times? We also want to determine whether different operators generate different segmentations of the same CT image. This research may have significant implications regarding the workflow of analysing CT images.

#### Do you have to take part?

Participating in this study is completely voluntarily and participants have a right to withdraw from the experiment at any time. Participating, not participating or withdrawing from this research will in no way influence your standing or relationship within the University.

#### What will you do in the project?

The participants will be asked to attend to 4 sessions of training. Each training session will last up to 1h. During the training session a tutorial sheet will explain and provide written guidance on the segmentation process. Once trained, volunteers will attend the experimental session for approximately two hours. Participants will be allowed to reference the tutorial to remember the steps involved. The volunteers will be asked to segment the same CT scan image file five times in order to determine the variability within a person.

#### Why have you been invited to take part?

As a Biomedical Engineering student, you have the ideal technical and anatomical understanding for this project. We are only recruiting Biomedical Engineers, as this process would be typically done by a biomedical engineer as part of their job.

We have some necessary inclusion and exclusion criteria, which are:

The place of useful learning

The University of Strathclyde is a charitable body, registered in Scotland, number SC015263

## Appendix D

# Consent Form

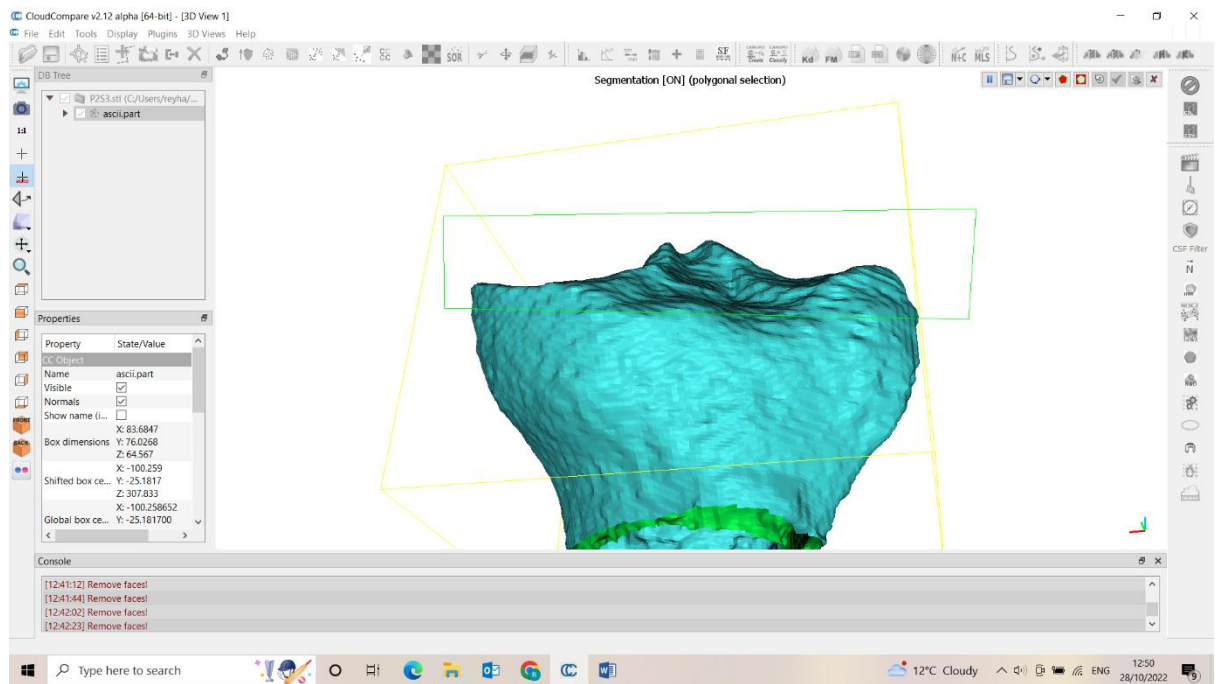
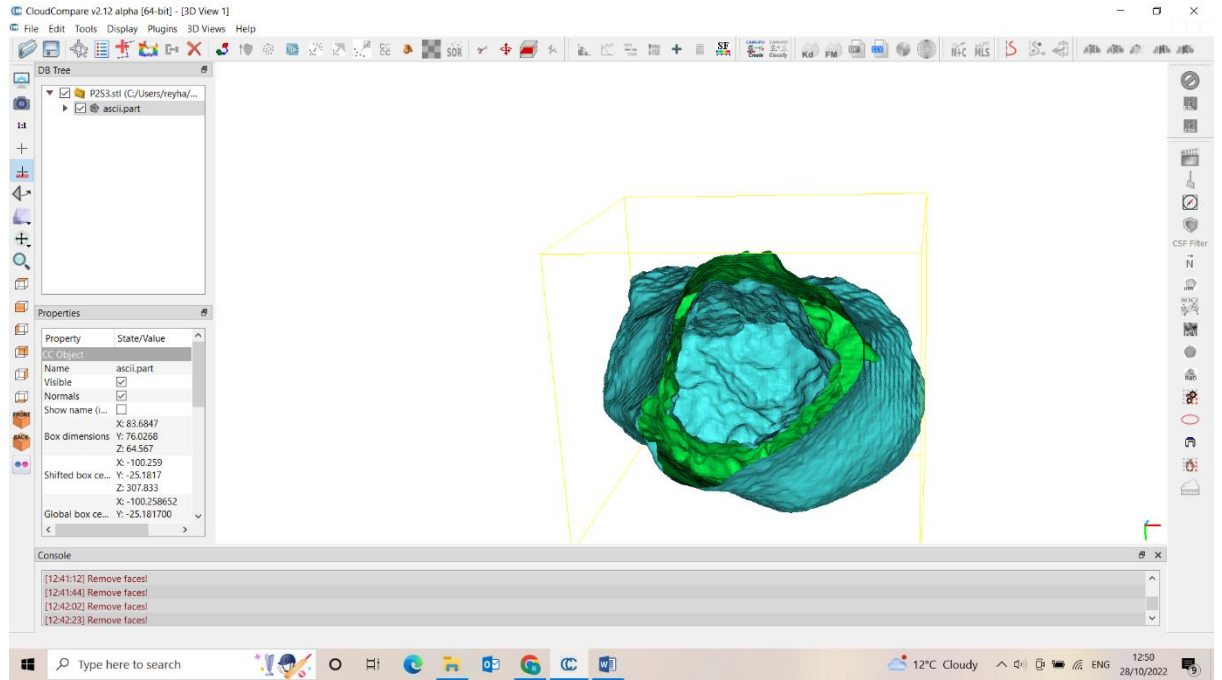
**Name of department: Biomedical Engineering**

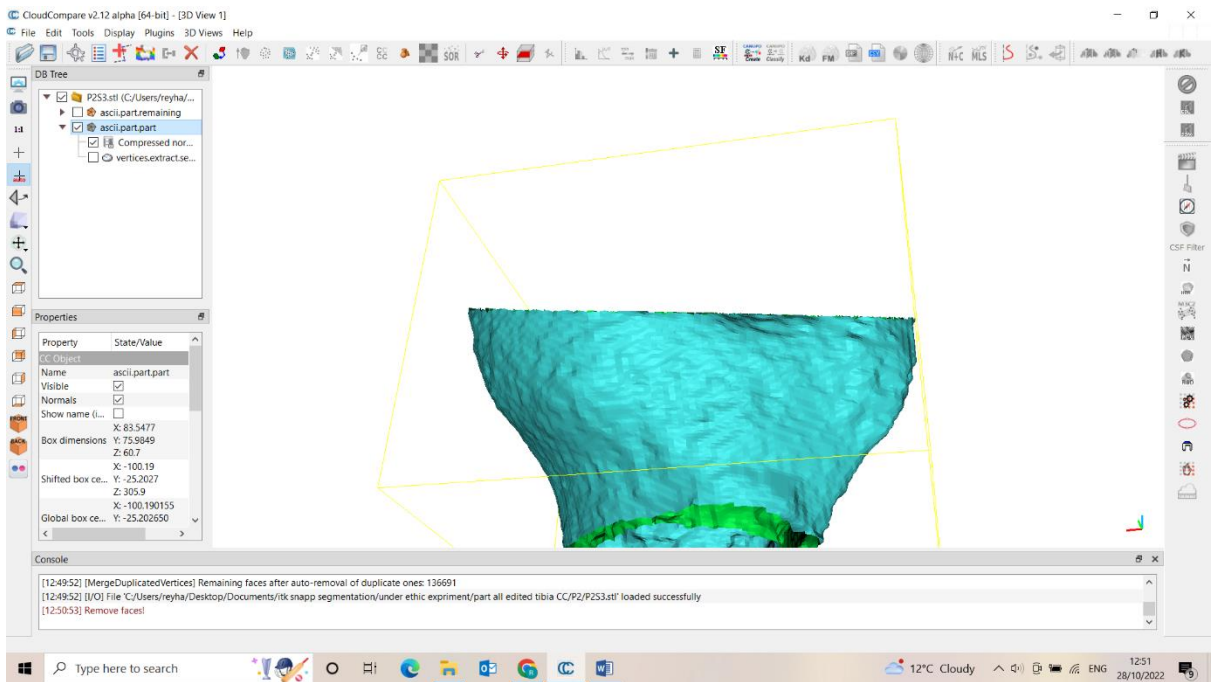
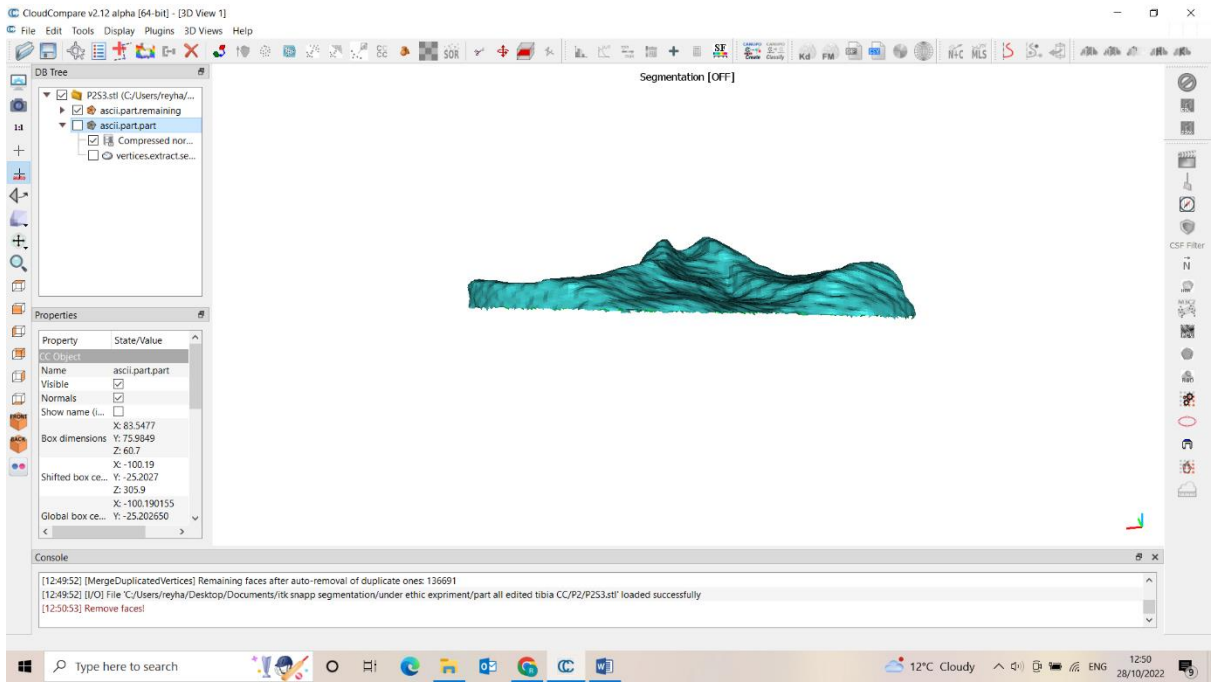
**Title of the study: Inter- and intra-examiner variability of 4DCT image segmentation of the knee**

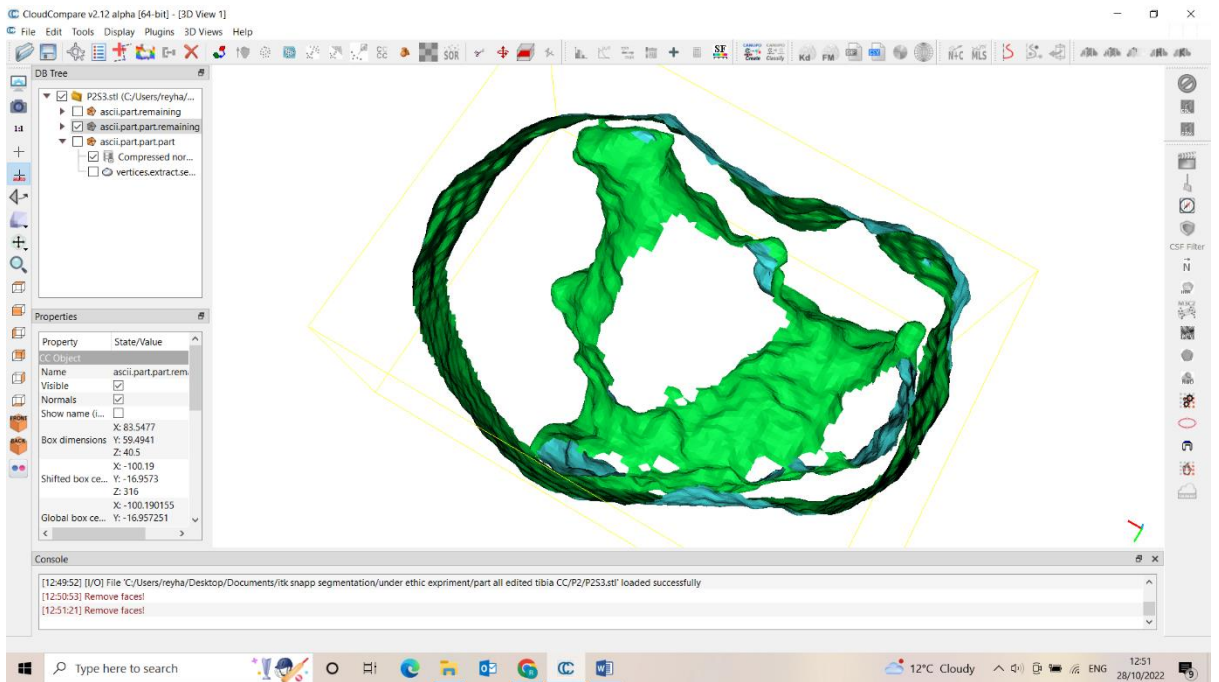
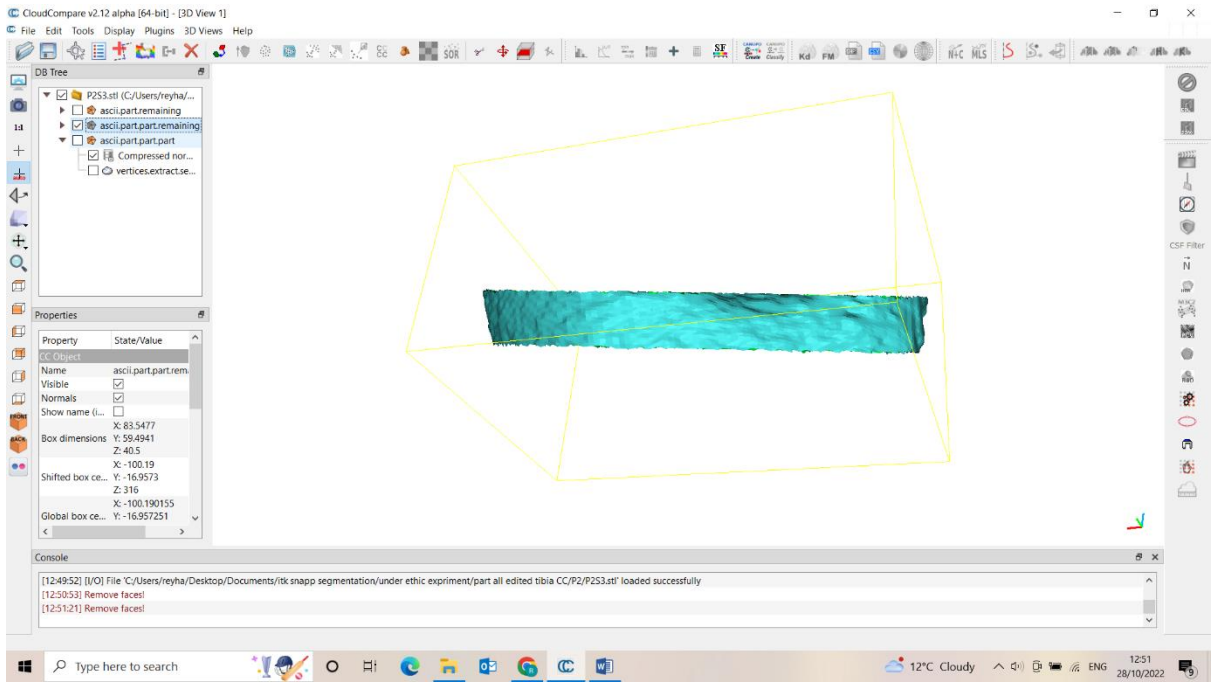
- I confirm that I have read and understood the Participant Information Sheet for the above project and the researcher has answered any queries to my satisfaction.
- I confirm that I have read and understood the Privacy Notice for Participants in Research Projects and understand how my personal information will be used and what will happen to it (i.e. how it will be stored and for how long).
- I understand that my participation is voluntary and that I am free to withdraw from the project at any time, up to the point of completion, without having to give a reason and without any consequences.
- I understand that I can request the withdrawal from the study of some personal information and that whenever possible researchers will comply with my request.
- I understand that anonymised data (i.e. data that do not identify me personally) cannot be withdrawn once they have been included in the study.
- I understand that any information recorded in the research will remain confidential and no information that identifies me will be made publicly available.
- I consent to being a participant in the project.

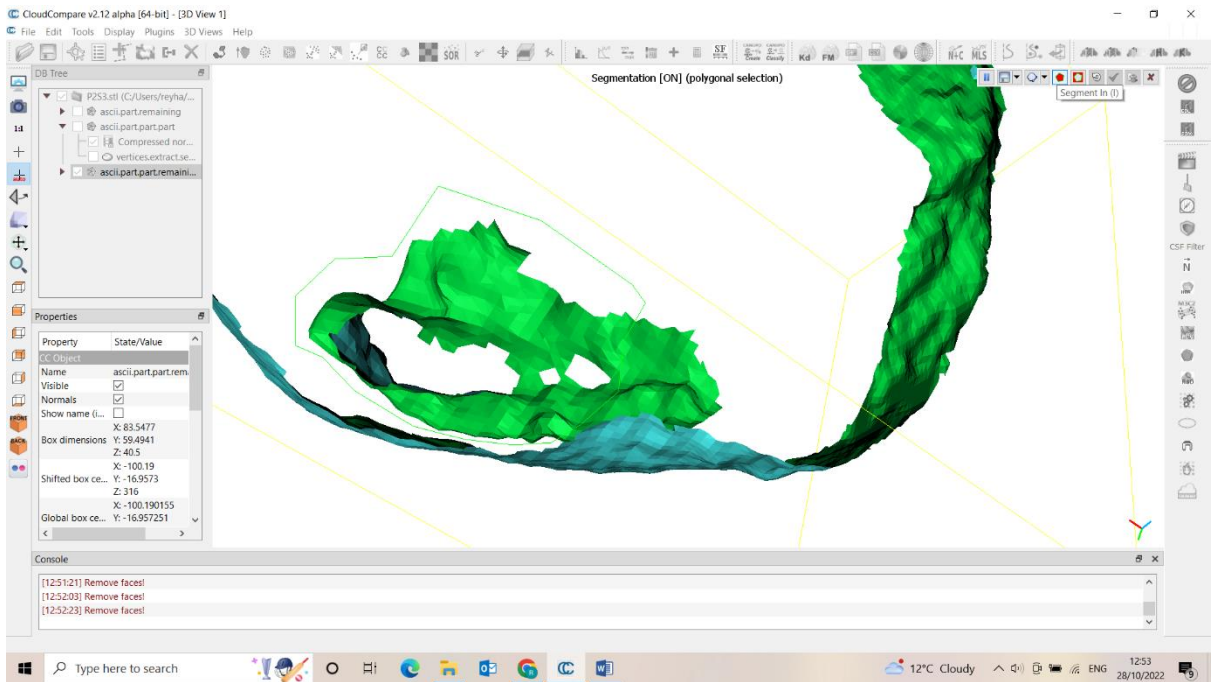
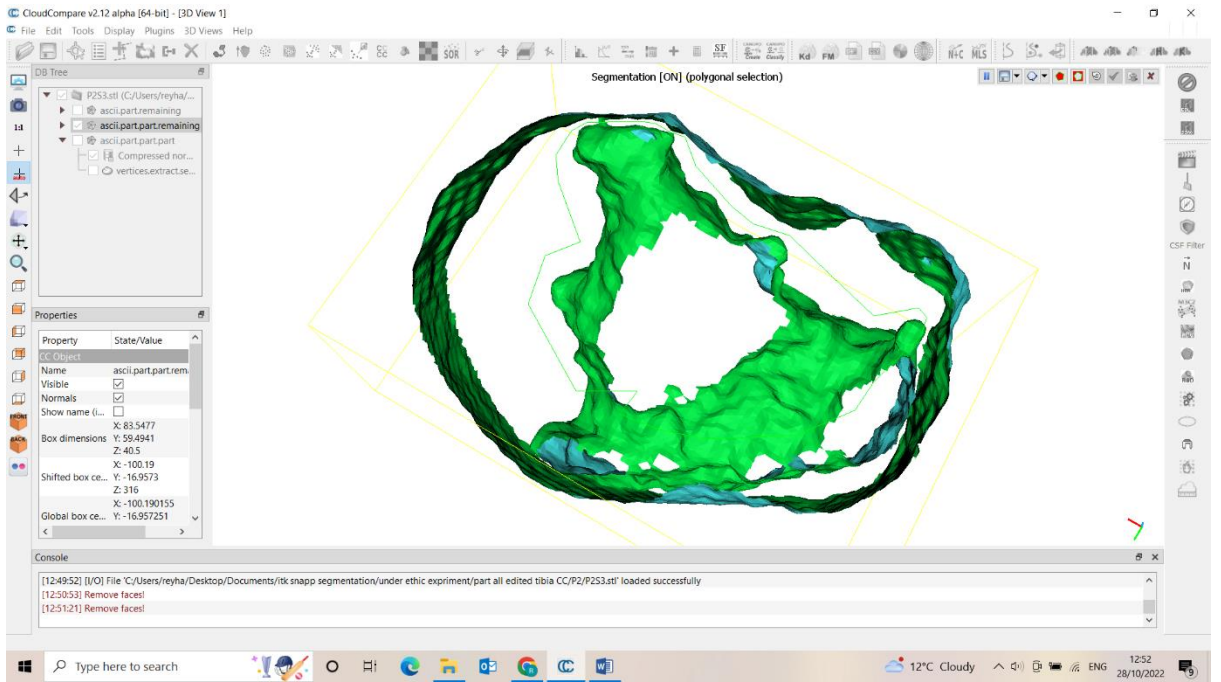
(PRINT NAME)	
Signature of Participant:	Date:

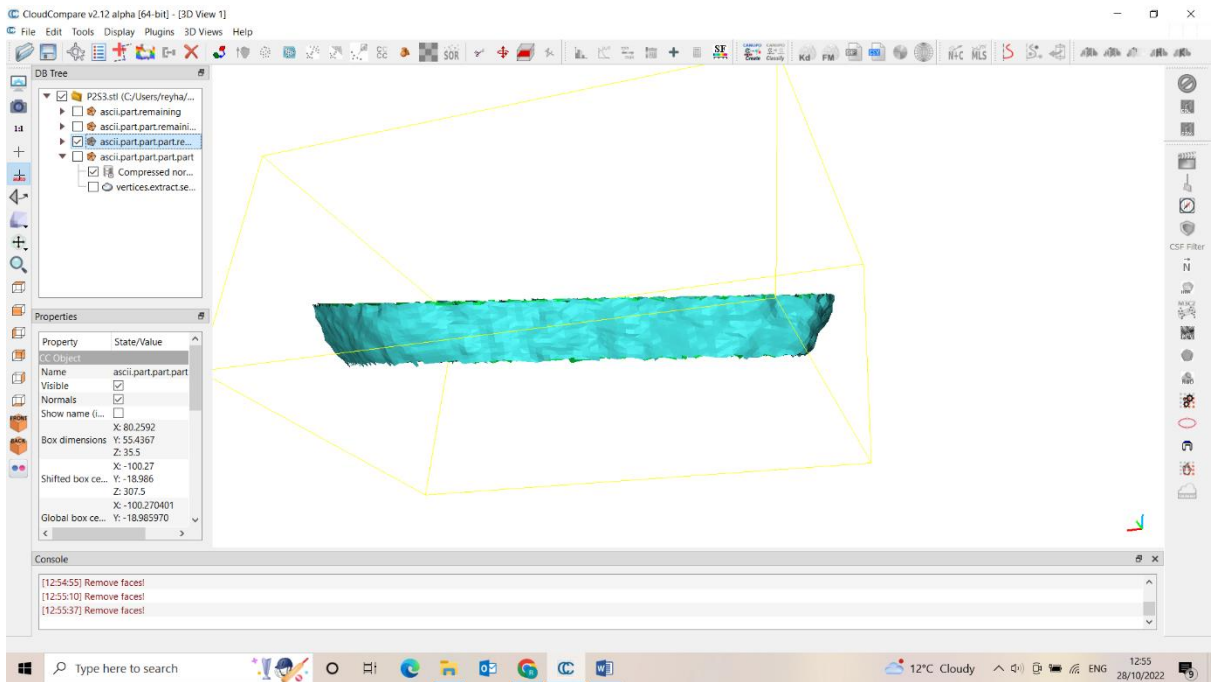
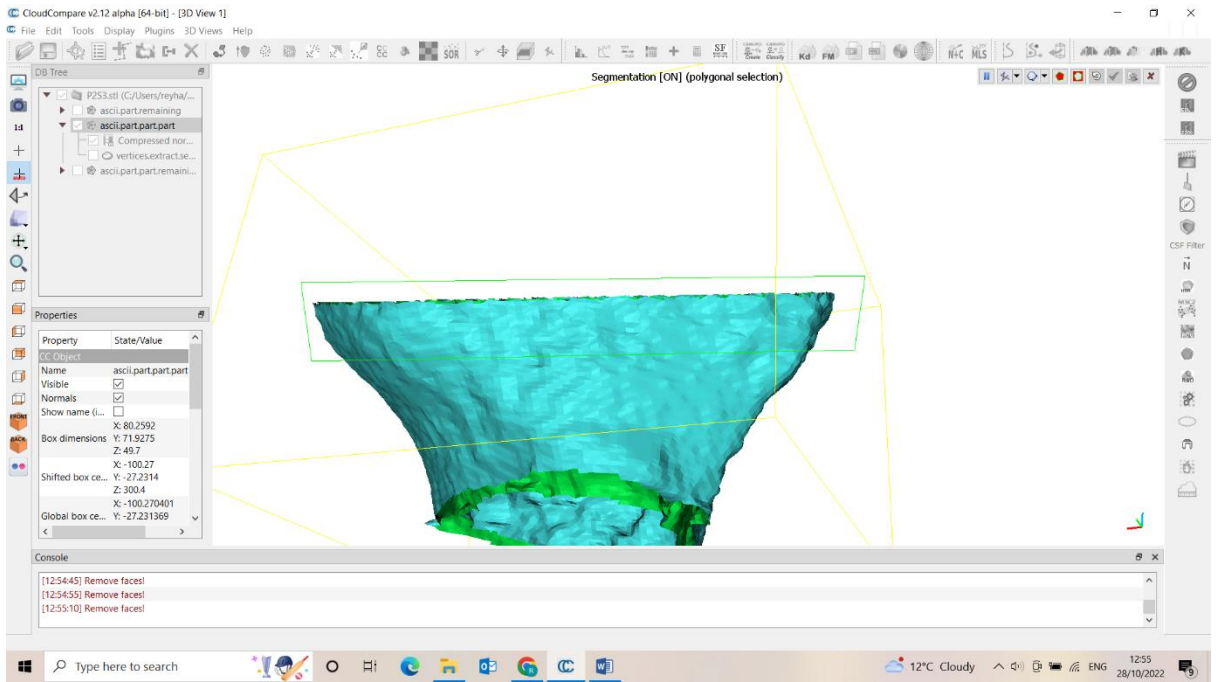
# Appendix E

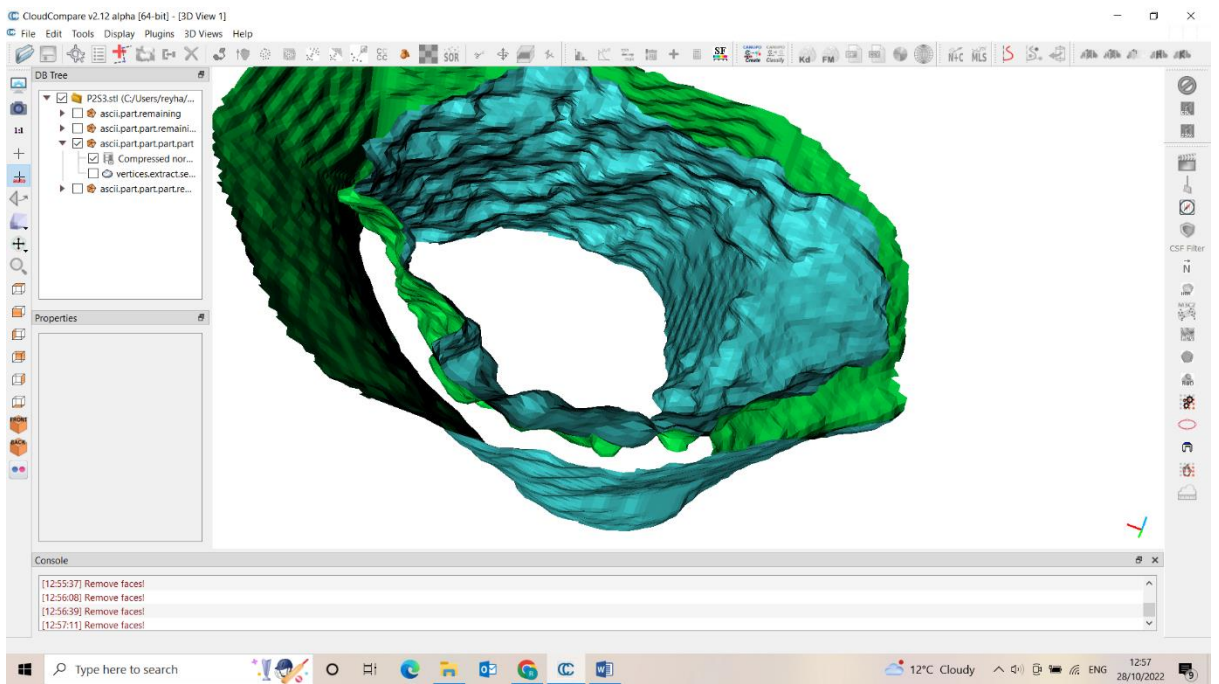
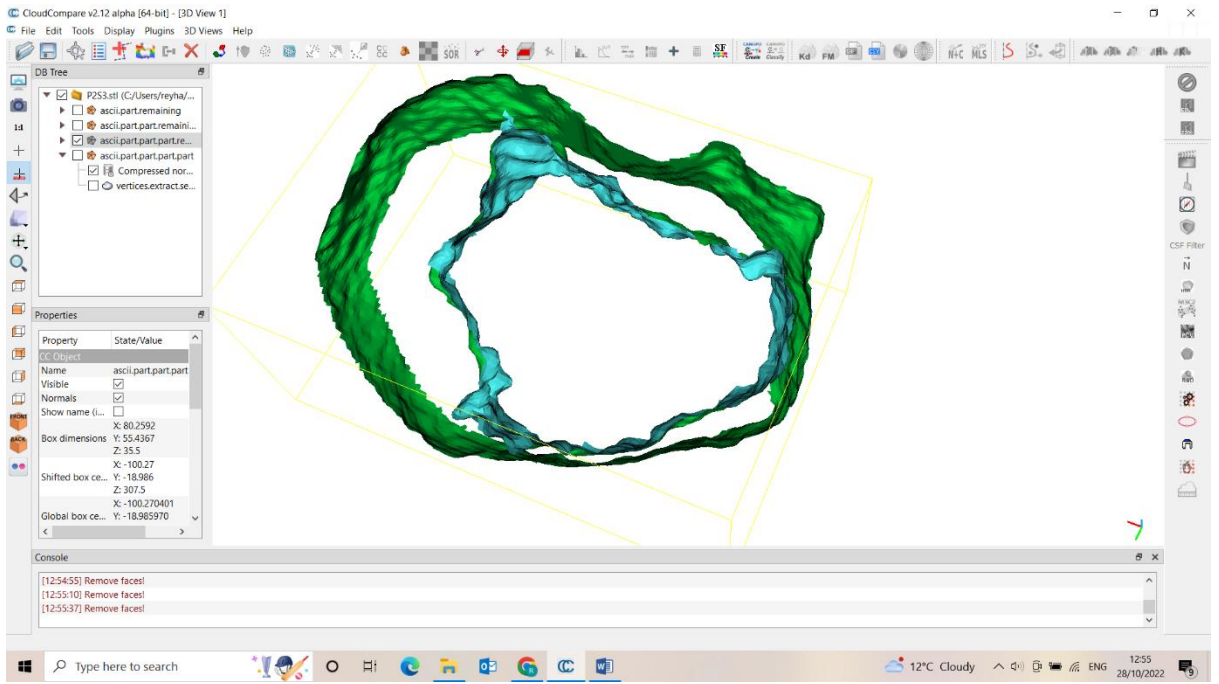


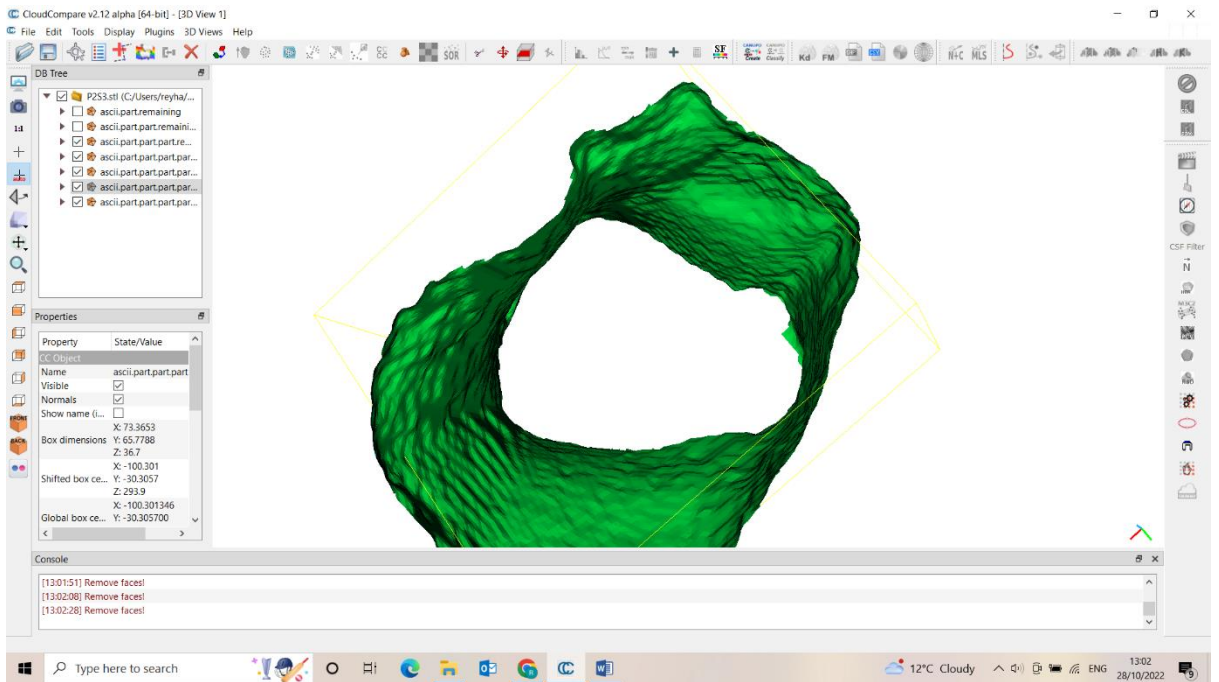
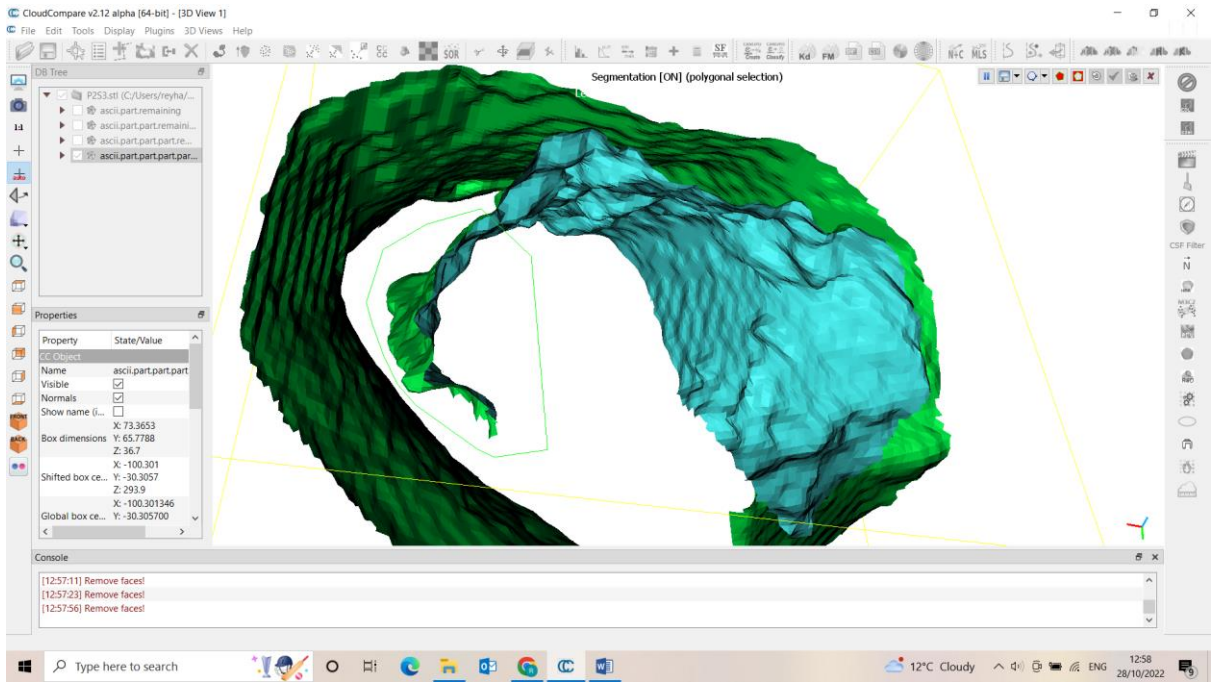


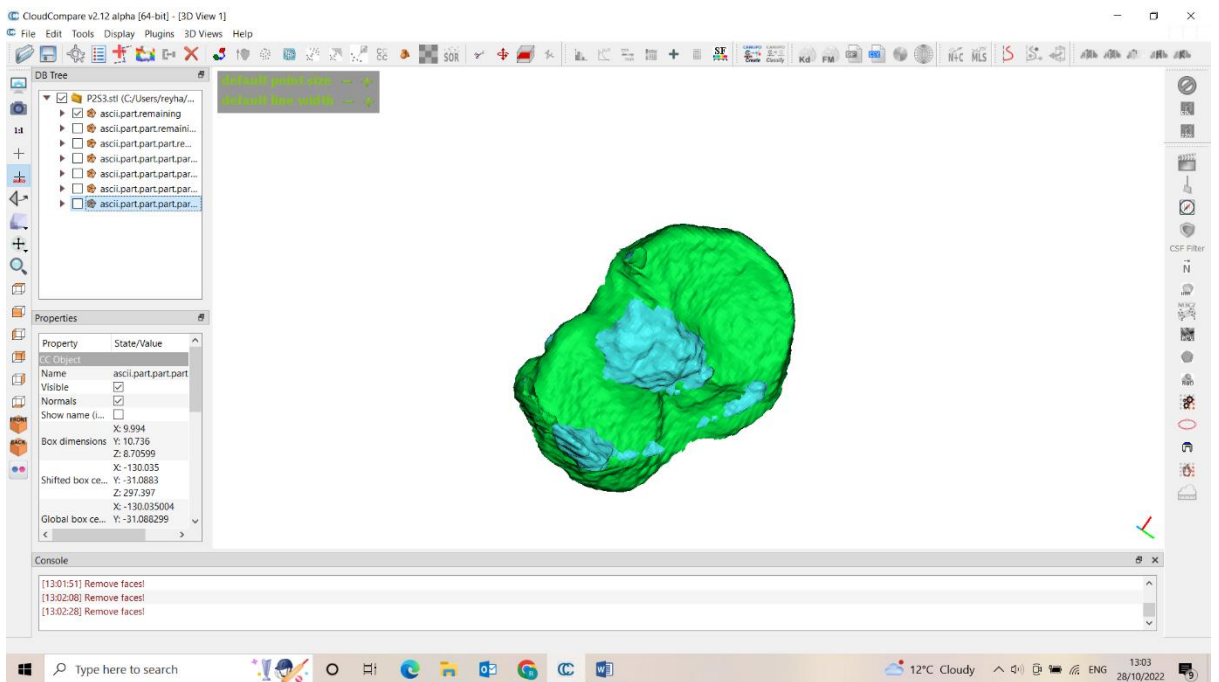
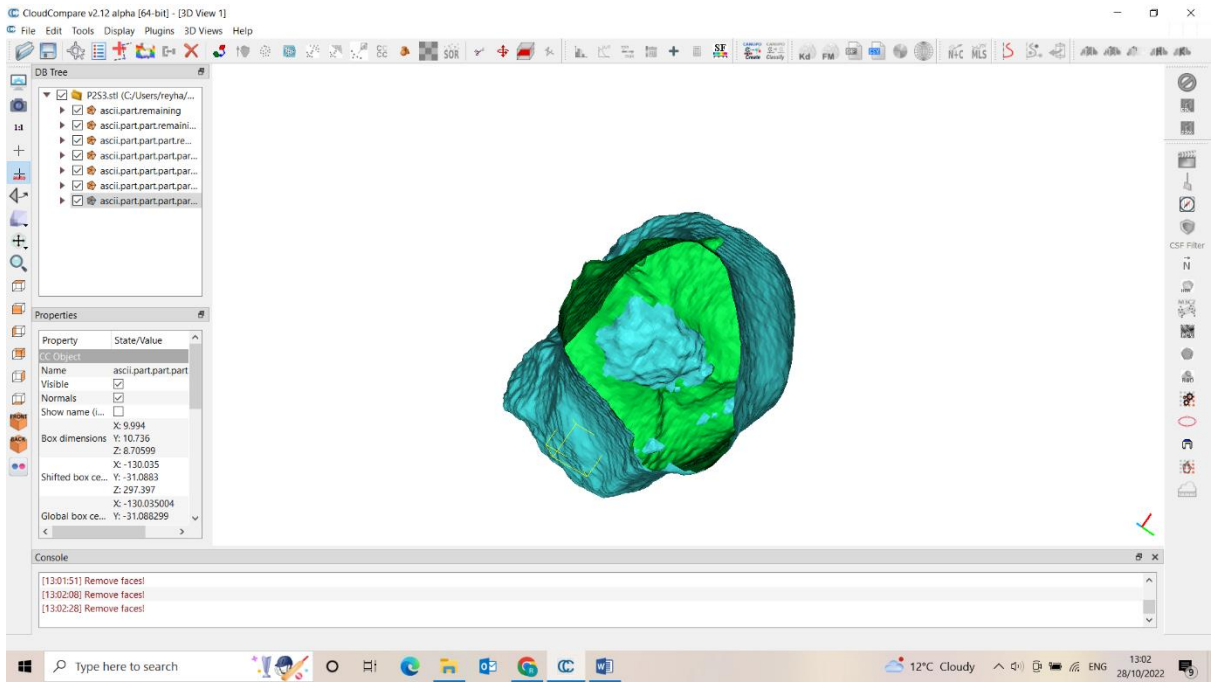




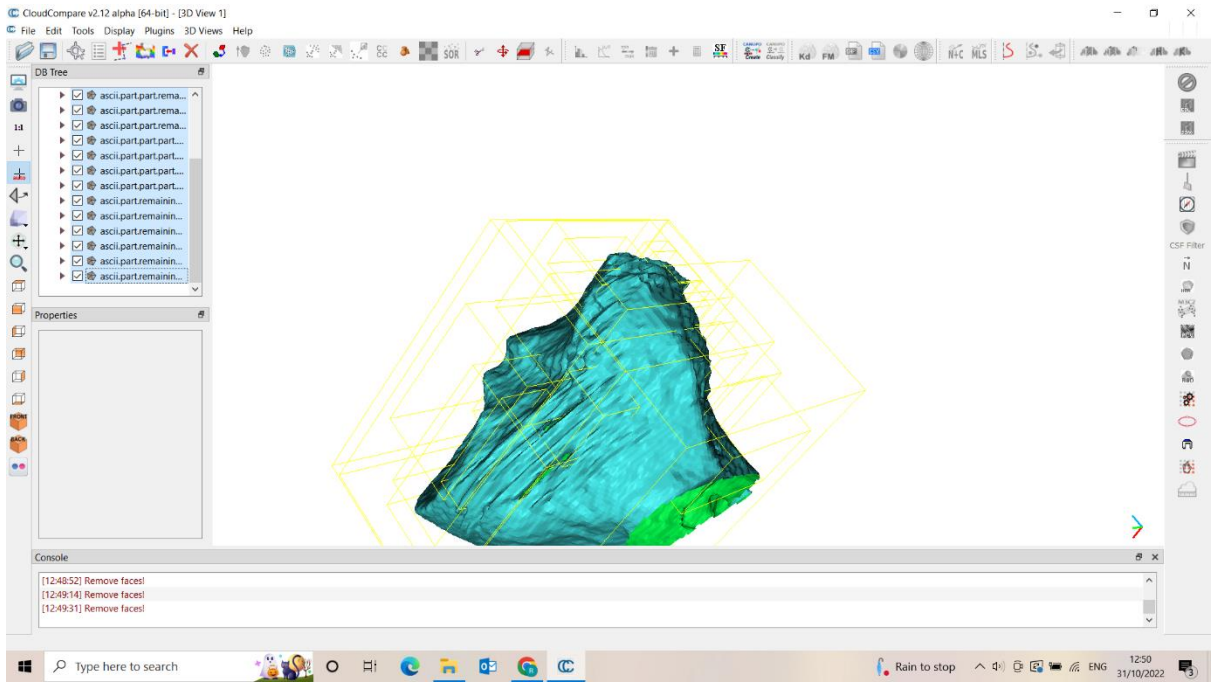
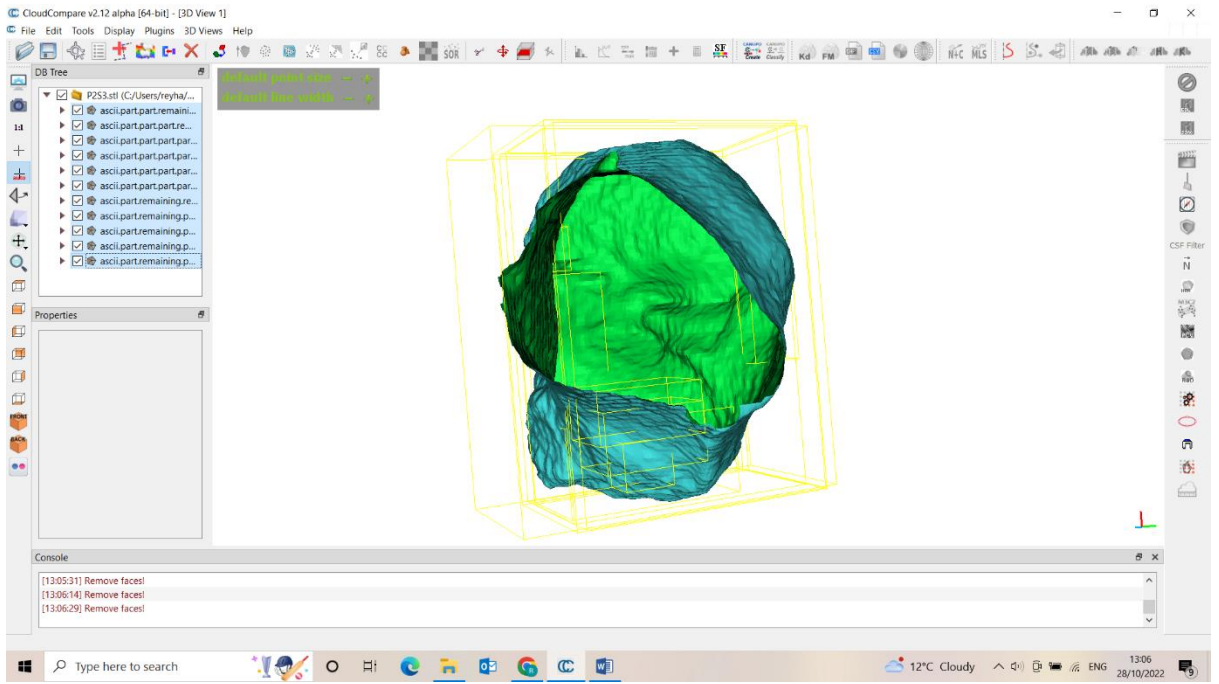




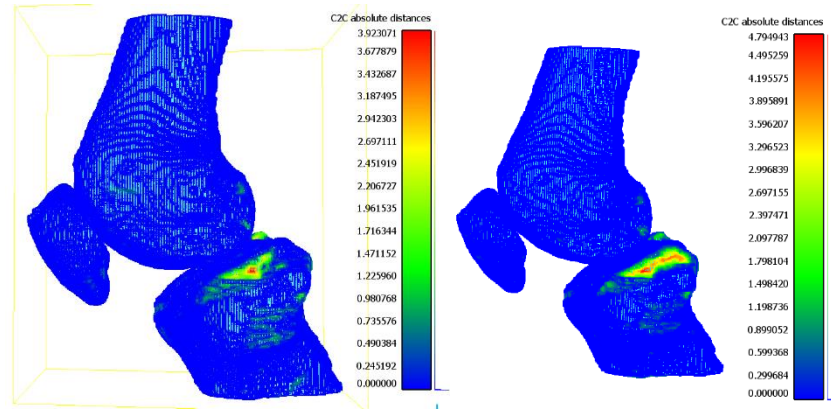




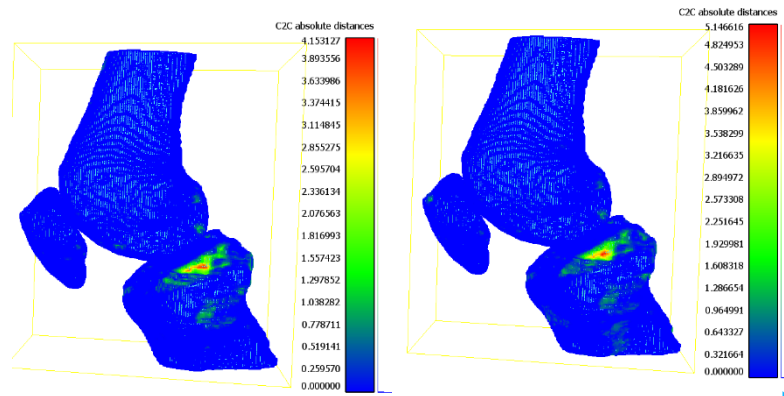




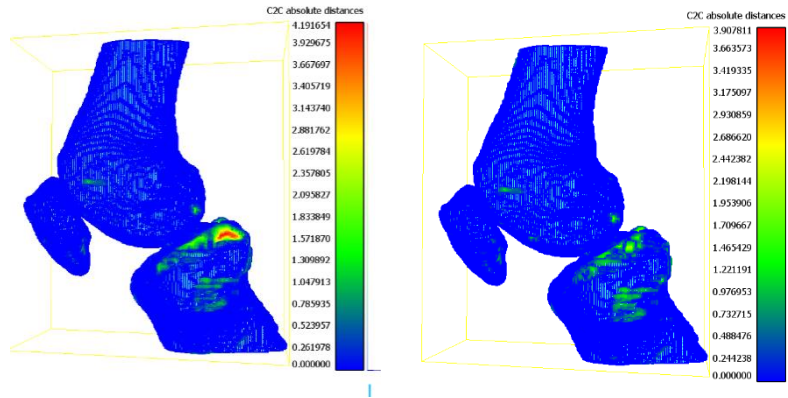
## Appendix F



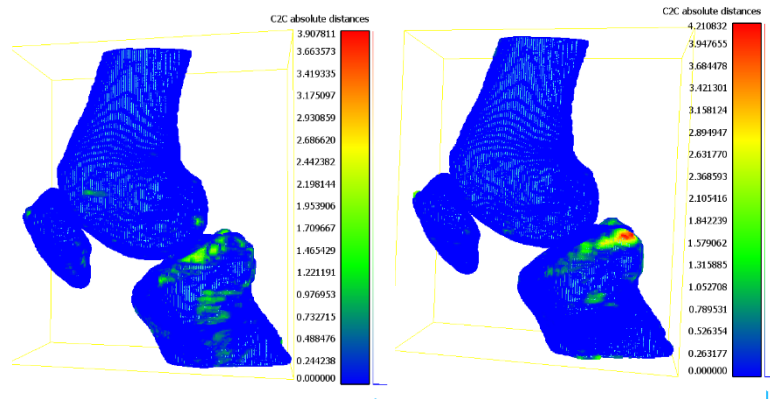
a) C2C distance comparison of S1 and S2. (b) C2C distance comparison of S1 and S2



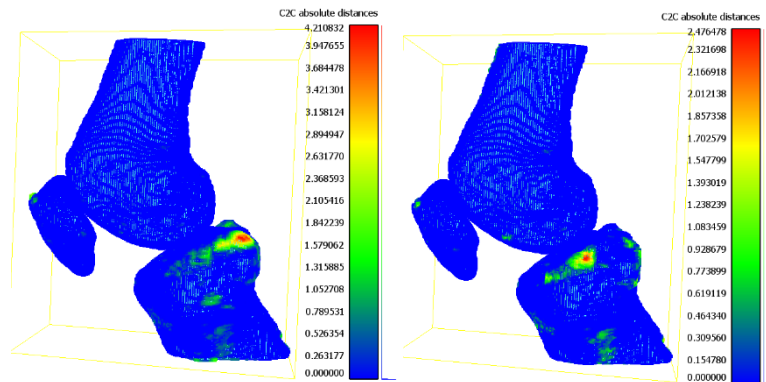
(a) C2C distance comparison of S1 and S4. (b) C2C distance comparison of S1 and S5



(a) C2C distance comparison of S2 and S3. (b) C2C distance comparison of S2 and S4



(a) C2C distance comparing of S2 and S5. (b) C2C distance comparison of S3 and S4



(a) C2C distance comparison of S3 and S5. (b) C2C comparison of S4 and S5

## Appendix G

Main all:

```
clear all;
close all
clc;

% Select folder containing the STL files
folder_path = uigetdir;
if folder_path == 0
    return;
end
file_list = dir(fullfile(folder_path, '*.stl'));
num_files = length(file_list);

% Initialize the results table
results = [];

% Loop through every pair of files
for i = 1:num_files
    for j = i+1:num_files
        % Read and process the STL files
        file1 = fullfile(folder_path, file_list(i).name);
        file2 = fullfile(folder_path, file_list(j).name);

        [hd, dsc, ji, pc1_count, pc2_count, n_similar_nodes,
        threshold, false_positives, false_negatives, mean_dist,
        median_dist, max_dist, std_dist, volume_similarity] =
        compare_stl_files(file1, file2);

        % Save the results
        results = [results; {file_list(i).name,
        file_list(j).name, hd, dsc, ji, pc1_count, pc2_count,
        n_similar_nodes, threshold, false_positives, false_negatives,
        mean_dist, median_dist, max_dist, std_dist,
        volume_similarity}];
    end
end

% Save the results to an Excel file
results_table = cell2table(results, 'VariableNames', {'File1',
'File2', 'Hausdorff_Distance', 'Dice_Similarity_Coefficient',
'Jaccard_Index', 'Points_in_Mesh1', 'Points_in_Mesh2',
'Similar_Nodes', 'Threshold', 'False_Positives',
'False_Negatives', 'Mean_Distance', 'Median_Distance',
'Max_Distance', 'Standard_Deviation', 'Volume_Similarity'});
writetable(results_table, 'results.xlsx');

% Extract the Hausdorff distances
hd_values = cell2mat(results(:, 3));

% Initialize the matrix for Hausdorff distances
hd_matrix = zeros(num_files);
```

```

% Fill the matrix
index = 1;
for i = 1:num_files
    for j = i+1:num_files
        % Use the index variable to access the right element
in hd_values
        hd_matrix(i, j) = hd_values(index);
        hd_matrix(j, i) = hd_values(index);
        index = index + 1;
    end
end

% Calculate the ICC
[~, ~, ~, ICC_results] = ICC(hd_matrix, 'A-1');
ICC_results
% Repeat the process for other measurement types (dsc, ji,
etc.)

```

### Compare stl files:

```

function [hd, dsc, ji, pc1_count, pc2_count, n_similar_nodes,
threshold, false_positives, false_negatives, mean_dist,
median_dist, max_dist, std_dist, volume_similarity] =
compare_stl_files(file1, file2)
    % Read the STL files
    tri1 = stlread(file1);
    tri2 = stlread(file2);

    % Extract vertices
    vertices1 = tri1.Points;
    vertices2 = tri2.Points;

    % Create point clouds
    % Create point clouds
    pc1 = pointCloud(vertices1);
    pc2 = pointCloud(vertices2);

    % Assign point counts
    pc1_count = pc1.Count;
    pc2_count = pc2.Count;

    % Align point clouds
    [tform, pc2_aligned] = pcregrigid(pc2, pc1, 'InlierRatio',
0.7, 'MaxIterations', 1000, 'Tolerance', [1e-4, 1e-4]);

    % Calculate the Hausdorff distance
    hd = hausdorff(pc1, pc2_aligned);

    % Calculate the Dice similarity coefficient and Jaccard
index
    threshold = 0.012;
    distances = pdist2(pc1.Location, pc2_aligned.Location,
'euclidean', 'smallest', 1);

```

```

    n_similar_nodes = sum(distances <= threshold);
    dsc = 2 * n_similar_nodes / (pc1.Count +
pc2_aligned.Count);
    ji = n_similar_nodes / (pc1.Count + pc2_aligned.Count -
n_similar_nodes);

    % Calculate false positive and false negative errors
    false_positives = sum(distances > threshold);
    false_negatives = pc2_aligned.Count - n_similar_nodes;

    % Calculate mean, median, max, and standard deviation of
distances
    mean_dist = mean(distances);
    median_dist = median(distances);
    max_dist = max(distances);
    std_dist = std(distances);

function hd = hausdorff(A, B)
    n = size(A.Location, 1);
    d = zeros(n, 1);

    parfor i = 1:n
        d(i) = min(pdist2(A.Location(i, :), B.Location));
    end

    hd = max(d);
end

end

```

## Appendix H

Average of 3 bones ten comparisons over three matrix

	DSC mean	JI mean	HD mean	DSC Std error	JI Std error	HD Std error
S1S2	0.884	0.804	3.638	0.019	0.027	0.316
S1S3	0.879	0.796	3.712	0.019	0.027	0.298
S1S4	0.870	0.785	3.650	0.020	0.028	0.266
S1S5	0.874	0.791	3.756	0.020	0.028	0.268
S2S3	0.892	0.815	3.173	0.017	0.024	0.237
S2S4	0.883	0.803	3.283	0.017	0.025	0.255
S2S5	0.886	0.807	3.071	0.018	0.026	0.290
S3S4	0.892	0.816	3.219	0.014	0.021	0.267
S3S5	0.898	0.824	3.118	0.016	0.022	0.270
S4S5	0.905	0.834	2.875	0.009	0.013	0.189

Table 12. Univariate Tests

Univariate Tests							
Source	Measure		Type III Sum of Squares	df	Mean Square	F	Sig.
bone	DSC	Sphericity Assumed	1.244	2	.622	25.850	<.001
		Greenhouse- Geisser	1.244	1.714	.726	25.850	<.001
		Huynh-Feldt	1.244	1.929	.645	25.850	<.001
		Lower-bound	1.244	1.000	1.244	25.850	<.001
	JI	Sphericity Assumed	2.937	2	1.468	33.235	<.001
		Greenhouse- Geisser	2.937	1.866	1.574	33.235	<.001
		Huynh-Feldt	2.937	2.000	1.468	33.235	<.001
		Lower-bound	2.937	1.000	2.937	33.235	<.001
	HD	Sphericity Assumed	767.739	2	383.870	94.003	<.001
		Greenhouse- Geisser	767.739	1.679	457.162	94.003	<.001

		Huynh-Feldt	767.739	1.882	407.886	94.003	<.001
		Lower-bound	767.739	1.000	767.739	94.003	<.001
Error(bone)	DSC	Sphericity Assumed	.674	28	.024		
		Greenhouse-Geisser	.674	23.990	.028		
		Huynh-Feldt	.674	27.010	.025		
		Lower-bound	.674	14.000	.048		
	JI	Sphericity Assumed	1.237	28	.044		
		Greenhouse-Geisser	1.237	26.124	.047		
		Huynh-Feldt	1.237	28.000	.044		
		Lower-bound	1.237	14.000	.088		
	HD	Sphericity Assumed	114.341	28	4.084		
		Greenhouse-Geisser	114.341	23.511	4.863		
		Huynh-Feldt	114.341	26.351	4.339		
		Lower-bound	114.341	14.000	8.167		
comparison	DSC	Sphericity Assumed	.046	9	.005	2.631	.008
		Greenhouse-Geisser	.046	2.077	.022	2.631	.087
		Huynh-Feldt	.046	2.446	.019	2.631	.076
		Lower-bound	.046	1.000	.046	2.631	.127
	JI	Sphericity Assumed	.090	9	.010	2.739	.006
		Greenhouse-Geisser	.090	2.145	.042	2.739	.077
		Huynh-Feldt	.090	2.546	.035	2.739	.066
		Lower-bound	.090	1.000	.090	2.739	.120
	HD	Sphericity Assumed	39.543	9	4.394	2.506	.011
		Greenhouse-Geisser	39.543	3.845	10.283	2.506	.055
		Huynh-Feldt	39.543	5.483	7.211	2.506	.033
		Lower-bound	39.543	1.000	39.543	2.506	.136
Error(comparison)	DSC	Sphericity Assumed	.242	126	.002		

		Greenhouse-Geisser	.242	29.085	.008		
		Huynh-Feldt	.242	34.244	.007		
		Lower-bound	.242	14.000	.017		
	JI	Sphericity Assumed	.459	126	.004		
		Greenhouse-Geisser	.459	30.036	.015		
		Huynh-Feldt	.459	35.643	.013		
		Lower-bound	.459	14.000	.033		
	HD	Sphericity Assumed	220.868	126	1.753		
		Greenhouse-Geisser	220.868	53.837	4.103		
		Huynh-Feldt	220.868	76.769	2.877		
		Lower-bound	220.868	14.000	15.776		
bone * comparison	DSC	Sphericity Assumed	.016	18	.001	.917	.558
		Greenhouse-Geisser	.016	4.116	.004	.917	.462
		Huynh-Feldt	.016	6.043	.003	.917	.487
		Lower-bound	.016	1.000	.016	.917	.354
	JI	Sphericity Assumed	.033	18	.002	.940	.531
		Greenhouse-Geisser	.033	4.410	.007	.940	.454
		Huynh-Feldt	.033	6.690	.005	.940	.477
		Lower-bound	.033	1.000	.033	.940	.349
	HD	Sphericity Assumed	39.551	18	2.197	1.288	.195
		Greenhouse-Geisser	39.551	4.366	9.059	1.288	.283
		Huynh-Feldt	39.551	6.590	6.002	1.288	.267
		Lower-bound	39.551	1.000	39.551	1.288	.275
Error(bone*comparison)	DSC	Sphericity Assumed	.240	252	.001		
		Greenhouse-Geisser	.240	57.618	.004		
		Huynh-Feldt	.240	84.604	.003		
		Lower-bound	.240	14.000	.017		

JI	Sphericity Assumed	.489	252	.002		
	Greenhouse-Geisser	.489	61.746	.008		
	Huynh-Feldt	.489	93.664	.005		
	Lower-bound	.489	14.000	.035		
HD	Sphericity Assumed	429.801	252	1.706		
	Greenhouse-Geisser	429.801	61.121	7.032		
	Huynh-Feldt	429.801	92.255	4.659		
	Lower-bound	429.801	14.000	30.700		

### Pairwise Comparisons

Measure	(I) bone	(J) bone	Mean Difference (I-J)	Std. Error	Sig. <sup>b</sup>	95% Confidence Interval for Difference <sup>b</sup>	
						Lower Bound	Upper Bound
DSC	1	2	.124*	.018	<.001	.076	.172
		3	.031	.015	.146	-.008	.071
	2	1	-.124*	.018	<.001	-.172	-.076
		3	-.092*	.021	.002	-.149	-.036
	3	1	-.031	.015	.146	-.071	.008
		2	.092*	.021	.002	.036	.149
JI	1	2	.193*	.023	<.001	.130	.256
		3	.059	.022	.057	-.002	.119
	2	1	-.193*	.023	<.001	-.256	-.130
		3	-.134*	.027	<.001	-.209	-.060
	3	1	-.059	.022	.057	-.119	.002
		2	.134*	.027	<.001	.060	.209
HD	1	2	-2.393*	.259	<.001	-3.096	-1.690
		3	.643*	.175	.008	.167	1.119
	2	1	2.393*	.259	<.001	1.690	3.096
		3	3.036*	.257	<.001	2.338	3.733
	3	1	-.643*	.175	.008	-1.119	-.167
		2	-3.036*	.257	<.001	-3.733	-2.338

Based on estimated marginal means

\*. The mean difference is significant at the .05 level.

b. Adjustment for multiple comparisons: Bonferroni.

## Appendix I

P_ID	DSCFS1S2	DSCFS1S3	DSCFS1S4	DSCFS1S5	DSCFS2S3	DSCFS2S4	DSCFS2S5	DSCFS3S4	DSCFS3S5	DSCFS4S5
P1	0.96	0.91	0.94	0.93	0.9	0.93	0.93	0.92	0.92	0.97
P2	0.96	0.96	0.94	0.95	0.96	0.94	0.95	0.96	0.97	0.97
P3	0.75	0.75	0.77	0.76	0.74	0.75	0.75	0.75	0.75	0.94
P4	0.62	0.64	0.65	0.65	0.79	0.79	0.78	0.91	0.91	0.93
P5	0.96	0.95	0.94	0.94	0.97	0.94	0.95	0.96	0.97	0.97
P6	0.95	0.98	0.96	0.96	0.96	0.94	0.95	0.96	0.97	0.96
P7	0.96	0.97	0.97	0.97	0.97	0.97	0.98	0.98	0.98	0.98
P8	0.96	0.96	0.96	0.96	0.96	0.96	0.96	0.97	0.97	0.97
P9	0.97	0.97	0.97	0.97	0.97	0.97	0.97	0.97	0.97	0.97
P10	0.96	0.96	0.96	0.96	0.97	0.98	0.97	0.97	0.97	0.98
P11	0.97	0.98	0.99	0.98	0.98	0.98	0.99	0.99	0.98	0.98
P12	0.97	0.97	0.97	0.97	0.96	0.97	0.97	0.97	0.97	0.97
P13	0.97	0.96	0.97	0.97	0.97	0.97	0.97	0.96	0.97	0.97
P14	0.97	0.97	0.96	0.97	0.97	0.97	0.97	0.97	0.96	0.97
P15	0.97	0.98	0.98	0.97	0.97	0.96	0.96	0.98	0.97	0.96

### Intraclass Correlation Coefficient

	Intraclass Correlation <sup>b</sup>	95% Confidence Interval		F Test with True Value 0			
		Lower Bound	Upper Bound	Value	df1	df2	Sig
Single Measures	.794 <sup>a</sup>	.655	.909	39.46 5	14	126	<.001
Average Measures	.975	.950	.990	39.46 5	14	126	<.001

Two-way random effects model where both people effects and measures effects are random.

- a. The estimator is the same, whether the interaction effect is present or not.
- b. Type C intraclass correlation coefficients using a consistency definition. The between-measure variance is excluded from the denominator variance.

P_ID	DSCTS1S2	DSCTS1S3	DSCTS1S4	DSCTS1S5	DSCTS2S3	DSCTS2S4	DSCTS2S5	DSCTS3S4	DSCTS3S5	DSCTS4S5
P1	0.68	0.68	0.58	0.63	0.76	0.65	0.7	0.76	0.83	0.76
P2	0.84	0.84	0.85	0.81	0.82	0.83	0.79	0.88	0.85	0.88
P3	0.5	0.53	0.54	0.51	0.54	0.56	0.53	0.59	0.56	0.63
P4	0.68	0.67	0.66	0.67	0.76	0.76	0.76	0.86	0.84	0.86
P5	0.8	0.76	0.76	0.83	0.71	0.74	0.78	0.71	0.75	0.76
P6	0.87	0.86	0.86	0.87	0.89	0.87	0.89	0.86	0.9	0.87
P7	0.86	0.85	0.62	0.67	0.89	0.63	0.7	0.63	0.69	0.76
P8	0.92	0.9	0.91	0.89	0.9	0.91	0.9	0.9	0.88	0.9
P9	0.88	0.86	0.84	0.87	0.85	0.84	0.88	0.84	0.85	0.84
P10	0.88	0.87	0.87	0.89	0.9	0.89	0.92	0.87	0.89	0.89
P11	0.91	0.91	0.93	0.94	0.9	0.91	0.92	0.91	0.92	0.93
P12	0.92	0.91	0.91	0.9	0.9	0.9	0.9	0.89	0.88	0.89
P13	0.86	0.85	0.8	0.85	0.86	0.81	0.86	0.8	0.86	0.81
P14	0.85	0.86	0.84	0.86	0.89	0.88	0.88	0.88	0.89	0.86
P15	0.86	0.86	0.83	0.87	0.86	0.81	0.85	0.81	0.86	0.83

### Intraclass Correlation Coefficient

	Intraclass Correlatio n <sup>b</sup>	95% Confidence Interval		F Test with True Value 0			
		Lower Bound	Upper Bound	Value	df1	df2	Sig
Single Measures	.839 <sup>a</sup>	.722	.931	53.19 0	14	126	<.001
Average Measures	.981	.963	.993	53.19 0	14	126	<.001

Two-way random effects model where both people effects and measures effects are random.

a. The estimator is the same, whether the interaction effect is present or not.

b. Type C intraclass correlation coefficients using a consistency definition. The between-measure variance is excluded from the denominator variance.

P_ID	DSCPS1S2	DSCPS1S3	DSCPS1S4	DSCPS1S5	DSCPS2S3	DSCPS2S4	DSCPS2S5	DSCPS3S4	DSCPS3S5	DSCPS4S5
P1	0.84	0.83	0.81	0.8	0.82	0.82	0.8	0.92	0.93	0.93
P2	0.96	0.95	0.97	0.96	0.93	0.95	0.94	0.94	0.94	0.96
P3	0.85	0.83	0.82	0.78	0.84	0.81	0.77	0.82	0.77	0.86
P4	0.87	0.87	0.85	0.88	0.91	0.87	0.91	0.87	0.94	0.88
P5	0.92	0.94	0.93	0.92	0.94	0.95	0.9	0.96	0.91	0.91
P6	0.85	0.78	0.86	0.81	0.84	0.89	0.85	0.87	0.91	0.89
P7	0.94	0.93	0.9	0.95	0.95	0.92	0.95	0.93	0.94	0.91
P8	0.89	0.91	0.91	0.91	0.94	0.95	0.9	0.93	0.91	0.91
P9	0.88	0.88	0.87	0.88	0.96	0.95	0.95	0.98	0.98	0.97
P10	0.93	0.95	0.95	0.94	0.93	0.93	0.93	0.95	0.94	0.94
P11	0.93	0.91	0.92	0.93	0.94	0.95	0.95	0.93	0.94	0.95
P12	0.92	0.91	0.9	0.89	0.94	0.91	0.92	0.91	0.91	0.9
P13	0.96	0.96	0.95	0.94	0.95	0.95	0.93	0.94	0.94	0.93
P14	0.96	0.95	0.95	0.98	0.95	0.94	0.96	0.92	0.95	0.94
P15	0.83	0.83	0.85	0.83	0.83	0.94	0.9	0.82	0.83	0.89

### Intraclass Correlation Coefficient

	Intraclass Correlation <sup>b</sup>	95% Confidence Interval		F Test with True Value 0			
		Lower Bound	Upper Bound	Value	df1	df2	Sig
Single Measures	.702 <sup>a</sup>	.534	.860	24.52 7	14	126	<.001
Average Measures	.959	.920	.984	24.52 7	14	126	<.001

Two-way random effects model where both people effects and measures effects are random.

a. The estimator is the same, whether the interaction effect is present or not.

b. Type C intraclass correlation coefficients using a consistency definition. The between-measure variance is excluded from the denominator variance.